

## Distribution Agreement

In presenting this thesis as a partial fulfillment of the requirements for an advanced degree from Emory University, I hereby grant to Emory University and its agents the non-exclusive license to archive, make accessible, and display my thesis or dissertation in whole or in part in all forms of media, now or hereafter known, including display on the world wide web. I understand that I may select some access restrictions as part of the online submission of the thesis or dissertation. I retain all ownership rights to the copyright of the thesis or dissertation. I also retain the right to use in future works (such as articles or books) all or part of this thesis or dissertation.

Signature:

---

Arventh Velusamy

---

Date

DNA mechanocapsules: Force responsive tetrahedral DNA  
nanostructures with modular cargo delivery for targeting  
mechanical phenotypes of diseases

by

Arventh Velusamy  
Doctor of Philosophy  
Chemistry

---

Khalid Salaita, Ph.D.  
Advisor

---

David Lynn, Ph.D.  
Committee Member

---

Yonggang Ke, Ph.D.  
Committee Member

Accepted

---

Kimberly J. Arriola, PhD, MPH  
Dean of the James T. Laney School of Graduate Studies

---

Date

DNA mechanocapsules: Force responsive tetrahedral DNA  
nanostructures with modular cargo delivery for targeting  
mechanical phenotypes of diseases

by

Arventh Velusamy

B.S. Chemistry, Indian Institute of Science, 2016

M.S. Chemistry, Indian Institute of Science, 2017

Advisor: Khalid Salaita, Ph.D.

An abstract of  
a dissertation submitted to the Faculty of the  
James T. Laney School of Graduate Studies of Emory University  
in partial fulfillment of the requirements for the degree of  
Doctor of Philosophy  
in Chemistry  
2023

## Abstract

DNA mechanocapsules: Force responsive tetrahedral DNA nanostructures with modular cargo delivery for targeting mechanical phenotypes of diseases

by Arventh Velusamy

The mechanical dysregulation of cells is associated with a number of disease states, that spans from fibrosis to tumorigenesis. Hence, it is highly desirable to develop strategies to deliver drugs based on the “mechanical phenotype” of a cell. To achieve this goal, we designed and characterized DNA mechanocapsules (DMC) comprised of DNA tetrahedrons that are force responsive. Modeling showed the trajectory of force-induced DMC rupture and predicted how applied force spatial position and orientation tunes the force-response threshold. DMCs functionalized with adhesion ligands mechanically denature *in vitro* as a result of cell receptor forces. DMCs were designed to encapsulate macromolecular cargos such as dextran and oligonucleotide drugs with minimal cargo leakage and high nuclease resistance. Force-induced release and uptake of DMC cargo was validated by flow cytometry. Finally, we demonstrate force-induced mRNA knockdown of HIF1 $\alpha$  in a manner that is dependent on the magnitude of cellular traction forces. These results show that DMCs can be effectively used to target biophysical phenotypes which may find useful applications in immunology and cancer biology.



DNA mechanocapsules: Force responsive tetrahedral DNA  
nanostructures with modular cargo delivery for targeting  
mechanical phenotypes of diseases

by

Arventh Velusamy

B.S. Chemistry, Indian Institute of Science, 2016

M.S. Chemistry, Indian Institute of Science, 2017

Advisor: Khalid Salaita, Ph.D.

a dissertation submitted to the Faculty of the  
James T. Laney School of Graduate Studies of Emory University  
in partial fulfillment of the requirements for the degree of  
Doctor of Philosophy  
in Chemistry

2023

## Acknowledgement

I would like to take this opportunity to express my gratitude to my mentors, friends, and family whose invaluable support made the completion of this dissertation possible.

I have a profound sense of appreciation for Dr. Khalid Salaita whose mentorship has been indispensable to my growth as a researcher. I am immensely grateful to him for his support and for persuading me to continue the path towards a PhD. It would not be an understatement to mention here that without his guidance, I would not have progressed this far in my academic career. His scientific rigor and broad knowledge have motivated me to expand my thought processes and his approach to science will continue to have a deep impact on my future research. I would like to further express the support and guidance of my committee members Dr. Yonggang Ke and Dr. David Lynn. Their feedback and thoughtful discussions played a pivotal role in nurturing my scientific ideas and contributed immensely to their success.

I am immensely grateful for the wonderful people at Salaita lab, both past and present, who I am privileged to consider as colleagues: Alisina, Jessica, Rong, Dale, Brendan, Yixiao, Josh, Han, Roxy, Aaron, Jiahui, Anna, Allison, Hiroaki, Alex, Aysha, Radhika, Yuxin, Yuesong, Selma, Vageesha, Steven, Sarah, Yusha, Shuhong, Tharindu, Jhordan, Krista, Joe, Hus, Luona, Tianyi, Maia, Rachel, Rachel, and Thomas. I would also like to thank my collaborators Aysha, Rong, Yuesong, Victor, Radhika, Alisina, Dale, Hiroaki, Rachel, and Sarah who found my input valuable for their research. I would be remiss not to acknowledge the invaluable scientific input I received from Aysha, Radhika, Hiroaki, Steven, Alex, Rong, Joe, Vageesha and many other colleagues which were critical drivers for the success of my experiments. Personally, I would like to thank Aysha, Selma, Yuesong, Radhika, Alisina, Jessica, Sarah, Yusha, and Joe for being the warmest rays of light in the lab. I would also like to acknowledge Yuesong for being one of the lab members of all time.

My endeavor of pursuing a PhD while living far from home was only possible with the support of my friends. The personal support I had received from my roommates Palak, Sara, Siva, and specially Gokul has been my balancing pole on this six-year tight rope walk. I am immensely thankful to Deanna, Hector, Misael, T, Arunava, Satish, Viswa, Skillet, Ramraj, Rohini, Rohit, Lakshmi, Hema and San for their food, friendship, and everlasting memories. I am deeply

grateful to Aswin, Matta, Hamilton, Siva, and Keerthi for their support and friendship from afar through all these years. I would like to also thank my dearest bicycle buddies Ben, Leon, Mariah, Michael, Carolyn, Tom, and Ruth for the wonderful time we shared, both on the road and otherwise.

Finally, I would like to acknowledge both my parents and partner. Appa and Amma have never failed to support me in my aspirations and have always given me the freedom me to pursue studies that I desired. Their infinite affection and care for me has enabled me to get where I am today. My partner Anusree has been an absolute sweetheart and remained as an embodiment of unwavering support all these years despite the vagaries of time. She has been a shoulder that I could lean on, halfway around the world, from the start of my graduate school till now. I could not have achieved anything without her love and encouragement. To my parents and my better half, I dedicate this dissertation.

## Abbreviations

<b>DMC</b>	DNA mechanocapsules
<b>AFM</b>	Atomic force microscopy
<b>CMC</b>	Cardiac muscle cells
<b>pMHC</b>	peptide major histocompatibility complex
<b>APC</b>	antigen-presenting cells
<b>TCR</b>	T-cell receptors
<b>BCR</b>	B-cell receptor
<b>RGD</b>	arginine-glycine-aspartic acid
<b>cRGDfk</b>	cyclo-Arg-Gly-Asp-Phe-Lys
<b>TFM</b>	traction force microscopy
<b>FRET</b>	Forster resonance energy transfer
<b>ADC</b>	Antibody-drug conjugate
<b>TD</b>	Tetrahedral DNA
<b>CAP</b>	catabolite activator protein
<b>cAMP</b>	cyclic adenosine monophosphate
<b>AuNP</b>	gold nanoparticles
<b>pN</b>	piconewton
<b>ECM</b>	Extracellular matrix
<b>LINC</b>	linker of the nucleoskeleton and cytoskeleton
<b>YAP</b>	Yes-associated protein; TAZ
<b>FB</b>	Force bearing
<b>TGT</b>	Tension gauge tether
<b>MD</b>	Molecular dynamics
<b>EMA</b>	Exponential moving average
<b>ECM</b>	Extracellular matrix
<b>FA</b>	Focal adhesions
<b>AFM</b>	Atomic force microscopy
<b>WLC</b>	Worm-like-chain
<b>GFP</b>	Green fluorescent protein
<b>TGT</b>	Tension gauge tether
<b>SLB</b>	Supported lipid bilayers
<b>MFM</b>	Molecular force microscopy
<b>MTFM</b>	molecular tension fluorescence microscopy
<b>DNA-PAINT</b>	DNA-Points Accumulation for Imaging in Nanoscale Topography
<b>PCR</b>	Polymerase chain reaction
<b>RICM</b>	Reflection interference contrast microscopy
<b>TIRF</b>	Total internal reflection fluorescence
<b>HPLC</b>	High-performance liquid chromatography
<b>IC<sub>50</sub></b>	Half maximal inhibitory concentration
<b>RT</b>	Room temperature
<b>S/N</b>	Signal to noise ratio
<b>FRET</b>	Fluorescence Resonance Energy Transfer

<b>MEF</b>	Mouse embryonic fibroblasts
<b>BHQ2</b>	Black hole quencher 2
<b>DMEM</b>	Dulbecco's Modified Eagle Medium
<b>SEM</b>	Standard error of the mean
<b>SD</b>	Standard deviation
<b>LatB</b>	Latrunculin B
<b>Vin</b>	Vinculin
<b>Dex</b>	Dextran
<b>pMHC</b>	peptide-bound major histocompatibility complexes
<b>APTES</b>	(3-Aminopropyl) triethoxysilane

## Table of Contents

CHAPTER 1	MECHANICS OF BIOLOGICAL SYSTEMS	1
1.1	Mechanobiology of organisms across scales	2
1.1.1	Mechanical processes underlying physiological and pathological processes	2
1.1.2	Mechanobiology at a cellular scale	5
1.1.3	molecular underpinnings of mechanical interactions	7
1.1.4	Integrins as mechanosensors	11
1.2	Methods to study cellular forces	13
1.2.1	Force measurements on pliable substrates	13
1.2.2	Molecular tension fluorescence microscopy	15
1.3	Mechanical markers for medical applications	18
1.3.1	Clinical importance of mechanobiology	18
1.3.2	Leveraging mechanical cues	19
1.4	Developing mechanotargeting systems	21
1.4.1	Gap in the field	21
1.4.2	DNA nanocages	22
1.5	Aims and Scope of the dissertation	24
	References	27
CHAPTER 2	DESIGN AND <i>IN SILICO</i> MODELING OF DMCs	40
2.3.1	ab initio DNA mechanocapsule designs	43
2.3.2	oxDNA rupture force estimation	46
2.3.3	Design of force non-responsive DMC	48
2.3.4	Rupture dynamics with varying force orientations	50

2.3.5 DMC cargo leakage under force	55
CHAPTER 3           FUNCTIONAL VALIDATION OF DMCS	71
3.3.1 Synthesis of DMCS	74
3.3.2 Surface characterization	75
3.3.3 DMC response to cellular forces	79
3.3.4 Force selective DMC rupture	81
CHAPTER 4           FORCE INDUCED DRUG DELIVERY FROM DMCS	102
4.3.1 Small molecule delivery from DMCS	106
4.3.2 Macromolecular encapsulation inside DMCS	110
4.3.3 Macromolecular encapsulation inside DMCS	113
4.3.4 DMCS for force-responsive rna knockdown.	116
CHAPTER 5           SUMMARY AND OUTLOOK	147
5.2.1 DMCS for precision biophysical targeting <i>in vivo</i>	149
5.2.2 DMCS as durable force sensors	150
5.2.3 DMCS for high throughput mechanotagging	151
5.4.1 Magnitude of LFA-1/ICAM-1 forces fine-tune TCR-triggered T cell activation	155
5.4.2 DNA origami tension sensors (DOTS) to study T-cell receptor mechanics at fluid interfaces	157
5.4.3 Tension-activated cell tagging (TaCT) for mechanocytometry	159
5.4.4 Cell adhesion receptors detect the unfolding pathway of their ligands	162
5.4.5 Loading rate estimation with DNA force probes	163

## Table of figures

Figure 1.1 Mechanical detection of embryo fate	2
Figure 1.2 Osteogenesis and skeletal muscle fates	3
Figure 1.3 Tissue mechanics are altered in disease states	4
Figure 1.4 Membrane curvature sensing by cells	5
Figure 1.5 Bacterial mechanotransduction	6
Figure 1.6 Cellular mechanosensory proteins	8
Figure 1.7 Mechanosensing and mechanotransduction mechanisms in cells	9
Figure 1.8 Nanomechanical regulation of the cell matrix and the focal adhesions	10
Figure 1.9 Integrins as force sensors	12
Figure 1.10 Traction forces on hydrogels and microposts	14
Figure 1.11 Reversible DNA hairpin tension probes	15
Figure 1.12 Irreversible DNA tension probes	16
Figure 1.13 Mechanically triggered hybridization chain reaction	17
Figure 1.14 Unifying characteristics of mechanotransduction disorders	18
Figure 1.15 Traction-Force Activated Payloads	20
Figure 1.16 Protein positioning within a DNA tetrahedron	23
Figure 2.1 DNA tetrahedron strand sequences	43
Figure 2.2 DNA tetrahedron strand modification location	44
Figure 2.3 Tuning force threshold of DMCs	45
Figure 2.4 Simulation of DMC with 6 strand design	46
Figure 2.5 Simulation of DMC with 5 strand design	47
Figure 2.6 Simulation of Rigid DMCs	49
Figure 2.7 Fluorophore and quencher separation distance	50
Figure 2.8 Influence of force orientation on the threshold and rupture	53



Figure 2.9 Influence of force orientation on the threshold and rupture	53
Figure 2.10 Fluorophore-quencher separation with varying orientation	54
Figure 2.11 DMC cargo leakage under force	55
Figure 3.1 Representative synthetic scheme	74
Figure 3.2 DMC size characterization	76
Figure 3.3 Quenching efficiency of DMCs	76
Figure 3.4 Surface density of DMCs	77
Figure 3.5 DNase degradation of DMCs	78
Figure 3.6 Toehold mediated dequenching of DMCs	49
Figure 3.7 Fluorophore and quencher separation distance	50
Figure 3.8 Force-mediated dequenching of qDMC39pN due to integrin forces	80
Figure 3.9 Force selective DMC rupture	81
Figure 3.10 MCF-7, MCF-10A and MDA-MB-231 cells on DMC	82
Figure 3.1 Representative synthetic scheme	74
Figure 3.2 DMC size characterization	76
Figure 3.3 Quenching efficiency of DMCs	76
Figure 3.4 Surface density of DMCs	77
Figure 3.5 DNase degradation of DMCs	78
Figure 3.6 Toehold mediated dequenching of DMCs	49
Figure 3.7 Fluorophore and quencher separation distance	50
Figure 3.8 Force-mediated dequenching of qDMC39pN due to integrin forces	80
Figure 3.9 Force selective DMC rupture	81
Figure 3.10 MCF-7, MCF-10A and MDA-MB-231 cells on DMC	82

Figure 4.1 Figure 3.1 Representative synthetic	107
Figure 4.2 Cell viability on DMCs	108
Figure 4.3 Macromolecular encapsulation inside DMCs	110
Figure 4.4 Assembly and purification of dextran encapsulated DMCs	113
Figure 4.5 Validation of force-induced uptake of dextrans	114
Figure 4.6 Co-culture of VinKO and Vin-GFP MEF cells on the same DMC	115
Figure 4.7 DMCs for force-responsive RNA knockdown	117
Figure 5.1 Drug loaded DMC anchored to extracellular matrix	150
Figure 5.2 Unzipping TGT and shearing TGT systems	155
Figure 5.3 Simulated force application along four directions	156
Figure 5.4 Force-extension curves of hairpins	158
Figure 5.5 Force-induced peeling mechanism of oligonucleotides	160
Figure 5.6 MEF cells seeded on DMCs	161
Figure 5.7 Force-extension rates for reversible shearing and unzipping probes	162
Figure 5.8 Loading rate force sensor	163

# CHAPTER 1

## Mechanics of biological systems

For a considerable amount of time, it was postulated that many biological processes have underlying mechanical components.<sup>1</sup> Over the past few decades, it has become increasingly evident that mechanics of biological systems are integral for its regular functions such as tissue maturation,<sup>2</sup> synchronized cardiac muscle beating,<sup>3</sup> immune responses,<sup>4</sup> wound healing,<sup>5</sup> etc. Biomechanical dysregulation has also been implicated in diseases such as asthma, fibrosis, cardiomyopathy, and cancer. Biomechanical interactions are prevalent even in unicellular organisms such as bacteria where cellular mechanics dictate behaviors such as biofilm formation, locomotion, and infection.<sup>6</sup> Given the emerging importance of mechanobiology, it is imperative that the crucial role of mechanics and its interplay with biochemical processes be thoroughly investigated. Such a unified understanding will pave the way for deeper insights into human health, refined therapeutics, and better clinical outcomes.

In this chapter, we aim to introduce the role of mechanics experienced by living systems at all scales from tissue to molecular level with specific focus on integrin receptors. A summary of some popular methods used to measure cellular forces is described. Subsequently, a discussion of the importance of utilizing mechanical cues in medicine is presented. This represents an unmet need in the field that needs to be addressed and it will be discussed later, along with proposed solutions to develop a mechanically responsive drug delivery platform. Finally, the chapter concludes with the aims and scope of this dissertation.

## 1.1 Mechanobiology of organisms across scales

### 1.1.1 MECHANICAL PROCESSES UNDERLY PHYSIOLOGICAL AND PATHOLOGICAL PROCESS

The primacy of mechanics in biological processes has been overlooked for many years, as the vignettes often center around biochemical interactions to explain most phenomena. For instance, the traditional approach to predict the viability of fertilized embryos relied on using morphological assessments, which can be highly subjective. When the biomechanical characteristics of the human oocyte was taken into consideration, it became evident that oocytes undergoes hardening upon fertilization, and the stiffness of the embryo is a good predictor of viability<sup>7</sup> (Figure 1.1). It is conceivable that mechanical interactions can play defining roles in organisms beyond such early developmental stages. In reality, tissue mechanics play a vital role in brain and cardiac functioning,<sup>8</sup> stem cell differentiation,<sup>9</sup> wound healing, and cancer metastasis<sup>10</sup> to mention a few.

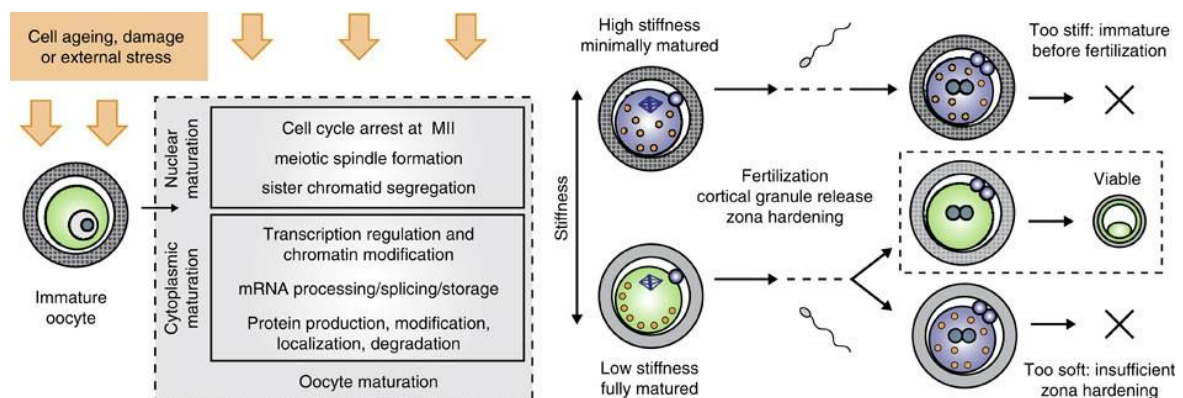


**Figure 1.1** Model for how embryo fate is determined and why it is detectable mechanically. Reproduced from *Nat. Comm.* 7, 10809 (2016) using creative commons CC BY license.

The influence of mechanics and its role in various biological functions are inexorably intertwined in many areas of biology. Advances in mechanobiology techniques have helped in understanding mechanical involvement at all biological stages ranging from development to diseases. Any perturbation to the mechanics of tissue can lead to alteration in responses of

cells to these physical cues leading to pathological conditions. It is known that the process of aging is known to decrease the viscoelasticity of brain tissues at the rate of 0.75% every year.<sup>11</sup> The mechanical properties of brain are also drastically altered compared to healthy brains in diseases such as Alzheimer's disease, multiple sclerosis, Parkinson's disease as well in repeated head injuries.<sup>12–14</sup>

Biological processes such as embryogenesis,<sup>9</sup> tissue morphogenesis, and wound healing<sup>5</sup> rely on the mechanical properties of their surrounding environment.<sup>15</sup> These processes invoke large scale reorganization and remodeling to close gaps in these tissues.<sup>16</sup> In cardiac tissue, differentiation and development are known to intimately influenced by the mechanical landscapes of the tissues.<sup>17</sup> Dysregulation of the mechanics can result in cardiac tissue stiffening which has been implicated in an array of maladies such as cardiac fibrosis, myocardial infraction, irregular heart beating and developmental defects.<sup>18–20</sup>

Throughout life, mechanical cues in the tissue's microenvironment shape the behavior of healthy tissues and changes in this can lead to pathological conditions. In stem cells, biochemical signals between tissues such as hormones, growth factors and genetic regulators

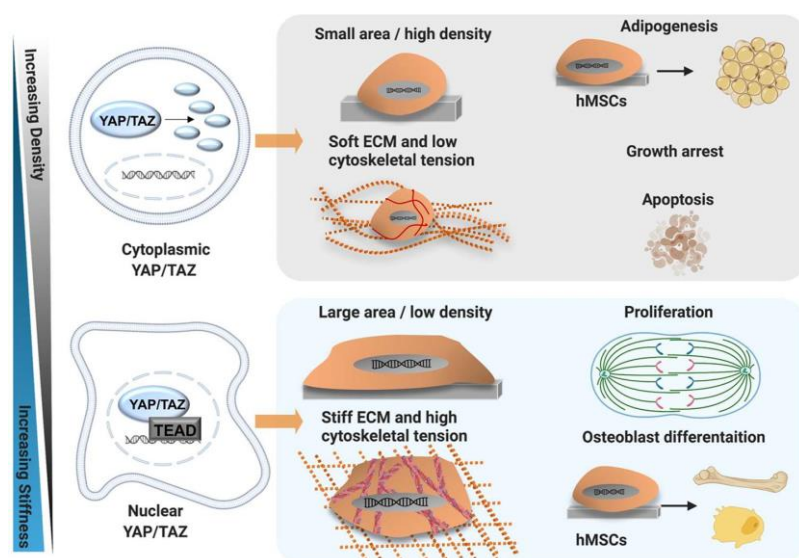


**Figure 1.2** Osteogenesis and skeletal muscle fates are promoted by stiff ECM and low density. Adipogenic fates are promoted by soft ECM and high cell density. Reproduced from *Front. Cell Dev. Biol.*, 9, 10809 (2021) using creative commons CC BY license.

drive differentiation<sup>21</sup> although they are not the sole operators. Stem cells rely on essential biophysical cues in their environment such as mechanical strength, matrix architecture, and topographical guidance.<sup>2</sup> Stem cells leverages these cues for proliferation, gene expression, differentiation and organ formation.<sup>9</sup> Past studies have shown

that, mesenchymal stem cells grown on stiffer substrates have higher potential towards osteogenic differentiation while on soft matrices, they tend towards adipogenic differentiation<sup>22,23</sup> (Figure 1.2). This shows the inescapable role of mechanics in the behavior and differentiation of stem cells.

In the case of cancerous tissues, the tumor microenvironment undergoes drastic physical changes such as ECM stiffening, increased cell contractility, elevated fluid pressure, and alterations to membrane tension.<sup>24,25</sup> Most tumors exhibit increased stiffness (Figure 1.3) with some exceptions to the rules.

Recent evidence supports the mechanical imbalance in cancers such as brain,<sup>26</sup> breast,<sup>27</sup> liver,<sup>28</sup> and colorectal<sup>29</sup> which have shown to be stiffer than the surrounding tissues.<sup>30</sup> This abnormal stiffening of tissues has been used as a diagnostic marker in cancers, notably making palpation a valuable diagnostic in breast cancers. Mechanics is yet another determinant of the ability of cancers to metastasize,

as cancer cells translocate between various microenvironments and their mechanical coping in such regions dictates their ability to colonize various tissues.<sup>31</sup> While stiffening of tissue is often seen in tumors, the concerted effort by individual cells to invade through basement membranes and ECM and pass through the circulatory system influences metastatic progression and tumor aggression.<sup>32</sup>

Assessments of mechanical properties must be done at all scales as bulk tissue studies are complex and might not always link the behavior to its molecular components.<sup>15,28</sup> Hence

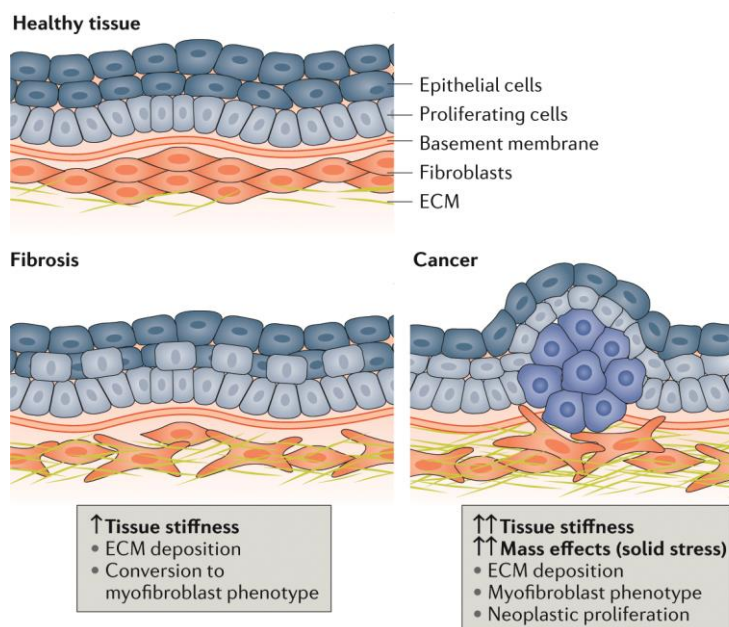


**Figure 1.3** Tissue mechanics are altered in disease states. Reproduced from *Nat. Rev. Mater.* 5, 351–370 (2020) with permission from Springer Nature.

mechanical components of pathology and physiology must be examined beyond the microscopic scale and into the nanoscopic scale where the cells sense and individually respond to its local mechanical environment.<sup>33</sup>

### 1.1.2 MECHANOBIOLOGY AT A CELLULAR SCALE

Isolated cells are complex, nonlinear, and viscoelastic materials but their mechanical properties are much simpler behavior to investigate than a collection of cells.<sup>34</sup> Cells exist in physically confined niches in tissues that are heterogeneous and have dynamic mechanical cues. To study cell mechanics under such conditions, a vast array of techniques have been advanced to deepen our understanding of the intimate relationship between mechanics and biochemistry.<sup>35</sup> This would enable materials mimicking the physiological environment to be engineered for controlling cell behavior.

Cells are known to sense curvature substrate topography like curvature, roughness, and periodicity.<sup>36</sup> For instance, astrocytes were found to preferentially bind to fibers with diameters larger than 100 nm.<sup>37</sup> Interestingly, a single fibroblast cell can't adhere to inner surface of hollow tubes whereas a collection of cells can attach to them which could be partially reasoned based on membrane tension.<sup>38</sup> Curvature on the inner and outer membrane leaflets have equal tension when they are in a planar configuration but exhibit different tensions on membrane bending. For example, certain ion channels are opened by convex membrane curvatures<sup>39</sup> (Figure 1.4). It has been proposed that concave and convex

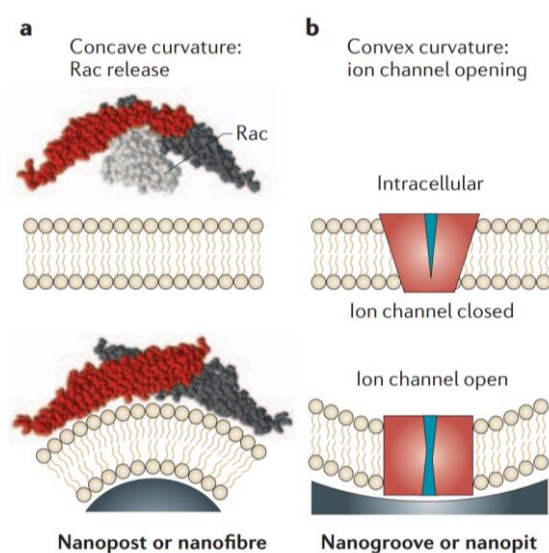


**Figure 1.4** Membrane curvature sensing by cells. Reproduced from *Nat. Rev. Mol. Cell Biol.* 7, 265–275 (2006) with permission from Springer Nature.



curvatures of the membrane could be sensed by two different molecular mechanisms.<sup>40</sup> The periodicity and spacing of the substrate can also alter cell behavior where large spacings between the integrin adhesion sites can compromise focal adhesion formation and cell adhesion in general.<sup>41</sup>

Apart from topographical cues, cells also require specific mechanical cues for the activation of certain pathways. Cardiac muscle cells (CMC), for example, require substrates that can withstand integrin forces for proper cell spreading, periodic beating and elongated morphology which are signs of a matured CMC.<sup>3</sup> It was observed that maturation was low on substrates where integrins cannot exert forces higher than 12 pN compared to substrates where the integrins can exert 56 pN or 160 pN. This is due to the stable integrin-surface bonding that can withstand higher forces allowing force transmission to facilitate CMC maturation. Similar regulatory mechanisms are also present in neuritogenesis where integrin

forces dictate neurite outgrowth in cortical neurons.<sup>42</sup> Even in organisms like bacteria which thrive in a wide range of environments, are known to respond to mechanical cues for motility, growth and surface adhesion.<sup>6</sup>

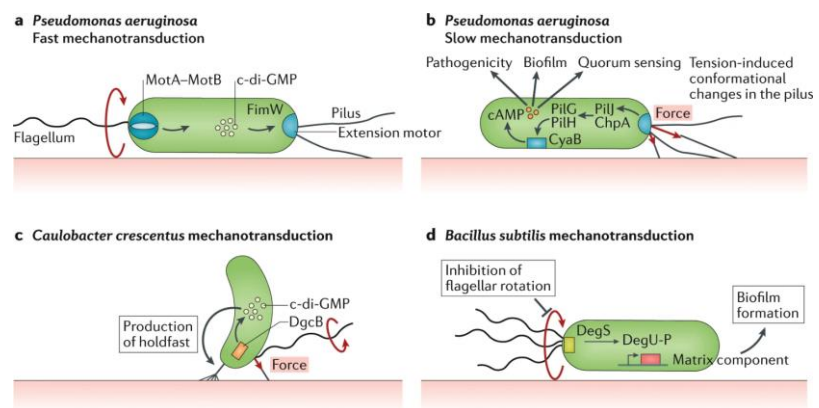


**Figure 1.5** Bacteria use mechanotransduction to regulate various phenotypes in response to forces. Reproduced from *Nat. Rev. Microbiol.* 18, 227–240 (2020) with permission from Springer Nature

Mechanical interactions are also prevalent in cells which are non-adherent such as T-cells, platelets, B-cells, etc. and require them for proper functioning. T cell receptors exhibit dynamic and ephemeral tension signals up to 12 pN which occur within seconds of binding to cognate pMHC. A rise in calcium flux occurs immediately after the TCR force exertion, which is a hallmark of T-cell activation. The TCR forces are modulated by the cytoskeleton as inhibiting its activity reduces the observed tension.<sup>43</sup> Similarly, LFA-1, an integrin receptor on



T-cells were also found to exert forces  $>4.7$  pN and a small subset of the receptors had forces exceeding 19 pN.<sup>4</sup> It has also been observed that naïve B-cells exert forces through B-cell receptor (BCR) antigen complexes around 7 pN. Germinal center B-cells are known to extract antigen with better affinity than naïve B-cells and this can be observed in the BCR mechanics.<sup>44</sup> BCR from germinal center B cells had forces greater than 7 pN with some population having  $>14$  pN of BCR-antigen forces.<sup>45</sup> These interesting examples highlight the importance of single receptor forces for T-cell, B-cell activation, and human immunology in general. Mechanical sensing is conserved across species, from bacteria to mammals and it underscores the cellular property of converting mechanical cues into physiological information. To understand how a cell perceives its environment and alters its function, further examination of mechanically-active protein sensors that transduce the mechanical information is warranted.

### 1.1.3 MOLECULAR UNDERPINNINGS OF MECHANICAL INTERACTIONS

Investigating the mechanisms by which cells sense and reply to the mechanical cues in their environment requires bottom-up operating machinery. A deeper comprehension of the conformational dynamics of proteins and nucleic acids under forces in their native cellular environment has emerged in the last few decades.<sup>39,46,47</sup> A recent report observed that a nascent protein exiting the ribosome exerts force at the exit tunnel due to protein folding which can reduce stalling in ribosomes.<sup>48</sup> Another handful of multi-scale studies have established a direct connection from the mechanical interactions of the biomolecules to the cellular and tissue functions.<sup>49–51</sup> Experiments involving proteins that act as nanomechanical devices at a molecular biology level, demonstrate that understanding the behavior of individual force sensitive molecules *in vitro* can translate to molecular functions in physiological cellular context.

Cellular components involved in mechanical sensing are coupled to other biochemical circuitry so that the cells can monitor their biophysical environment through molecular

mechanosensors and tune their responses (Figure 1.6). The cellular mechanism of sensing the surrounding mechanical habitat is known as mechanosensation and cellular tuning of function in concert with the mechanics is known as mechanotransduction.<sup>52</sup> Some of the best-known mechanotransducing proteins include TREK-1, PIEZO1, Rho/ROCK, and YAP/TAZ. In certain cases, mechanical cues are transmitted from the cytoskeleton to the nucleus by structural modification of cytoplasmic proteins and shuttling them to the nucleus where they have a key role in regulating gene expression. YES-associated protein (YAP) and transcription regulator protein 1 (TAZ), in fact translocate to the nucleus in response to extracellular mechanical signals and modulate gene expression.<sup>53</sup> YAP on its own is mechanically labile and prone to unfolding. YAP and other proteins have mechanical stability and molecular mass criteria for nuclear translocation.

Cells grown on stiff substrates have enhanced coupling between the nucleus and cytoskeleton. For example, YAP/TAZ has been found to localize in the nucleus of mesenchymal stem cells when culture on stiff substrates (40 kPa) and had osteogenic differentiation markers. On the other hand, cells grown on softer substrates (0.7 kPa) had YAP/TAZ localized to the cytosol and were shown to undergo adipogenesis.<sup>54</sup> It has been observed that direct force application on cells using atomic force microscopy induces nuclear import of YAP.<sup>53</sup> Hence, external forces are intertwined with YAP/TAZ proteins activity which is coupled to intracellular mechanical signals, nuclear mechanical properties, and nuclear transport.

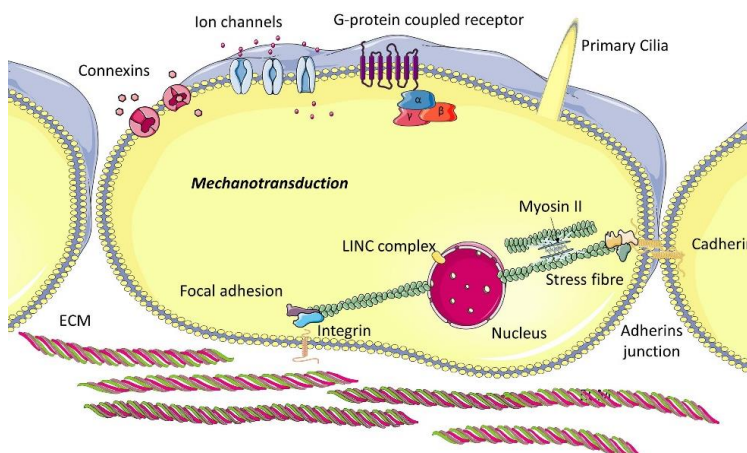


**Figure 1.6** Cellular mechanosensory proteins: The internal cytoskeleton transmits mechanical stimuli from the extracellular environment to the cell nucleus. This stimulus is mediated by transmembrane proteins located at focal adhesions, which bind to ECM ligands but also intracellular proteins. Cadherins connect the cytoskeleton of adjacent cells and thus enable cells to transmit force from one to another and allow movement of components within the plasma membrane. Reproduced from *Front. Bioeng. Biotechnol.*, 8, 2020) using creative commons CC BY license.

Rho/ROCK are yet another pair of biomolecules involved in mechanotransduction and are also known to play crucial roles. At the cellular level activated Rho promotes actomyosin stress fiber formation drastically increasing the stiffness and mechanical characteristics of cells.<sup>55</sup> Further, actin and Rho are also responsible for the YAP/TAZ translocation into nucleus. Recent reports also have unraveled mechanical interactions in G-protein coupled receptors further cementing the role of mechanics in cellular signaling.<sup>56</sup> In ion channels, mechanical sensitivity has been observed even in conventionally voltage-gated and ligand-gated channels.<sup>57</sup> Mechanical sensitivity in these proteins is due to membrane stress affecting the

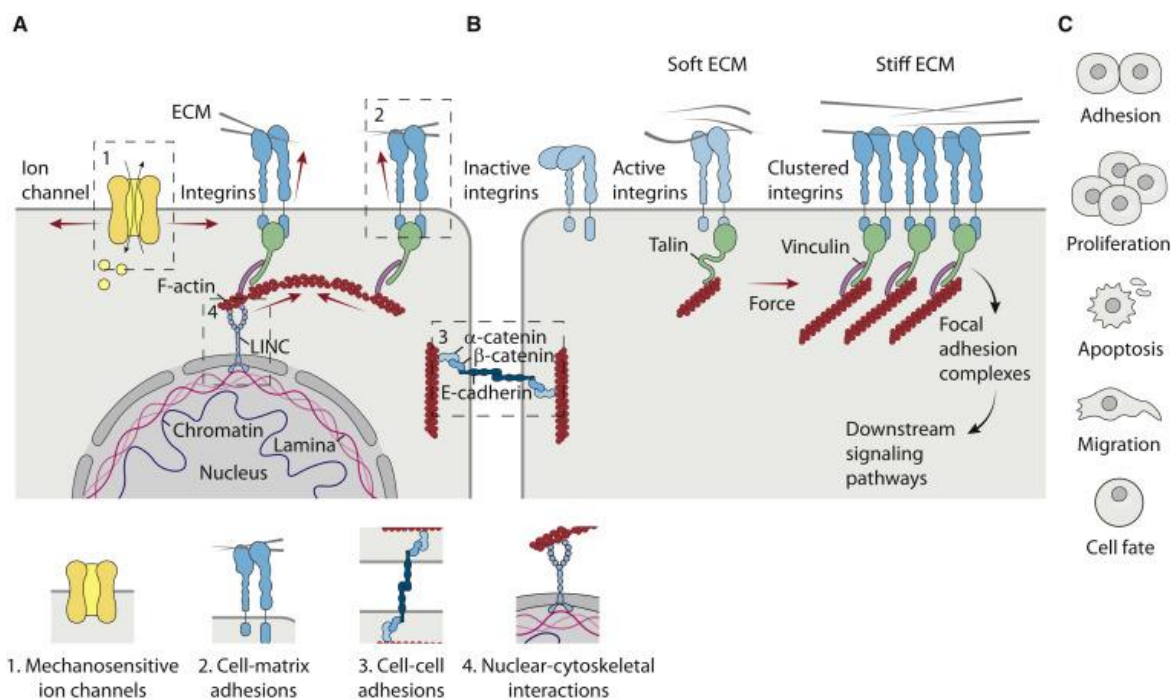


**Figure 1.7** Mechanosensing and mechanotransduction mechanisms in cells. Reproduced from *Dev. Cell*, 56, 13, 1833-1847 (2021) with permission from Elsevier. Copyright (2021).

domains that switch between closed and open conformations.<sup>58</sup> Mechanical sensitivity of biomolecules therefore is a rather general property.<sup>59,60</sup> Other biomolecular machinery in the cell is also involved in mechanosensing and transmitting the mechanical stimuli. The cytoskeleton is a dynamic structure that not only defines the 3D architecture of the cell but also relays the mechanical cues to the nucleus via the nucleoskeleton which is composed of LINC (linker of the nucleoskeleton and cytoskeleton) (Figure 1.7). In this way the mechanical signals propagated through the LINC complex induce changes in gene expression and as a result, protein expression.<sup>61</sup>

The cytoskeleton connects to the cell exterior through a complex choreography of molecular system termed as focal adhesions. The focal adhesion complexes interface with the extracellular matrix (ECM) through integrin receptors to activate intracellular proteins. The

ECM is a fibrous network of protein consisting of fibronectin, collagen, tenascin, elastin and laminin that forms the scaffold for cells and maintains the mechanical properties of the tissues.<sup>62</sup> The composition and arrangement of these molecules dictates the mechanical properties of ECM. Cells are known to remodel the mechanical properties

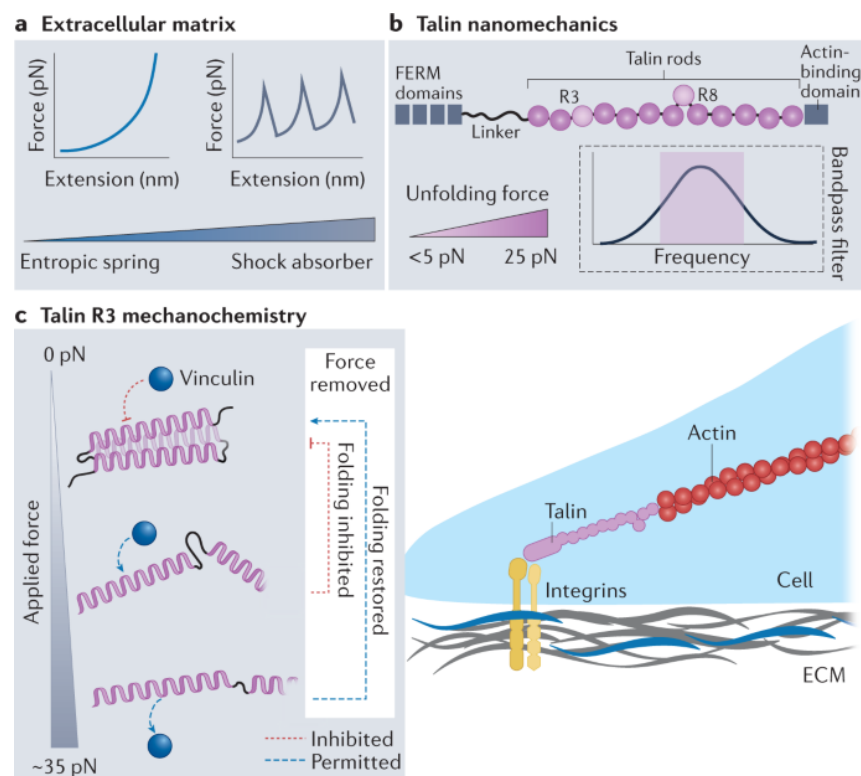


**Figure 1.8** Nanomechanical regulation of the cell matrix and the focal adhesions. Reproduced from *Nat. Rev. Mater.* 8, 10–24 (2023) with permission from Springer Nature

of the ECM by secreting metalomatrix proteases and exerting forces on them through cytoskeleton and mechanical components of the focal adhesions.<sup>63</sup> The fibronectin type III in the ECM is a mechanically stiff protein with domains that is stable up to ~200 pN of force.<sup>64</sup> The high stability of fibronectin domains is noteworthy since the rest of the ECM contrastingly have soft and malleable components.

Cells also interface with other neighboring cells through a family of cell-cell adhesion proteins known as cadherins that allow mechanical forces to be propagated through the tissues. Cadherins form a dimeric bridge between cells that intertwines to form a X shape structure that displays a biphasic mechanical response.<sup>65</sup> As the force increases between the two

cadherins the binding counterintuitively strengthens up to 30 pN which is known as catch-bond.<sup>66</sup> The binding then decreases with subsequent increase in force which is more commonly observed and termed as a slip-bond. Similar to cadherins, gap junction proteins create a channel between two cells with connexin proteins that are mechanically sensitive.<sup>67</sup> These channels can control intercellular signaling cascade, proliferation and differentiation based on mechanical communications.<sup>68</sup> Talin in particular has cryptic sites for vinculin binding that are hidden in its native conformation.<sup>69</sup>

In vitro experiments have revealed that talin exposes the vinculin binding sites under mechanical forces between 5 – 25 pN.<sup>70</sup> Similar mechanism is observed in  $\alpha$ -catenins which have cryptic binding sites for vinculin binding that can be unraveled with <15 pN of force.<sup>71</sup> Talin when stretched in the presence of vinculin stays in its stretched unfolded conformation for hours while in the absence of vinculin it refolds to its original conformation quickly. Talin couples to integrin's amino terminus and to F-actin at its carboxyl terminus. Talin together with other mechanosensitive proteins such as vinculin, paxillin and integrin comprise the focal adhesion complexes<sup>46</sup> (Figure 1.8). Integrins are crucial proteins known to provide the attachment to the ECM and as such, they are perfectly positioned to serve as mechanosensors.

#### 1.1.4 INTEGRINS AS MECHANOSENSORS

Integrins are heterodimeric transmembrane proteins responsible for the inside-out signaling of the cells.<sup>35</sup> Integrins in conjunction with talin and actin form the mechanosensing circuitry that sense ECM mechanical properties.<sup>70,72</sup> Integrins further aid cells in intracellular biochemical pathways as well as in locomotion. Integrins consist of two non-covalently interacting  $\alpha$ -subunits (18 types) and  $\beta$ -subunits (8 types) that produce 24 unique combinations. Almost 12 integrin combinations contain the  $\beta_1$  subunit and about five have the  $\alpha_v$  subunit.<sup>73</sup> Despite having a variety of combinations, at least 8 integrins were known to bind to fibronectin with the arginine-glycine-aspartic acid (RGD) being the consensus binding motif, albeit with varying binding affinities. Recent evidence suggests that integrins associate with other membrane-spanning molecules, such as growth factor receptors, proteoglycans and

tetraspanins, in some cases utilizing them as a ‘third subunit’ to influence the cellular signaling and functions.<sup>74</sup>

Integrins are active signaling molecules that transmit signals to the cellular interior when bound to ECM moieties. The signaling can be initiated from outside by the binding of integrins to ECM (outside-in) or can be started from the cytoplasmic proteins (inside-out).<sup>35</sup> Continuing the theme of the signaling proteins being mechanically sensitive, integrins possess distinct biomechanical properties. Integrins undergo conformational changes on binding their ligands. Integrins on binding to a ligand transition from a bent and close conformation to an extended and open conformation that activated them leading to downstream signaling processes where cellular proteins bind on the cytoplasmic tail of integrins.<sup>75</sup> Once activated integrins cluster and bind to other members of the focal adhesion complex such as vinculin, talin and paxillin. These activated integrins form focal adhesions that the cells use to transmit piconewtons of forces and sense their mechanical environment to activate chemical pathways.<sup>47</sup>

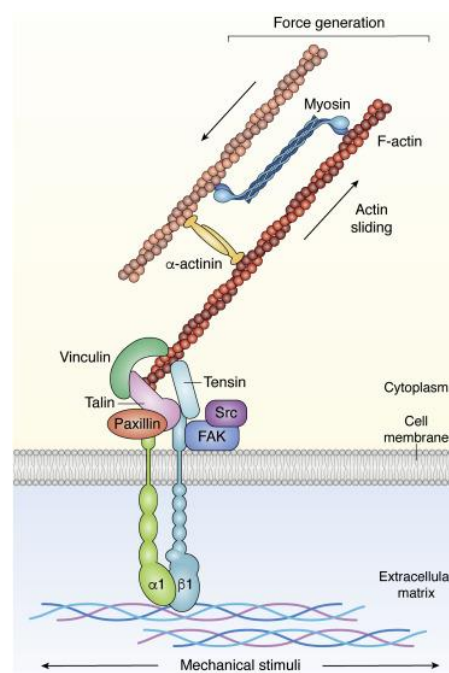


**Figure 1.9** Integrins as force sensors. Reproduced from *JBC Reviews*, 298, 5, 101867, (2022) under creative commons CC-BY license.

The focal adhesion kinase is a central member of the downstream signaling that directly binds to talins in newly formed focal adhesions. The focal adhesions support stress fiber formations that can further initiate signaling cascades.<sup>76</sup> The cells exert forces through these focal adhesions using myosin motor activity and actin filament crosslinking. Integrins are essential mechanosensors since the cells use them for adhesion, motility, and the majority of the cytoskeletal forces are transmitted through these receptors.<sup>47</sup> Integrins have been found to exert forces in the range of 10 - 100 pN.<sup>41,77</sup> Integrins are also known to have a biphasic mechanical binding to their ligands where they exhibit catch-bond behavior where the bond lifetimes increase with force followed by a decrease with increasing forces.<sup>78</sup>

Integrins are also implicated in cancers and are responsible for tumor proliferation, migration, and invasion.<sup>79</sup> Many cancers have over expression of certain integrins and antagonists that inhibit integrins have potential to impede tumor progression.<sup>80,81</sup> Integrins are crucial for ECM sensing and signaling in cancer cells, but they are not oncogenic in their own regard. The importance of integrins in tumors has made them attractive targets for cancer therapeutics.<sup>82</sup> Hence, integrins are crucial mechanosensors that are central to cellular homeostasis as well as in pathological conditions.

## 1.2 Methods to study cellular forces

The study of cellular forces can be broadly classified into two broad sections (i) active response methods where the cellular response to an applied force is studied (ii) passive methods, where the platform senses the intrinsic forces generated by cells. Cell traction forces can be studied using various passive platforms that measure forces from the micron scale to single-receptor nanometer scale. This section compares some popular techniques used for measuring passive cellular forces and lists their advantages and areas for future improvement.

### 1.2.1 FORCE MEASUREMENTS ON PLIABLE SUBSTRATES

The earliest observation of cells exerting forces was reported when cells were cultured on cross-linked soft silicone where a distortion on the elastic substrate was visible as wrinkles.<sup>83</sup> Further advancements in field of materials and fabrication made traction force microscopy possible. Traction force microscopy (TFM) uses a soft polyacrylamide gel substrate to quantify cell traction forces and the forces exerted by cells by are calculated by measuring the deformation at the cell-substrate interface. This is usually done by embedding fluorescent beads that act as displacement markers.<sup>84</sup> By measuring the bead locations before and after, the stress on the elastic substrate and the forces exerted by the cells can be calculated. The



substrate stiffness of these polymers can be tuned at will by changing the polymer cross-linker composition, allowing for a wide range of cellular force measurements.<sup>85</sup>

Despite making whole cell force imaging possible, TFM can only detect forces 3 orders of magnitude higher than single cell receptors. Traction force maps are mathematically complex and require manual filtering of parameters to compute forces directly from the fluorescent displacement field. Further, TFM is limited by the fact that it assumes that the cellular forces are lateral and therefore cannot measure perpendicular forces. Hence, TFM falls short of providing accurate and dynamic forces map of live cells using accessible displacement processing algorithms.<sup>86</sup>

Micropillar or micropost arrays are similar to TFM in that they sense forces by measuring the displacement of cylindrical beams instead of fluorescent beads (Figure 1.10). The micropillars have one end fixed to a substrate with the other end free to move laterally. Hence, any lateral forces exerted by the cells will be recorded as directional deflections of the micropillars.<sup>87</sup> Ideally, the micropillar should behave like a spring, with deflection of the pillar tops being proportional to the applied force. The force exerted by the cell can then be calculated using displacements of the microposts through the Euler–Bernoulli beam theory.<sup>88</sup> Micropillar arrays greatly simplify the mathematical calculations to arrive at the cellular force maps. Here, the stiffness of the substrate can be tuned by changing the diameter of the micropillars. Despite the advantages, micropillar arrays suffer from similar limitations to the TFM as they do not register vertical forces on the substrate.

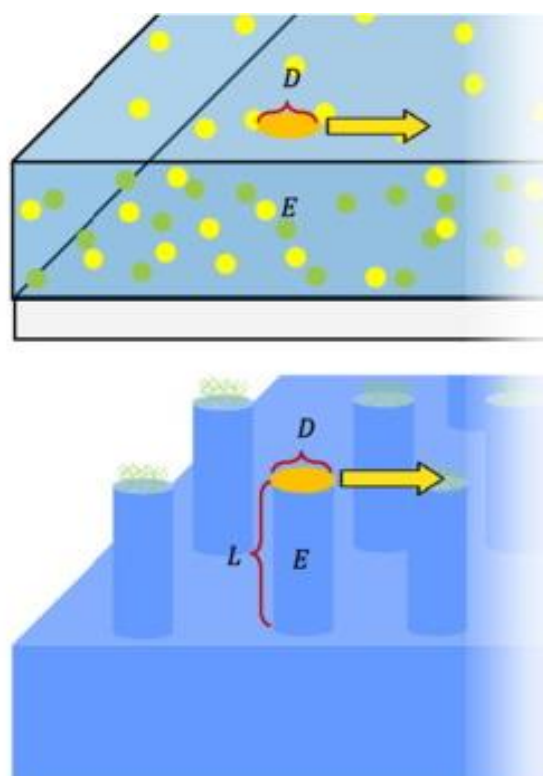


**Figure 1.10** Comparison of how cells pull and induce traction forces on hydrogels and microposts. *Methods* 94, 1, 51–64 (2016) with permission from Elsevier. Copyright (2016).



Further, the spatial resolution of the micropillars is limited as the cylindrical posts are typically in the scale of microns. To improve these 2D soft substrate force measurements to yield high temporal and spatial resolution, advancements in the field of novel materials and microfabrication technology are necessary.

## 1.2.2 MOLECULAR TENSION FLUORESCENCE MICROSCOPY

Plethora of molecular force sensing elements such as DNA, polymers and proteins have been described in literature. While force-sensors based on proteins can be genetically incorporated and expressed in live cells they are not conducive for extracellular tension measurements. Proteins are difficult to synthesize and tuning their force thresholds can be tedious. DNA structures on the other hand are ideal for extracellular force sensing because of their predictable mechanical properties, base-pair interaction tunability, and commercial availability with fluorophores, linkers and bioorthogonal handles.<sup>90</sup>

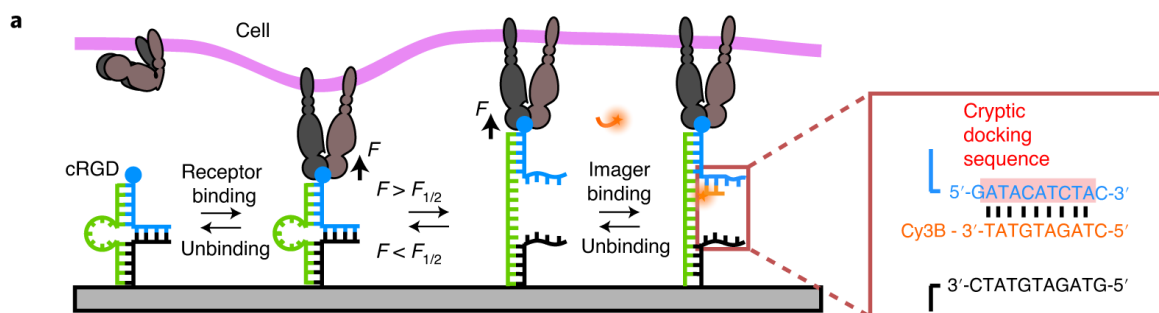


**Figure 1.11** Reversible DNA hairpin tension probes for super resolved cellular tension imaging. Reproduced from *Nat. Methods* 17, 1018–1024 (2020) with permission from Springer Nature.

DNA structures such as ssDNA, hairpins and pseudoknots are reversible and preserve the mechanical link of the receptor to the substrate and thus preserve mechanosignaling pathways.<sup>91</sup> On the contrary, rupturable structures such as duplex and certain DNA origami disrupts mechanotransduction.<sup>3</sup> Reversible structures report instantaneous tension and require additional techniques to integrate the signal over time as the signal.<sup>92</sup>

Reversible probes are characterized by DNA hairpin like element that will refold upon force termination.<sup>43</sup> Usually, these reversible motifs are surrounded by molecular rulers such as FRET sensors or fluorophore-quencher pair that will report out the extension of the reversible element. Once the force applied on the probes exceeds the force threshold ( $F_{1/2}$ ) the structure extends, and it is read out through two orders of enhancement of fluorescence.<sup>93</sup> The  $F_{1/2}$  for mechanical rupture or melting can be tuned by varying the length and sequences of the stem regions and in fact hairpin probes with  $F_{1/2}$  varying from 2.1 pN to 19 pN have been reported. Since they have low force threshold, reversible DNA tension probes have been used to study a variety of transient mechanical pathways, ranging from T cell receptors<sup>4</sup> to cell adhesion and platelet activation.<sup>77</sup> The main limitation of the reversible probes is usually that they are not suitable for receptors with high forces.

Rupturable probes provide cumulative tension signal over a period since the structures separate irreversibly.<sup>94</sup> The rupture force and dynamics is dependent on the force application point and the two extreme cases are classified as unzipping and shearing (Figure 1.12).

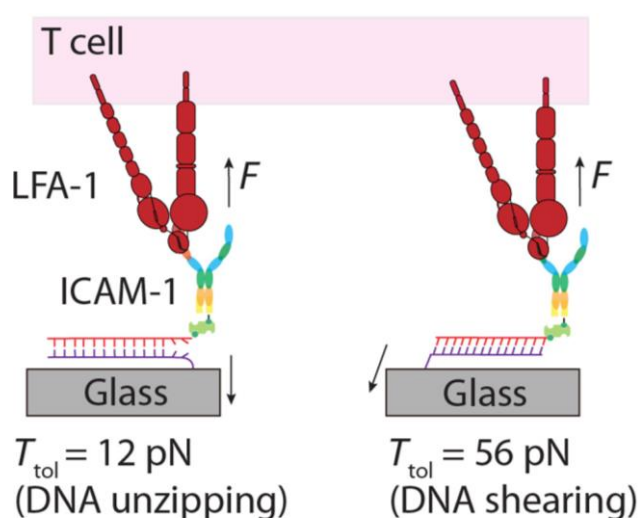


**Figure 1.12** Mechanochemical stabilization of LFA-1/ICAM-1 bonds potentiate TCR-triggered T cell activation. Reproduced from *Sci. Adv.* 8, eabg4485 (2022) using creative commons CC-BY license.

Shearing involves antiparallel force application on both the strands and on opposite end of the duplex (e.g., 3'-3' or 5'-5') while unzipping requires force application on the same end of a duplex (e.g., 5'-3'). The force threshold for dsDNA unzipping rupture is lower compared to shearing. Force application at any points in between would result in a mixed shearing and unzipping modes of rupture, with a rupture force intermediate to unzipping and shearing modes.

The rupture force of dsDNA can be estimated using the de Gennes model<sup>95</sup> and other refined variants of the model which assumes dsDNA as an elastic ladder held together using hydrogen

bonds. These models assume that a rupture can occur only when all base pairs become unstable, and it does not account for finite time scales and metastability. The rupture of dsDNA is an activating process where force takes the duplex into a metastable state which eventually dissociates the strands. Any amount force on the duplex, provided with long enough time will lead to duplex dissociation. For a given time of observation, the force must be large enough to decrease the free-energy barrier opposing dissociation. The difference between shearing and unzipping modes comes from the fact that a sheared base pair is still more stable than an unzipped base pair. This is due to the fact that there is a greater increase in extension upon rupture in the unzipping. The force required to separate the duplex hence is a function of the duplex length which in turn dictates the free energy of dissociation. Smaller forces are sufficient for dissociation in longer time windows whereas larger forces are required to rupture duplex in shorter time frames.<sup>96</sup>

Irreversible probes have a higher force range sensing compared to reversible DNA probes and

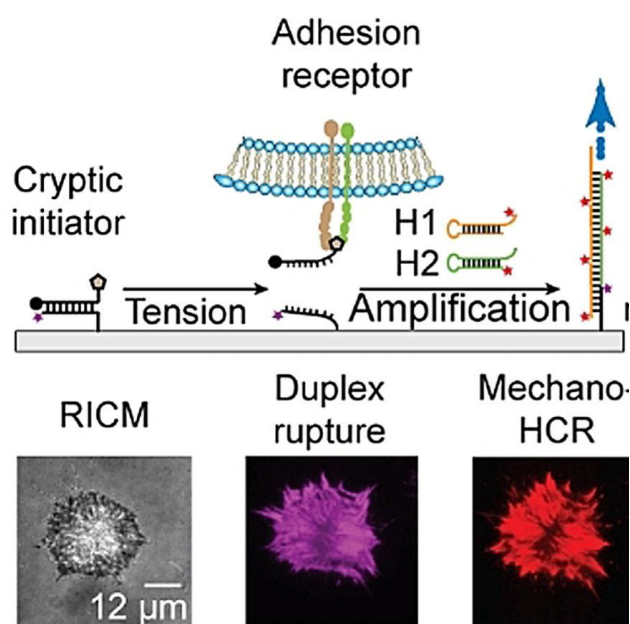


**Figure 1.13** Mechanically triggered hybridization chain reaction for the detection and amplification of cell mechanics. Reproduced from *Angew. Chem. Int. Ed.*, 60, 19974, (2021) with permission from WILEY.

are usually referred to as tension gauge tethers<sup>94</sup> (TGTs). However, due to irreversibility the signals accrue over time, recording a history of all the mechanical events. There are multiple ways to counteract this problem of tension history accumulation instead of real time signals. Improvements to TGTs have been made using hybridization chain reaction to improve signal-to-noise ratio (Figure 1.13) and even reversible TGTs have been constructed by synthesizing a single-stranded DNA that can form a duplex with all the modifications.<sup>97</sup>

Furthermore, TGTs and irreversible tension probes in general have been impactful, enabling

discoveries such as TCR signaling,<sup>4</sup> the involvement of integrin receptor mechanics in processes such as cardiomyocyte maturation,<sup>3</sup> and platelets activation.<sup>77</sup>

## 1.3 Mechanical markers for medical applications

### 1.3.1 CLINICAL IMPORTANCE OF MECHANOBIOLOGY

Mechanical properties of tissues and cells constitute an integral component of living organisms along with their biochemical and genetic properties. The importance of mechanics necessitates careful consideration of human diseases and the associated biochemical pathways from a biophysical perspective. The following examples will reinforce the idea that such a unified perspective can get us close to understanding in vivo phenomena in their natural conditions.

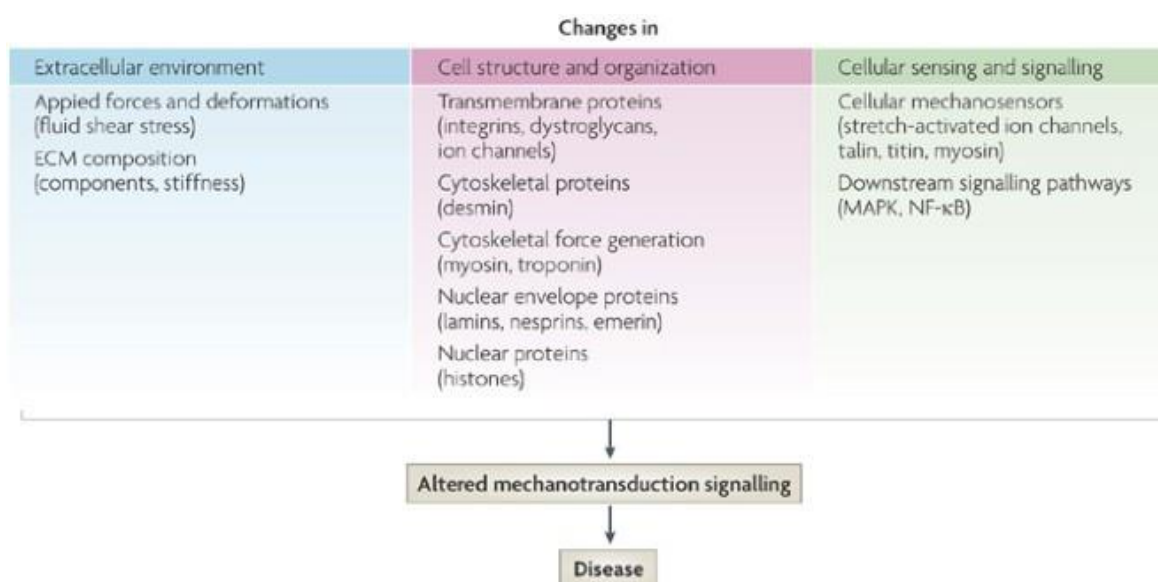


**Figure 1.14** Unifying characteristics of mechanotransduction disorders. Reproduced from *Nat. Rev. Mol. Cell Biol.* 10, 63–73 (2009). with permission from Springer Nature.

Currently there is a fundamental gap in understanding the mechanics of tissues and this leads to failures in clinical scenarios where there is a mismatch between the tissue and interacting

system.<sup>98</sup> In abdominal hernias, the stiffness and mechanical anisotropy of abdominal wall is never matched in the implanted biomaterials used for treatment. Mechanical mismatch is believed to be one of the reasons for implant failure and hernia recurrence.<sup>99</sup> Comprehensive mechanical studies are lacking for most diseases and common drugs used for treatment can have unintended consequences as result. For instance, anti-tumor drugs have been deliberately designed to target cancer cell mechanics, specifically the cytoskeleton, since they can be potent cytotoxic drugs. Taxol inhibits metastasis by suppressing microtubule depolymerization. In the case of leukemia, chemotherapy was found to be a risk factor in certain cases where chemotherapy can cause leukemia cells to clog the blood vessels of lungs and brain. Anti-cancer drugs such as daunorubicin can cause cell stiffening up to two orders of magnitude in acute lymphoblastic leukemia (ALL) and acute myeloid leukemia (AML) cells during cell death.<sup>100</sup> This increased stiffness due to the chemotherapeutic drug have been ascribed to the obstruction of blood flow to lungs and brain causing death. Hence, the role of mechanics at all scales should be carefully considered for better therapeutics and clinical outcomes.

### 1.3.2 LEVERAGING MECHANICAL CUES

Antibody drug conjugates represent an exciting area of targeted drug delivery and to date there are 13 FDA approved ADCs.<sup>101</sup> Antibody-drug conjugates (ADCs) usually consist of an antibody or peptide attached to a potent cytotoxic agent. Developing a similar modular targeting platform that mechanical inputs in addition to the biochemical signals can produce a new class of targeting that may catapult a new branch of responsive drugs. Force-triggered drug release in this context is highly advantageous as most delivery systems do not take advantage of the mechanical information in the target tissue. Up to this point, drug activation is based on small molecules,<sup>102</sup> nucleic acids,<sup>103</sup> pH<sup>104,105</sup> and redox<sup>106</sup> as logic inputs whereas a general approach for drug delivery based on *mechanical activity* remains unexplored.

To the best of our knowledge, no modular force-triggered platforms like ADCs respond to specific molecular magnitudes of force. For example, Ingber and colleagues created shear-

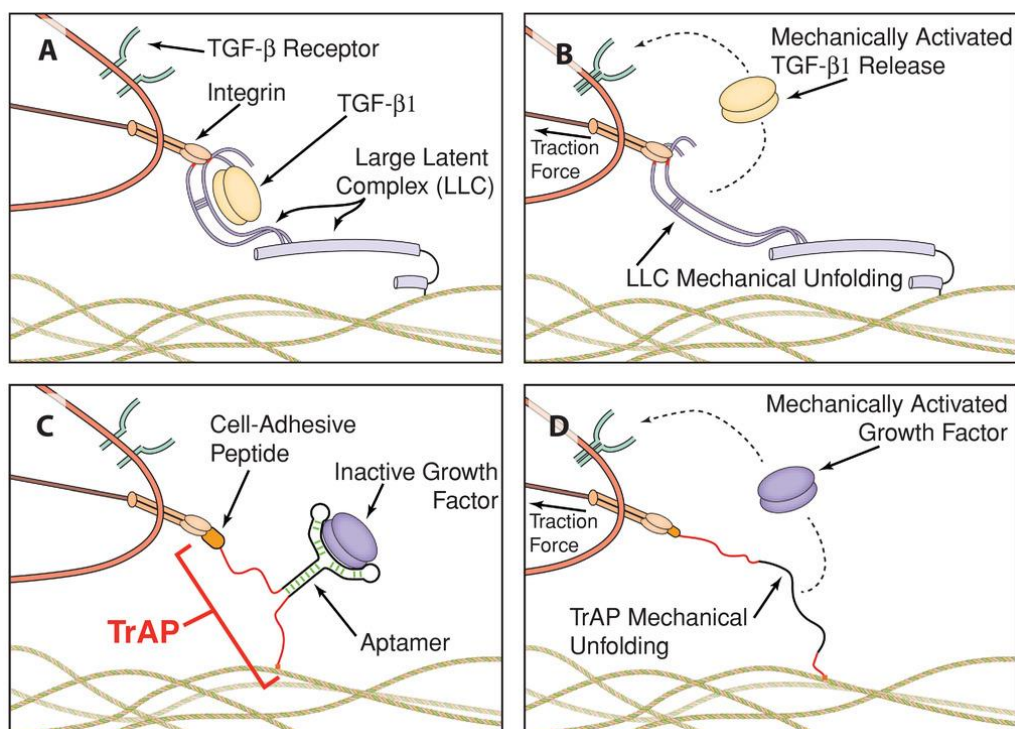


**Figure 1.15** Bioinspired aptamers enable the creation of synthetic mimics of the natural TGF- $\beta$ 1 large latent complex (LLC). TrAPs: Traction-Force Activated Payloads. Reproduced from *Adv. Mater.*, 31, 1806380, (2019). Using creative commons CC-BY license.

activated microparticles that release clot-dissolving drugs upon encountering obstructed blood vessels.<sup>107</sup> Such force-activated drugs are triggered by a broad range of force responses and can support only protein cargoes. A DNA based force sensing system, in this regard, could offer sensitivity at a molecular level that can be fine-tuned to a binary response. Almquist and colleagues developed a DNA aptamer evolved to bind TGF- $\beta$ 1 using SELEX and has been demonstrated to release cargo under mechanical forces<sup>108</sup> (Figure 1.15). Drawing broad applications from such an approach is challenging, as aptamer selection is required for each new cargo and the force threshold for delivery of an aptamer-cargo system cannot be altered as it depends on the aptamer-cargo binding affinity. Double stranded DNA has also been used as simple duplexes to plug the nanopores of silica microparticles loaded with drug molecules.<sup>109</sup> The drug can be released when the pores are opened due to dehybridization of the dsDNA using T-cell forces. It must be noted that silica microparticles suffer from poor tissue penetration and distribution while the smaller silica nanoparticles have promiscuous cell uptake which excludes them from many drug delivery applications. Hence, there is an

unmet need for a modular platform for delivering biomolecules such as proteins, nucleic acids, and small molecules with piconewton precision.

## 1.4 Developing mechanotargeting systems

### 1.4.1 GAP IN THE FIELD

The rapidly developing field of mechanobiology has brought to awareness the mechanical undertones prevalent in diseases. Rather than utilizing biochemical chemical markers as a proxy to identify disease states, an approach based on chemo biomechanical targeting can discriminate the targets effectively and achieve high levels of selectivity and specificity. Nascent attempts at developing a force-based drug delivery system lacks in a lot of aspect such as tunability to target cells at-will, the ease of formulating a wide variety of drugs, size ideal for efficient biodistribution, etc. (Table 1.1).

**Table 1.1** A summary of the force sensitive drug delivery systems reported in the literature.

Force sensitive platform	Sensitivity	Tunable	Drug/cargo	Size	Journal (Year)
Polymer aggregates	N/A	No	Proteins	~1-5 $\mu\text{m}$	<i>Science</i> (2012) <sup>1</sup>
DNA aptamers	N/A	No	Aptamer specific protein	~ 10 nm	<i>Advanced Materials</i> (2019) <sup>2</sup>
Silica microparticles	~50 pN	No	Small molecules	~1-5 $\mu\text{m}$	<i>Materials Horizons</i> (2020) <sup>3</sup>

DNA based probes have been demonstrated to have tunable well-defined force thresholds. The commercial availability of oligonucleotides furnished with chemical modifications for ligand, drug and fluorophore conjugations makes DNA based system the ideal candidate for designing

force-responsive drug delivery systems. A force-based therapeutic could be formulated by anyone using “off the shelf” oligonucleotides in a few steps.<sup>90</sup> Despite a lot of progress in the field of mechanobiology it remains an unmet need to produce accessible drug delivery systems leveraging cellular mechanics.

#### 1.4.2 DNA NANOCAGES

Nanosystems that are inherently biocompatible and have modular properties are considered as rational carriers for drug delivery. Among nanocarriers, DNA origami is ideal for nanoscopic device construction owing to its favorable properties such as predictive assembly through Watson–Crick–Franklin base pairing, rigid structure, and well-defined geometry.<sup>110</sup> One of the common uses for DNA nanostructures is cargo encapsulation for biochemically targeted delivery. While higher order DNA structures can be assembled through multiple smaller DNA motifs using sticky end interactions, such large structures suffer from high cost, poor yields requiring further purification, and *in vivo* degradation.<sup>111</sup>

Simple DNA cages can be constructed in one-pot assembly of all the strands. DNA tetrahedron was the first nanocage that can be self-assembled in few seconds by one step annealing protocol.<sup>112</sup> Tetrahedral DNA is renowned as one of the practical DNA nanoconstructs as it has more viable *in vivo* drug delivery and it can be constructed from four DNA strands which makes it a cost-effective origami. Tetrahedral DNA (TD) assembly process is stereoselective and yields a single diastereomer with the major grooves facing inwards at the vertices. The hybridization required to form the tetrahedron is faster and happens in an intermolecular fashion. Hence, DNA tetrahedrons can be assembled efficiently with yields as high as ~95% for the single diastereomer in the nanomolar concentrations.



TDs could be nanofabricated to hold a sphere of radius of  $\sim 2.6$  nm which corresponds to a globular protein with a molecular weight of  $\sim 60$  kDa. The encapsulation of cytochrome C inside a TD has been demonstrated by conjugating the protein to one of the four DNA strands and simply annealing them together. The position of the protein relative to the nanocage could be controlled by the point of attachment to one of the edges. By moving the attachment point on the double-helical along the edge of the tetrahedron, the linked cargo can be rotated by about  $35^\circ$  which allows it to be placed on the inside at the 8<sup>th</sup> nucleotide and outside at the 13<sup>th</sup> nucleotide<sup>113</sup> (Figure 1.16). TDs have also been used for non-covalent encapsulation of proteins such as catabolite activator protein (CAP) by editing one of the edges to contain the CAP binding site edge in the presence of its allosteric effector cyclic adenosine monophosphate<sup>114</sup> (cAMP). Such a caging technique renders the transcription factor inactive which can be used for triggered activation by opening the tetrahedron with DNase I.

Larger DNA tetrahedron has also been used for the efficient encapsulation of other cargo such as gold nanoparticles (AuNP) and oligonucleotides. For example, AuNP conjugated to ssDNA can be captured inside the cavity of a TD by having a complementary overhang for DNA hybridization. Using this technique, a 10 nm AuNP with a thiol-modified DNA was linked to the “open form” of the TD strands and closed by annealing the additional DNA strands.<sup>115</sup> Similarly, the nicks of a TD have been used to place overhangs for hybridization of siRNA cargo and up to six strands can be bound to one tetrahedral

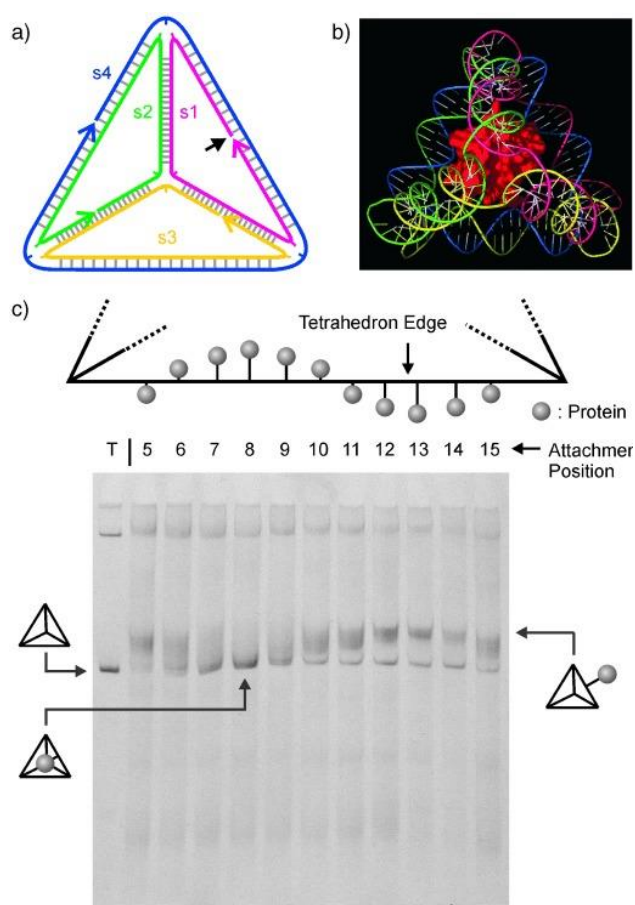


**Figure 1.16** Positioning a protein within a DNA tetrahedron. Reproduced from *Angew. Chem. Int. Ed.*, 45, 7414-741 (2006) with permission from WILEY

nanocage.<sup>116</sup> TDs can also be used to load intercalating molecules and drugs such as YOYO-1, doxorubicin, daunorubicin, etc<sup>117</sup>.

With the ability to encapsulate a wide array of cargoes, it is unsurprising that TDs are extensively used for drug delivery applications.<sup>118</sup> Moreover, TDs exhibit higher uptake, minimal toxicity, and possess substantial physiological stability.<sup>119</sup> TDs are the smallest DNA origami and due to its relatively compact size (~10 nm) it can overcome many barriers commonly encountered in drug delivery applications. TDs can also be configured to release cargo upon binding of biomolecules in cells. Such a smart drug delivery system would enable the transport of cargo to cells and release them in response to biomolecular triggers depending on cell state.

Given the existing knowledge body, most force sensors are constructed based on a DNA structure. Similarly in drug delivery, DNA tetrahedrons are ideal drug carriers with programmable delivery. Taken together, TDs have potential for force sensing applications as well as force-based nanocage opening to release its encapsulated contents. While classic DNA force probes are linear structures such as a duplex or hairpin, a complex structure such as a tetrahedron has never been used as a force sensing element. Since, TDs are versatile drug delivery vehicles and has the force sensing potential, it constitutes an ideal candidate for the development of force responsive nanostructures which we refer to as 'DNA mechanocapsules' for modular cargo delivery and for clinical applications targeting mechanical phenotypes of diseases.

## 1.5 Aims and scope of the dissertation

The field of mechanobiology has vastly improved our understanding of biological systems, which has been possible due to the technological advancements in mechanical characterization. At a molecular level, the development of single molecule force spectroscopy and molecular tension probes have given us insight on the nanomechanical forces exerted by

various biomolecules in the cell. However, the implications of these biomechanical activities in various diseases are poorly understood and their utilization as markers of diseases has been severely lacking. Hence, developing a force responsive system with tunable force thresholds with modular cargo encapsulation techniques would open new avenues in targeted drug delivery. DMCs in this regard can not only improve the specificity of existing therapeutics but could also make previously untargetable diseases possible.

In this dissertation, the DNA tetrahedron is engineered to be force responsive in physiological context to enable the release of therapeutics cargo based on mechanical phenotypes. The following questions will be tackled 1) How can a 3D DNA nanostructure be designed to rupture at specified force thresholds? 2) Do the DMCs confer any advantage over traditional DNA probes in force sensing and other DNA origami in terms of drug delivery 3) Can DMCs distinguish diseased cells from healthy cell populations and target them specifically for drug release? 4) How can a wide array of cargoes be formulated and delivered in a force responsive manner? 5) Can a subpopulation of cells with a high force phenotype be discriminated without collateral uptake from surrounding tissue? 6) Can DMCs improve the specificity and potency of known drugs?

The dissertation aims to answer the aforementioned question and is arranged in the following sequence. A detailed description of using coarse grain simulation to engineer DNA mechanocapsules is presented in **Chapter 2**. These force responsive TDs are the smallest of DNA nanocages and represent the first tunable, modular, mechanical triggerable drug delivery system. In **Chapter 3**, the synthesis of these DNA mechanocapsules with various modifications are addressed, followed by the characterization of these DMCs on surface. The force specific *in vitro* denaturing of DMCs using various cell lines along with cell subtype selectivity based on the receptor forces is also described. **Chapter 4** elaborates on the different techniques to load drugs on the DMCs. This chapter also includes DMCs' various applications such as high throughput mechanical activity tagging, force-based mRNA knockdown which can be used to modulate cellular phenotypes with specific receptor forces. Finally, Chapter 5 will summarize the development and demonstration of DMCs' capabilities.

The chapter will conclude with an outline of DMC applications and potential therapeutics *in vivo* that could be constructed with this force sensitive drug delivery platform.

## References

1. On Form and Mechanical Efficiency. in *On Growth and Form* (eds. Thompson, D. W. & Bonner, J. T.) 221–267 (Cambridge University Press, 1992).  
doi:10.1017/CBO9781107325852.012.
2. Naqvi, S. M. & McNamara, L. M. Stem Cell Mechanobiology and the Role of Biomaterials in Governing Mechanotransduction and Matrix Production for Tissue Regeneration. *Frontiers in Bioengineering and Biotechnology* **8**, (2020).
3. Rashid, S. A. *et al.* DNA Tension Probes Show that Cardiomyocyte Maturation Is Sensitive to the Piconewton Traction Forces Transmitted by Integrins. *ACS Nano* **16**, 5335–5348 (2022).
4. Ma, V. P.-Y. *et al.* The magnitude of LFA-1/ICAM-1 forces fine-tune TCR-triggered T cell activation. *Science Advances* **8**, eabg4485 (2022).
5. Tetley, R. J. *et al.* Tissue fluidity promotes epithelial wound healing. *Nat. Phys.* **15**, 1195–1203 (2019).
6. Dufrêne, Y. F. & Persat, A. Mechanomicrobiology: how bacteria sense and respond to forces. *Nat Rev Microbiol* **18**, 227–240 (2020).
7. Yanez, L. Z., Han, J., Behr, B. B., Pera, R. A. R. & Camarillo, D. B. Human oocyte developmental potential is predicted by mechanical properties within hours after fertilization. *Nat Commun* **7**, 10809 (2016).
8. Carlos-Oliveira, M., Lozano-Juan, F., Occhetta, P., Visone, R. & Rasponi, M. Current strategies of mechanical stimulation for maturation of cardiac microtissues. *Biophys Rev* **13**, 717–727 (2021).

9. Petzold, J. & Gentleman, E. Intrinsic Mechanical Cues and Their Impact on Stem Cells and Embryogenesis. *Frontiers in Cell and Developmental Biology* **9**, (2021).
10. Li, Z. *et al.* Cellular traction forces: a useful parameter in cancer research. *Nanoscale* **9**, 19039–19044 (2017).
11. Hall, C. M., Moeendarbary, E. & Sheridan, G. K. Mechanobiology of the brain in ageing and Alzheimer's disease. *European Journal of Neuroscience* **53**, 3851–3878 (2021).
12. Barnes, J. M., Przybyla, L. & Weaver, V. M. Tissue mechanics regulate brain development, homeostasis and disease. *Journal of Cell Science* **130**, 71–82 (2017).
13. Murphy, M. C. *et al.* Regional brain stiffness changes across the Alzheimer's disease spectrum. *NeuroImage: Clinical* **10**, 283–290 (2016).
14. McKee, A. C., Stein, T. D., Kiernan, P. T. & Alvarez, V. E. The Neuropathology of Chronic Traumatic Encephalopathy. *Brain Pathology* **25**, 350–364 (2015).
15. Ladoux, B. & Mège, R.-M. Mechanobiology of collective cell behaviours. *Nat Rev Mol Cell Biol* **18**, 743–757 (2017).
16. Vedula, S. R. K. *et al.* Mechanics of epithelial closure over non-adherent environments. *Nat Commun* **6**, 6111 (2015).
17. Corbin, E. A. *et al.* Tunable and Reversible Substrate Stiffness Reveals a Dynamic Mechanosensitivity of Cardiomyocytes. *ACS Appl. Mater. Interfaces* **11**, 20603–20614 (2019).
18. Xie, J. *et al.* Substrate stiffness-regulated matrix metalloproteinase output in myocardial cells and cardiac fibroblasts: Implications for myocardial fibrosis. *Acta Biomaterialia* **10**, 2463–2472 (2014).

19. Tallawi, M., Rai, R., Boccaccini, Aldo. R. & Aifantis, K. E. Effect of Substrate Mechanics on Cardiomyocyte Maturation and Growth. *Tissue Engineering Part B: Reviews* **21**, 157–165 (2015).
20. Ghanta, R. K. *et al.* Influence of Supraphysiologic Biomaterial Stiffness on Ventricular Mechanics and Myocardial Infarct Reinforcement. *Acta Biomaterialia* **149**, 30–39 (2022).
21. Kwon, S. G., Kwon, Y. W., Lee, T. W., Park, G. T. & Kim, J. H. Recent advances in stem cell therapeutics and tissue engineering strategies. *Biomaterials Research* **22**, 36 (2018).
22. D'Angelo, F. *et al.* Tuning Multi/Pluri-Potent Stem Cell Fate by Electrospun Poly(l-lactic acid)-Calcium-Deficient Hydroxyapatite Nanocomposite Mats. *Biomacromolecules* **13**, 1350–1360 (2012).
23. Wang, Y.-K. & Chen, C. S. Cell adhesion and mechanical stimulation in the regulation of mesenchymal stem cell differentiation. *Journal of Cellular and Molecular Medicine* **17**, 823–832 (2013).
24. Pickup, M. W., Mouw, J. K. & Weaver, V. M. The extracellular matrix modulates the hallmarks of cancer. *EMBO reports* **15**, 1243–1253 (2014).
25. Padera, T. P. *et al.* Cancer cells compress intratumour vessels. *Nature* **427**, 695–695 (2004).
26. Hughes, J. D. *et al.* Higher-Resolution Magnetic Resonance Elastography in Meningiomas to Determine Intratumoral Consistency. *Neurosurgery* **77**, 653 (2015).
27. Spencer, A. *et al.* Biomechanical regulation of breast cancer metastasis and progression. *Sci Rep* **11**, 9838 (2021).
28. Li, N. *et al.* Multiscale biomechanics and mechanotransduction from liver fibrosis to cancer. *Advanced Drug Delivery Reviews* **188**, 114448 (2022).

29. Brás, M. M., Sousa, S. R., Carneiro, F., Radmacher, M. & Granja, P. L. Mechanobiology of Colorectal Cancer. *Cancers* **14**, 1945 (2022).
30. Butcher, D. T., Alliston, T. & Weaver, V. M. A tense situation: forcing tumour progression. *Nat Rev Cancer* **9**, 108–122 (2009).
31. Netti, P. A., Berk, D. A., Swartz, M. A., Grodzinsky, A. J. & Jain, R. K. Role of Extracellular Matrix Assembly in Interstitial Transport in Solid Tumors<sup>1</sup>. *Cancer Research* **60**, 2497–2503 (2000).
32. Kraning-Rush, C. M., Califano, J. P. & Reinhart-King, C. A. Cellular Traction Stresses Increase with Increasing Metastatic Potential. *PLOS ONE* **7**, e32572 (2012).
33. McNamara, L. E. *et al.* The role of microtopography in cellular mechanotransduction. *Biomaterials* **33**, 2835–2847 (2012).
34. Kasza, K. E. *et al.* The cell as a material. *Current Opinion in Cell Biology* **19**, 101–107 (2007).
35. Mohammed, D. *et al.* Innovative Tools for Mechanobiology: Unraveling Outside-In and Inside-Out Mechanotransduction. *Frontiers in Bioengineering and Biotechnology* **7**, (2019).
36. Nguyen, A. T., Sathe, S. R. & Yim, E. K. F. From nano to micro: topographical scale and its impact on cell adhesion, morphology and contact guidance. *J. Phys.: Condens. Matter* **28**, 183001 (2016).
37. McKenzie, J. L., Waid, M. C., Shi, R. & Webster, T. J. Decreased functions of astrocytes on carbon nanofiber materials. *Biomaterials* **25**, 1309–1317 (2004).
38. Bade, N. D., Kamien, R. D., Assoian, R. K. & Stebe, K. J. Curvature and Rho activation differentially control the alignment of cells and stress fibers. *Science Advances* **3**, e1700150 (2017).



39. Kung, C. A possible unifying principle for mechanosensation. *Nature* **436**, 647–654 (2005).
40. Luciano, M. *et al.* Cell monolayers sense curvature by exploiting active mechanics and nuclear mechanoadaptation. *Nat. Phys.* **17**, 1382–1390 (2021).
41. Galior, K., Liu, Y., Yehl, K., Vivek, S. & Salaita, K. Titin-Based Nanoparticle Tension Sensors Map High-Magnitude Integrin Forces within Focal Adhesions. *Nano Lett.* **16**, 341–348 (2016).
42. Chen, Y.-C. *et al.* DNA tension assays reveal that force-dependent integrin activation regulates neurite outgrowth in primary cortical neurons. *Biomaterials Advances* **150**, 213431 (2023).
43. Zhang, Y., Ge, C., Zhu, C. & Salaita, K. DNA-based digital tension probes reveal integrin forces during early cell adhesion. *Nat Commun* **5**, 5167 (2014).
44. Kwak, K. *et al.* Intrinsic properties of human germinal center B cells set antigen affinity thresholds. *Science Immunology* **3**, eaau6598 (2018).
45. Natkanski, E. *et al.* B Cells Use Mechanical Energy to Discriminate Antigen Affinities. *Science* **340**, 1587–1590 (2013).
46. Beedle, A. E. M. & Garcia-Manyes, S. The role of single-protein elasticity in mechanobiology. *Nat Rev Mater* **8**, 10–24 (2023).
47. Kechagia, J. Z., Ivaska, J. & Roca-Cusachs, P. Integrins as biomechanical sensors of the microenvironment. *Nat Rev Mol Cell Biol* **20**, 457–473 (2019).
48. Mechanical force releases nascent chain-mediated ribosome arrest in vitro and in vivo | Science. <https://www-science-org.proxy.library.emory.edu/doi/10.1126/science.1261909>.

49. Vollrath, M. A., Kwan, K. Y. & Corey, D. P. The Micromachinery of Mechanotransduction in Hair Cells. *Annual Review of Neuroscience* **30**, 339–365 (2007).
50. Klein-Nulend, J., Bacabac, R. G., Veldhuijzen, J. P. & Van Loon, J. J. W. A. Microgravity and bone cell mechanosensitivity. *Advances in Space Research* **32**, 1551–1559 (2003).
51. Hammerschmidt, S., Kuhn, H., Gessner, C., Seyfarth, H.-J. & Wirtz, H. Stretch-Induced Alveolar Type II Cell Apoptosis. *Am J Respir Cell Mol Biol* **37**, 699–705 (2007).
52. Martino, F., Perestrelo, A. R., Vinarský, V., Pagliari, S. & Forte, G. Cellular Mechanotransduction: From Tension to Function. *Frontiers in Physiology* **9**, (2018).
53. Elosegui-Artola, A. *et al.* Force Triggers YAP Nuclear Entry by Regulating Transport across Nuclear Pores. *Cell* **171**, 1397–1410.e14 (2017).
54. Dupont, S. *et al.* Role of YAP/TAZ in mechanotransduction. *Nature* **474**, 179–183 (2011).
55. Katoh, K., Kano, Y. & Noda, Y. Rho-associated kinase-dependent contraction of stress fibres and the organization of focal adhesions. *Journal of The Royal Society Interface* **8**, 305–311 (2010).
56. Scholz, N. *et al.* Molecular sensing of mechano- and ligand-dependent adhesion GPCR dissociation. *Nature* **615**, 945–953 (2023).
57. Sachs, F. Stretch-Activated Ion Channels: What Are They? *Physiology* **25**, 50–56 (2010).
58. Vogel, V. & Sheetz, M. Local force and geometry sensing regulate cell functions. *Nat Rev Mol Cell Biol* **7**, 265–275 (2006).
59. Markin, V. S. & Sachs, F. Thermodynamics of mechanosensitivity. *Phys. Biol.* **1**, 110 (2004).
60. Markin, V. S. & Martinac, B. Mechanosensitive ion channels as reporters of bilayer expansion. A theoretical model. *Biophysical Journal* **60**, 1120–1127 (1991).

61. Davidson, P. M. & Lammerding, J. Broken nuclei – lamins, nuclear mechanics, and disease. *Trends in Cell Biology* **24**, 247–256 (2014).
62. Frantz, C., Stewart, K. M. & Weaver, V. M. The extracellular matrix at a glance. *Journal of Cell Science* **123**, 4195–4200 (2010).
63. Guimarães, C. F., Gasperini, L., Marques, A. P. & Reis, R. L. The stiffness of living tissues and its implications for tissue engineering. *Nat Rev Mater* **5**, 351–370 (2020).
64. Rief, M., Gautel, M., Schemmel, A. & Gaub, H. E. The Mechanical Stability of Immunoglobulin and Fibronectin III Domains in the Muscle Protein Titin Measured by Atomic Force Microscopy. *Biophysical Journal* **75**, 3008–3014 (1998).
65. Harrison, O. J. *et al.* Two-step adhesive binding by classical cadherins. *Nat Struct Mol Biol* **17**, 348–357 (2010).
66. Manibog, K. *et al.* Molecular determinants of cadherin ideal bond formation: Conformation-dependent unbinding on a multidimensional landscape. *Proceedings of the National Academy of Sciences* **113**, E5711–E5720 (2016).
67. Salameh, A. & Dhein, S. Effects of mechanical forces and stretch on intercellular gap junction coupling. *Biochimica et Biophysica Acta (BBA) - Biomembranes* **1828**, 147–156 (2013).
68. Wong, R. C. B., Pera, M. F. & Pébay, A. Role of Gap Junctions in Embryonic and Somatic Stem Cells. *Stem Cell Rev* **4**, 283–292 (2008).
69. Gingras, A. R. *et al.* Mapping and Consensus Sequence Identification for Multiple Vinculin Binding Sites within the Talin Rod \*. *Journal of Biological Chemistry* **280**, 37217–37224 (2005).

70. del Rio, A. *et al.* Stretching Single Talin Rod Molecules Activates Vinculin Binding. *Science* **323**, 638–641 (2009).
71. Pang, S. M., Le, S., Kwiatkowski, A. V. & Yan, J. Mechanical stability of  $\alpha$ T-catenin and its activation by force for vinculin binding. *MBoC* **30**, 1930–1937 (2019).
72. Elosegui-Artola, A., Trepap, X. & Roca-Cusachs, P. Control of Mechanotransduction by Molecular Clutch Dynamics. *Trends in Cell Biology* **28**, 356–367 (2018).
73. Bridgewater, R. E., Norman, J. C. & Caswell, P. T. Integrin trafficking at a glance. *Journal of Cell Science* **125**, 3695–3701 (2012).
74. Ramovs, V., te Molder, L. & Sonnenberg, A. The opposing roles of laminin-binding integrins in cancer. *Matrix Biology* **57–58**, 213–243 (2017).
75. Chen, Y. *et al.* An integrin  $\alpha$ IIb $\beta$ 3 intermediate affinity state mediates biomechanical platelet aggregation. *Nat. Mater.* **18**, 760–769 (2019).
76. Cavalcanti-Adam, E. A. *et al.* Cell Spreading and Focal Adhesion Dynamics Are Regulated by Spacing of Integrin Ligands. *Biophysical Journal* **92**, 2964–2974 (2007).
77. Zhang, Y. *et al.* Platelet integrins exhibit anisotropic mechanosensing and harness piconewton forces to mediate platelet aggregation. *Proceedings of the National Academy of Sciences* **115**, 325–330 (2018).
78. Rakshit, S. & Sivasankar, S. Biomechanics of cell adhesion: how force regulates the lifetime of adhesive bonds at the single molecule level. *Phys. Chem. Chem. Phys.* **16**, 2211–2223 (2014).
79. Hamidi, H. & Ivaska, J. Every step of the way: integrins in cancer progression and metastasis. *Nat Rev Cancer* **18**, 533–548 (2018).

80. Schnell, O. *et al.* Expression of Integrin  $\alpha\beta 3$  in Gliomas Correlates with Tumor Grade and Is not Restricted to Tumor Vasculature. *Brain Pathology* **18**, 378–386 (2008).
81. Desgrosellier, J. S. & Cheresh, D. A. Integrins in cancer: biological implications and therapeutic opportunities. *Nat Rev Cancer* **10**, 9–22 (2010).
82. Stupp, R. *et al.* Cilengitide combined with standard treatment for patients with newly diagnosed glioblastoma with methylated MGMT promoter (CENTRIC EORTC 26071-22072 study): a multicentre, randomised, open-label, phase 3 trial. *The Lancet Oncology* **15**, 1100–1108 (2014).
83. Harris, A. K., Wild, P. & Stopak, D. Silicone Rubber Substrata: A New Wrinkle in the Study of Cell Locomotion. *Science* **208**, 177–179 (1980).
84. Holenstein, C. N., Silvan, U. & Snedeker, J. G. High-resolution traction force microscopy on small focal adhesions - improved accuracy through optimal marker distribution and optical flow tracking. *Sci Rep* **7**, 41633 (2017).
85. Zanca, A., Mozetic, P., Orsini, M., Forte, G. & Rainer, A. A primer to traction force microscopy. *Journal of Biological Chemistry* **298**, (2022).
86. Liu, Z., Cui, X., Fan, Y. & Li, Z. The continuous evolution of 2D cell-traction forces quantification technology. *Innovation* **3**, (2022).
87. Ribeiro, A. J. S., Denisin, A. K., Wilson, R. E. & Pruitt, B. L. For whom the cells pull: Hydrogel and micropost devices for measuring traction forces. *Methods* **94**, 51–64 (2016).
88. Schoen, I., Hu, W., Klotzsch, E. & Vogel, V. Probing Cellular Traction Forces by Micropillar Arrays: Contribution of Substrate Warping to Pillar Deflection. *Nano Lett.* **10**, 1823–1830 (2010).

89. Ham, T. R., Collins, K. L. & Hoffman, B. D. Molecular tension sensors: moving beyond force. *Current Opinion in Biomedical Engineering* **12**, 83–94 (2019).
90. Blanchard, A. T. & Salaita, K. Emerging uses of DNA mechanical devices. *Science* **365**, 1080–1081 (2019).
91. Hu, Y., Duan, Y. & Salaita, K. DNA Nanotechnology for Investigating Mechanical Signaling in the Immune System. *Angewandte Chemie International Edition* **n/a**, e202302967.
92. Ma, R. *et al.* DNA probes that store mechanical information reveal transient piconewton forces applied by T cells. *Proceedings of the National Academy of Sciences* **116**, 16949–16954 (2019).
93. Ma, V. P.-Y. & Salaita, K. DNA Nanotechnology as an Emerging Tool to Study Mechanotransduction in Living Systems. *Small* **15**, 1900961 (2019).
94. Wang, X. & Ha, T. Defining Single Molecular Forces Required to Activate Integrin and Notch Signaling. *Science* **340**, 991–994 (2013).
95. de Gennes, P.-G. Maximum pull out force on DNA hybrids. *Comptes Rendus de l'Académie des Sciences - Series IV - Physics* **2**, 1505–1508 (2001).
96. Mosayebi, M., Louis, A. A., Doye, J. P. K. & Ouldridge, T. E. Force-Induced Rupture of a DNA Duplex: From Fundamentals to Force Sensors. *ACS Nano* **9**, 11993–12003 (2015).
97. Bender, R. L., Ogasawara, H., Kellner, A. V., Velusamy, A. & Salaita, K. Unbreakable DNA tension probes show that cell adhesion receptors detect the molecular force-extension curve of their ligands. 2022.04.04.487040 Preprint at <https://doi.org/10.1101/2022.04.04.487040> (2022).
98. Özkale, B., Sakar, M. S. & Mooney, D. J. Active biomaterials for mechanobiology. *Biomaterials* **267**, 120497 (2021).

99. Deeken, C. R. & Lake, S. P. Mechanical properties of the abdominal wall and biomaterials utilized for hernia repair. *Journal of the Mechanical Behavior of Biomedical Materials* **74**, 411–427 (2017).
100. Lam, W. A., Rosenbluth, M. J. & Fletcher, D. A. Chemotherapy exposure increases leukemia cell stiffness. *Blood* **109**, 3505–3508 (2006).
101. Beck, A., Goetsch, L., Dumontet, C. & Corvaia, N. Strategies and challenges for the next generation of antibody–drug conjugates. *Nat Rev Drug Discov* **16**, 315–337 (2017).
102. Li, Y. *et al.* Positively Charged Polyprodrug Amphiphiles with Enhanced Drug Loading and Reactive Oxygen Species-Responsive Release Ability for Traceable Synergistic Therapy. *J. Am. Chem. Soc.* **140**, 4164–4171 (2018).
103. Zhang, J. *et al.* Conditional Deoxyribozyme–Nanoparticle Conjugates for miRNA-Triggered Gene Regulation. *ACS Appl. Mater. Interfaces* **12**, 37851–37861 (2020).
104. Qiu, Y., Bai, J., Feng, Y., Shi, X. & Zhao, X. Use of pH-Active Catechol-Bearing Polymeric Nanogels with Glutathione-Responsive Dissociation to Codeliver Bortezomib and Doxorubicin for the Synergistic Therapy of Cancer. *ACS Appl. Mater. Interfaces* **13**, 36926–36937 (2021).
105. Meng, H. *et al.* Autonomous in Vitro Anticancer Drug Release from Mesoporous Silica Nanoparticles by pH-Sensitive Nanovalves. *J. Am. Chem. Soc.* **132**, 12690–12697 (2010).
106. Lu, H., Xu, S., Guo, Z., Zhao, M. & Liu, Z. Redox-Responsive Molecularly Imprinted Nanoparticles for Targeted Intracellular Delivery of Protein toward Cancer Therapy. *ACS Nano* **15**, 18214–18225 (2021).
107. Korin, N. *et al.* Shear-Activated Nanotherapeutics for Drug Targeting to Obstructed Blood Vessels. *Science* **337**, 738–742 (2012).

108. Stejskalová, A., Oliva, N., England, F. J. & Almquist, B. D. Biologically Inspired, Cell-Selective Release of Aptamer-Trapped Growth Factors by Traction Forces. *Advanced Materials* **31**, 1806380 (2019).
109. Lei, K. *et al.* Cancer-cell stiffening via cholesterol depletion enhances adoptive T-cell immunotherapy. *Nat Biomed Eng* **5**, 1411–1425 (2021).
110. Chandrasekaran, A. R. & Levchenko, O. DNA Nanocages. *Chem. Mater.* **28**, 5569–5581 (2016).
111. Chandrasekaran, A. R. Nuclease resistance of DNA nanostructures. *Nat Rev Chem* **5**, 225–239 (2021).
112. Goodman, R. P. *et al.* Rapid Chiral Assembly of Rigid DNA Building Blocks for Molecular Nanofabrication. *Science* **310**, 1661–1665 (2005).
113. Erben, C. M., Goodman, R. P. & Turberfield, A. J. Single-Molecule Protein Encapsulation in a Rigid DNA Cage. *Angewandte Chemie International Edition* **45**, 7414–7417 (2006).
114. Crawford, R. *et al.* Non-covalent Single Transcription Factor Encapsulation Inside a DNA Cage. *Angewandte Chemie International Edition* **52**, 2284–2288 (2013).
115. Zhang, C. *et al.* DNA Nanocages Swallow Gold Nanoparticles (AuNPs) to Form AuNP@DNA Cage Core–Shell Structures. *ACS Nano* **8**, 1130–1135 (2014).
116. Lee, H. *et al.* Molecularly self-assembled nucleic acid nanoparticles for targeted in vivo siRNA delivery. *Nature Nanotech* **7**, 389–393 (2012).
117. Wang, F. *et al.* Gint4.T-Modified DNA Tetrahedrons Loaded with Doxorubicin Inhibits Glioma Cell Proliferation by Targeting PDGFR $\beta$ . *Nanoscale Research Letters* **15**, 150 (2020).



118. Duangrat, R., Udomprasert, A. & Kangsamaksin, T. Tetrahedral DNA nanostructures as drug delivery and bioimaging platforms in cancer therapy. *Cancer Science* **111**, 3164–3173 (2020).
119. Mathur, D. *et al.* Determining the Cytosolic Stability of Small DNA Nanostructures In Cellula. *Nano Lett.* **22**, 5037–5045 (2022).

## CHAPTER 2

# Design and *in silico* modeling of DMCs

This chapter is adapted from a manuscript in submission to Nature Communications: DNA mechanocapsules for programmable piconewton responsive drug delivery. Arventh Velusamy, Radhika Sharma, Sk Aysha Rashid, Hiroaki Ogasawara and Khalid Salaita.

Aysha Rashid performed SLB calibration, assisted in characterization of DMCs with cells.

### 2.1 Abstract

DNA based probes have been widely used as force sensors that have illuminated the underlying mechanical processes of many cellular components including various disease states. Targeting diseases based on dysregulated forces has not been reliably achieved due to the lack of force responsive cargo carriers. Here, we report DNA mechanocapsules based on the DNA tetrahedron that has been demonstrated to encapsulate an array of cargoes and for drug delivery. Using oxDNA coarse-grain simulations, we show that these nanostructures are indeed responsive to piconewtons of force which can be tuned to meet targeting and drug release requirements. Computational modeling illustrates a predictable rupture pathway that releases the encapsulated drug irrespective of force orientation. Further we engineer non-responsive structures that do not terminate mechanotransduction and for their utility in experiments as controls. Finally, we demonstrate that all mechanocapsules have minimal leakage of non-covalently encapsulated cargo despite having multiple pores. The consistent mechanical properties of DMCs as evident in these simulations, makes the DNA mechanocapsules a robust platform for therapeutic release based on cellular forces.

## 2.2 Introduction

Cellular forces are a useful diagnostic marker since malignant states have dysregulated mechanics and measuring them has been important in understanding their role in physiological and pathological functions.<sup>1-4</sup> Force sensing is usually done with polymeric structures such as DNA and proteins that are responsive in the piconewton regime. Proteins are well suited for intracellular applications where they can be genetically encoded but is not amenable for chemical modifications designs.<sup>5,6</sup> Several DNA based extracellular sensors have been constructed owing to its predictable structure, hydrogen bonding, and commercial availability. DNA duplex has been used as tension gauge tethers (TGTs) that can be used to sense receptor forces from 12-56 pN.<sup>7</sup> Since the rupture force depends on the orientation, TGTs can be tuned by controlling the rupture geometry by strategic ligand placement on the duplex. DNA hairpins are dynamic and can sense instantaneous forces in the 4-20 pN range.<sup>8</sup> They can be tuned by altering the hairpin sequence and length. DNA duplex can also rupture when both the ends of a given strand are stretched by a mechanism known as peeling or overstretching.<sup>9</sup> This has been leveraged to for force sensing and cellular tagging for downstream applications. While DNA structures are optimal cellular force sensors that can produce defined, digital fluorescence responses they lack the ability to deliver drugs based on biophysical inputs. Theoretically, a DNA duplex can be attached with a desired molecular payload that can be released either through a duplex rupture or overstretching based on forces. Such an approach can potentially lead to non-specific drug action since it lacks a prodrug activation step to trigger the cargo to perform its intended function. For this purpose, the drug needs to be sealed in its inactive form until a force converts into its therapeutically active form at vicinity of mechanically deranged tissue site. To achieve this a new form of DNA based piconewton force sensor that can encase therapeutics in their prodrug form and act as a drug delivery vehicle that can be activated based on force inputs from diseased tissues. DNA tetrahedron is a small and modular origami that has been used for encapsulating various molecules,<sup>10,11</sup> inactivating enzymes,<sup>12</sup> and drug delivery.<sup>13</sup> While DNA origami platforms have been used for manipulating cellular behavior,<sup>14</sup> drug delivery<sup>15</sup> and even force sensing by decorating them with hairpins and TGTs,<sup>16,17</sup> they have not been employed as a force sensor on its own. The mechanics of TGTs and hairpins are easily predictable with readily available

mathematical models that can quantify rupture forces.<sup>18</sup> Although, the initial report on the preparation of the DNA tetrahedron examined its response under compressive forces of an AFM cantilever,<sup>19</sup> such a mechanism is not appropriate for triggered release of molecular medicine based on forces. On the contrary, the mechanical response of a DNA tetrahedron to pulling forces has not been studied thus far since it requires complex modeling to understand its dynamics under force.

One of the most widely employed models for predicting the thermal and mechanical properties of DNA structures is oxDNA.<sup>20</sup> Published in 2011<sup>21</sup> and improved over the years,<sup>20</sup> has been known to accurately capture the behavior of DNA. Owing to the coarse grain nature of the model, it can model short strands to giant origami constructions without difficulty. oxDNA has been used to predict DNA overstretching forces for strands of varying length.<sup>9</sup> It is also valuable for modeling DNA based molecular machines such as bipedal walkers<sup>22</sup> and motors.<sup>23,24</sup> Further, oxDNA model provides a complete picture of the unzipping and shearing geometries of rupture commonly observed in TGTs while other models fail to capture the underlying physics of the process.<sup>25</sup> oxDNA is also a useful tool in visualizing structures and their dynamics under forces, providing a nanoscopic view of the structural states with picosecond resolutions.<sup>26</sup> Experimental approaches such as atomic force microscopy, optical traps and biomembrane force probes are useful tools for rupture force estimation but do not provide insight into the mechanical transition states. An understanding of the dynamics is required for tuning and improving the designing of novel force sensing systems such as the DNA tetrahedron.

This chapter tackles the problem of designing an innovative, DNA based origami-structured force sensor that can act as a smart drug delivery vehicle that responds to elevated forces found in disease states. The *ab initio* designs utilized the fundamental principles of DNA to arrive at force responsive DNA mechanocapsules (DMCs) that were then modeled using oxDNA to predict its rupture force and dynamics. Coarse-grain modeling was further employed to refine and tune the nanostructures to produce a wide range of responses. Finally, the dimensional requirements for a kinetically trapped cargo were also gauged to decrease the probability of nonspecific release under experimental conditions.

## 2.3 Results and discussion

### 2.3.1 AB INITIO DNA MECHANOCAPSULE DESIGNS

To design a force responsive structure that ruptures in a predictable fashion *in vivo* and release its contents, we adopted the 20 bp regular DNA tetrahedron (Figure 2.1) as the DNA mechanocapsules (DMC). The orientation of the terminal nicks in the tetrahedron can be controlled by strategically moving them along the DNA helix on the edge. With the unpaired nucleotide at the hinge as 0<sup>th</sup> nucleotide, the 8<sup>th</sup> nucleotide faces the inside of the tetrahedron and the 13<sup>th</sup> nucleotide is on the outside, moving along the 5' to 3' direction.<sup>27</sup>

#### 20 bp Regular Tetrahedron | 4 Nicks

A denotes the unpaired hinge. Colours matched sections are complementary tetrahedron edges.

```

S1 - AGGCAGTTGAG A CGAACATTCTAAGTCTGAA A TTTATCACCCGCCATAGTAG A CGTATCACC
S2 - CTTGCTACACG A TTCAGACTTAGGAATGTTCTG A CATGCGAGGGTCCAATACCG A CGATTACAG
S3 - GGTGATAAAA A CGGTAGCAAGCTGTAATCG A CGGGAAGAGCATGCCATCC A CTACTATGGCG
S4 - CCTCGCATG A CTCAACTGCCTGCTGATACG A GGATGGGCATGCTCTTCCCG A CGGTATTGGAC
  
```

**Figure 2.1** DNA tetrahedron strand sequences published in *Science*, 310, 5754, 1661-1665 (2005)

Since, the DMC needed attachment points for the ligand, fluorophore-quencher pairs, and anchors; we initially modified the strands to have 2 nicks with the nucleotide modifications facing outside (13<sup>th</sup> nucleotide) on two different edges where the ligand for receptor interaction as well as the anchor for the surface adhesion can be conjugated. The ligand conjugated strand was named the force bearing (FB) strand. The nomenclature was chosen to reflect the fact that the receptor force initially gets transmitted through the strand (S3a in Figure 2.2). The other terminus of the force bearing strand was nicked to have docking points on the inside of the DMC for fluorophore-quencher pairs or therapeutic cargoes. To accommodate the modifications and their respective placements the 4 strands in the original DNA tetrahedron were strategically cleaved into 6 strands in the DMC.

The fluorophore-quencher pairs can be used for fluorescence read out when the FB strand in the DMCs get mechanically denatured by the cells. On the contrary, denaturation of the anchor

strand (strand S4) can lead to a case where the two edges flanking the fluorophore-quencher pairs (black and blue edges) can remain intact, failing to separate fluorophore-quencher beyond (10 nm). The lack of separation can fail to produce a fluorescence signal to read out the mechanical denaturing. To reduce or even eliminate the possibility of the anchor strand denaturing due to mechanical forces, the anchor strand was made longer such that the force bearing strand has a higher probability of rupture. The DMC was engineered to have a weak point in the structure that will predictably rupture and produce a fluorescence signal under the influence of cellular receptor forces. It must be noted that any rupture dynamic could still be beneficial in that it can still potentially rupture the DMC structure and release the encapsulated cargo.

Furthermore, the thermal stability of all six DMC strands were theoretically estimated to ensure that the force bearing strand has the lowest stability among the strands experiencing force in the structure (Table 2.1). While other strands in the DMC have lower predicted thermal melting points, the mechanical melting points can differ due to different parts of the structure experiencing differential loads. It must be noted that mechanical denaturation is also highly dependent on the loading rate and orientation of the forces.<sup>25</sup>

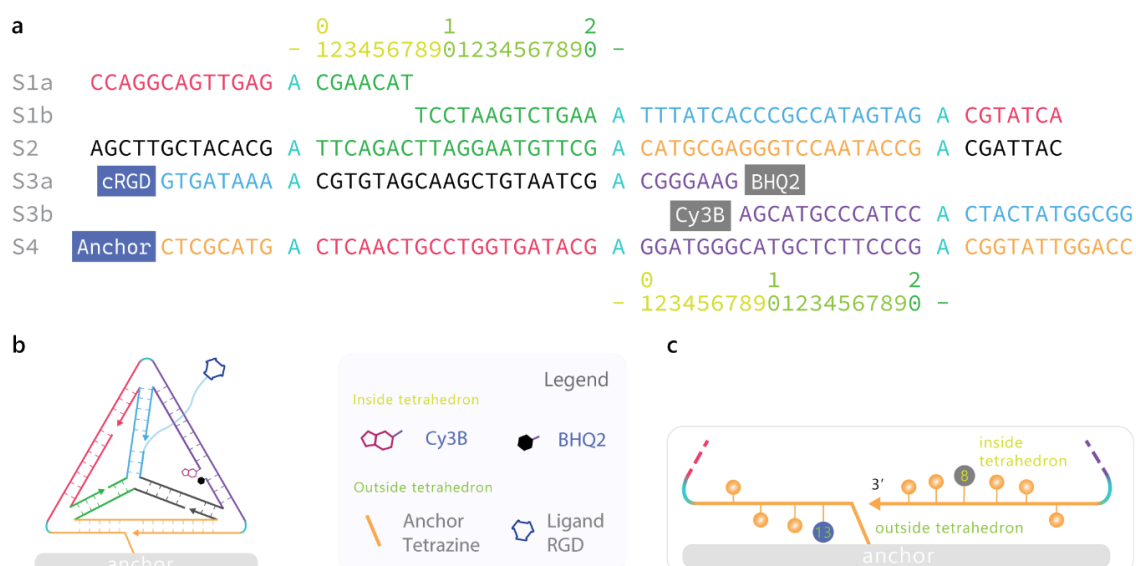


**Figure 2.2** DNA tetrahedron strands modified to display a ligand and anchor on the outside and a fluorophore-quencher pair on the inside adjacent to each other.

Similarly, two more chemically identical DMCs were designed, to produce DMCs with different force thresholds for rupture (Figure 2.3). This was achieved by truncating the length of the force bearing strands of DMCs and moving the ligand attachment points. The strand S2 was also ligated to avoid having multiple nicks on the same edge of the DMC since it can contribute to DMC's instability. Unlike the first design the FB strands were prioritized to have sufficient length to avoid spontaneous dehybridization. Correspondingly, the S3b strands were elongated to account for truncation in the force-bearing strand.

To tune the force thresholds further, the ligand attachment points were strategically placed on the terminus and in the middle of the FB strand. The remaining DMC strands were maintained at the same length as before. To assure cargo is oriented facing the inside of the DMC, internal modifications on the major groove of the FB strand were utilized as attachment point. These attachment points could also be used for quencher modifications as done in the initial design.

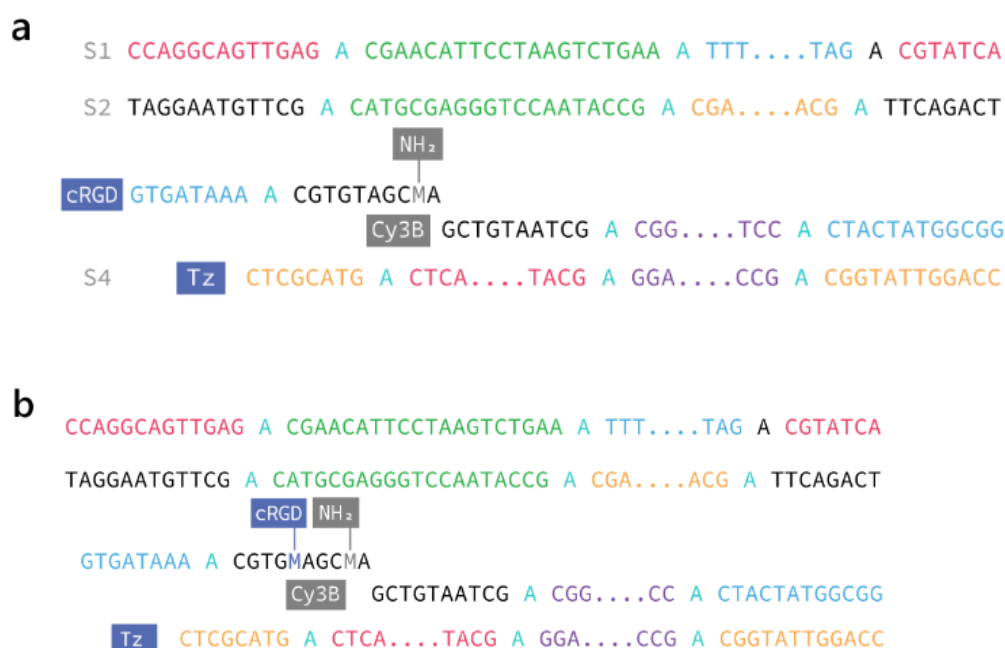


**Figure 2.3** Force threshold of DMCs were tuned by decreasing the length of force-bearing strand. (a, b) The force-bearing strand sequence can be chemically modified using internal alkynes (facing outward, blue M) and amines (facing inward, gray M) for the attachment of ligand and cargo respectively.

The three DMC designs were then further evaluated using coarse grain simulations to estimate force rupture thresholds as well as rupture dynamics.

### 2.3.2 oxDNA RUPTURE FORCE ESTIMATION

We designed three chemically identical DMCs to strategically deform and dehybridize, releasing encapsulated contents when pulled by cells. Attachment points on the outside were created for adhesion ligand and surface anchor, while fluorophore, cargo and quencher were placed inside. The nanocages were designed using 6 strands for 'high force' DMC and 5 strands for 'low force' DMC, with the adhesion ligand at the 5' terminus of the primary force-bearing strand which we speculate can be threaded out with pN forces.

The engineered DMCs were modelled to simulate responses under forces using oxDNA2 model.<sup>20</sup> The ligand and anchor point on the DMCs were pulled with harmonic trap. Harmonic traps act effectively like springs with arbitrary stiffness in the simulation, exerting forces when

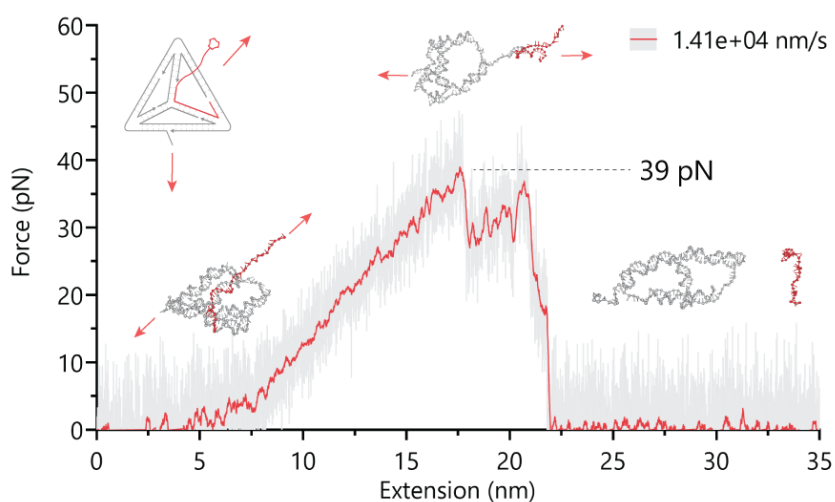


**Figure 2.4** Simulation of initial DMC with 6 strand design. The diagram on the left shows force application points on the DMC. The DMC structures along the graph in red and gray represent snapshots from the oxDNA simulations. The ligand (cRGD) attachment point on DMC was pulled at a rate of 14,100 nm/s while the anchor point was fixed. It is plotted along with their exponential moving averages of 40 data points in red.



its stretched due to pulling. They are useful in mimicking attachment to an anchor or to simulate constant extension experiments like AFM or optical traps. Parameters such as trap extension, particle distances and number of base pairs were extracted from the simulation. The DMC with six strands was simulated in oxDNA and it was found that a larger fraction of the structure disassembled under with higher loading rates (Figure S1). As the loading rate reduced, the disruption of the structure minimized to the dehybridization of the force bearing strand.

Finally, at the slowest loading rate of  $1.4 \times 10^4$  nm/s along the z-axis the force ruptured only the force bearing strand of the DMC (Supplementary Video 1). We found that DMC initially oriented along the z-axis when given sufficient time. Then the DMC deformed along the force axis followed by gradual dehybridization and complete rupture of FB strand (red strand) as the force ramped up. The plot in Figure 2.4 shows the trajectory of DMC undergoing significant deformation prior to the release of FB strand at  $39.0 \pm 0.5$  pN followed by a force drop due to rupture. The six strand nanocage was therefore named DMC<sub>39pN</sub> to indicate its force threshold.

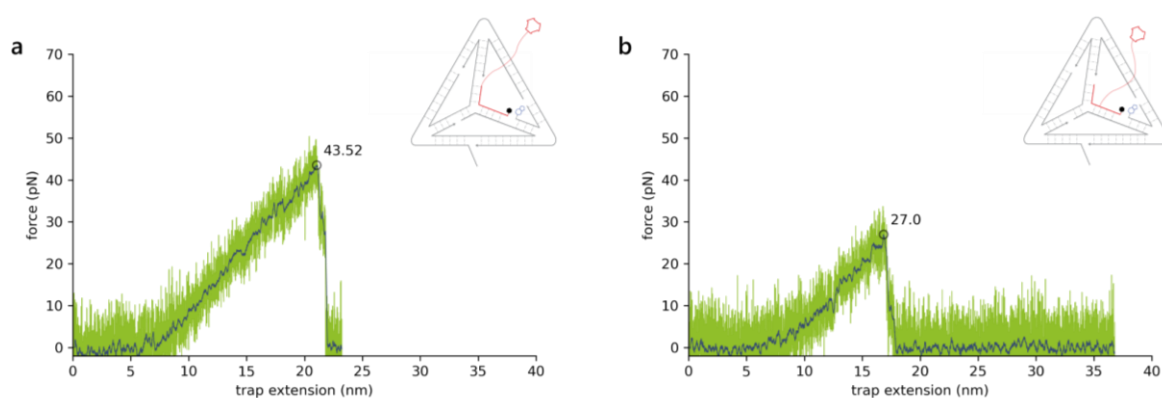


**Figure 2.5** (a, b) The five strand DMCs were modelled using oxDNA. The ligand attachment point on DMC was pulled at a rate of 14,100 nm/s and their force extension curves were plotted along with their exponential moving averages of 40 data points.

Subsequently the other two DMCs with shorter FB strands were also modeled and they exhibited a rupture force of  $27.0 \pm 0.6$  pN, and  $43.5 \pm 0.5$  pN (Supplementary Video 2,3).

These DMCs were also named DMC<sub>27pN</sub> and DMC<sub>44pN</sub> as per the previous nomenclature. The number of hydrogen bonds ruptured in all three DMCs over the course of the simulation was also quantified. The loss of base pairs in all three DMCs corresponded to the length of the FB strand (Figure S2). Further, the dependence of loading rate on the rupture force threshold was also determined. It was found that the force threshold of the DMCs decrease at as the force loading rate is reduced (Figure S3)

Other ligand attachment points around the DMC<sub>27pN</sub> were further evaluated to test for lower FB rupture thresholds (Figure S4). Since thymine base was the only internal modification that was commercially available, the T bases were picked for tuning the forces for rupture. Further the physical constrains of the cage requires the ligands be available for receptor binding by being displayed outside the nanocage. Hence two more chemically identical DMC designs were evaluated with a faster loading rate to accelerate the prediction. Neither of the DMCs had a lower force rupture compared to the DMC<sub>27pN</sub> and were not used for further valuation

### 2.3.3 DESIGN FORCE NON-RESPONSIVE DMC

DNA nanocages are prone to non-specific rupture when used in an *in vivo* context and delivery studies involving DMCs must be controlled for such instances. Hence, we engineered a structure that has a high rupture force and is mechanically non-responsive under cellular forces. To engineer a non-responsive DMC the cRGD was placed internally on the oligonucleotide with the surface anchor (Figure 2.6). This would produce a DMC with a single contiguous strand that bridges the cell receptor to the substrate or surface.

Then a library of these force non-responsive DMCs was created by shifting the internal RGD modification to different points (sites 1 – 5 in Figure 2.6) and tested them *in silico* by applying forces using oxDNA. To evaluate DMCs for non-responsiveness in a cellular context, the total number of hydrogen bonded base pairs in the DMC were extracted from the simulations. Base pairs indicate the dehybridization of the DMC as well as the structural integrity. The anchor

point was maintained constant at the initial position but the cRGD was varied along the T bases with major groove facing outside.

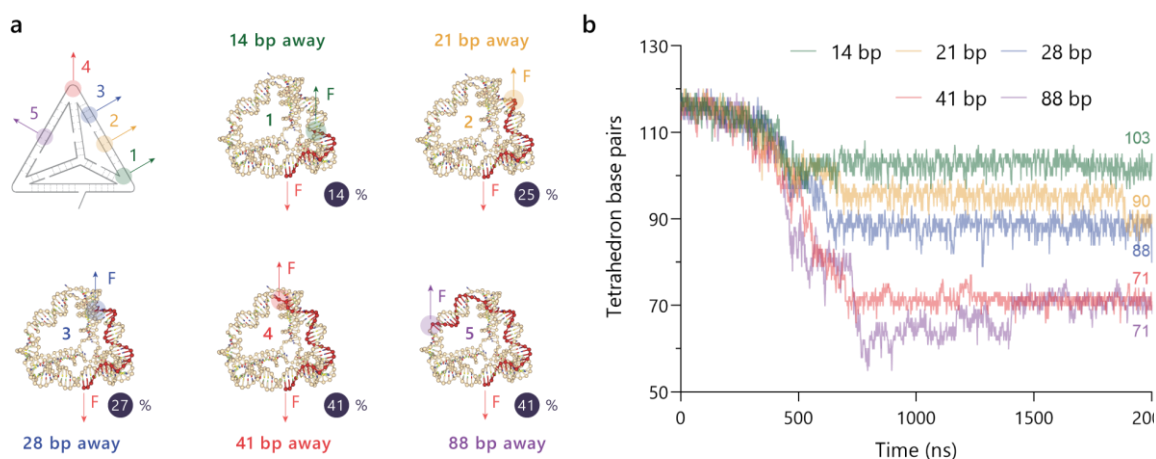


**Figure 2.6** DMCs (with force pulling positions 1-5) were subjected to force ramps with peak force as high as 500 pN in oxDNA and the number of base pairs ruptured due to the force were recorded as a function of time. These specific bases were chosen since only T bases can be modified with alkyne handles commercially and among the T bases only those that had the modifications displayed on the outside were selected. (a) Different points along the anchor strand on which the force was applied while the anchoring strand was immobilized. The values in circles represent the percentage of total base pairs ruptured at the end of a simulation. (b) Change in base pairs due to increasing forces as a function of time in nanoseconds. The nucleotides on the anchoring strands (1-5) were pulled along the z-axis at a loading rate of  $2.81 \times 10^5$  nm/s.

As anticipated, a greater fraction of base-pairs was denatured due to DNA overstretching with increasing separation between the ligand and surface anchoring groups (Figure 2.6). For example, pulling on the DMC on position 5 led to 41% of base-pair to denature, which when compared to position 1 with the RGD ligand 14 bp from the anchor terminus, which showed only 14% of base pairs denatured (Figure 2.6, Supplementary Video 4). To quantify the fluorescence response of the DMCs the spatial separation between the fluorophore-quencher was also obtained from the simulations (Figure S5). The force application on position 1 did not denature the strands sufficiently to separate the fluorophore-quencher beyond the FRET

radius ( $\sim 10$  nm) whereas in the case of position 5 they were well-separated and would produce a fluorescence response (Figure 2.7).

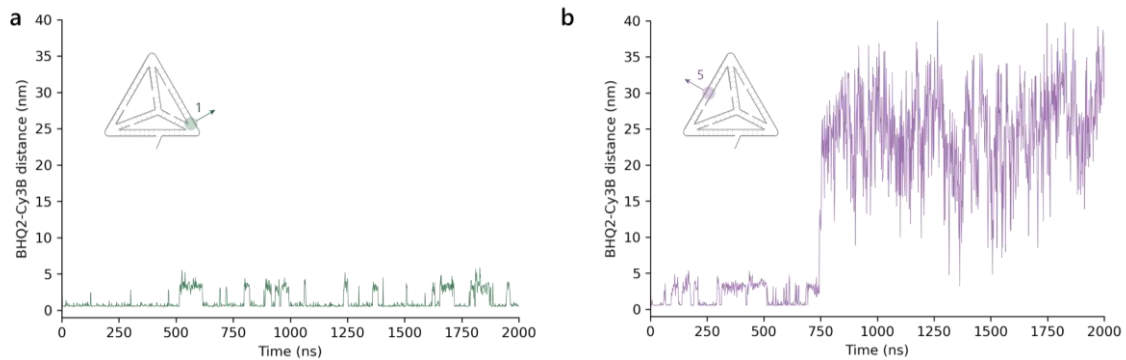


**Figure 2.7** (a, b) The separation distance between the fluorophore (Cy3B) and quencher (BHQ2) attachment points on the DMCs as a function of time was measured to check for Cy3B dequenching. In the case of DMC-1 (DMC<sub>rigid</sub>) the fluorophore-quencher pairs are maintained within quenching radius. On the contrary, DMC-5 had well separated fluorophore-quencher pairs by the end of simulation indicating structural collapse.

Hence, we used the DMC with force application point 1, as our force non-responsive DMC in subsequent experiments. This DMC was labelled DMC<sub>rigid</sub> to denote the non-responsive structure with maximal structural integrity under cell receptor forces. Unlike other DMCs which release the FB strand upon mechanical pulling, the DMC<sub>rigid</sub> retains the adhesion ligand and does not interrupt mechanotransduction in a cellular context.

#### 2.3.4 RUPTURE DYNAMICS WITH VARYING FORCE ORIENTATIONS

Cellular receptors are known to be anisotropic force sensors. In fact, it has been reported that platelet and fibroblast integrin forces are oriented at  $\sim 30^\circ$ - $50^\circ$  angles to the substrate plane.<sup>28</sup> Therefore application of forces along the z-axis on DMCs does not accurately capture the biological context. Hence, the effect of force direction on the DMC<sub>39pN</sub> was explored to assess changes in rupture dynamics and force tolerances.

DMC<sub>39pN</sub> was subjected to forces along six different directions with one physically impossible orientation due to receptor-DMC steric interactions. The rupture dynamics of the DMC was monitored by observing the FB and anchor strand rupture. Specifically, the average distances of the strands to their complimentary strands in each edge were extracted. As the force increases and breaks the hydrogen bonds, the average FB and anchor strand distance increases from a given edge DMC. The DMC force-extension curves as well as the fluorophore-quencher pair separations for all six force vectors were also obtained to observe the rupture force change with force orientation.

The rupture force for the FB strand varied between the 39-45 pN range (Figure 2.8) excluding the physically impossible force orientation. The rupture force fluctuations could be explained through the inherent stochasticity present in coarse grain simulations. In the excluded force orientation, the size of integrin receptor is prohibitively larger than the DMC to allow force exertion along (0, -1, -1). It would be impossible in that case to exert forces along the axis of the ligand modified edge due to the steric hindrance of integrin-DMC complexes.

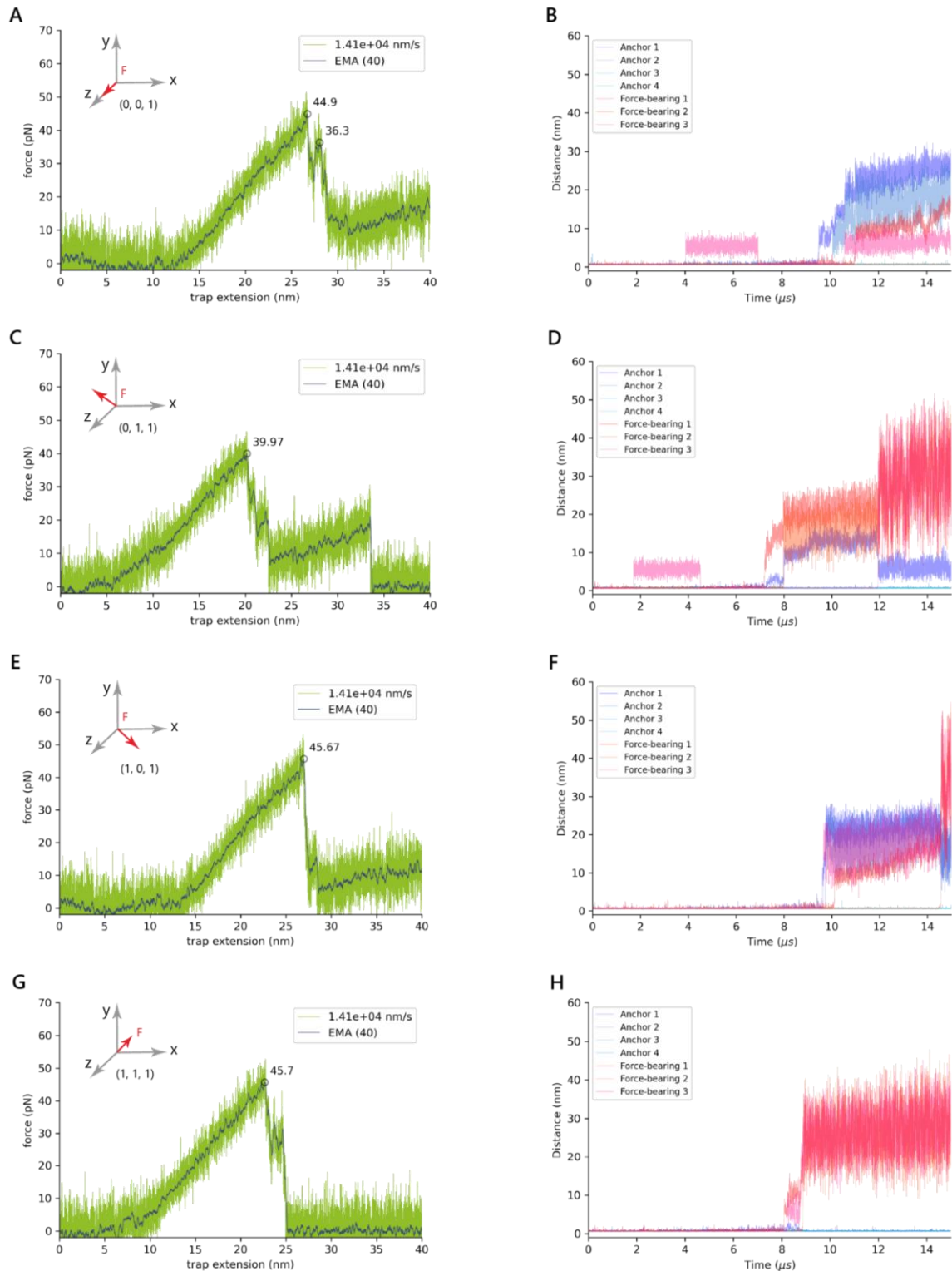


**Figure 2.8** The influence of force orientation on the threshold and rupture dynamics of  $DMC_{39pN}$  was tested with forces vectors along different directions. (a, c, e, g) Force extension curves of  $DMC_{39pN}$  shows the peak force of rupture for a specific force orientation in  $oxDNA$  simulation. (b, d, f, h). Distance of separation of strands from its corresponding complement in the  $DMC$  as the force ramps up.

Modeling further showed that force application on the FB strand along various directions, ruptured the DMC with a loss of 30-51% of base pairs. The FB strand alone can result in an irreversible 30% base pair loss when threaded out of the nanostructure. The additional loss of base pairs (up to 21%) can be attributed to partial dehybridization of anchor strand as it can be mechanically labile under certain force orientations compared to FB strand. But the anchor strand is 1.7 times longer with higher stability allowing it to remain partially hybridized to the DMC even if the FB strand is fully dissociated. Since only a fraction of the anchor strand ruptures, the loss of base pairs can be reversed provided the simulations were run for longer durations which can be computationally expensive. In experimental timescales, an intramolecular hybridization is more probable and hence the structure can be assumed to refold after FB strand rupture.

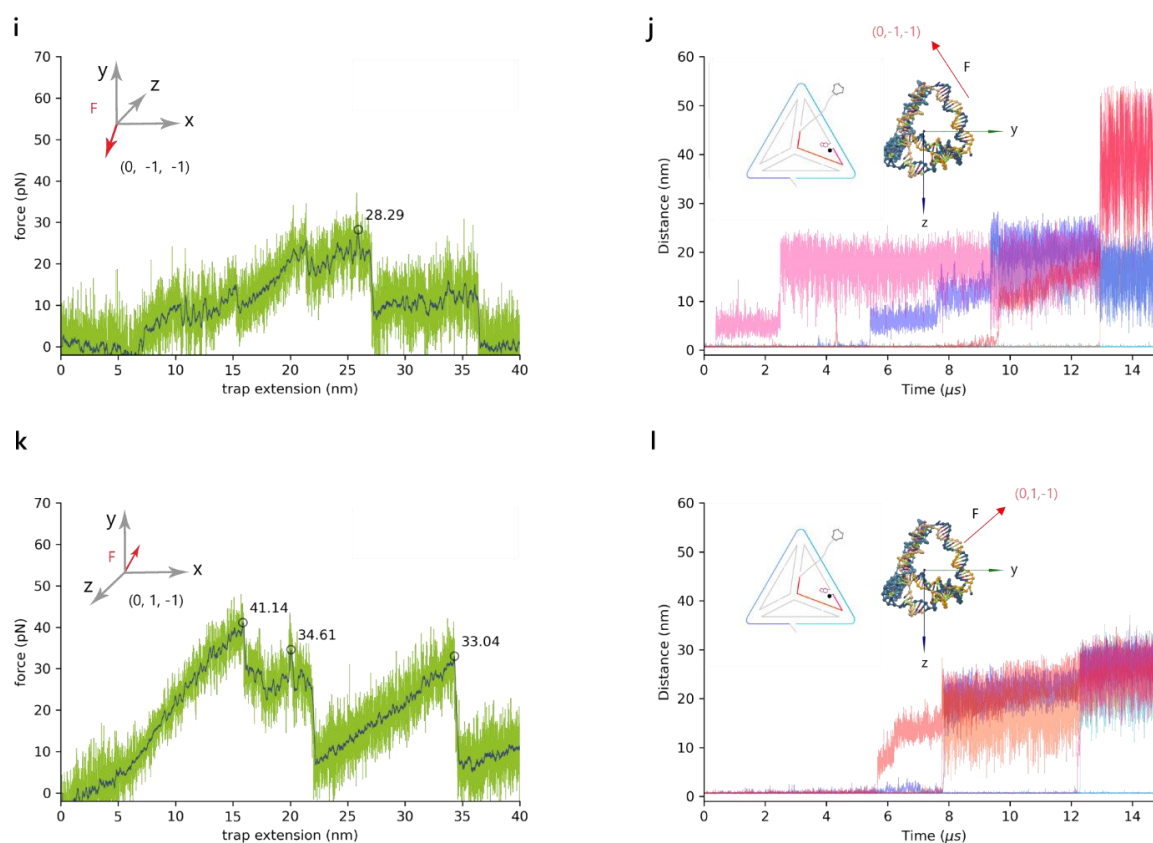


**Figure 2.9** (a, c) Force extension curves of  $DMC_{39pN}$  shows the peak force of rupture for a specific force orientation in  $oxDNA$  simulation. (b, d). Distance of separation of strands from its corresponding complement in the DMC as the force ramps up.

Finally, the quencher-fluorophore distances were examined in the simulation for  $DMC_{39pN}$  with forces in the direction of (a) z axis (b) y, z axis (c) x, z axis (d) x, y, z axis (e) -y, -z axis (f) y, -z axis. The quencher-fluorophore separation on the DMC in all cases was separated by at least 10 nm, which would generate a positive fluorescence signal (Figure 2.10). Taken together, oxDNA modeling predicts that DMCs rupture regardless of vector orientation, as suggested by  $DMC_{39pN}$  study which shows that it ruptures upon experiencing forces  $>39$  pN. This makes the DMC designs suitable for force-mediated cargo delivery.

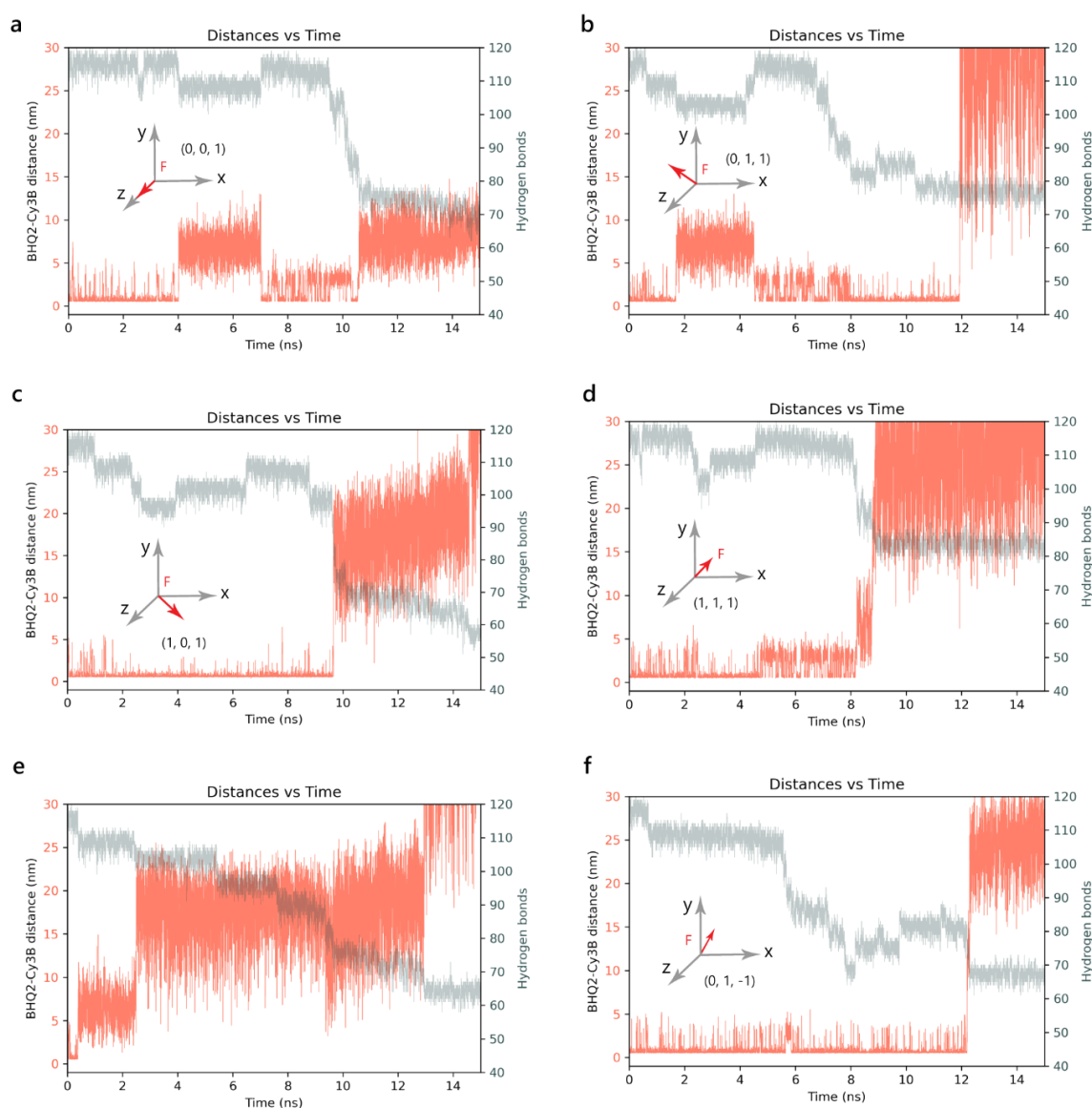


**Figure 2.10** (a-f) The number of base pairs in the DMC were also plotted in grey and the corresponding distances between the fluorophore and quencher pair were plotted in red.



### 2.3.5 DMC CARGO LEAKAGE UNDER FORCE

While DMCs can rupture irrespective of force orientation, cargo leakage from a force-stretched DMC remains yet another problem hindering force sensitive drug release. To simplify the problem of cargo leakage, the four pores in the DMC were approximated as triangles. The shape of the encapsulated cargo can also be simplified as a sphere. At least one of the pores must be dilated enough to accommodate a circle wider than the largest cross-section of the encapsulated sphere. For a given triangle, the largest circle it can encompass can be calculated using fundamental geometrical principles and it is known as the incircle of a triangle. If all the four incircle radii never exceeds the radius of the encapsulated sphere, it can never escape through the pores of the DMC.

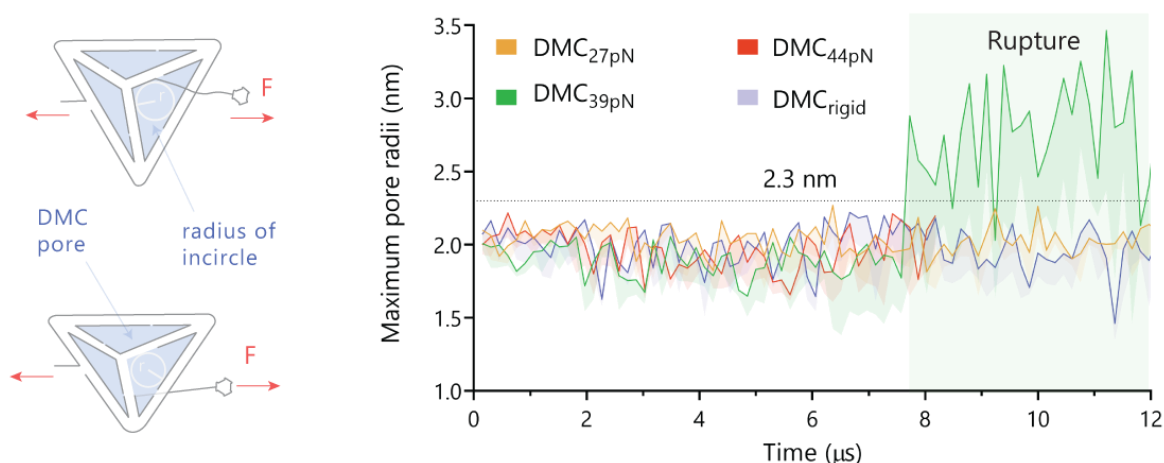


**Figure 2.11** (Left) Illustration of the stretching of the DMCs under force and the triangular approximation of the tetrahedral face of DMC. (Right) Plot of pore radii of DMC<sub>27pN</sub>, DMC<sub>39pN</sub>, DMC<sub>44pN</sub>, DMC<sub>rigid</sub> when subjected to a force ramp of  $1.4 \times 10^4$  nm/s. The solid lines indicate the maximum of the pore radii and the region between the maximum and mean radii are shaded.

To establish that cargo leakage does not occur under force, the average size of all four pores approximated as an incircle on the triangular faces of the DMCs were calculated. They were plotted as the average and range of DMC pore sizes under force (Figure 2.11). The pore radii for DMC<sub>27pN</sub>, DMC<sub>39pN</sub>, DMC<sub>44pN</sub>, and DMC<sub>rigid</sub> averaged around 2 nm and did not exceed 2.3 nm for the four structures tested if the force remained below the rupture force. This indicates that cargo  $>2.3$  nm would not leak as long as the DMCs do not rupture. Modeling also predicts that only the DMC<sub>39pN</sub> undergoes significant structural deformation upon unthreading of the

FB strand. Since the FB strand is longer for the DMC<sub>39pN</sub> structure, denaturation can lead to loss of TD edge integrity which can then release the encapsulated cargo.

## 2.4 Conclusions

In summary, DMCs were designed using fundamental principles and validated using coarse grain simulations to produce force-responsive nanostructures. To the best of our knowledge this represents the first characterization of a DNA origami as a force sensing element. While there have been reports of DNA hairpin force sensors on origami structures, none of them utilize a complex 3D structure like the tetrahedron for force sensing. DMCs were initially designed using from scratch using the stability and double helix geometry of dsDNA to produce nanostructures that could respond to cellular forces. These designs were further evaluated using oxDNA coarse grain simulations to predict the rupture force and dynamics. Results from the DMC modeling indicate that the force of rupture can be fine-tuned like a conventional TGTs by controlling the length of the force bearing strand and the ligand attachment point. The length of the FB strand also determines the extent of DMC rupture which is critical in cargo release. If all the edges of the DMC are intact after rupture, then caged cargo would not be released. Thus, DMCs can be engineered to respond to a range of mechanical forces and can be fashioned into smart nanocarriers that can release the encapsulated cargo at defined force thresholds or withhold it. Moreover, the DMCs can be rendered to be non-responsive by placing the ligand adjacent to the anchoring site. Combining the ligand and the anchor on the same oligonucleotide transmits the force to the other end of the DMC without rest of the structure bearing the load. Therefore, ensuring minimal separation between the two sites can significantly reduce the disruption caused due to DNA overstretching. The rapid screening of a DMC library to produce a non-responsive structure further exemplifies the ease at which structures can be designed to invoke a specific response. The engineered DMC<sub>rigid</sub> can be useful in cases where the DMC must remain intact and uninterrupted mechanotransduction is desired. DMC<sub>39pN</sub> was also found to rupture in the 39-45 pN force range for all force vector orientations. This demonstrates that the DMCs have a robust response regardless of force direction. Hence, the 3D tetrahedron nanostructure can be

customized to rupture at a given force for the reliable release of molecular cargo to cells with a certain mechanical phenotype.

Lastly, DMCs can be easily configured for a predefined response using computational modeling and then quickly assembled by purchasing commercially available DNA strands with required linker chemistry. DMCs thus represent a force-tunable, easily accessible, cargo agnostic drug delivery vehicle for targeting single receptor biophysics as opposed to conventional biochemical signals.

## 2.5 Methods

The simulations were modelled using oxDNA2 model (version 2.4 published in June 2019). We ran the MD simulations on CPUs and GPUs. The following parameters were used extensively in the simulations run on CPUs.

```
backend = CPU
sim_type = MD
T = 37C
steps = 1e9
print_conf_interval = 1e7
print_energy_every = 1e5
max_io = 10
box_type = orthogonal

no_stdout_energy = false
time_scale = linear
restart_step_counter = 1
refresh_vel = 1
interaction_type = DNA2
use_average_seq = 1

fix_diffusion = 0
back_in_box = 0
```

```
verlet_skin = 0.05
salt_concentration = 0.156
thermostat = john
newtonian_steps = 103
diff_coeff = 2.5
dt = 0.005
```

The following parameters were used extensively in the simulations run on GPUs.

```
backend = CUDA
backend_precision = mixed
CUDA_list = verlet
CUDA_sort_every = 0
max_density_multiplier = 2000000
use_edge = 1
edge_n_forces = 1
seed = 19332
debug = 1
box_type = orthogonal

sim_type = MD
T = 37C
steps = 1e8
print_conf_interval = 1e6
print_energy_every = 1e5
max_io = 10

no_stdout_energy = false
time_scale = linear
restart_step_counter = 1
refresh_vel = 1
interaction_type = DNA2
use_average_seq = 1
fix_diffusion = 0
back_in_box = 0
```

```

verlet_skin = 0.05
salt_concentration = 0.156
thermostat = john
newtonian_steps = 103
diff_coeff = 2.5l
dt = 0.005

```

The following force files were used in simulations

```

{
type = trap
particle = 251# Tetrazine anchor site
pos0 = 132.198, -101.474, 10.776 #x, y, z coordinates
stiff = 0.2
rate = 0.0
dir = 0, 0, 1
}

{
type = trap
particle = 162 #cRGD Ligand site
pos0 = 130.82182105, -94.350050242, 6.5388553480
stiff = 0.2 #the force is stiff * dx
rate = 1e-6 #length simulation units/time steps
dir = 0, 1, -1
}

```

### 7.1 Force-extension curves

The DNA sequences of the DMCs were imported into oxDNA format. The DMCs were then minimized and relaxed using the input parameters from published literature<sup>5</sup> and examples available at [dna.physics.ox.ac.uk](http://dna.physics.ox.ac.uk) website. The DMC rupture was modelled by adding harmonic traps (which act like springs) to the cRGD and the methyl tetrazine attachment points on the DMCs. Each trap was assigned a stiffness constant of 11.42 pN/nm, and the trap attached to

the cRGD was moved at a specified loading rate with respect to the other fixed trap. The effective stiffness constant of the two traps in series can be calculated using:

$$\frac{1}{k_{\text{eff}}} = \frac{1}{k_1} + \frac{1}{k_2}$$

where  $k_1$  and  $k_2$  are the stiffness constants of the two traps and  $k_{\text{eff}}$  is the effective stiffness constant. The  $k_{\text{eff}}$  of the system is calculated to be 5.71 pN/nm. The traps are moved at a rate of  $5 \times 10^{-8}$  (length per unit of time in oxDNA units). This rate can be converted into SI units as shown here:

$$\text{Loading rate} = \frac{5 \times 10^{-8} \times 0.8518 \text{ nm}}{3.03 \times 10^{-12} \text{ s}} = 1.4 \times 10^4 \text{ nm/s}$$

The net force exerted at a given point in time was calculated by multiplying the total displacement of both the harmonic traps from respective nucleotides with  $k_{\text{eff}}$ . The obtained force was then projected along the axis in which the traps are moved to get the force due to harmonic traps. This force was then plotted along the trap extensions at that given time along with an exponential moving average (EMA) of the force. Other parameters such as total number of base pairs, total energy and specific particle distances were also extracted for analysis. The output was analysed using python with the NumPy, SciPy, Pandas and Matplotlib packages.

## 7.2 DMC pore size

The four faces of a DMC were assumed to be triangles with the hinge nucleotides at the vertices. The macromolecular cargo inside the DMC was assumed to be spherical. The radius ( $r$ ) of the largest circle that can fit inside a triangle is given by the incircle of triangle formula:

$$r = 2 \times \frac{\text{Area of triangle}}{\text{Perimeter of triangle}}$$

DMCs are considered leaky when the incircle radius is larger than the radius of the cargo. The positions of the hinge nucleotides were extracted from the force-extension simulation trajectories of the DMCs. The hinge nucleotides positions were used to calculate the area and perimeter of each face of the tetrahedron which was then converted into incircle radii. The

incircle radii from all four faces were then plotted as the maximum with the shaded region depicting the range between maximum and mean.

### 7.3 DMC rupture dynamics

The cRGD attachment point on the DMCs were subjected to forces along different directions. The number of hydrogen bonded base pairs in the DMC as well as fluorophore-quencher distances were obtained from the simulation. Various particle positions on the force-bearing strand and the anchoring strand were also extracted. The separation distance of these strands from their complementary edges on the DMC were then estimated. It was plotted as a function of time to depict DMC rupture dynamics.

## Appendix

**Figure S1** Simulation of initial DMC with varying loading rates. The cRGD attachment point on DMC was pulled at rates of (a)  $2.8 \times 10^8$  nm/s, (b)  $2.8 \times 10^7$  nm/s, (c)  $2.8 \times 10^6$  nm/s, while the anchor point was fixed. The base pairs denote the amount of the structure dehybridized as the force bearing strand was pulled.

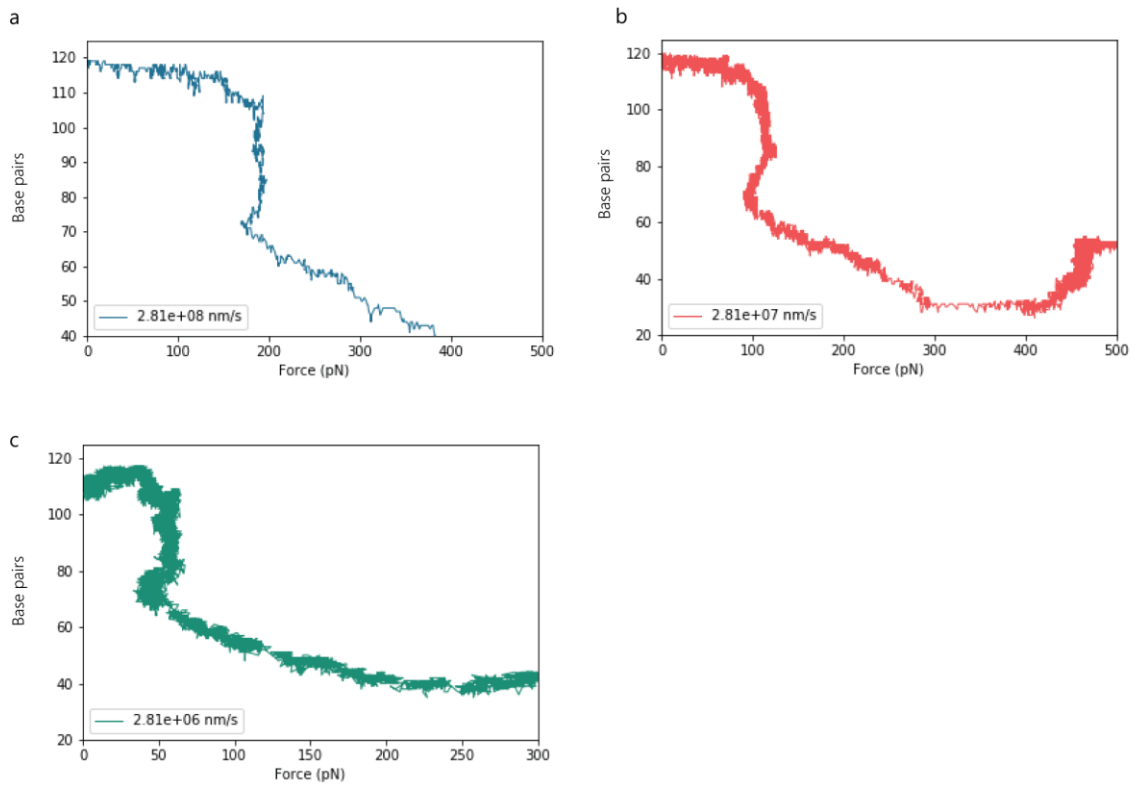




**Figure S2** The number of hydrogen bonded base pairs in the DMC as a function of time. The force on the DMC was increased as the time progressed causing the force bearing strand to rupture from the DMC breaking an equivalent number of base pairs corresponding to the length of FB strand.

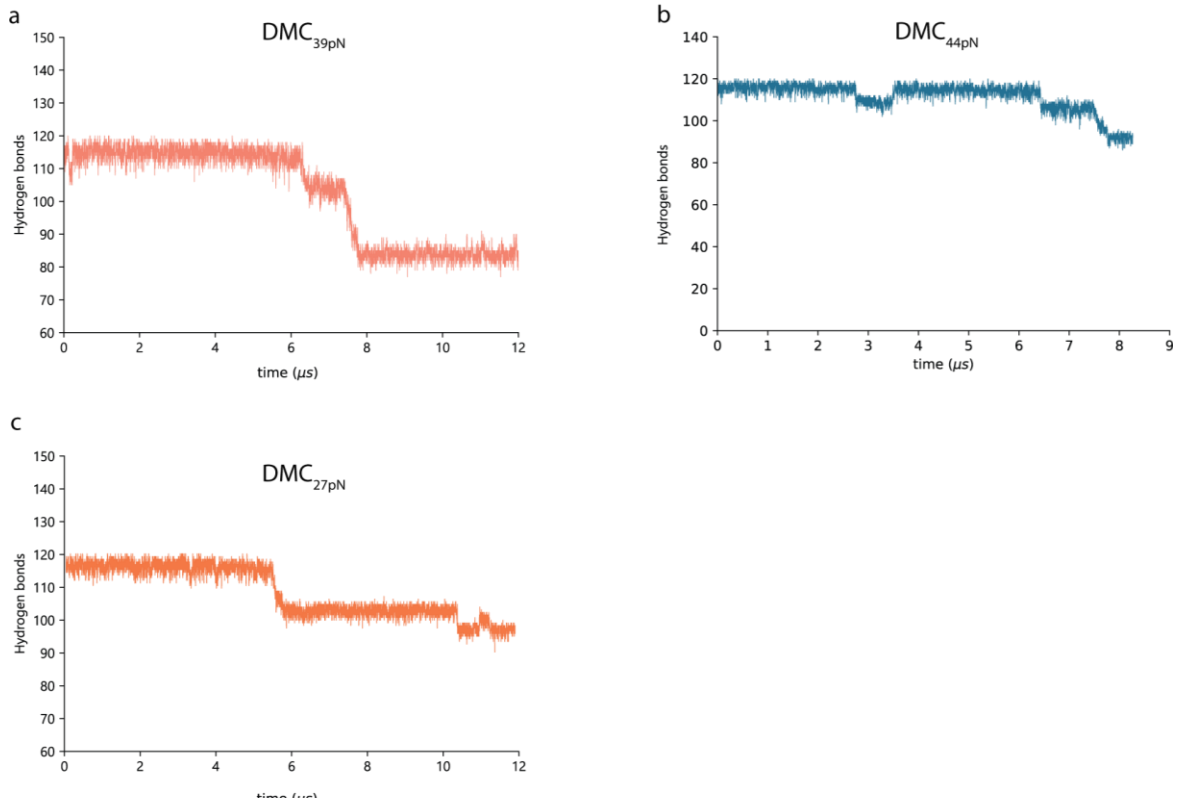


**Figure S3** The rupture force on the  $DMC_{27pN}$  was estimated with varying loading rates. As the loading rates decreased the force required to rupture also decreases. This is due to the thermal processes aiding in denaturing the strands at a slower loading rate when they are held under a force whereas the forces required to rupture it rapidly can be significantly higher as they are far from equilibrium.

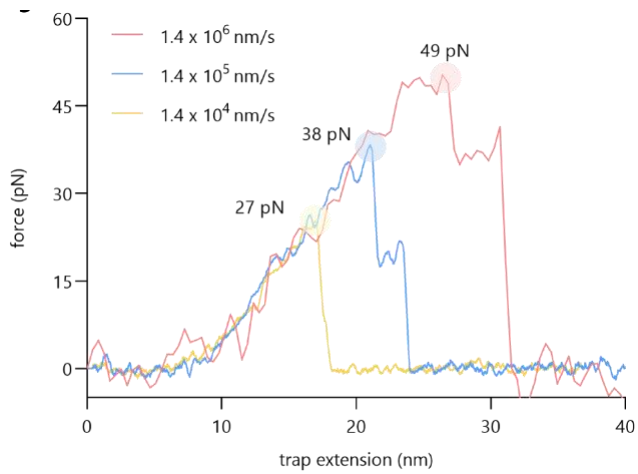


**Figure S4** The rupture force on the five strand DMC was further tuned by moving the ligand attachment point to various T bases on the force bearing strand (a) n-5 (b) n (c) n+2, where n refers to the point of ligand attachment in DMC<sub>27pN</sub>. The DMC design (b) was used in further experiments as its had comparatively lower force thresholds and can be easily ruptured.

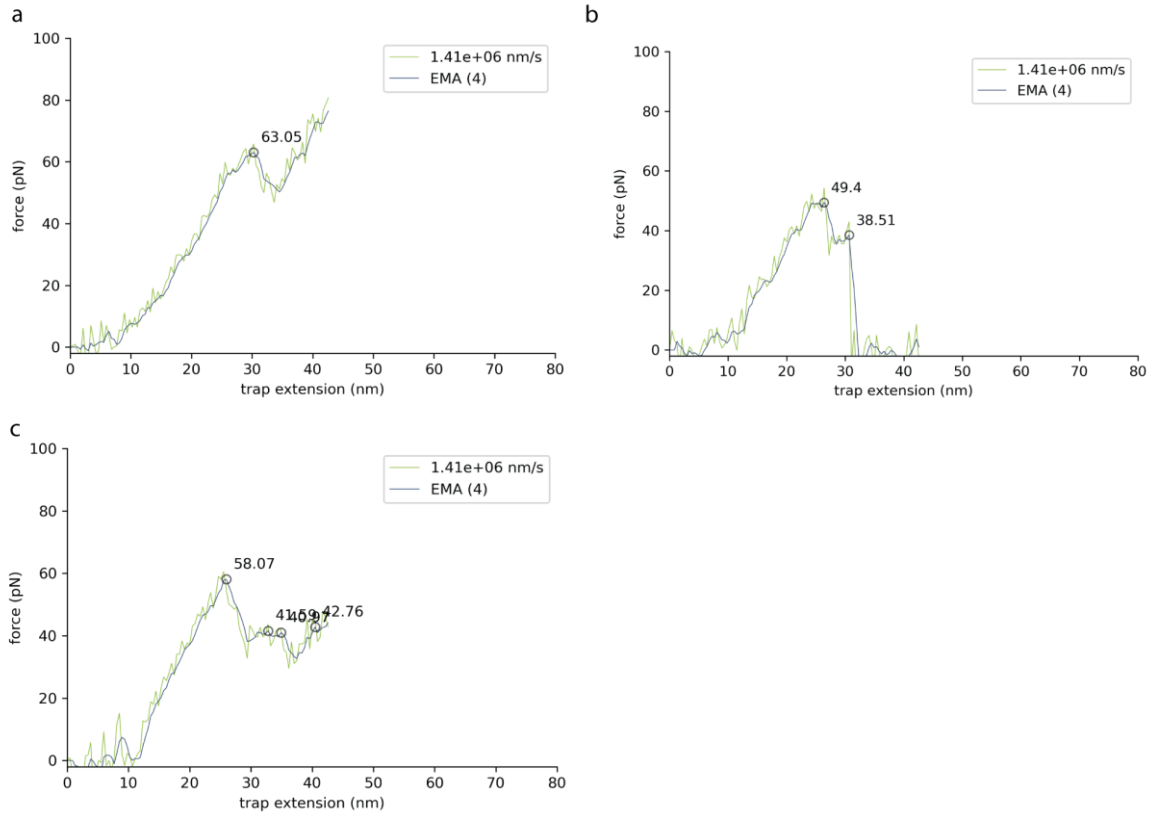


**Figure S5** A library of DMCs (1-5) were screened for mechanical non-responsiveness. The DMCs were held under increasing forces and DMC deformation were observed. The fluorophore-quencher distances (a-5, b-4, c-3, d-2, e-1) were noted over a period of time when the pulling forces ramped to values as high as 500 pN. Notably, only DMC 5 had a separation of the fluorophore-quencher complex which would lead to an increase in fluorescence.

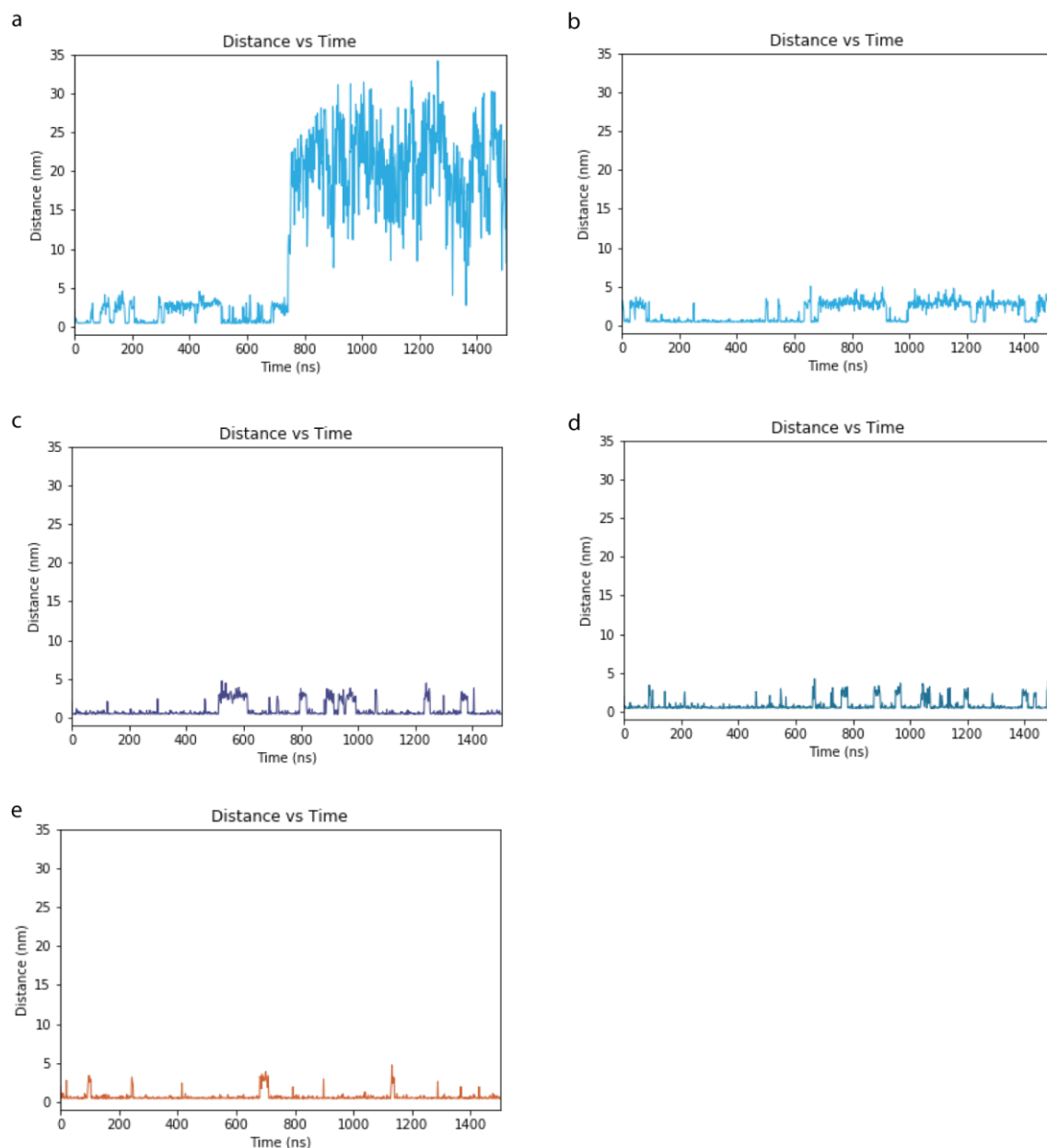


**Table 2.1** Length of DNA tetrahedron strands and the corresponding melting points to their complements

<b>Strand</b>	<b>Length (bp)</b>	<b>Melting temp (°C)</b>
<b>S1a</b>	21	63
<b>S1b</b>	42	71
<b>S2</b>	63	78
<b>S3a</b>	37	71
<b>S3b</b>	26	71
<b>S4</b>	63	80

## References

1. Li, Z. *et al.* Cellular traction forces: a useful parameter in cancer research. *Nanoscale* **9**, 19039–19044 (2017).
2. Scholz, N. *et al.* Molecular sensing of mechano- and ligand-dependent adhesion GPCR dissociation. *Nature* **615**, 945–953 (2023).
3. Rakshit, S. & Sivasankar, S. Biomechanics of cell adhesion: how force regulates the lifetime of adhesive bonds at the single molecule level. *Phys. Chem. Chem. Phys.* **16**, 2211–2223 (2014).
4. Suresh, S. Biomechanics and biophysics of cancer cells. *Acta Materialia* **55**, 3989–4014 (2007).
5. Ham, T. R., Collins, K. L. & Hoffman, B. D. Molecular tension sensors: moving beyond force. *Current Opinion in Biomedical Engineering* **12**, 83–94 (2019).
6. Ma, R., Deal, B. R. & Salaita, K. Mechanotransduction at the Cell Surface and Methods to Study Receptor Forces. (2022) doi:10.1039/9781839165375-00044.
7. Wang, X. & Ha, T. Defining Single Molecular Forces Required to Activate Integrin and Notch Signaling. *Science* **340**, 991–994 (2013).
8. Zhang, Y., Ge, C., Zhu, C. & Salaita, K. DNA-based digital tension probes reveal integrin forces during early cell adhesion. *Nat Commun* **5**, 5167 (2014).
9. Romano, F., Chakraborty, D., Doye, J. P. K., Ouldridge, T. E. & Louis, A. A. Coarse-grained simulations of DNA overstretching. *J. Chem. Phys.* **138**, 085101 (2013).
10. Wang, F. *et al.* Gint4.T-Modified DNA Tetrahedrons Loaded with Doxorubicin Inhibits Glioma Cell Proliferation by Targeting PDGFR $\beta$ . *Nanoscale Research Letters* **15**, 150 (2020).
11. Dai, B., Hu, Y., Duan, J. & Yang, X.-D. Aptamer-guided DNA tetrahedron as a novel targeted drug delivery system for MUC1-expressing breast cancer cells in vitro. *Oncotarget* **7**, 38257–38269 (2016).

12. Crawford, R. *et al.* Non-covalent Single Transcription Factor Encapsulation Inside a DNA Cage. *Angewandte Chemie International Edition* **52**, 2284–2288 (2013).
13. Duangrat, R., Udomprasert, A. & Kangsamaksin, T. Tetrahedral DNA nanostructures as drug delivery and bioimaging platforms in cancer therapy. *Cancer Science* **111**, 3164–3173 (2020).
14. Du, Y. *et al.* Membrane-anchored DNA nanojunctions enable closer antigen-presenting cell–T-cell contact in elevated T-cell receptor triggering. *Nat. Nanotechnol.* 1–10 (2023)  
doi:10.1038/s41565-023-01333-2.
15. Zhang, Q. *et al.* DNA Origami as an In Vivo Drug Delivery Vehicle for Cancer Therapy. *ACS Nano* **8**, 6633–6643 (2014).
16. Dutta, P. K. *et al.* Programmable Multivalent DNA-Origami Tension Probes for Reporting Cellular Traction Forces. *Nano Letters* (2018) doi:10.1021/acs.nanolett.8b01374.
17. Su, H. *et al.* Massively Parallelized Molecular Force Manipulation with On-Demand Thermal and Optical Control. *J. Am. Chem. Soc.* **143**, 19466–19473 (2021).
18. de Gennes, P.-G. Maximum pull out force on DNA hybrids. *Comptes Rendus de l'Académie des Sciences - Series IV - Physics* **2**, 1505–1508 (2001).
19. Goodman, R. P. *et al.* Rapid Chiral Assembly of Rigid DNA Building Blocks for Molecular Nanofabrication. *Science* **310**, 1661–1665 (2005).
20. Snodin, B. E. K. *et al.* Introducing improved structural properties and salt dependence into a coarse-grained model of DNA. *J. Chem. Phys.* **142**, 234901 (2015).
21. Ouldrige, T. E., Louis, A. A. & Doye, J. P. K. Structural, mechanical, and thermodynamic properties of a coarse-grained DNA model. *The Journal of Chemical Physics* **134**, 085101 (2011).
22. Ouldrige, T. E. *et al.* Optimizing DNA Nanotechnology through Coarse-Grained Modeling: A Two-Footed DNA Walker. *ACS Nano* **7**, 2479–2490 (2013).
23. Šulc, P., Ouldrige, T. E., Romano, F., Doye, J. P. K. & Louis, A. A. Simulating a burnt-bridges DNA motor with a coarse-grained DNA model. *Nat Comput* **13**, 535–547 (2014).

24. Khara, D. C. *et al.* DNA bipedal motor walking dynamics: an experimental and theoretical study of the dependency on step size. *Nucleic Acids Research* **46**, 1553–1561 (2018).
25. Mosayebi, M., Louis, A. A., Doye, J. P. K. & Ouldrige, T. E. Force-Induced Rupture of a DNA Duplex: From Fundamentals to Force Sensors. *ACS Nano* **9**, 11993–12003 (2015).
26. Snodin, B. E. K., Schreck, J. S., Romano, F., Louis, A. A. & Doye, J. P. K. Coarse-grained modelling of the structural properties of DNA origami. *Nucleic Acids Research* **47**, 1585–1597 (2019).
27. Erben, C. M., Goodman, R. P. & Turberfield, A. J. Single-Molecule Protein Encapsulation in a Rigid DNA Cage. *Angewandte Chemie International Edition* **45**, 7414–7417 (2006).
28. Brockman, J. M. *et al.* Mapping the 3D orientation of piconewton integrin traction forces. *Nat Methods* **15**, 115–118 (2018).



## CHAPTER 3

# Functional validation of DMCs

This chapter is adapted from a manuscript in submission: DNA mechanocapsules for programmable piconewton responsive drug delivery. Arventh Velusamy, Radhika Sharma, Sk Aysha Rashid, Hiroaki Ogasawara and Khalid Salaita.

### 3.1 Abstract

Cellular force targeting marks a departure from conventional drug delivery based on biochemical detection. Here we engineer DNA tetrahedrons as mechanosensitive nanovehicles and demonstrate tunable force responses ideal for targeting cellular forces. These DNA mechanocapsules were found to have enhanced resistance to degradation and to provide sufficient ligand density on surfaces for adhesion. DMCs functionalized with adhesion ligands were shown to mechanically denature when 3T3 fibroblasts bind to the ligand and transmit force through the structure. Further the DMC signal observed under HeLa cells responses were validated to from overwhelmingly from mechanical rupture events rather than non-specific degradation. Importantly, the DMCs with a lower threshold were found to be capable of discriminating breast cancer cells from normal cells.

## 3.2 Introduction

An approach for reducing off-target effects and increasing drug efficacy involves creating inactive drugs that are activated upon encountering a unique stimulus in diseased tissue.<sup>1</sup> The most common strategy for creating smart drugs involves protecting the therapeutic until a chemical signal such as pH,<sup>2,3</sup> redox state,<sup>4</sup> small molecules,<sup>5</sup> enzymatic activity,<sup>6,7</sup> nucleic acids,<sup>8</sup> and proteins<sup>9</sup> triggers its release. Antibody-drug conjugates employ such a biochemical targeting strategy to treat cancers by binding cell surface receptors and concentrating a potent, nonspecific, cytotoxic drug at the target site.<sup>10</sup> Such responsive drugs are also growing with many examples of FDA-approved pro-drugs that are activated at the site of diseased tissues or cells.<sup>11</sup> Hence, developing new types of responsive drugs is of paramount importance and may catapult a new branch of responsive drugs.

The potential of DNA beyond its intended genetic functions has been realized over the last few decades and it has propelled DNA nanotechnology to predominance. Particularly, DNA origami has revolutionized the bottom-up creation of precise nanostructures that has spawned novel nanovehicles for drug delivery. DNA nanostructures have superior versatility and nanometer spatial programmability along with biocompatibility making them ideal drug carriers. A vast swathe of literature has been published exploring drug delivery using DNA origami (Table 3.1). In most cases DNA origami structures have been used to deliver intercalating drugs such as doxorubicin (Dox) which can be loaded at high efficiency<sup>12,13</sup>. For example, 2- [3-(1,3-dicarboxy propyl)-ureido] pentanedioic acid ligand was tethered to DNA origami for the delivery of Dox to cells expressing prostate-specific membrane antigen.<sup>14</sup> Importantly, these classes of nanovehicles release the drugs passively via degradation of DNA origami after endocytosis within the cell. Multiple other cargoes such as siRNA and proteins have also been used for delivery with origami structures. A DNA nanobot to trigger coagulation was engineered by shutting the origami using nucleolin aptamers that can release encapsulated thrombin.<sup>15</sup>

DNA-origami have also been engineered as force sensors with predictable response to cellular forces. In fact, our lab has produced the first example of DNA origami tension probes (DOTP)

that integrates mechanosensitive DNA hairpins into origami nanostructures.<sup>16</sup> These DOTPs are highly modular and consist of assembled 6-helix bundles that present RGD peptides on one terminus and surface anchoring groups on the other terminus. Using single molecule force-spectroscopy techniques and computational modeling, it was established that DOTP had force thresholds of 5-20 pN for various permutations of hairpin force probes on the origami. We also demonstrated multiplex extensible hairpins which could be precision tuned to map the real-time integrin forces from human platelets.

While DNA origami platforms have been used for manipulating cellular behavior,<sup>17</sup> drug delivery<sup>12</sup> and even force sensing by decorating them with hairpins and TGTs,<sup>16,18</sup> they have not been employed as a force sensor in its entirety. It would thus be highly desirable to engineer such molecular containers that break and release cargo under force. Such systems can be tuned to release drugs at mechanically altered sites and provide specificity to non-specific drugs in a manner akin to ADCs. This constitutes a powerful strategy to increase the efficacy of drugs and to specifically deliver therapeutics to diseased cells.

To achieve this a novel DNA based piconewton force sensing platform that can encase therapeutics need to be engineered. DNA tetrahedron is a small and modular origami that has been used for encapsulating various molecules,<sup>19,20</sup> specifically for drug delivery applications.<sup>21</sup> Herein we describe the synthesis of DNA mechanocapsules (DMC) based on the DNA tetrahedron that can respond to integrin receptor piconewton forces. The folding of the DMCs were characterized using gel electrophoresis and DLS. Using a fluorescence calibration curve and the surface intensities of DMCs, the corresponding surface densities at various concentrations were estimated. DMCs decorated with a quencher-fluorophore pair were also used to determine the quenching efficiency of the nanostructure. Then it was used to observe the cellular forces exerted by the 3T3 cells colocalize with focal adhesions mapped using expressed GFP-Paxillin. DMC were also found to specifically rupture due to forces from HeLa cells with minimal degradation for shorter timepoints. Finally, DMCs with lower threshold were determined to be capable of discriminating MCF-7, MCF-10 and MD-MBA-231 breast cancer cell lines based on their integrin forces. Hence, the development of force-

induced drug delivery platforms such as the DMC will offer new avenues in enhancing the selectivity of drugs based on the mechanical state of cells.

### 3.3 Results and discussions

#### 3.3.1 SYNTHESIS OF DMCs

The requisite chemical tags for sensing integrin-specific forces were installed on the DMC through efficient and readily available copper-click, methyltetrazine-transcyclooctene (Tz-TCO) click, maleimide-thiol conjugation and NHS-ester amine conjugation protocols. In turn, a rapid assembly of the DMC is feasible using commercial DNA synthesis augmented with custom one-pot reactions and straightforward purifications. To target biophysical responses of receptors such as integrins a ligand specific to the receptor needs to be incorporated to the force bearing strand of the DMC. Most integrin subtypes bind to peptides with RGD motifs found in fibronectin and the specificity of the peptides can be tuned for receptor-subtype selectivity. cRGDfV peptide (cyclized Arg-Gly-Asp-D-Phe-Lys) is known to preferably bind to subtypes such as  $\alpha_v\beta_3$  which is overexpressed in cancers.<sup>22</sup> Hence, it was chosen as the DMC ligand to be displayed to target cancer cells with high force phenotypes.

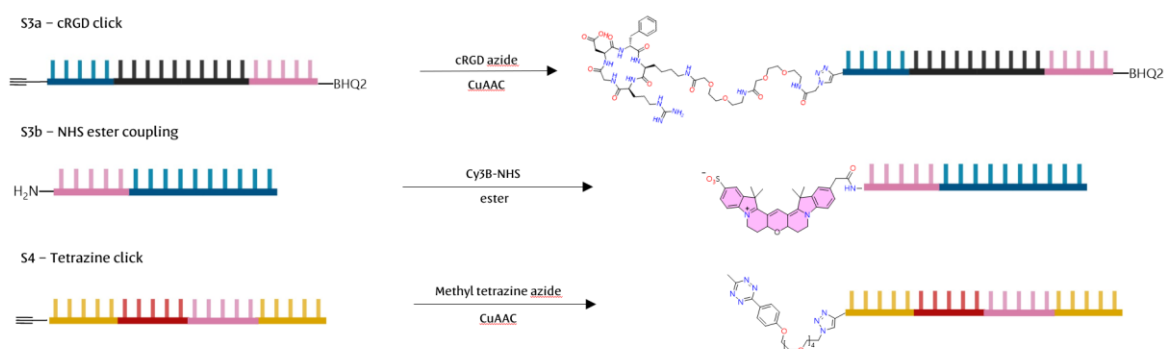


**Figure 3.1** Representative schematic of synthesis protocols employed on DMC strands. Conjugation to methyltetrazine (Tz), cRGD peptide was done using copper-catalyzed azide/alkyne cycloaddition reaction (CuAAC) and Cy3B installation was done using reactive NHS ester.

cRGD was introduced through copper-catalyzed azide-alkyne cycloaddition (CuAAC) reaction to the FB strand (S3a strand) with or without modifications such as BHQ2, Atto647N, and thiol handles (Figure 3.1). CuAAC chemistry is orthogonal to thiol-maleimide and NHS ester amine coupling which can be used to introduce fluorophores or drug conjugations. The 5' terminus of S3b strand was obtained with an amine modification suitable for fluorophore or drug conjugations. Fluorophores placed on this strand can be contact quenched since it is adjacent to the 3' terminus of FB strand where BHQ2 is located.

The challenge in engineering DMCs for force-triggered drug release pertains to generating a sufficiently high density of RGD-origami structures on the surface. DNA tension sensors are typically anchored using biotin-streptavidin binding. However, to withstand the large forces generated by integrin receptors, covalent chemistry would be required as the biotin-streptavidin complex dissociates upon experiencing  $\sim 20$  pN forces for  $\sim 20$  min.<sup>23,24</sup> Cell adhesion to a substrate also requires a minimum critical inter ligand spacing of  $< 60$  nm.<sup>25</sup> Hence, we used the Tz-TCO click reaction which is bio-orthogonal and has high second order rate constant ( $\sim 10^3$  M<sup>-1</sup>s<sup>-1</sup>), thus ideally suited for generating high surface densities. Accordingly, we covalently linked DMCs to surfaces using an outward-facing terminal methyltetrazine (Tz) group which could be installed to S4 strand through CuAAC or NHS ester chemistries. DMCs can then be folded into a tetrahedron using standard annealing protocols and then be “clicked” rapidly to TCO-coated glass surfaces.

### 3.3.2 SURFACE CHARACTERIZATION

To ensure the formation of DMCs, unmodified strands were annealed using the reported procedures and characterized using agarose gels. The presence of the DNA tetrahedron indicated by reduced mobility was observed when all the strands were annealed together at identical 1  $\mu$ M concentrations (Figure 3.2). Along with the DMC other higher order oligomeric structures were also observed at 1  $\mu$ M which was eliminated when annealed at a lower concentration of 50 nM. The folding of the unmodified DMC<sub>39pN</sub> with 6 strands nicks and additional nicks was compared to the original DNA tetrahedron with 4 strands reported by

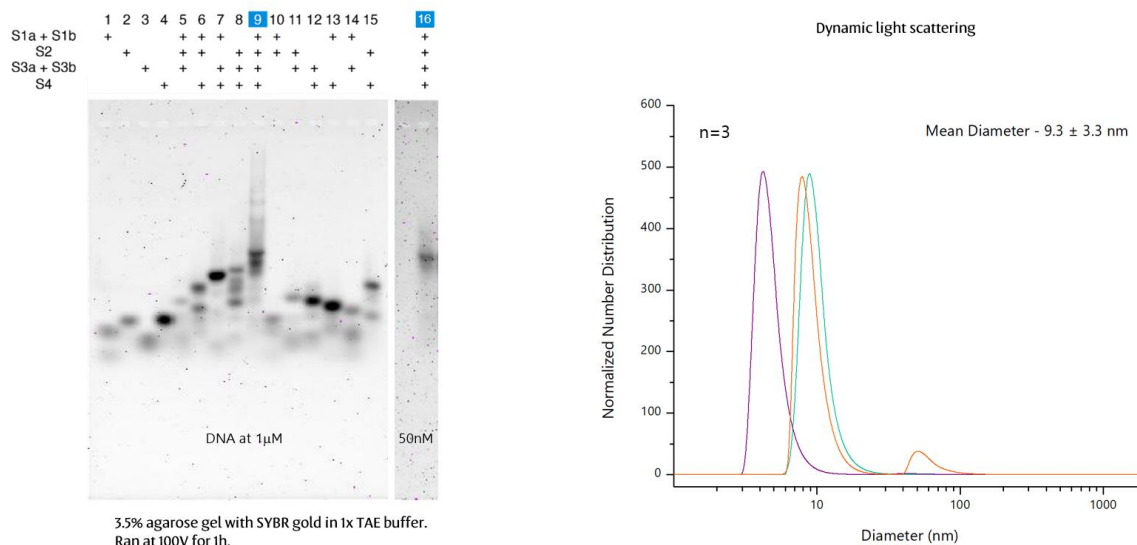


**Figure 3.2** DMC strands (without chemical modifications) of varying combinations at 1  $\mu$ M were subjected to the DMC annealing protocol and were run using 3.5% agarose gel at 100 V. Lane 9: shows DMC formation along with higher-order structures due to elevated concentration. DMC with various chemical modifications at 50 nM concentrations. DMCs fold with high yield (>95%) when annealed at lower concentrations. Dynamic light scattering of the DMC recorded at 25°C.

Goodman et al.<sup>26</sup> on agarose gel and were found to have identical mobility demonstrating proper folding of the DMCs (Figure S1). Furthermore, dynamic light scattering (DLS) analysis confirmed formation of DMC with  $9.3 \pm 1.9$  nm particle diameters (Figure 3.2) which is consistent with literature.<sup>19</sup>



**Figure 3.3** Quenching efficiency of 50 nM DMCs functionalized to surfaces using TCO-Tz click chemistry. Images show DMCs that are quenched on the left (black) and unquenched on the right (gray). 20  $\mu$ m in all images. The calibration bars accompanying the images indicate fluorescence values and display LUT. Scale bar = 20  $\mu$ m.

Having confirmed formation of DMCs, chemical modifications were introduced to enable surface tethering, and fluorescence reporting. The fluorescence intensity of quenched and

non-quenched DMCs (Cy3B and BHQ2-Cy3B) was used to determine the quenching efficiency of these structures to be  $87.2 \pm 6.9\%$ . This value indicates an 8-fold enhancement in fluorescence upon denaturing of the DMCs. (Figure 3.3)

Using a Tz group DMCs could be rapidly “clicked” to TCO functionalized glass surfaces within 1 hour. The surface density of the DMCs were also estimated by covalently linking them to surfaces and then using a fluorescence calibration curve to determine the DMC density. The Cy3B-DMCs clicked to a TCO slide could produce densities as high as  $2890 \pm 76$  DMC/ $\mu\text{m}^2$  at 50 nM at room temperature (Figure 3.4). This density when converted to average inter-DMC distance yields a spacing of  $\sim 18$  nm approaching maximum packing density since the dimensions of the DMC is around 10 nm. (Figure S2). Cell adhesion requires an inter-ligand spacing of  $< 60$  nm and DMC functionalized using Tz-TCO chemistry can achieve this density at concentrations as low as 3.12 nM.

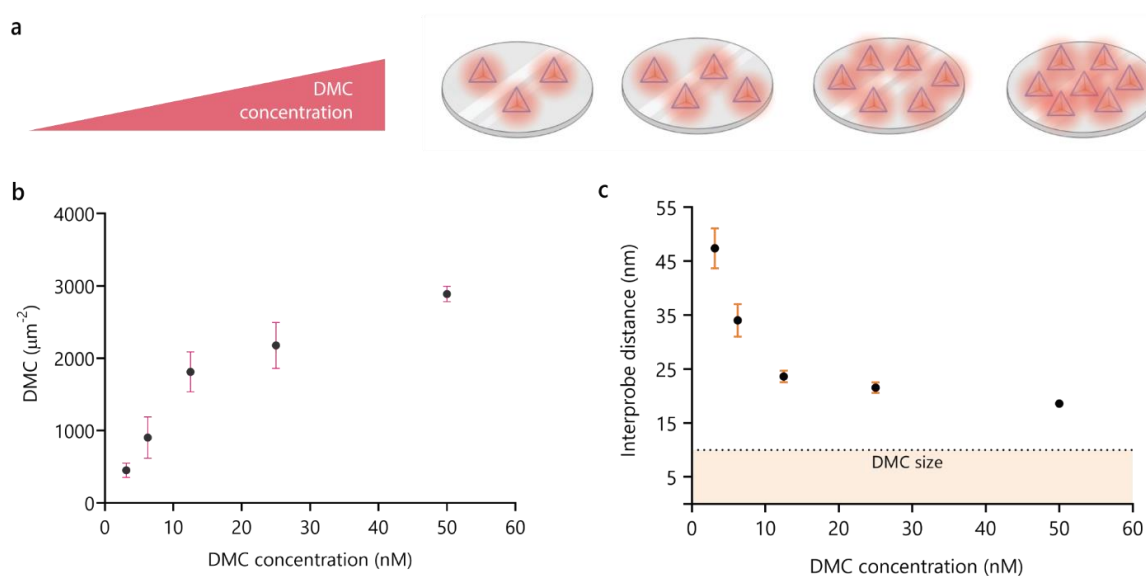


**Figure 3.4** DMCs with Cy3B of various concentrations were clicked to the surfaces for 1 hour and the intensity on the surface after washing the unbound DMCs were measured. (a, b) Schematic of increasing DMC concentration immobilized on the surface with increasing DMC solution concentration. The intensity of Cy3B labelled DMC on the surface was transformed to the number of DMCs/ $\mu\text{m}^2$  using Supported Lipid Bilayer (SLB) calibration curve. (c) The DMC density was converted to average distance between two DMCs on the surface. The 50 nM has a 3.72 standard error of mean. All error bars indicate SEM.

While the enhanced nuclease resistance of DNA tetrahedrons is well-documented in the solution phase, the stability of these nanostructures when immobilized has not been

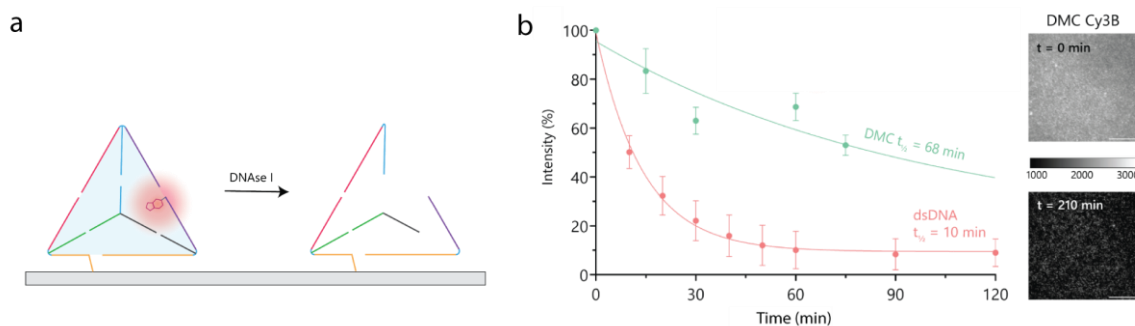


**Figure 3.5** (a) Schematic of DMC degradation by DNase. (b) Time course of DMC and dsDNA degradation using 10U DNase I in 10% FBS in DMEM. Error bars indicate SEM from three different surfaces. The half-life was obtained from a decay curve fit to the data. The calibration bars accompanying the images indicate fluorescence values and display LUT. Scale bar = 20  $\mu\text{m}$ .

characterized. To test if DMCs on the surface displayed enhanced nuclease resistance compared to dsDNA, we grafted surfaces with fluorescent DMCs and dsDNA and measured loss of signal following treatment with 10 U/mL DNase I in 10% FBS. It was found that DMCs had a  $t_{1/2} = 68$  min, which is  $\sim 7$  times more nuclease resistant as that of dsDNA with  $t_{1/2} = 10$  mins (Figure 3.5).

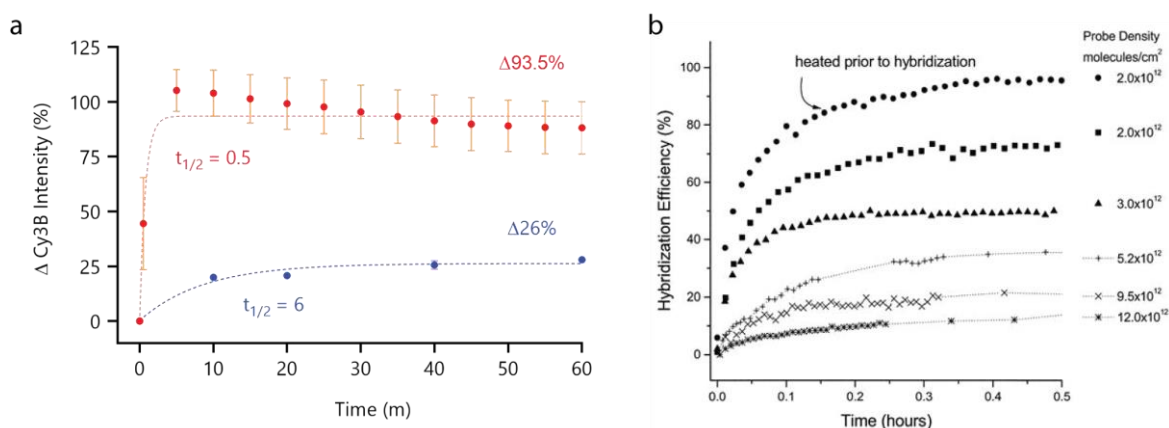


**Figure 3.6** Toehold mediated dequenching of qDMCs (BHQ2-Cy3B) grafted to the surface with a bulk concentration DMC = 10 nM (red) and 50 nM (blue). (b) Target hybridization kinetics as a function of probe density. Adopted from *Nucleic Acids Research*, 29, 24, 5163–5168 (2001) with permission from the publisher.



To validate that DMCs are functional on surfaces, we designed a toehold displacement reaction triggered by an invader strand leading to dissociation of the FB strand. The yield of the displacement reaction by using fluorophore-quencher tagged DMCs labeling the FB strand was quantified (Figure 3.6). Indeed, a rapid 94% increase in Cy3B fluorescence on the surface was observed within 10 min after adding 1  $\mu\text{M}$  invading strand. This shows that the DMCs are accessible and functional when clicked to TCO surfaces. When higher surface density of DMCs were tested by increasing the solution concentration from 10 nM to 50 nM, the fluorescence response was found to be slower and lower. This could be due to the poor efficiency of hybridization to surface functionalized DNA as observed in past literature<sup>27,28</sup>. Peterson et al. found that DNA density strongly dictates both the efficiency of duplex formation and the kinetics of target binding.<sup>28</sup> While the surface density of DMCs might not be similar to the reported dsDNA surface density due to the obvious size difference between a DMC (DNA tetrahedron) and a dsDNA, the hybridization principles are still applicable. The kinetics of toehold dequenching as well as the final efficiency drops with increasing density as observed in the initial slope and plateau of the time course experiments.

### 3.3.3 DMC RESPONSE TO CELLULAR FORCES

To monitor force-induced rupture DMCs that respond to cell generated forces were designed. As described before FB strand was functionalized with a 5' RGD at one terminus and a 3' BHQ2 (commercially purchased with the modification) on the other end. An adjacent strand (S3b strand) was tagged with Cy3B using an NHS ester to install the fluorophore on the 5' amine terminus. When the DMC is assembled the fluorophore and quencher forms a stable complex that does not emit fluorescence and hence the DMC is labelled as a quenched 39 pN DMC (qDMC<sub>39pN</sub>). When the FB strand is threaded out due to cellular force the BHQ2 will be removed from the DMC and the fluorophore will become dequenched.

A dense monolayer of qDMC<sub>39pN</sub> sufficient to support cell adhesion was generated and then NIH3T3 fibroblasts expressing GFP-Paxillin were seeded on these surfaces. Within 30 min of

seeding, dequenching was noted under cells with a ring pattern that resembled the size and perimeter of cells, indicating the rupture of qDMC<sub>39pN</sub> (Figure 3.7). Focal adhesions which include proteins such as paxillin, talin, and integrins are part of the cellular machinery that is responsible for traction force generation. Hence, cells NIH3T3 cell expressing GFP tagged Paxillin were used for these experiments and it paxillin was found to be colocalized with the dequenched DMC signal, validating the tight association between focal adhesion formation and force transmission (Figure 3.7).

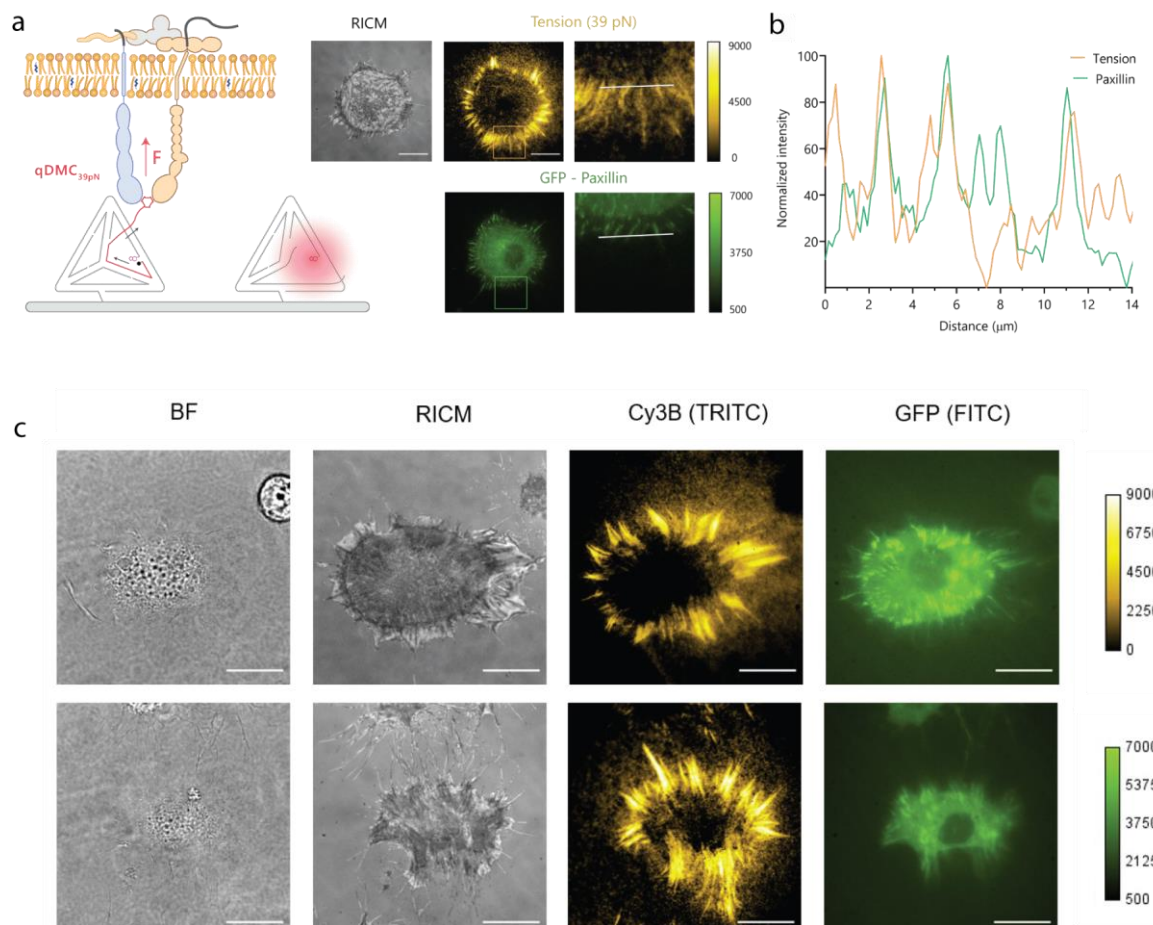


**Figure 3.7** (a) Schematic for force-mediated dequenching of qDMC<sub>39pN</sub> due to integrin forces. (b) microscopy images of NIH3T3 cells expressing GFP-Paxillin seeded on qDMC<sub>39pN</sub> surfaces in 0.1% FBS after 30 mins. RICM (reflection interference contrast microscopy) channel was used to observe spreading and image analysis. (c) Representative images for GFP-Paxillin NIH3T3 cells exerting tension on qDMC<sub>39pN</sub> surfaces. BF - bright field. The calibration bars accompanying the images indicate fluorescence values and display LUT. Scale bar = 20  $\mu\text{m}$ .

### 3.3.4 FORCE SELECTIVE DMC RUPTURE

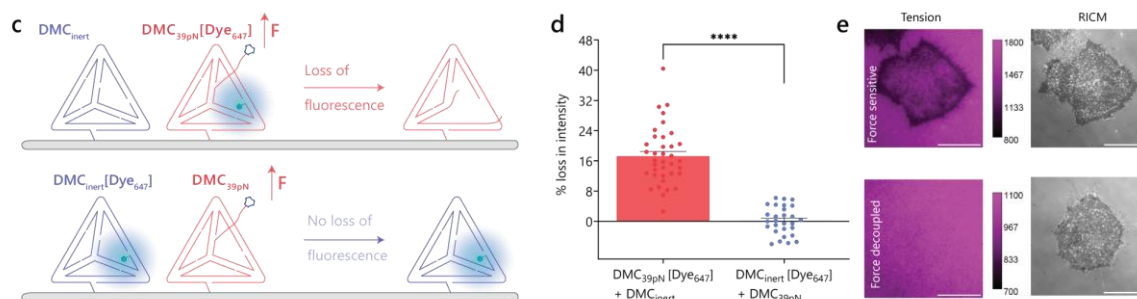


**Figure 3.8** c) Schematic of binary mixture of DMC<sub>39pN</sub> [Dye<sub>647</sub>] + DMC<sub>inert</sub> showing the mechanism of fluorescence loss due to integrin forces. d) Plot quantifying per cell loss of fluorescence normalized to background under HeLa cells in DMEM (0% FBS) after 1 h. Each data point was obtained from a single cell (n=3). \*\*\*\**P*<0.0001. e) Representative images of HeLa cells quantified in (d). Scale bar – 20 μm. All error bars indicate SEM from three replicates and each data point in plots is from a single cell. The calibration bars accompanying the images indicate fluorescence values and display LUT. Scale bar = 20 μm.

To further validate that the DMCs are ruptured exclusively due to mechanics, we prepared four types of FB strand variants and four corresponding DMCs: one that incorporated RGD and Alexa647 (DMC<sub>39pN</sub> [Dye<sub>647</sub>]), a second with RGD (DMC<sub>39pN</sub>), a third that lacked RGD but had the dye (DMC<sub>inert</sub> [Dye<sub>647</sub>]), and finally a DMC<sub>inert</sub> that was unlabeled. Cells grown on the binary mixture of DMC<sub>39pN</sub> [Dye<sub>647</sub>] + DMC<sub>inert</sub> showed 17% loss of Alexa647 fluorescence after 1 hour of seeding HeLa cells. In contrast, cells grown on DMC<sub>inert</sub> [Dye<sub>647</sub>] + DMC<sub>39pN</sub> did not show a change in fluorescence (Figure 3.8). To evaluate degradation and force-induced rupture of DMCs the experiment was repeated in the presence of serum. The force-induced fluorescence loss compared to background degradation dropped to 7% in the case of 1% FBS treatment. The increase in cellular forces at no serum condition could be potentially due to altered cellular behavior under starvation rather than an increased background degradation (Figure S4). These data confirm that DMCs respond to cellular forces by mechanical denaturation and suggests the feasibility of releasing encapsulated cargo.

To demonstrate that DMCs show cell-type specific responses, we seeded non-invasive breast cancer cells (MCF-7), non-cancer mammary cells (MCF-10A) and highly invasive breast cancer cells (MDA-MB-231) on DMC. Specifically, we used the qDMC<sub>27pN</sub> because these

structures showed the greatest response to traction forces (Figure S3). MCF-7 and MDA-MB-231 showed greater cell spreading area on qDMC<sub>27pN</sub> surfaces compared to MCF-10A (Figure 3.8). In contrast, MCF-10A and MDA-MB-231 showed 3-fold and 6-fold greater force-induced DMC rupture compared to that of the MCF-7 cells on DMC<sub>27pN</sub> (Figure 3.8). This result is consistent with past studies that showed that MCF-7 and MDA-MB-231 have greater traction forces compared to MCF-10A.<sup>29,30</sup> MCF-10A and MDA-MB-231 display  $\alpha_v\beta_3$  integrins while MCF-7 lacks the receptor.<sup>31-33</sup> Thus, the observed differences in traction forces are likely attributed to the differential expression levels of  $\alpha_v\beta_3$  integrins which have 2 nM affinity towards the cRGDfK ligand.<sup>22</sup> Taken together, DMCs show cell specific responses leveraging

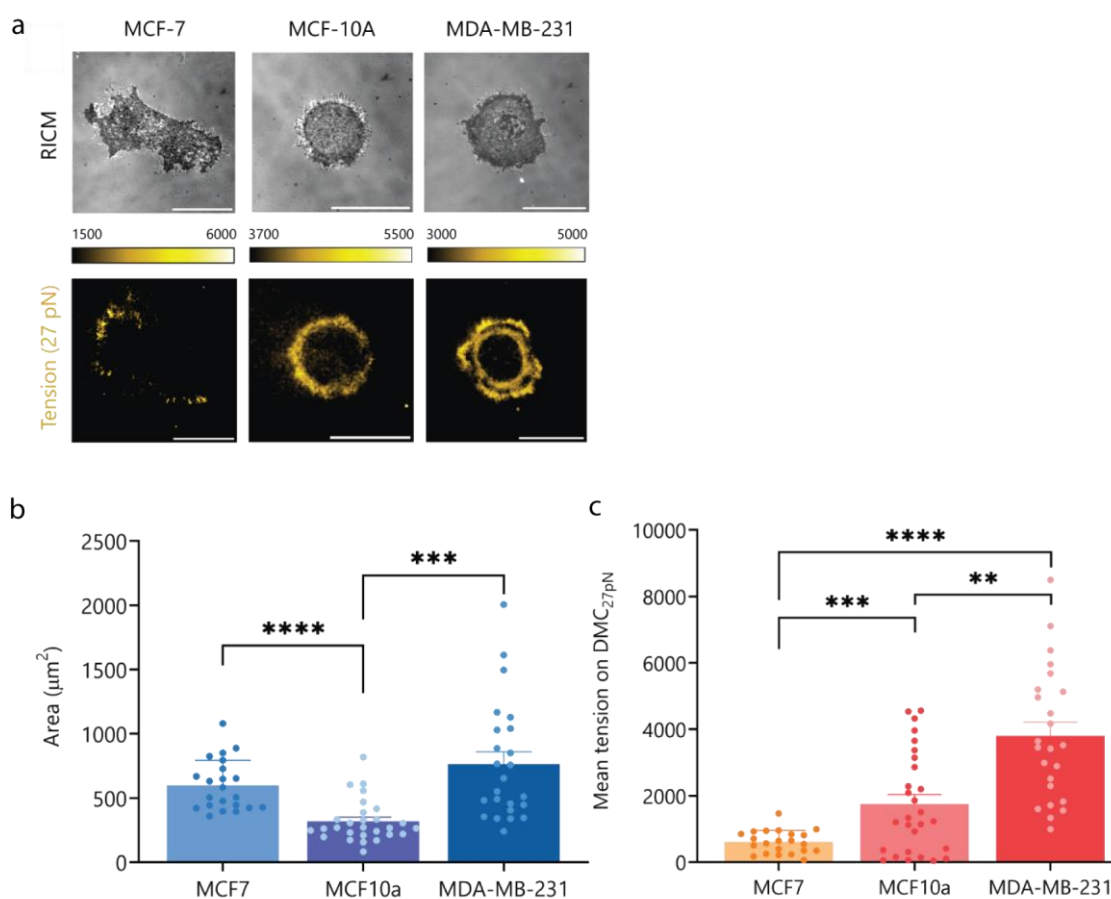


**Figure 3.9** a) Microscopy images of MCF-7, MCF-10A and MDA-MB-231 cells in 1% FBS DMEM on qDMC<sub>27pN</sub> after seeding on the surface for 1 hour cell ( $n=3$ ). (b) Cell spreading area of the three cell types (\*\* $P=0.0003$ , \*\*\*\* $P<0.0001$ ). (c) Mean tension per cell (\*\* $P=0.0017$ , \*\*\* $P=0.0005$ , \*\*\*\* $P<0.0001$ ). Fluorescence indicates DMC rupture due to integrin receptor forces. All error bars indicate SEM from three replicates and each data point in plots is from a single cell. The calibration bars accompanying the images indicate fluorescence values and display LUT. Scale bar = 20  $\mu\text{m}$ .

the chemical specificity of the ligand coupled with the force transmission through that ligand-receptor complex.

### 3.5 Conclusion

DNA mechanocapsules (DMC) based on the DNA tetrahedron were synthesized with cRGD ligands and tetrazine anchors that can be coated to TCO surfaces and made to respond to integrin receptor piconewton forces. The synthesis was done using facile, readily available molecular tags and click handles that allows for construction of the modified DMCs in a few synthetic steps. The folding of the DMCs were characterized using gel electrophoresis and DLS. The DMCs were found to produce higher yields when annealed in lower concentrations using a supported lipid bilayer fluorescence calibration curve. DMCs were found to produce dense monolayers on the TCO surface with sufficient ligand density to promote cell adhesion. Further the surface coating can be achieved at concentrations as low as 3 nM. This efficient covalent tethering of the DMCs is pivotal to the initial evaluation of mechanical rupture the DMC as it avoids the force-induced dissociations. DMCs on surface also exhibited higher stability compared to conventional double stranded DNA probes. Further surface anchored DMCs were found to be properly folded and functional using toehold mediated strand displacement. Interestingly, the surface density was observed to influence the nanostructure activity negatively at higher concentrations consistent with past literature findings.

DMCs with the Cy3B quenched (qDMC<sub>39pN</sub>) were found to produce an 8-fold increase in signal on rupture making it ideal to observe cellular forces on DMC functionalized surfaces. qDMC<sub>39pN</sub> were also used to observe the integrin forces exerted by the NIH3T3 cells. Further the rupture of the DMCs through integrin forces were confirmed using GFP-Paxillin markers for focal adhesions that colocalized with tension maps underneath the cells. The DMCs were also demonstrated to rupture in a force induced manner under cancer cells. Specifically, a mixture of force responsive and force decoupled DMCs were coated on surfaces and HeLa cells ruptured only the DMCs on which it can exert forces. Further the force decoupled surfaces had

minimal to no degradation under the cells in a one-hour timepoint compared to background. These data effectively demonstrates that the DMCs can respond to integrin forces and rupture in force specific manner with minimal rupture due to nonspecific events such as degradation.

Finally, DMCs were tested for their ability to sense cancer cells with high force phenotype and their ability to efficiently discern them from normal cells in the surrounding tissue. This was demonstrated by using a DMC engineered to rupture under lower integrin forces (qDMC<sub>27pN</sub>). The breast cancer cells MCF-7, MD-MBA-231 were used along with MCF-10 normal breast cell line on qDMC<sub>27pN</sub> surfaces. The DMCs were found to rupture with higher selectivity under the triple negative MD-MBA-231 cancer cells that have higher expression of  $\alpha_v\beta_3$  integrins. This two-factor chemical and mechanical authentication to release drugs can enhance the selectivity of the encapsulated drugs. These fluorescence microscopy measurements confirm that DMCs are robust delivery vehicles with high stability, and triggerable cargo release on demand. Hence, the development of the force-induced drug delivery platforms such as the DMC will offer new avenues in enhancing the selectivity of drugs based on the mechanical state of cells in addition to the widely prevalent chemical selectivity.

## 3.6 Methods

### 3.6.1 Materials

All Oligonucleotides were custom-synthesized (Table S2 and S3) by Integrated DNA Technologies (Coralville, IA, USA). The cRGDfK peptide (PCI-3696-PI) was purchased from Vivitide (MA, USA). DMCs were characterized using DLS on a NanoPlus DLS Nano Particle Size (Micromeritics Instrument Corporation, Norcross, GA, USA) instrument. Agarose gels were visualized on Amersham Typhoon laser scanner (Cytiva, Marlborough, MA, USA). Gels were run on a Bio-Rad Powerpac Basic Electrophoresis Supply (Hercules, CA, USA). P2-gels (1504118) were acquired from Bio-Rad (Hercules, CA, USA). TCO-NHS, TCO-PEG<sub>4</sub>-NHS, Methyltetrazine-PEG<sub>4</sub>-azide, Tris- hydroxypropyl triazolyl methylamine (THPTA, 1010-100) and Methyltetrazine-PEG<sub>4</sub>-NHS ester were obtained from Click chemistry tools (Scottsdale, AZ). Azido acetic NHS ester was obtained from BroadPharm (San Diego, CA). ATTO chambers, SMCC (22360), 6× Loading dye (R0611), were obtained from ThermoFisher Scientific (Waltham, MA, USA). Atto 647N NHS ester (18373-1MG-F) were purchased from Millipore Sigma. N,N-dimethylformamide (DMF, 227056), N,N-diisopropylethylamine (DIPEA, 496219), (3-Aminopropyl)triethoxysilane (APTES, 440140, 99% purity), sodium L-ascorbate (A4034-100G), 1-Methyl-2-pyrrolidinone (328634), were purchased from Sigma-Aldrich (St. Louis, MO, USA). Cy3B-NHS ester (PA63101) was purchased from GE Healthcare Life Sciences. Fetal Bovine Serum (35-015-CV), Penicillin–Streptomycin (30-002-CI), Trypsin EDTA (25-053-CI), DMEM (45000-336) from Corning (Tewksbury, MA, USA). Human recombinant Insulin and MEGM Mammary Epithelial Cell Growth Medium BulletKit was purchased from Lonza (USA). Cholera Toxin - azide free (19654) was purchased from Cayman chemicals. Triethylamine Acetate (TEAA, 2.0 M) solution was purchased from Glen Research.

### 3.6.2 DMC annealing

All the strands of the DMC were prepared at a concentration of 200 nM and mixed with 100  $\mu$ L of 10x TM buffer which was then diluted to 1 ml. The DMCs were annealed at 10-100  $\mu$ L volumes in a thermal cycler using the following annealing protocol: heat to 95°C in 2 mins;

hold at 95°C for 5 mins; cool down to 4°C over 10 mins and then held at 4°C until it was added to the TCO functionalized surfaces. For dextran encapsulation, the DMCs were annealed with an excess of dye-labelled 10 kDa dextran (typically 10  $\mu$ M) using the following protocol: heat to 95°C in 2 mins; hold at 95°C for 5 mins; rapidly cooled down to 4°C and then held at 4°C.

### 3.6.3 Agarose gel for DMC formation

1.75 g of agarose was dissolved in a conical flask with 1x TAE (50 ml) and was microwaved until its completely dissolved to produce a clear solution. It was allowed to cool for a few minutes and then 5  $\mu$ L of SYBR gold dye was added. It was then cast with a 15 well comb in the dark at r.t. for 2 hrs. The wells were loaded with 6  $\mu$ L of the sample (1  $\mu$ L of 6x loading dye + 5  $\mu$ L DNA sample) and was run at 100 V for 1 hr and visualized using SYBR gold stain.

### 3.6.4 Dynamic light scattering of DMCs

1mL of DMC (1  $\mu$ M) was annealed and transferred to a 1 ml cuvette. The cuvette center was determined using a cell center detector function in the instrument. Dynamic light scattering was recorded in a cuvette with 1 cm path length with a 50  $\mu$ m pinhole with 10 accumulations at a 165° scattering angle at 25°C.

### 3.6.5 Trans cyclooctene-functionalization of glass slides

Glass slides were washed with water and then fried using freshly prepared piranha solution (30% v/v H<sub>2</sub>O<sub>2</sub> [9.8 M] in conc. H<sub>2</sub>SO<sub>4</sub>) for 30 min. The slides were washed with 18.2 M $\Omega$  water (x3) and then with ethanol (x3). The washed slides were immersed in 1% v/v (3-Aminopropyl) triethoxysilane in ethanol and stirred for 30 min. Slides were then washed with ethanol (x4) and then baked in a hot air oven for 60 min. TCO-NHS (trans cyclooctene) or TCO-PEG<sub>4</sub>-NHS ester in DMSO (~10 mM) was added to one glass slide (50  $\mu$ L TCO soln. for 25 mm circular slides; 200  $\mu$ L for 25 x 75 mm slides) and sandwiched with another glass slide on top and allowed to react for 12 hrs. Finally, the slides were washed with ethanol (x2) and mounted on ATTO chambers for use.



### 3.6.6 DMC functionalization on TCO-glass slides

DMCs functionalized with a methyl-tetrazine on the anchoring strand were annealed at 200  $\mu$ M. TCO-functionalized glass circular coverslips were mounted on ATTO chambers after washing with ethanol. The mounted coverslips were then washed with 10 ml continuous flow of 18.2 M $\Omega$  water, followed by 10 ml of 1x TM buffer. 50  $\mu$ L of annealed DMCs were added to the 1x TM on TCO surfaces (final DMC concentration  $\sim$  16 nM) and allowed to click in the dark at room temperature over 60-90 mins.

### 3.6.7 Cell culture

NIH3T3 and NIH3T3 cells transfected with GFP-Paxillin were cultured in DMEM (10% CCS, 1% Penicillin-Streptomycin) at 37°C in an incubator with humidified 5% CO<sub>2</sub> atmosphere. MEF, HeLa and MDA-MB-231 cells were cultures under similar conditions but with 10% FBS DMEM and 1% Penicillin-Streptomycin. MCF-10A cells were cultured using Mammary Epithelial Cell Growth Medium supplemented with 100 ng/ml cholera toxin and BulletKit from Lonza. MCF-7 cells were grown in 10% FBS DMEM and 1% Penicillin-Streptomycin added with 0.01 mg/ml human recombinant insulin. Cells were cultured as per ATCC specifications and passaged either using 0.25% trypsin (5 min) or 50 mM EDTA in 1x PBS (10 min) and reseeded in a new flask with suitable media at lower density.

### 3.6.8 DNase I degradation

DMCs with Cy3B and dsDNA (Cy3B\_TD1-S3b and Tz\_TD1-S4) with Cy3B were clicked to a TCO surface for 1 hr. Surfaces were washed with 10% FBS DMEM and then added with 1 U of DNase I to a 1 ml of DMEM media in the chambers. The surface was imaged over 24 hours to visualize the kinetics of dsDNA and DMC degradation.

### 3.6.9 Opening DMCs on surface

DMCs with toehold and BHQ2 were clicked to a TCO surface for 1 hr at a concentration of 10 nM. The surfaces were washed with 10% FBS DMEM and added with the invading strand (final

conc. 1  $\mu\text{M}$ ) to commence the toehold mediated opening of the immobilized DMCs. Images of the surface was acquired every 5 mins over 2 hours to visualize the kinetics of DMC opening.

## Fluorescence microscopy

### 3.6.10 Imaging NIH3T3 cell tension

Imaging was conducted with a Nikon Ti2-E microscope. The NIH3T3 fibroblast cells expressing GFP-Paxillin were seeded onto a qDMC (cRGD, BHQ2, Cy3B, and tetrazine modifications) grafted coverslip in DMEM (1% CCS, 1% Penicillin-Streptomycin) and allowed to attach to the surfaces for 30 min at 37°C in the incubator with a 5% CO<sub>2</sub> atmosphere. The cells were then imaged at room temperature (~15 min) in RICM, FITC, and TRITC channels. The images were quantified using ImageJ2 software as described below.

### 3.6.11 Imaging non-force mediated degradation

DMCs (50  $\mu\text{L}$ ) each were annealed separately, mixed and clicked directly to 550  $\mu\text{L}$  of 1x TM TCO surfaces. After 1.5 hrs the chambers were washed with 10 ml of DMEM (with 1% P/S, 0% FBS and no phenol red). HeLa cells ( $5.0 \times 10^4$ ) were seeded to DMC grafted coverslips and allowed to spread for 1 hr. It was then imaged at room temperature (~5 min) in RICM and Cy5 channels. The images were quantified using ImageJ2 software as described below. The intensity loss below each cell was normalized to its background.

### 3.6.12 Imaging MCF-7, MCF-10a and MDA-MB-231

qDMC<sub>27pN</sub> were (50  $\mu\text{L}$ ) annealed separately and clicked directly to 550  $\mu\text{L}$  of 1x TM TCO surfaces. After ~1.5 hrs the ATTO chambers were washed with 1% FBS DMEM media with Penicillin-Streptomycin. Then respective cells ( $5.0 \times 10^4$ ) were added to separate chambers and allowed to attach to the surfaces for 30 min at 37°C in the incubator with a 5% CO<sub>2</sub> atmosphere. The cells were imaged room temperature after 1 hour in RICM and TRITC channels. The images were quantified using ImageJ2 software as described below.

### 3.6.13 Image analysis

Fluorescence images were processed using the ImageJ2 software. The fluorescence background around a cell was averaged and subtracted from the whole image. Cell spreading was measured by the total area of cell as observed in RICM. Fluorescence from tension probes or GFP-Paxillin was measured within the cell spread area. Brightness and contrast of microscopy images were adjusted for clearness. Quenching efficiency is given by the formula:

$$Q.E. = 1 - \frac{I_{quenched}}{I_{unquenched}} \times 100$$

## Oligonucleotide modifications

### 3.6.14 NHS-ester amine-DNA coupling

Amine modified DNA was dissolved in 10  $\mu$ L water (1 mM) and added with 2  $\mu$ L of 1 M  $\text{NaHCO}_3$ . NHS-modified functional group was dissolved in 10  $\mu$ L DMSO (Cy3B-NHS, Atto647N-NHS, etc.) or 10  $\mu$ L acetonitrile (Methyltetrazine-NHS) or 40  $\mu$ L DMF/NMP (Succinimidyl-4-(N-maleimidomethyl) cyclohexane-1-carboxylate) to obtain a final concentration of 10-100 mM. These solutions were mixed and reacted at r.t. for 30-60 mins. The reaction was quenched with addition of 100  $\mu$ L water and was filtered with P2 gel to remove excess NHS reagent and purified using HPLC. Integrin ligand c(RGD)fk-(PEG<sub>2</sub>)<sub>2</sub>-NH<sub>2</sub> can be functionalized in a similar manner by reacting it with azido acetic acid NHS in DMSO for 12 hours and directly purifying using HPLC.

### 3.6.15 Alkyne-azide conjugation

Alkyne functionalized DNA strand was dissolved in 5  $\mu$ L water to yield a 4 mM solution. Azide reagent (10 equivalences, 20 mM) dissolved in 10  $\mu$ L acetonitrile was added to this. In a separate tube,  $\text{CuSO}_4$  (1 equivalence, 1  $\mu$ L), Tris (3-hydroxypropyltriazolyl methyl) amine (4 equivalences, 2  $\mu$ L), sodium ascorbate (2 equivalence, 1  $\mu$ L) and 1  $\mu$ L triethylamine were mixed. This was added to the Alkyne-azide mixture and reacted at r.t. for 60-90 mins. The reaction was quenched with addition of 100  $\mu$ L EDTA solution, filtered with 0.2  $\mu$ m filters and purified using HPLC.

### 3.6.16 HPLC purification of peptide and oligonucleotides

Advanced oligonucleotide C18 column was used for the purification of chemically modified DNA. The column was run with 0.1 M TEAA in water as solvent A and acetonitrile as solvent B. DNA was purified using the following method, 10% for 3 minutes followed by 10-35% solvent B gradient over 25 min at 0.5 mL/min flow rate. Tetrazine conjugated DNA was purified using a similar method but using a 10-60% solvent B over 25 min at 0.5 mL/min. Peptides were purified using a Grace C18 column which was eluted with water as solvent A and acetonitrile as B both containing 0.05% TFA. A gradient of 10-40% solvent B over 30 min at 1 mL/min was used for peptide purification. Separated fractions were dried in a vacuum concentrator overnight. The purified oligonucleotide conjugates were reconstituted in 1x TE buffer and were stored at -30°C. The concentration of oligonucleotides and peptides were determined using its absorbance at 260 nm and 214 nm, respectively.

### 3.6.17 Supported Lipid Bilayer Preparation

To prepare Supported Lipid Bilayer (SLBs), SUVs were primed by mixing 99.9 mol% 1,2-dioleoyl-sn-glycero-3-phosphocholine (DOPC) and 0.1 mol% Texas Red 1,2 dihexadecanoyl-sn-glycero-3-phosphoethanolamine, triethylammonium salt (TR-DHPE, T1395MP, ThermoFisher Scientific) in a round bottom flask with chloroform. Lipids were then dried for 30 min under rotary evaporation followed by an ultra-high-purity nitrogen stream to remove residual chloroform. The dried lipid film was hydrated with 18.2 MΩ water (2 mg/mL) before conducting three freeze-thaw cycles. The mixture was then passed through 10mL LIPEX® thermobaric extruder 10 times (Evonik Industries, Essen, Germany) using an 80 nm polycarbonate filter.

### 3.6.18 Small unilamellar vesicles

In this calibration, the intensity of labelled oligonucleotides and small unilamellar vesicles (SUVs) in solution are compared to determine the F factor, which relates molecular brightness of the two fluorophores. To prepare SUVs in glass bottom plates, the glass was treated with a 2 M NaOH etching solution. It was then thoroughly washed with water and 1x PBS. The ratio

of the calibration curve slopes was used to determine the “F factor” for the labelled oligonucleotide and the SUV samples. The F-factor was calculated as follows:

$$F = \frac{I_{Cy3B-DNA}}{I_{TR-DHPE}}$$

where  $I_{Cy3B-DNA}$  and  $I_{TR-DHPE}$  represent the fluorescence intensities of the DNA and SUV samples, respectively. The quality of the calibration curve for DNA and SUVs was assessed by measuring the linear regression between the concentration of the known oligonucleotide (or the SUV sample) and its fluorescence intensity, as deviations can indicate nonspecific adsorption.

### 3.6.19 Bulk Probe Density Calculation

Supported Lipid Bilayer allows one to convert the raw fluorescence intensity of the surface to the molecular density of fluorescent molecules<sup>34</sup>. In this assay, lipid membranes were used as calibrated fluorescence standards, based on the known documented molecular density of phospholipids within membranes<sup>35</sup>. To create a fluorescence calibration curve, glass was passivated with 0.1% BSA in PBS for 20-30 min. Then, SLBs with varying fluorophore concentration were prepared by adding mixtures of labelled and unlabelled SUVs in known stoichiometries. Excess SUVs were rinsed using 1xPBS. The intensity of the SLBs was measured using epifluorescence microscopy. Using the known lipid footprint (0.72 nm<sup>2</sup>), the generated graph was used to relate the density of fluorophores to arbitrary fluorescence units. The intensity of probes on surface was then corrected using F factor. Using the generated density curve, we converted the fluorescence intensity of DNA to probes density per μm<sup>2</sup>.

### 3.6.20 Statistics

Quantitative results for experiments unless mentioned otherwise were presented as Mean ± SEM. All statistical analysis was performed using GraphPad Prism software package. Statistical analyses were performed by the t-test or analysis of variance (ANOVA) tests. P values were corrected for multiple comparisons unless otherwise noted as individual P values. P values were considered significant if the tested P value was smaller than 0.05(\*), 0.01(\*\*), 0.001(\*\*\*) or 0.0001(\*\*\*\*).

**Table 3.1** Representative literature on DNA origami-based drug delivery vehicles

Type	Cargo	<i>In vivo</i> models	Notes	Representative Citation
Intercalated	Small molecules (Dox)	Mouse	Enhances drug uptake & reduced side effects	<i>ACS Nano</i> <b>2014</b> , 7, 6633
Encapsulated	Protein, small molecules	Mouse, pig	Allows for homing and enhances stability, $t_{1/2}$ & efficacy	<i>Nature Biotech.</i> <b>2018</b> , 36, 258
Interwoven	siRNA, ASO	Mouse	Enhances stability, $t_{1/2}$ efficacy	<i>Angew. Chem. Int. Ed.</i> <b>2017</b> , 56, 16023

**Table 3.2 Oligonucleotides and chemical modifications used for DMCs.** DNA strands were synthesized by Integrated DNA Technologies. The modifications in the oligonucleotides are highlighted depending on the chemistry used for linking the functional group as follows: 1) **Alkyne-azide copper click** 2) **SMCC-thiol** 3) **Amine NHS-ester** 4) **commercially available modification**. The retention times of the modified strands are also provided wherever applicable.

Name	R <sub>t</sub> (min)	Sequence
TD1-S1a	—	CCAGGCAGTTGAGACGAACAT
TD1-S1b	—	TCCTAAGTCTGAAATTTATCACCCGCATAGTAGACGTATCA
TD1-S2	—	AGCTTGCTACACGATTCAGACTTAGGAATGTTCTGA CATGCCAGGGTCCAATACCGACGATTAC
cRGD_TD1-S3a_BHQ	23.0	<b>/cRGD/</b> GTGATAAAACGTGTAGCAAGCTGTAATCGACGGGAAG <b>/BHQ2/</b>
Cy3B_TD1-S3b	17.7	<b>/Cy3B/</b> AGCATGCCCATCCACTACTATGGCGG
Tz_TD1-S4	13.7	<b>/Tetrazine/</b> CTCGCATGACTCAACTGCCTGGTGATACGAGGATG GGCATGCTCTTCCCGACGGTATTGGACC
Tz_TD3-S4_cRGD	14.4	<b>/Tetrazine/</b> CTCGCATGACTCAAC <b>/cRGD/</b> GCCTGGTGATACGAGGATGGGCATGCTCTTCCCGACGGTATTGGACC
S3a Invader	—	CTTCCCGTCGATTACAGCTTGCTACACGTTTTATCA <u>CTCTCTCTC</u>
S3a toe BHQ	—	<u>GAGAGAGA</u> GTGATAAAACGTGTAGCAAGCTGTAATCGACGGGAAG <b>/BHQ2/</b>
S3a toehold	—	<u>GAGAGAGA</u> GTGATAAAACGTGTAGCAAGCTGTAATCGACGGGAAG
TD4-S1	—	CCAGGCAGTTGAGACGAACATTCCTAAGTCTGAAATTT ATCACCCGCATAGTAGACGTATCA
TD4-S3	—	GTGATAAAACGTGTAGCAAGCTGTAATCGACGGGAAG AGCATGCCCATCCACTACTATGGCGG
cRGD_TD5-S3a_A647	16.3	<b>/cRGD/</b> GTGATAAAACGTGTAGCAAGCTGTAATCGACGGGAAG <b>/Alexa647/</b>
TD7-S2	—	TAGGAATGTTTCGACATGCGAGGGTCCAATACCGA CGATTACAGCTAGCTACACG A TTCAGACT
cRGD_TD7-S3a BHQ	21.6	<b>/cRGD/</b> GTGATAAAACGTGTAGCTA <b>/BHQ2/</b>
Cy3B_TD7-S3b	17.0	<b>/Cy3B/</b> GCTGTAATCGACGGGAAGAGCATGCCCATCCACTACTATGGCGG
cRGD_TD8-S3a_BHQ	21.3	GTGATAAAACGTG <b>/cRGD/</b> AGCTA <b>/BHQ2/</b>
TD5-S3a_A647	14.7	GTGATAAAACGTGTAGCAAGCTGTAATCGACGGGAAG <b>/Alexa647/</b>
cRGD_TD1-S3a	15.2	<b>/cRGD/</b> GTGATAAAACGTGTAGCAAGCTGTAATCGACGGGAAG

**Figure S1** (Left) DMC with various chemical modifications at 50 nM concentrations. DMCs fold with high yield (>95%) when annealed at lower concentrations. (Right) DNA tetrahedron with 4 strands (lane 6) reported by Goodman et al.<sup>4</sup> along with the DMC (lane 5) and the individual tetrahedron strands for comparison (lane 1 - 4).

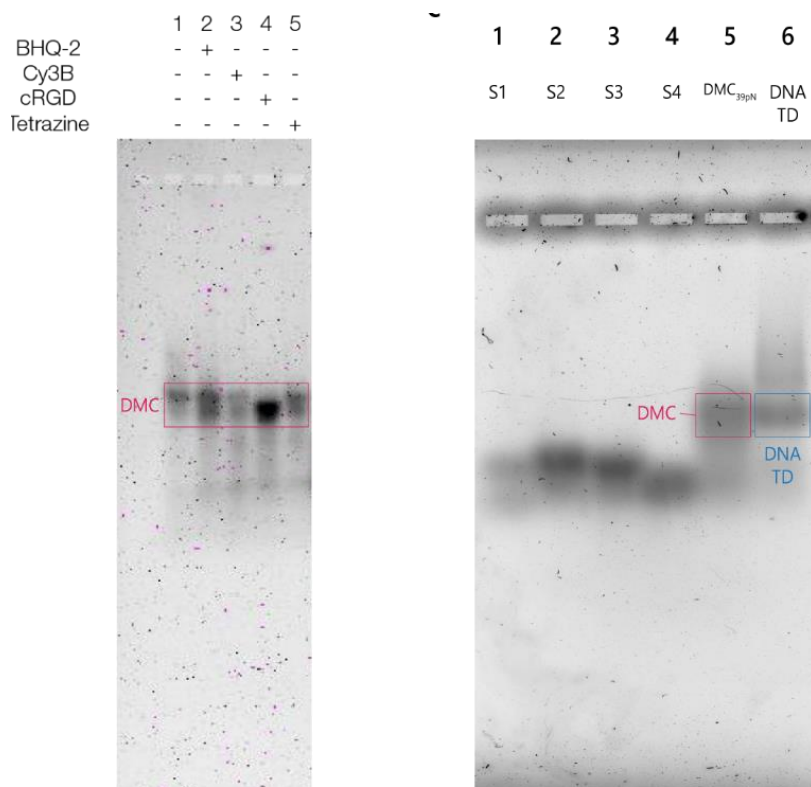




**Figure S2** (Left) SLB calibration: Intensity of Texas Red DHPE (N-(Texas Red sulfonyl)-1,2-dihexadecanoyl-snglycero-3-phosphoethanolamine, triethylammonium salt) to the number of molecules on the surface. (Right) F-factor plot estimation using concentrations of labelled oligonucleotide and SUVs (small unilamellar vesicles) in solution to compare the fluorescence intensity with density. The ratio of the calibration curve slopes was used to determine the “F factor” for the labelled oligonucleotide and the SUV samples. The F-factor was calculated as follows:  $F = I_{\text{Cy3B-DNA}} / I_{\text{TR-DHPE}}$ , where  $I_{\text{Cy3B-DNA}}$  and  $I_{\text{TR-DHPE}}$  represent the fluorescence intensities of the DNA and SUV samples, respectively.

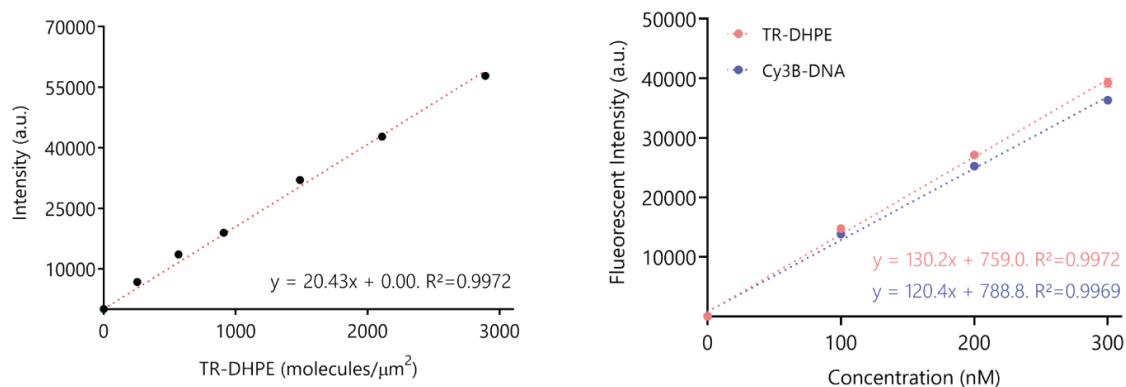


**Figure S3** (a) Representative images of HeLa cells on force sensitive DMCs (left) and force decoupled DMCs. Scale bar – 20  $\mu\text{m}$ . (b) Intensities of DMC functionalized surfaces. (c) Cell spread area of HeLa cells on both the surfaces. Each data point was obtained from a single cell ( $n=3$ ). (d) Plot quantifying per cell loss of fluorescence normalized to background under HeLa cells in DMEM (1% FBS) after 1 hour. \*\*\*\* $P < 0.0001$ . All error bars indicate SEM and each data point in plots is from a single cell. The calibration bars accompanying the images indicate fluorescence values and display LUT.

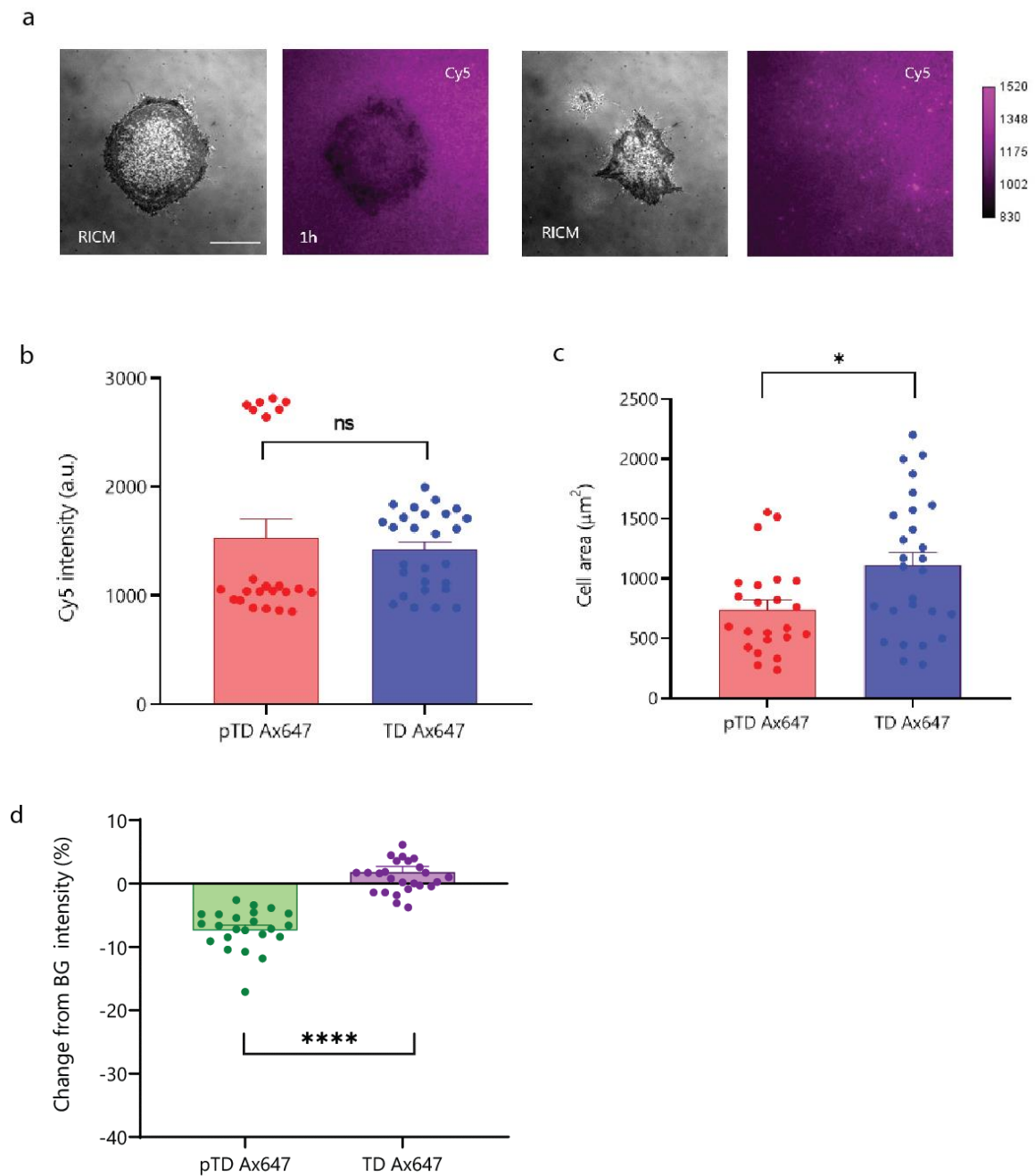
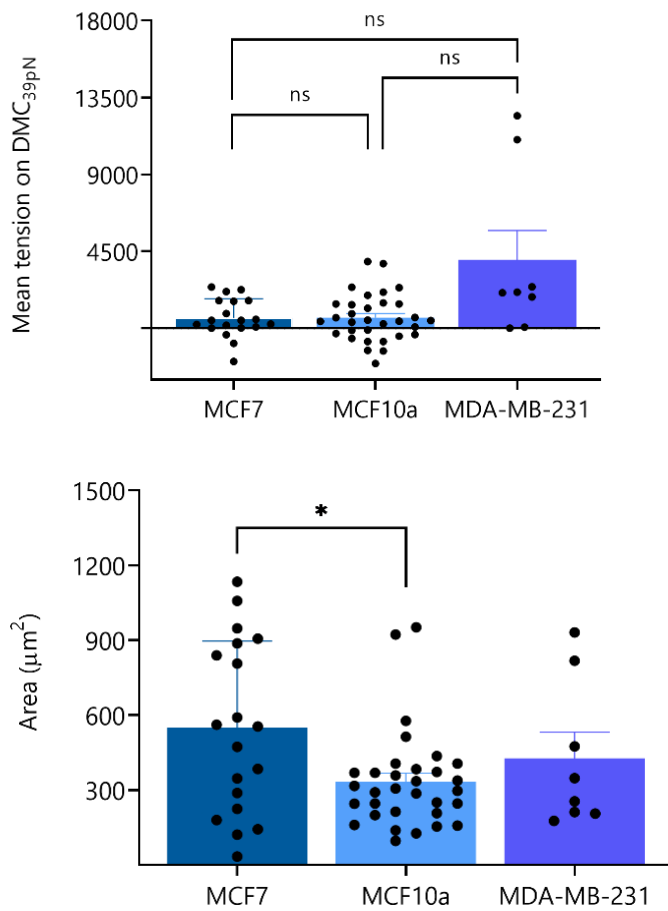


**Figure S4** (Top) Mean tension per cell of MCF-7, MCF-10A and MDA-MB-231 cells in 1% FBS DMEM on qDMC<sub>39pN</sub> after seeding on the surface for 1 hour cell. (Bottom) Mean spread area per cell of the three cell lines. Fluorescence indicates DMC rupture due to integrin receptor forces. All error bars indicate SEM from three replicates and each data point in plots is from a single cell. The calibration bars accompanying the images indicate fluorescence values and display LUT.



## References

1. Manzari, M. T. *et al.* Targeted drug delivery strategies for precision medicines. *Nat Rev Mater* **6**, 351–370 (2021).
2. Qiu, Y., Bai, J., Feng, Y., Shi, X. & Zhao, X. Use of pH-Active Catechol-Bearing Polymeric Nanogels with Glutathione-Responsive Dissociation to Codeliver Bortezomib and Doxorubicin for the Synergistic Therapy of Cancer. *ACS Appl. Mater. Interfaces* **13**, 36926–36937 (2021).
3. Li, Y. *et al.* Combinatorial Library of Cyclic Benzylidene Acetal-Containing pH-Responsive Lipidoid Nanoparticles for Intracellular mRNA Delivery. *Bioconjugate Chem.* **31**, 1835–1843 (2020).
4. Lu, H., Xu, S., Guo, Z., Zhao, M. & Liu, Z. Redox-Responsive Molecularly Imprinted Nanoparticles for Targeted Intracellular Delivery of Protein toward Cancer Therapy. *ACS Nano* **15**, 18214–18225 (2021).
5. Wang, G.-H. *et al.* ATP triggered drug release and DNA co-delivery systems based on ATP responsive aptamers and polyethylenimine complexes. *J. Mater. Chem. B* **4**, 3832–3841 (2016).
6. Wang, B. *et al.* Potent and Prolonged Innate Immune Activation by Enzyme-Responsive Imidazoquinoline TLR7/8 Agonist Prodrug Vesicles. *Journal of the American Chemical Society* **142**, 12133–12139 (2020).
7. Han, H. *et al.* Dual Enzymatic Reaction-Assisted Gemcitabine Delivery Systems for Programmed Pancreatic Cancer Therapy. *ACS Nano* **11**, 1281–1291 (2017).
8. Zhang, J. *et al.* Conditional Deoxyribozyme–Nanoparticle Conjugates for miRNA-Triggered Gene Regulation. *ACS Appl. Mater. Interfaces* **12**, 37851–37861 (2020).
9. Chen, W.-H. *et al.* Targeted VEGF-triggered release of an anti-cancer drug from aptamer-functionalized metal–organic framework nanoparticles. *Nanoscale* **10**, 4650–4657 (2018).
10. Modi, S. *et al.* Trastuzumab Deruxtecan in Previously Treated HER2-Low Advanced Breast Cancer. *New England Journal of Medicine* **387**, 9–20 (2022).

11. Rautio, J. *et al.* Prodrugs: design and clinical applications. *Nat Rev Drug Discov* **7**, 255–270 (2008).
12. Zhang, Q. *et al.* DNA Origami as an In Vivo Drug Delivery Vehicle for Cancer Therapy. *ACS Nano* **8**, 6633–6643 (2014).
13. Zhao, Y.-X. *et al.* DNA Origami Delivery System for Cancer Therapy with Tunable Release Properties. *ACS Nano* **6**, 8684–8691 (2012).
14. Ge, Z. *et al.* DNA Origami-Enabled Engineering of Ligand–Drug Conjugates for Targeted Drug Delivery. *Small* **16**, 1904857 (2020).
15. Li, S. *et al.* A DNA nanorobot functions as a cancer therapeutic in response to a molecular trigger in vivo. *Nat Biotechnol* **36**, 258–264 (2018).
16. Dutta, P. K. *et al.* Programmable Multivalent DNA-Origami Tension Probes for Reporting Cellular Traction Forces. *Nano Letters* (2018) doi:10.1021/acs.nanolett.8b01374.
17. Du, Y. *et al.* Membrane-anchored DNA nanojunctions enable closer antigen-presenting cell–T-cell contact in elevated T-cell receptor triggering. *Nat. Nanotechnol.* 1–10 (2023) doi:10.1038/s41565-023-01333-2.
18. Su, H. *et al.* Massively Parallelized Molecular Force Manipulation with On-Demand Thermal and Optical Control. *J. Am. Chem. Soc.* **143**, 19466–19473 (2021).
19. Wang, F. *et al.* Gint4.T-Modified DNA Tetrahedrons Loaded with Doxorubicin Inhibits Glioma Cell Proliferation by Targeting PDGFR $\beta$ . *Nanoscale Research Letters* **15**, 150 (2020).
20. Dai, B., Hu, Y., Duan, J. & Yang, X.-D. Aptamer-guided DNA tetrahedron as a novel targeted drug delivery system for MUC1-expressing breast cancer cells in vitro. *Oncotarget* **7**, 38257–38269 (2016).
21. Duangrat, R., Udomprasert, A. & Kangsamaksin, T. Tetrahedral DNA nanostructures as drug delivery and bioimaging platforms in cancer therapy. *Cancer Science* **111**, 3164–3173 (2020).

22. Kapp, T. G. *et al.* A Comprehensive Evaluation of the Activity and Selectivity Profile of Ligands for RGD-binding Integrins. *Sci Rep* **7**, 39805 (2017).
23. Jurchenko, C., Chang, Y., Narui, Y., Zhang, Y. & Salaita, K. S. Integrin-Generated Forces Lead to Streptavidin-Biotin Unbinding in Cellular Adhesions. *Biophysical Journal* **106**, 1436–1446 (2014).
24. Rashid, S. A. *et al.* DNA Tension Probes Show that Cardiomyocyte Maturation Is Sensitive to the Piconewton Traction Forces Transmitted by Integrins. *ACS Nano* (2022)  
doi:10.1021/acsnano.1c04303.
25. Liu, Y. *et al.* Nanoparticle Tension Probes Patterned at the Nanoscale: Impact of Integrin Clustering on Force Transmission. *Nano Lett.* **14**, 5539–5546 (2014).
26. Goodman, R. P. *et al.* Rapid Chiral Assembly of Rigid DNA Building Blocks for Molecular Nanofabrication. *Science* **310**, 1661–1665 (2005).
27. Hagan, M. F. & Chakraborty, A. K. Hybridization dynamics of surface immobilized DNA. *J. Chem. Phys.* **120**, 4958–4968 (2004).
28. Peterson, A. W., Heaton, R. J. & Georgiadis, R. M. The effect of surface probe density on DNA hybridization. *Nucleic Acids Research* **29**, 5163–5168 (2001).
29. Li, Z. *et al.* Cellular traction forces: a useful parameter in cancer research. *Nanoscale* **9**, 19039–19044 (2017).
30. Kraning-Rush, C. M., Califano, J. P. & Reinhart-King, C. A. Cellular Traction Stresses Increase with Increasing Metastatic Potential. *PLOS ONE* **7**, e32572 (2012).
31. Veneti, E., Tu, R. S. & Auguste, D. T. RGD-Targeted Liposome Binding and Uptake on Breast Cancer Cells Is Dependent on Elastin Linker Secondary Structure. *Bioconjugate Chem.* **27**, 1813–1821 (2016).
32. Popielarski, M., Ponamarczuk, H., Stasiak, M., Watała, C. & Świątkowska, M. Modifications of disulfide bonds in breast cancer cell migration and invasiveness. *Am J Cancer Res* **9**, 1554–1582 (2019).

33. Taherian, A., Li, X., Liu, Y. & Haas, T. A. Differences in integrin expression and signaling within human breast cancer cells. *BMC Cancer* **11**, 1–15 (2011).
34. Galush, W. J., Nye, J. A. & Groves, J. T. Quantitative Fluorescence Microscopy Using Supported Lipid Bilayer Standards. *Biophysical Journal* **95**, 2512–2519 (2008).
35. Vacklin, H. P., Tiberg, F. & Thomas, R. K. Formation of supported phospholipid bilayers via co-adsorption with  $\beta$ -d-dodecyl maltoside. *Biochimica et Biophysica Acta (BBA) - Biomembranes* **1668**, 17–24 (2005).

## Chapter 4

# Force induced drug delivery from DMCs

This chapter is adapted from a manuscript in submission to Nature Communications: DNA mechanocapsules for programmable piconewton responsive drug delivery. Arventh Velusamy, Radhika Sharma, Sk Aysha Rashid, Hiroaki Ogasawara and Khalid Salaita.

Arventh Velusamy and Radhika Sharma designed and performed the qPCR experiments. Hiroaki Ogasawara synthesized Cy3B-labelled RGD constructs for uptake visualization.

### 4.1 Abstract

The mechanical dysregulation of cells is associated with a number of disease states, that span from fibrosis to tumorigenesis. Hence, it is highly desirable to develop strategies to deliver drugs based on the mechanical phenotype of a cell. To achieve this goal, we designed and characterized DNA mechanocapsules (DMC) comprised of DNA tetrahedrons that are force responsive. Initially, Doxorubicin was used in conjunction with DMCs for force responsive delivery which could not be achieved due to the inherent limitations of the small molecule. DMCs were then designed to encapsulate macromolecular cargos such as dextran and oligonucleotide drugs with minimal cargo leakage and high nuclease resistance. Force-induced release and uptake of DMC cargo was validated by flow cytometry. DMCs were also shown to selectively target high force phenotypic cells in a mixed population. Finally, we demonstrate force-induced mRNA knockdown of HIF1 $\alpha$  in a manner that is dependent on the magnitude of cellular traction forces. These results show that DMCs can be effectively used to target biophysical phenotypes which may find useful applications in immunology and cancer biology.



## 4.2 Introduction

A powerful strategy to increase the efficacy of drugs is to specifically deliver therapeutics to diseased cells. A complementary approach for reducing off-target effects and increasing drug efficacy involves creating inactive drugs that are activated upon encountering a unique stimulus in diseased tissue<sup>1</sup>. In this chapter, we present a strategy to release and activate drugs using *mechanical inputs* generated by cell surface receptors. The motivation for using a specific magnitude mechanical force as a cue comes from quantitative measurements of forces generated by many classes of receptors such as Integrins<sup>2,3</sup>, T cell<sup>4,5</sup>, and B cell receptors<sup>6,7</sup>, Notch<sup>8,9</sup> among others<sup>10,11</sup>. The mechanical forces generated by cells and transmitted to their cell surface receptors is important to biological processes such as signaling<sup>4,9</sup>, migration<sup>12,13</sup>, cell cycle progression<sup>14,15</sup>, as well as giving cells and tissues their intrinsic shape and architecture<sup>16</sup>.

Many drug delivery platforms including FDA-approved drugs use antibody, peptide and aptamer homing to deliver drugs in a tissue or cell specific context, but this vast body of work has thus far ignored cell mechanics to enhance selectivity. To the best of our knowledge, no force-triggered drugs have been developed that respond to specific molecular magnitudes of force. Instead, prior research reported on force-activated drugs that respond to broad ranges of force. For example, Ingber and colleagues created shear-activated microparticles that release clot-dissolving drugs upon encountering obstructed blood vessel.<sup>17</sup> Other examples include tethered DNA aptamer that releases TGF- $\beta$ 1 upon mechanical denaturation and silica microparticles that release drug molecules upon forces that displace a blocking DNA strand.<sup>18</sup> Mechanical activity represents an exciting and growing frontier in drug delivery but an important cue that is often ignored is the mechanical state of a cell.

Mechanical cues play vital, orthogonal roles to biochemical signals and mechanical forces generated by cells provide unique marker of disease state. For example, it has been shown that within the collective invasion pack in lung cancer, groups of leader cells are highly invasive, and display elevated integrin forces compared to follower cell from the same tumor.<sup>19</sup> It would be highly desirable to create molecular drug delivery systems that respond to mechanical cues.

Such probes can be tuned to release drugs at mechanically altered sites and provide specificity to non-specific drugs in a manner akin to ADCs. Developing new types of responsive drugs is of paramount importance and may catapult a new branch of responsive drugs. Hence, drugs that can be tailored to respond to specific magnitudes of forces are essential and this chapter addresses the unmet need for a modular platform for delivering drugs with pN precision.

In principle, mechano-targeting can augment the advances in the area of targeted delivery<sup>20,21</sup>. Moreover, mechanical dysregulation can indicate a diseased state even when cells have a biochemical composition and morphology identical to those of healthy cells<sup>20</sup>. Leveraging the altered mechanics of diseased cells as a trigger for drug deployment could, therefore, allow one to target diseased cells effectively. For example, cell traction forces are upregulated during fibrosis,<sup>22</sup> and asthma.<sup>23</sup> Most lung diseases are characterized by changes in cell mechanics.<sup>24</sup> As mentioned in chapter 1, the viability of human embryos can be predicted noninvasively by simply measuring the stiffness of a fertilized egg.<sup>25</sup> Tumors generate a microenvironment with elevated stiffness and elevated cellular traction forces. Therefore, mechanical forces generated by cells are associated with unique pathologies that may offer a new frontier in selective drug delivery.

DNA nanostructures offer well-defined structures for targeting and drug-delivery in contrast to synthetic polymers and liposomes that lack defined structures for biomolecule modification and high cargo loading efficiency.<sup>26</sup> A force-sensitive DNA device for cargo delivery can improve the specificity of broad-spectrum drugs when released spatiotemporally to diseased cells with altered mechanics. A localized force-based release mechanism benefits from the ability to produce a high concentration of drug in intimate proximity to the cell of interest. For example, only 1000 drug molecules are required to achieve a concentration of 1 nM in a HeLa cell. Hence, a force-triggered DNA nanostructure can protect its cargo safely until it reaches its destination and release it there for maximum efficacy. This vastly reduces the concentration of DNA nanostructures required thereby minimizing off-target effects of systemic delivery. DNA nanocages can be designed in a variety of sizes and shapes. Larger DNA structures can carry macromolecular payloads such as proteins, nanoparticles and even antibodies due to the

high volume of their cavity. Smaller nanocages on the other hand can only carry cargo of lower molecular weight but offer a simpler design which can be synthesized with high yields.

The DNA tetrahedron (TDs) structure has been widely used for drug delivery because its nanoscale size minimizes clearance and displays enhanced cell uptake while the constrained geometry offers improved nuclease resistance.<sup>27</sup> TDs have an internal cavity that can hold a cargo of radius 2.6 nm (~60 kDa) which can accommodate macromolecular cargos like proteins, nanoparticles, and oligonucleotides.<sup>28,29</sup> Further the DNA in the structure can be used to intercalate drugs like doxorubicin (Dox) which is one of the most widely used drug that can effectively impede the growth of tumor cells.<sup>30-32</sup> DNA origami, especially DNA tetrahedrons, have been extensively used in studies for doxorubicin delivery to cells and tissues.<sup>33,34</sup> DNA nanostructures can act like sponges that can soak up doxorubicin by intercalating them and carry them target tissue.<sup>33</sup> TDs can improve the specificity of doxorubicin by leveraging homing ligands that can improve directed delivery. Further, macromolecules such as Dextran, gold nano particles and ASOs can be encapsulated through various means and can be used for drug delivery. Hence, DNA mechanocapsules fashioned out of TDs can be loaded with these cargoes and studied for drug loading to quantify the available dosage, kinetics of leakage, and efficacy. Such an approach would represent a first step toward opening up the area of mechanically-triggered drugs.

Herein we report a DNA mechanocapsule (DMC) that expands the toolset for precision drug delivery. We employed DNA structures given their well-characterized force-responses using single molecule force spectroscopy and modeling<sup>35</sup>. DMCs were designed using tetrahedral DNA (TD) structures with encapsulated or interwoven cargos because of TD's efficient assembly and high tailorability<sup>36</sup>, coupled with extensive work demonstrating *in vitro* and *in vivo* therapeutic delivery of small molecules<sup>37</sup>, nucleic acids<sup>38,39</sup>, and proteins<sup>40,41</sup>. We targeted integrin adhesion receptors because these are broadly expressed in adherent cells and transmit 10-50 pN forces to their ligands in a cell and tissue-specific manner<sup>9</sup>. In the following, we describe the design and synthesis of drug-containing DMCs and characterize their stability and force-induced release. As a final proof-of-concept we demonstrate force-triggered

knockdown of HIF1 $\alpha$  using an antisense oligonucleotide that is currently in clinical testing as an anti-cancer therapeutic<sup>42</sup>.

## 4.3 Results and discussions

### 4.3.1 SMALL MOLECULE DELIVERY FROM DMCs

DMC was tested for the delivery of small molecules by intercalating doxorubicin molecules since doxorubicin is widely used as a cargo for drug delivery studies. Doxorubicin has a  $K_D$  of  $1.6 \text{ nM} \pm 0.5 \text{ nM}$  and can intercalate approximately 40-44 doxorubicin molecules into a single DNA Tetrahedron.<sup>43</sup> Further doxorubicin is fluorescent and can be excited at 308 nm and at 532 nm and is capable of self-quenching at high concentrations.<sup>44</sup> When the DMCs are ruptured under force the doxorubicin molecules are released due to the dehybridization of the force bearing strand as they can only bind to double stranded DNA. The released doxorubicin molecules can be detected using fluorescence while the TD bound doxorubicin molecules are quenched. The detection of doxorubicin release can be facilitated by fluorescence measurements under such conditions.

The DMC<sub>39pN</sub> was grated to the TCO surfaces along with excess concentrations of doxorubicin in the solution ( $\sim 10 \mu\text{M}$ ) to ensure that the structures are saturated with the intercalating drug. The unbound DMC and doxorubicin in the solution were then washed away before seeding NIH 3T3 cells to the DMC<sub>39pN</sub> [Dox] surfaces in 1% CCS. Initially, the DMCs were evaluated for the release and apoptosis triggering by using Annexin V live-cell staining. Annexin binds to apoptotic cells and can be used as a marker for successful delivery of cytotoxic drugs. It was observed that while doxorubicin signal was observed in the cells, doxorubicin at high concentrations could potentially be triggering other cell death pathways than apoptosis (Figure S1). Then doxorubicin fluorescence alone was used to measure the extent of drug release based on cellular forces.

The release of doxorubicin was then evaluated at various time points to measure the optimal time frame for drug delivery. To control for non-specific uptake of the doxorubicin, a  $DMC_{inert}$  was used which does not undergo force mediated rupture.  $DMC_{39pN}[Dox]$  and  $DMC_{inert}[Dox]$  grafted surfaces were then seeded with NIH 3T3 cells and were imaged for doxorubicin

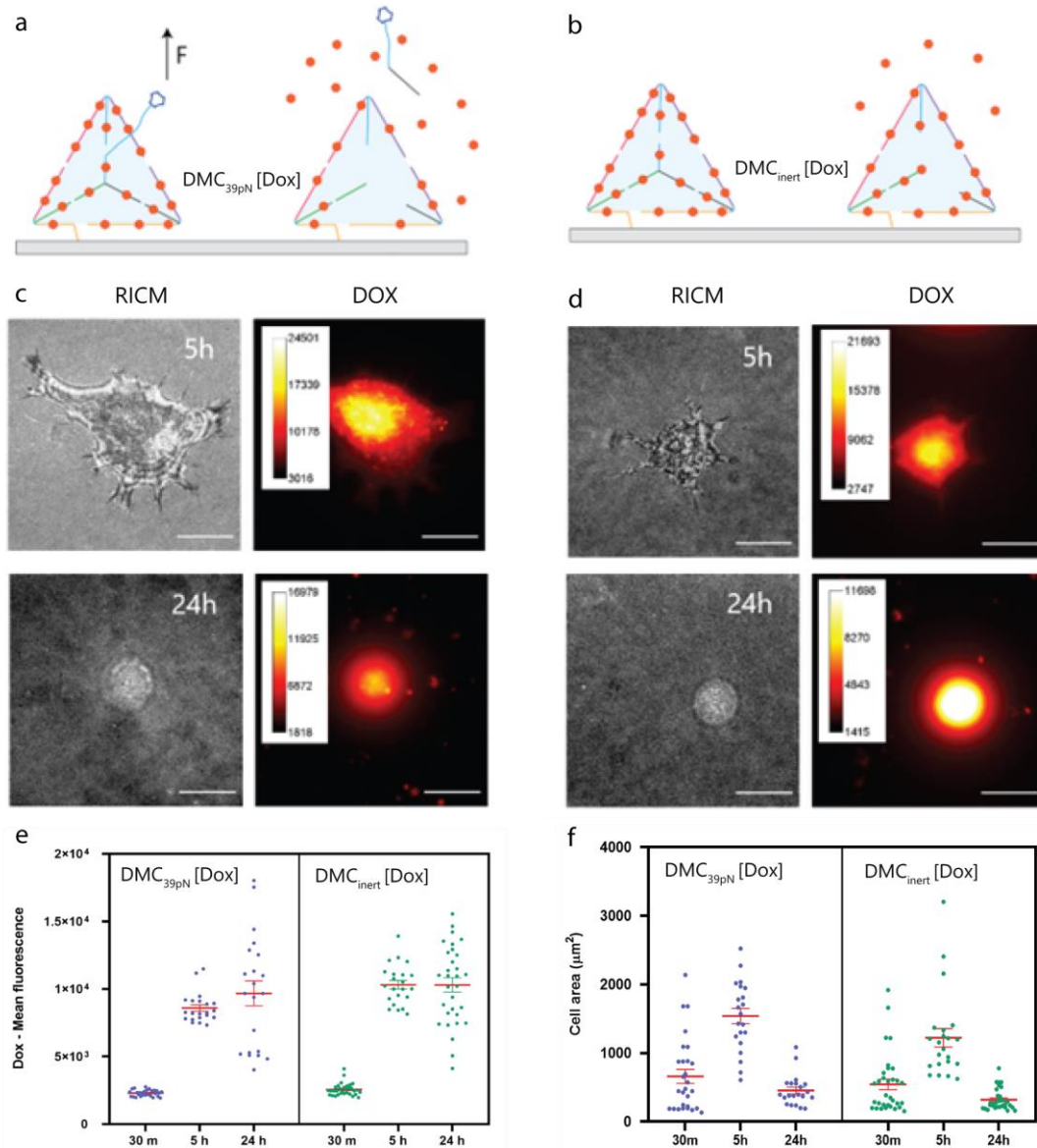


**Figure 4.1** Schematic of force-induced doxorubicin release from (a)  $DMC_{39pN}[Dox]$  and (b) non-specific leakage  $DMC_{inert}[Dox]$ . Representative images of 3T3 cells seeded on (c)  $DMC_{39pN}[Dox]$  and (d)  $DMC_{inert}[Dox]$  grafted surfaces. Gray images represent - RICM and images in hot red LUT represent doxorubicin fluorescence intensity. Doxorubicin bound to DMCs on the surfaces remain self-quenched. (e) Mean doxorubicin fluorescence intensity and (f) cell spread area of 3T3 cells at various time points. All error bars indicate SEM from three replicates and each data point in plots is from a single cell. The calibration bars accompanying the images indicate fluorescence values and display LUT. Scale bar = 20  $\mu m$ .

fluorescence (Figure 4.1). The mean doxorubicin fluorescence intensity in each cell increased as time progressed as evident in the 30 min, 5- and 24-hour time points. The cell surface area on the  $DMC_{39pN}$  was higher than the  $DMC_{inert}$  as expected due to the presence of cell adhesion ligands. The control condition performed similarly or worse than the force-mediated condition in that there was a higher fluorescence of doxorubicin in the cells. Furthermore, the cytotoxic effect of doxorubicin kills the cells and detaches them from the surface making it hard to visualize under a microscope. Hence, imaging cells using fluorescence microscopy might not be indicative of drug uptake for the whole population of cells.

To combat cells detaching due to the drug uptake and the ensuing bias in microscopy, the total number of viable cells in the population were counted using cell viability assays. This was done using the robust WST-8 assay in which the tetrazolium salt is reduced by dehydrogenases to

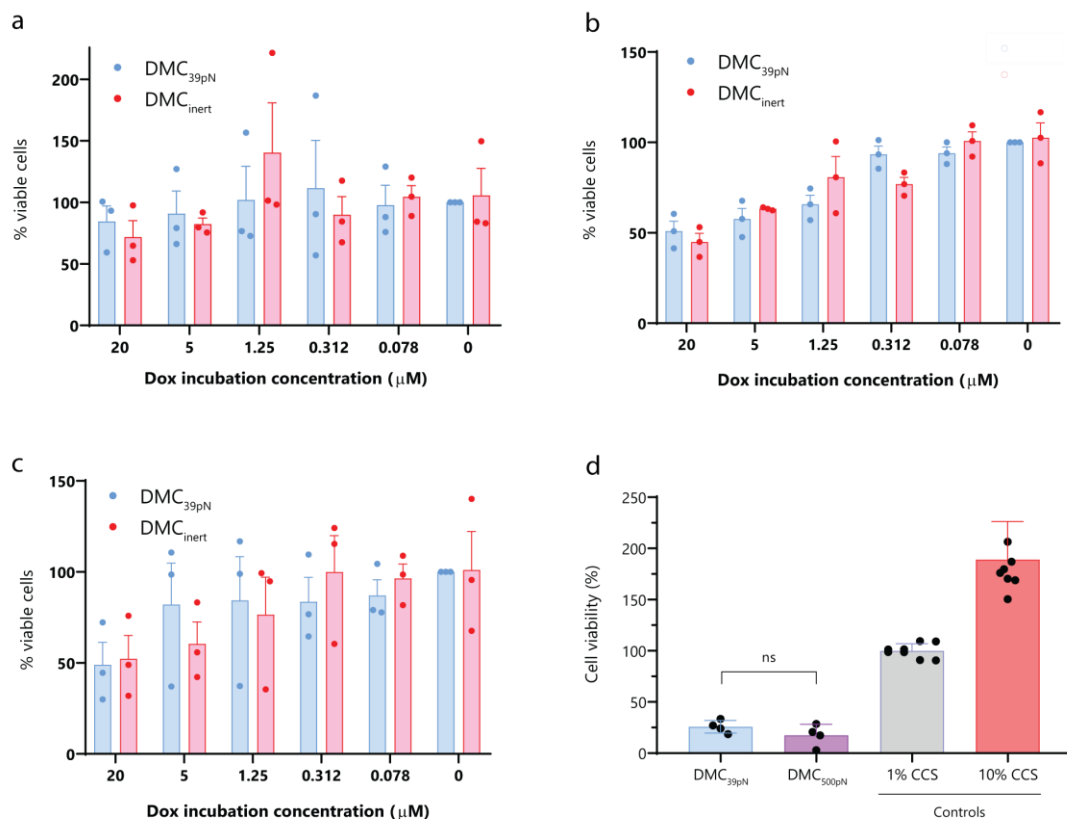


**Figure 4.2** Cell viability on  $DMC_{39pN}[Dox]$  and  $DMC_{inert}[Dox]$  surfaces after a) 24 b) 36 and c) 72 hours. 3T3 cells were culture in 1% CCS on the surfaces for the required duration and then WST assay reagents in PBS were added and incubated for 2 hours. d) Cell viability on  $DMC_{39pN}[Dox]$  and  $DMC_{500pN}[Dox]$  surfaces after 24 hours with cells grown in 1% CCS and 10% CCS as controls. All error bars indicate SEM from three replicates.

produce a formazan (460 nm) in the culture media. The number of cells and subsequently the amount of formazan produced can be directly measured using absorbance. The concentration of the doxorubicin for loading to the DMCs was varied to find the optimal concentration for force induced drug release as well as to minimize the non-specific leakage of drug molecules. 3T3 cells were seeded on DMCs loaded with varying concentrations ranging from 20  $\mu\text{M}$  to 78 nM and allowed to grow on these surfaces. The viability of the cells was then measured at different days to evaluate the impact of force-induced release and it was observed that the viability decreased with increasing doxorubicin loading concentrations (Figure 4.2). But there was no significant difference between the  $\text{DMC}_{39\text{pN}}[\text{Dox}]$  and  $\text{DMC}_{\text{inert}}[\text{Dox}]$  grafted surfaces at all concentrations and all cell populations had comparable viability.

Since the  $\text{DMC}_{\text{inert}}$  lacks the cRGD ligand to promote cell growth and adhesion, it could be reasoned that the lack of the cRGD could have reduced the viability of the cells in the control condition. Hence, the experiment was repeated with a modified control where the  $\text{DMC}_{\text{inert}}$  was replaced with  $\text{DMC}_{500\text{pN}}$ . This ensures that the cells have ligand for cell adhesion while resisting rupture due to cellular forces. 3T3 cells were seeded to these surface conditions and the viability of the cells were measured after 24 hours. It was noted that the viability of both  $\text{DMC}_{39\text{pN}}$  and  $\text{DMC}_{500\text{pN}}$  surfaces remained the same after a day, indicating no significant force mediated release in doxorubicin compared to non-specific conditions.

These experimental studies demonstrate that the intercalating drugs like doxorubicin can leak from the DMC systems due to inherent  $k_{\text{off}}$  of the DMC-drug complexes. Releasing such intercalating drugs based on dehybridization can be done only in cases where the drug has a very low  $k_{\text{off}}$  to the vehicle. This notion was further substantiated in the later publication by Ijäs et al. where they describe that about 70% of the doxorubicin molecules initially bound to DNA leaked and stabilized into an equilibrium within 10 minutes.<sup>34</sup> The authors also noted that doxorubicin aggregates which usually form at high concentrations have been largely ignored in most of the DNA-Doxorubicin studies. The aggregates are seldom separated from the DNA-Dox complexes using conventional purification protocols and are a major source of incoherence in experimental results. This suggests that doxorubicin is an unsuitable candidate

for not just for force-mediated drug delivery demonstration but also for most drug delivery experiments involving DNA-Dox complexes.

### 4.3.2 MACROMOLECULAR ENCAPSULATION INSIDE DMCs

Dextran is polysaccharides that are biologically inert due to their uncommon poly-( $\alpha$ -D-1,6-glucose) linkages. Dextran is a complex branched polysaccharide derived from glucose with low toxicity and low immunogenicity. Fluorescently labelled dextrans in particular are commonly used in experiments to visualize cellular uptake. Dextrans can readily enter cells through a combination of receptor-mediated endocytosis and pinocytosis. Dextrans have also been shown to be encapsulated within DNA nanostructures by thermally annealing it together and kinetically trapping it non-covalently inside nanostructures. DMCs have an inner cavity that can hold cargoes of up to  $\sim 2.6$  nm radius which roughly corresponds to a globular protein

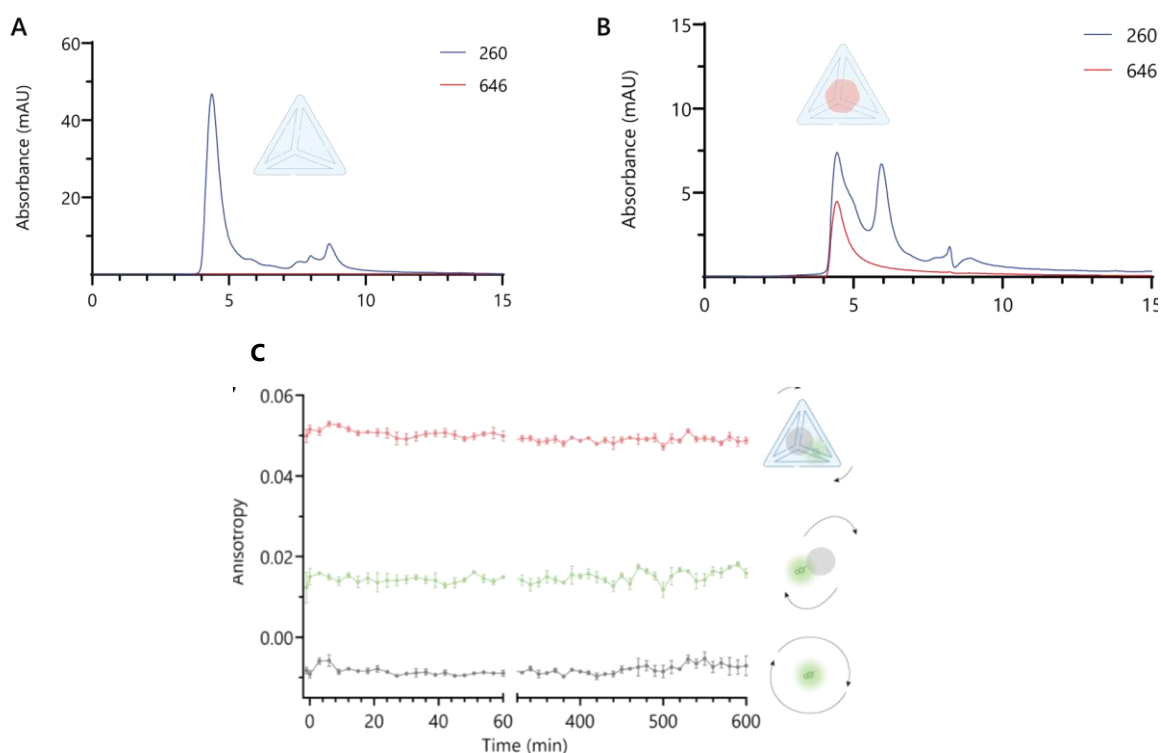


**Figure 4.3** Size exclusion chromatograph of a) DMC and b) DMC[Dex<sub>Cy5</sub>] Blue and Red indicate absorbance at  $\lambda = 260$  and  $\lambda = 646$  nm respectively. c) Fluorescence anisotropy of DMC[Dex<sub>488</sub>] (red line), free Dex<sub>488</sub> (green line) and free Alexa488 dye (gray line) over 10 hours ( $n = 3$ ).



of molecular weight 60 kDa. Since the commercially available dextrans are 6 kDa and 10 kDa dextrans, we used fluorescently labelled 10 kDa dextrans (radius  $\sim 2.3$  nm<sup>45</sup>) as a proof-of-concept for encapsulation.<sup>40</sup> Encapsulation of dextran was achieved by annealing the DMC oligonucleotide strands with the dextran cargo and removing the excess using a 30 kDa size-exclusion cutoff filter given the 60 kDa of the cargo (Figure 4.4).

To confirm the encapsulation of the dextran inside the DMC, size exclusion chromatography of the Dex<sub>Cy5</sub> loaded into the DMC (DMC<sub>39pN</sub> [Dex<sub>Cy5</sub>]) was performed. It was found out that the DMC<sub>39pN</sub> [Dex<sub>Cy5</sub>] had the same retention time as an empty DMC, providing further evidence for cargo encapsulation (Figure 4.3). Dex<sub>Cy5</sub> had a much higher retention time indicating its small molecular weight. Further, the size exclusion chromatograph of DMC<sub>39pN</sub> [Dex<sub>Cy5</sub>] had a second peak after the initial peak without the Dye<sub>Cy5</sub> absorbance at 646 nm. This could potentially be DMCs or denatured structures without the dextran. When the peak was reinjected, it had identical retention time as DMC<sub>39pN</sub> and DMC<sub>39pN</sub> [Dex<sub>Cy5</sub>] indicating that it could be DMC that was initially unfolded during the purification steps and later folded by the time it was reanalyzed (Figure S2). Further evidence of encapsulation was derived by running DMC<sub>39pN</sub> [Dex<sub>Cy5</sub>] structures on agarose gels with controls (Figure 4.4). Briefly, DMC<sub>39pN</sub> [Dex<sub>Cy5</sub>] structures were run with DMC, Dye<sub>Cy5</sub>, DMC<sub>39pN</sub> + Dex<sub>Cy5</sub> and unpurified DMC<sub>39pN</sub> [Dex<sub>Cy5</sub>] among other controls. DMC<sub>39pN</sub> [Dex<sub>Cy5</sub>] had no change in mobility compared to DMCs that were run in the gel. Further, purified DMC<sub>39pN</sub> [Dex<sub>Cy5</sub>] had excess Dye<sub>Cy5</sub> that was not removed in the initial purification.

To further confirm encapsulation and test stability we used fluorescence anisotropy which can distinguish between encapsulated and free cargo. Fluorescence anisotropy showed distinct values that identified free Alexa488 ( $r = -0.08$ ), Alexa488 conjugated dextran (Dex<sub>488</sub>;  $r = 0.015$ ), and Dex<sub>488</sub> encapsulated in DMC (DMC[Dex<sub>488</sub>];  $r = 0.049$ ) (Figure 4.3). Importantly, we observed no change in anisotropy over 10 hours indicating the exceptional stability of cargo-encapsulated DMCs. To obtain the optimal encapsulation and purification protocol, DMCs were annealed with varying concentrations of dextrans and were run on agarose gels. A maximal encapsulation efficiency of 44% could be achieved when the DMCs at 200 nM were annealed in the presence of 0.2 mM concentration of Cy5-labelled dextran. Although this

protocol produces a higher cargo loading it requires multiple rounds of purification to remove the excess Cy5 labelled dextran (Figure S3). Hence, to strike a balance between encapsulation and purification a concentration of 10  $\mu\text{M}$  for fluorescent dextran was used for annealing DMCs at 200 nM.

After confirming the products of cargo-loaded DMCs, they were tested for their functionality in the presence of a macromolecular cargo. This was achieved by engineering a DMC with a toehold FB strand with BHQ2 and by synthesizing a Cy3B modified dextran ( $\text{Dex}_{\text{Cy3B}}$ ). By loading this toehold DMC with  $\text{Dex}_{\text{Cy3B}}$  ( $\text{DMC}[\text{Dex}_{\text{Cy3B}}]$ ) and upon adding an invading strand (1 mM) complementary to the FB strand, a rapid (<10 min) increase in fluorescence was noted confirming the toehold exchange threaded out the FB strand along with the BHQ2. This leads to dequenching of the  $\text{Dex}_{\text{Cy3B}}$  that was encapsulated inside the DMC (Figure 4.4). This data confirms that  $\text{Dex}_{\text{Cy3B}}$  is loaded inside and the rapid functional response of DMCs. Taken

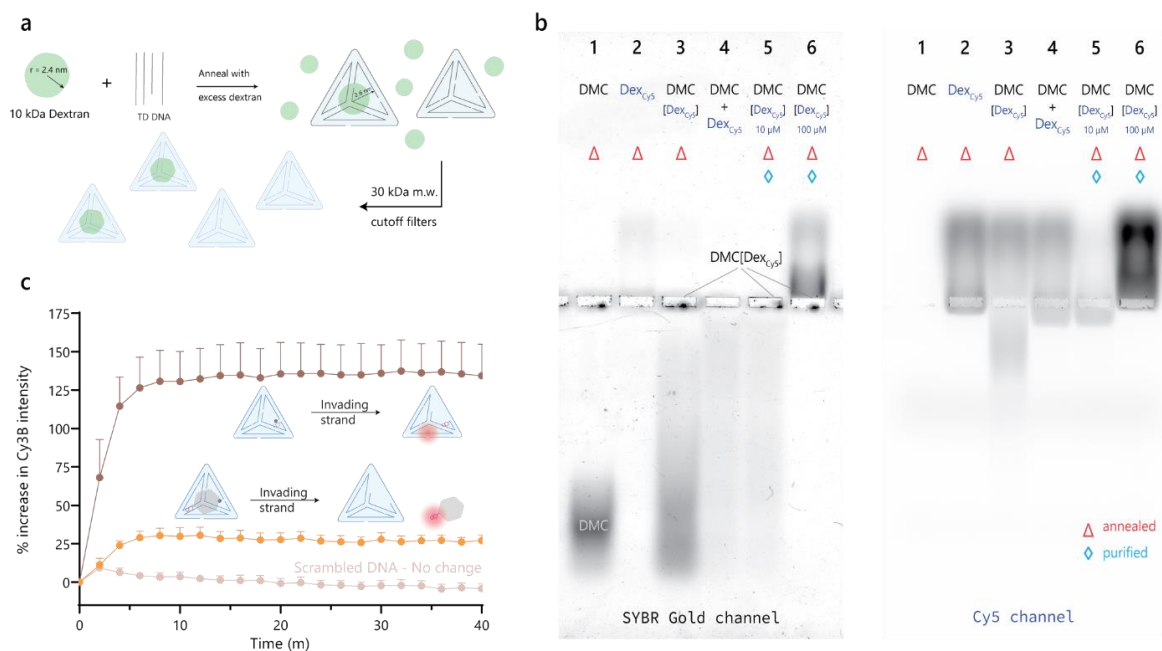


**Figure 4.4** (a) Assembly and purification protocol for the dextran encapsulated DMCs. (b) Validating Cy5-labelled dextran ( $\text{Dex}_{\text{Cy5}}$ ) encapsulation in DMCs. Lane 1: DMC. Lane 2:  $\text{Dex}_{\text{Cy5}}$ . Lane 3: DMC and  $\text{Dex}_{\text{Cy5}}$  annealed ( $\Delta$ ) together Lane 4: DMC and  $\text{Dex}_{\text{Cy5}}$  annealed separately and mixed Lane 5: DMC and  $\text{Dex}_{\text{Cy5}}$  annealed together at  $10 \mu\text{M}$  and purified ( $\diamond$ ) using 30 kDa filters. Lane 6: DMC and  $\text{Dex}_{\text{Cy5}}$  annealed together at  $100 \mu\text{M}$  and purified (c) Toehold mediated release of  $\text{Dex}_{\text{Cy3B}}$  from DMC with BHQ2 (orange dots), DMC with Cy3B and BHQ2 without encapsulated dextran (brown dots, positive control), Cy3B release from DMC with BHQ2 in the presence of a scrambled invader (beige dots, negative control)

together, our data shows that DMCs can retain cargoes with minimal leakage and are thus appropriate for force-activated delivery applications.

### 4.3.3 MACROMOLECULAR ENCAPSULATION INSIDE DMCs

Initial delivery of macromolecules was tested with DMC<sub>39pN</sub> using two 10kDa dextrans that were labeled using either Cy5 or Atto647N. These DMCs were then attached to TCO surfaces and then seeded with NIH 3T3 cells and the uptake of was then quantified using flow cytometry (Figure S4). As expected Atto647N labeled dextrans produced better signal than their Cy5 counterpart due to their increased hydrophobicity and high quantum yield. Then the Dex647N encapsulation in DMCs was done at lower concentrations than the initial 10  $\mu$ M to estimate the minimum detection threshold in cells on flow cytometer. As the encapsulation concentration decreased the uptake by the cells decreased and fell below the detection threshold (Figure S4). Hence, the concentration of 10  $\mu$ M of Atto647N labeled dextrans were used for encapsulation and releases from DMCs.

It was noted during uptake experiments that free, unencapsulated dextrans nonspecifically bind to the TCO functionalized surfaces. DMC<sub>39pN</sub> and Dex<sub>Cy5</sub> were separately subjected to the annealing protocol and were added together to TCO functionalized surfaces. The surface intensity of the Dex<sub>Cy5</sub> was much higher than the DMC<sub>39pN</sub> [Dex<sub>Cy5</sub>] indicating that the Dex<sub>Cy5</sub> can nonspecifically bind to the TCO surface when they are not anchored through a DMC. Since the nonspecific dextrans could be uptaken by cells various passivation methods were screened to minimize the dextran binding to surfaces (Figure S5). It was found that reducing the hydrophobicity of the surfaces by adding PEG linkers to the TCO handles reduced dextran binding. Unfortunately, longer linkers also reduced the DMC density on the surfaces. Hence to avoid lower DMC density, TCO-PEG<sub>4</sub> was chosen as the optimal linker length for further experiments.

Size based purification can produce lower DNA yields which can also hamper the ligand density on TCO surfaces. It was estimated that about ~50% of the DNA nanostructures were lost during purification (Figure S5). Since purification is essential for removing free, unencapsulated dextrans, the surfaces needed to be supplemented with additional cRGD ligands for promoting healthy cell adhesion. TCO-PEG<sub>4</sub> surfaces were added with 10-30 nM concentrations of DCM<sub>39pN</sub> for increasing ligand densities. A 30 nM concentration was found

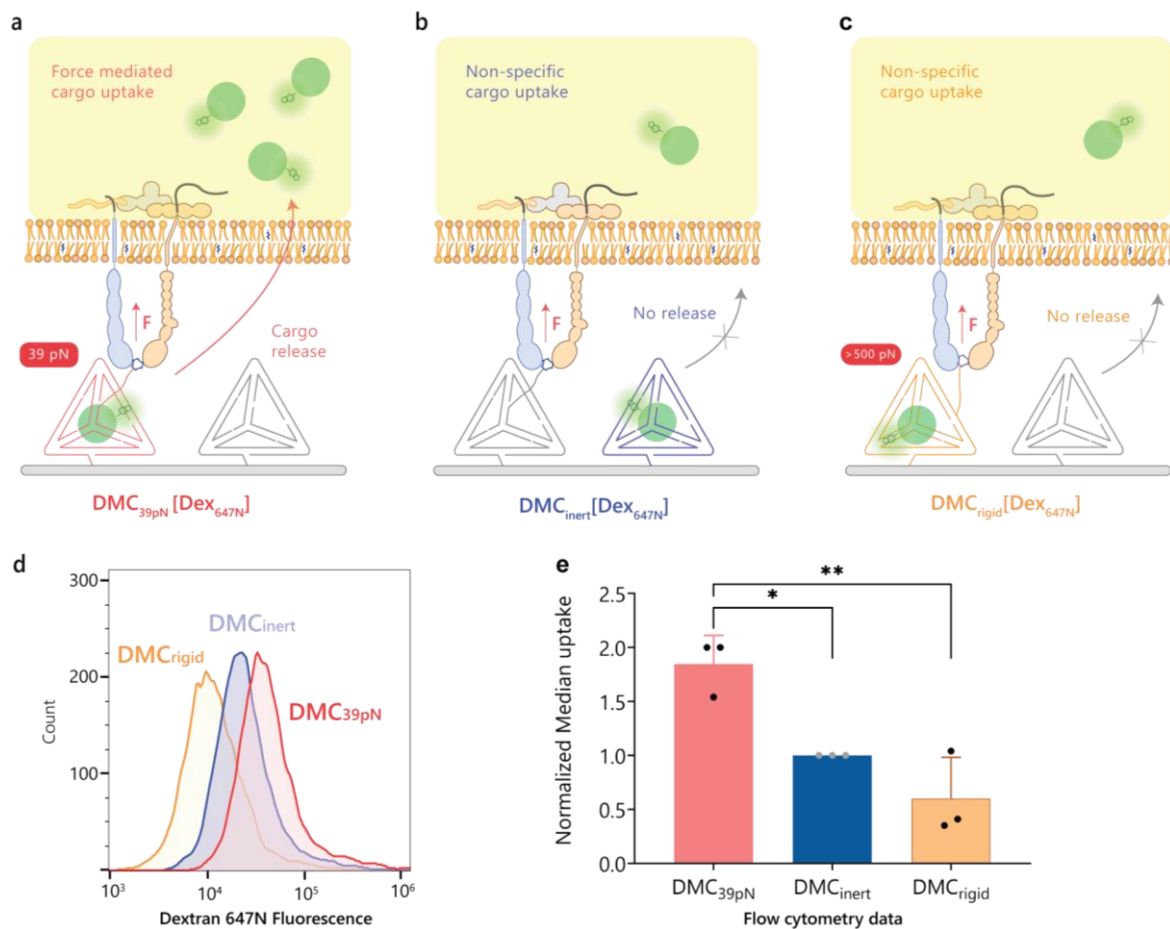


**Figure 4.5** (a-c) Schematics showing three binary surfaces used to validate force-induced uptake of dextran cargo. d) Representative flow histograms of HeLa cell uptake of Dex<sub>647N</sub> in 10% FBS DMEM media after 2 h. e) Normalized flow data from (d). The plot shows median fluorescence intensity (MFI) for HeLa cells on DMC<sub>39pN</sub> [Dex<sub>647N</sub>] + DMC<sub>inert</sub> (red), DMC<sub>inert</sub> [Dex<sub>647N</sub>] + DMC<sub>39pN</sub> (blue), and DMC<sub>rigid</sub> [Dex<sub>647N</sub>] + DMC<sub>inert</sub> (orange) surfaces. Data normalized to the DMC<sub>inert</sub> group ( $n=3$ ). \*\* $P=0.0069$ , \* $P=0.0269$ . All error bars indicate SEM from three replicates and each data point is the MFI from a single flow cytometry experiment.

to reduce surface density inconsistencies and ideally suited for the force-mediated uptake of dextrans from DMCs (Figure S6).

To emulate delivery of macromolecular cargo to cells exerting high integrin forces, we grafted surfaces with DMCs encapsulating Atto647N dextrans (DMC[DeX<sub>647N</sub>]). To distinguish between nonspecific DMC degradation and force-mediated release we used a mixture of DMCs as follows: 1) DMC<sub>39pN</sub> [DeX<sub>647N</sub>] + DMC<sub>inert</sub> to quantify force-mediated delivery 2) DMC<sub>inert</sub> [DeX<sub>647N</sub>] + DMC<sub>39pN</sub> to measure non-specific cargo delivery and 3) DMC<sub>rigid</sub> [DeX<sub>647N</sub>] + DMC<sub>inert</sub> to measure uptake when DMC are clamped closed (Figure 4.5). The choice of binary mixtures of DMCs ensured that the surfaces have identical RGD and DMC density thus offering a chemically identical surface for anchoring RGD groups while displaying differential response to force.

HeLa cells were seeded to these surfaces having 10% FBS in DMEM and the uptake of dextran was measured by running flow cytometry after 2 hours. We performed the force-induced uptake measurement at the 2 hour time point because prior work showed DNA tension signal

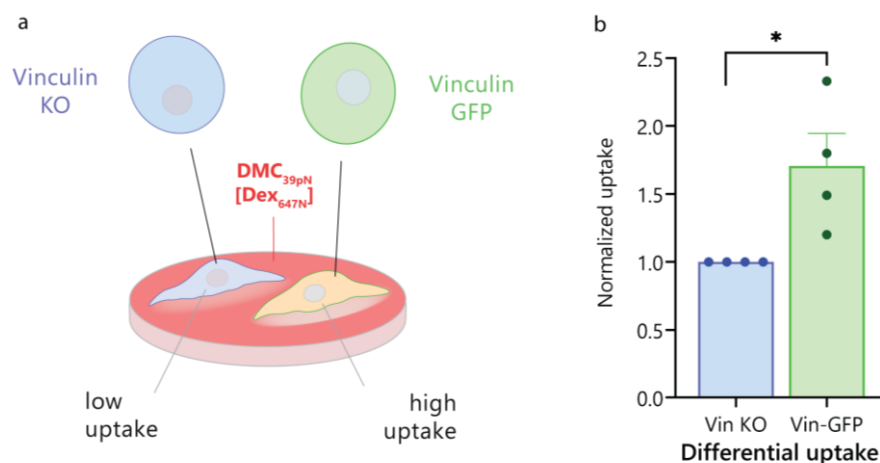


**Figure 4.6** (a) Schematic of a co-culture of VinKO and Vin-GFP MEF cells on the same DMC<sub>39pN</sub> [DeX<sub>647N</sub>] surface. (b) Normalized uptake from the VinKO and Vin-GFP MEF cell co-culture. Each data point was the MFI from a single flow cytometry experiment. Data normalized to the VinKO group ( $n=4$ ).  $*P= 0.0267$ . All error bars depict SEM.

30-90 min after cell seeding on a substrate<sup>10,46</sup> (Figure S7). We observed that the force-mediated uptake of Dex<sub>647N</sub> (group 1) was ~2-fold or greater than that of the controls (group 2 and 3). These data confirm that DMCs respond to cellular forces by mechanical denaturation and suggests the feasibility of releasing encapsulated cargo.

We also wanted to evaluate the collateral uptake into cells with low force among a high force cell population. To measure collateral uptake, we co-cultured MEF cells expressing GFP-tagged vinculin (Vin-GFP) and MEF cells with vinculin knocked out (VinKO) on a surface functionalized with DMC<sub>39pN</sub>[Dex<sub>647N</sub>]. We observed that MEF cells that express vinculin (high force phenotype) had 2-fold higher uptake compared to MEF cells without vinculin (low force phenotype) (Figure S8). Taken together, the data demonstrates that the uptake was predominantly due to cell receptor forces and specific to cell population with receptor forces higher than the DMC force threshold.

#### 4.3.4 DMCs FOR FORCE-RESPONSIVE RNA KNOCKDOWN.

We then aimed to demonstrate mechanically triggered delivery of nucleic acid therapeutics to cells. In principle, this approach could be used to target specific cells that display high traction forces which is often associated with invasive cancer cells.<sup>47,48</sup> Mechanically-mediated delivery could augment conventional targeting strategies that employ cancer biomarkers such as folate receptors<sup>49</sup> and HER2<sup>50</sup> receptors. Here we employed an antisense oligonucleotide (ASO) drug that inhibits the mRNA encoding for hypoxia-inducible factor 1 $\alpha$  (HIF1 $\alpha$ ) which is a transcription factor that activates an array of genes under hypoxic conditions.<sup>51</sup> Importantly, HIF1 $\alpha$  is a key gene that aids in cancer cell survival and HIF1 $\alpha$  ASOs were in clinical trials to

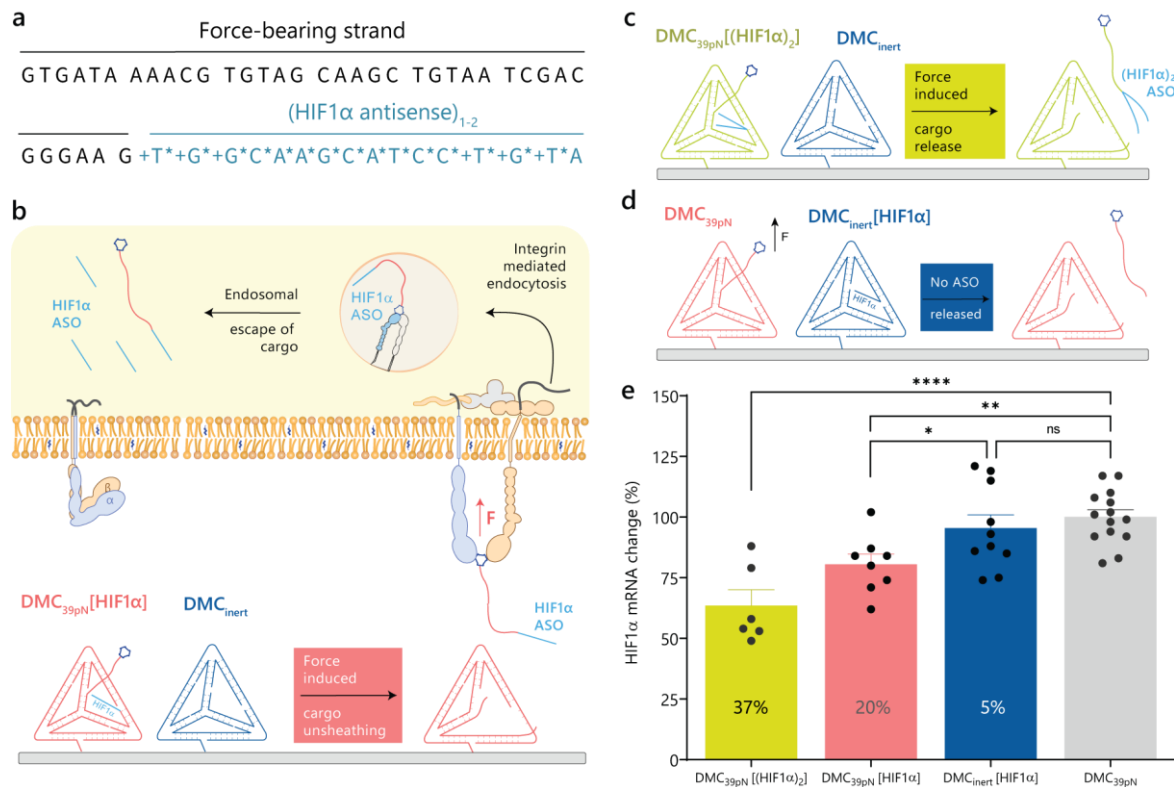


**Figure 4.7** a) DNA sequence of RGD conjugated force-bearing strand linked to the HIF1α ASO (blue) with LNA (+) and PS modifications (\*). (b) Schematic of force-induced unsheathing of HIF1α ASO from DMC<sub>39pN</sub> [HIF1α] which can then be taken up into cells by endocytosis of the integrin-cRGD-HIF1α ASO complex. (c and d) Schematics of force-induced unsheathing of two HIF1α ASOs from DMC<sub>39pN</sub> [(HIF1α)<sub>2</sub>] and control experiment with DMC<sub>39pN</sub> where release of HIF1α ASO is placed in the DMC<sub>inert</sub> [HIF1α] and is decoupled from the force-induced rupture. (e) Plot of HIF1α mRNA levels quantified with RT-qPCR. The data is plotted as percent change compared to cells cultured on DMC<sub>39pN</sub> after 24 hrs. Each dot represents a single surface, and each group was replicated at least three times. The error bar represents SEM. Individual *P* values - \*\*\*\**P*<0.0001, \*\**P*=0.0034, \**P*=0.0310, ns – not significant. HIF1α mRNA levels were measured relative to 18S mRNA.

treat solid tumors<sup>42</sup> and also for hepatocarcinoma.<sup>52,53</sup> Hence, we conjugated this ASO to the FB strand of DMC<sub>39pN</sub> to construct the HIF1α interwoven DMC<sub>39pN</sub> [HIF1α] and DMC<sub>39pN</sub> [(HIF1α)<sub>2</sub>] (Figure 4.7) which have close to 100% drug encapsulation efficiencies due to covalent conjugation. The DMC<sub>39pN</sub> [HIF1α] and DMC<sub>39pN</sub> [(HIF1α)<sub>2</sub>] liberate one and two ASOs respectively. The release occurs in a force-induced manner which will likely be endocytosed by integrin recycling pathways<sup>54,55</sup> as the ASOs are covalently linked with the integrin-binding RGD peptide (Figure 4.7).

To control for non-specific release, DMCs were designed with ASOs linked to a strand adjacent to FB strand (DMC<sub>inert</sub> [HIF1 $\alpha$ ]) which would not release upon force application (Figure 4.6). To maintain identical surface densities of DNA and RGD the DMCs were formulated as a binary mixture: 1) DMC<sub>39pN</sub> [(HIF1 $\alpha$ )<sub>2</sub>] + DMC<sub>inert</sub> 2) DMC<sub>39pN</sub> [HIF1 $\alpha$ ] + DMC<sub>inert</sub> 3) DMC<sub>inert</sub> [HIF1 $\alpha$ ] + DMC<sub>39pN</sub>. HeLa cells were cultured on these DMC grafted surfaces with an initial 6-hour serum starvation phase followed by 10% serum addition and growth. The mRNA levels of these cells were then quantified using RT-qPCR after 24 hours. The force responsive DMC<sub>39pN</sub> [(HIF1 $\alpha$ )<sub>2</sub>] and DMC<sub>39pN</sub> [HIF1 $\alpha$ ] produced a 37 $\pm$ 8% and 20 $\pm$ 7% knockdown of HIF1 $\alpha$  RNA levels, respectively, whereas the unresponsive DMC<sub>inert</sub> [HIF1 $\alpha$ ] had almost no change in mRNA levels (~5% reduction) compared to cells cultured on a DMC<sub>39pN</sub> (Figure 4.6). Taken together these results demonstrate the capabilities of DMCs in releasing cargo to diseased cells specifically to those displaying high receptor force phenotypes. Importantly, these experiments represent a proof-of-concept demonstration and virtually any validated ASO or approved drug could be delivered using DMCs in a mechanically selective manner.



## 4.4 Conclusion

The DMC nanostructure platform is modular and can be programmed to rupture at tunable force magnitudes in the piconewton regime to release a wide variety of cargoes to cells. The novelty of the approach rests on drug activation using mechanical cues that are innately generated by cells as opposed to the precedent of using physical cues such as ultrasound, thermal, optical, and magnetic actuation which are not a unique marker of the disease state. The noncovalent encapsulation of cargo can easily be achieved in DMCs as demonstrated using size exclusion and gel electrophoresis with the 10 kDa dextran as the model cargo. Anisotropy and fluorescence microscopy measurements confirm that DMCs are robust delivery vehicles with high stability, and triggerable cargo release on demand. Force-specific delivery of fluorescently labeled dextran as a macromolecular model cargo to cells was demonstrated in flow cytometry experiments. Dextran was used as a scaffold to load fluorophores in DMC and in principle a wide variety of small molecules conjugated to dextran can be encapsulated using the same strategy. This is a viable strategy for the delivery of drugs such as doxorubicin which cannot be delivered using non-covalent intercalation methods. Further such a technique allows for fluorescent tagging of cells based on their mechanical forces which can be analyzed and manipulated in high throughput for downstream applications. DMCs have chemo-mechanical selectivity and can discriminate cells even in a mixed population. Using a coculture of MEF cells with Vin-GFP and Vinculin knocked out cell lines it was shown that DMCs can discriminate cell types based on their mechanical phenotype.

We also demonstrated a complementary strategy of creating covalently encapsulated drug molecules that can be released from the DMC in response to mechanical inputs which leads to a 7.4-fold differential between force responsive and inert DMCs in triggering knockdown of mRNA. Another key advantage of mechanically mediated delivery is that the total concentration of the drug is massively reduced. For example, we estimate that only femtomoles of the ASO drug are immobilized on the chip surface and generating this magnitude of knockdown from DMC<sub>39pN</sub>[HIF1 $\alpha$ ] and DMC<sub>39pN</sub>[(HIF1 $\alpha$ )<sub>2</sub>] would require bulk ASO concentration of ~50 nM and ~100 nM, respectively. This represents a 1000-fold reduction in the amount of required drug because the delivery is highly localized (Figure S9).

It is important to state that in order to use our force-induced drug delivery strategy *in vivo*, DMCs must be tethered to the ECM. There are existing strategies to target peptide and antibody drugs to the ECM<sup>56-59</sup> and these approaches suggest feasibility. Taken together, our results demonstrate that DMCs can be used to deliver therapeutic cargo in a force selective manner to target cells with specific biophysical phenotypes.

## 4.5 Methods

All Oligonucleotides and primers for RT-qPCR were custom-synthesized (Table S2 and S3) by Integrated DNA Technologies (Coralville, IA, USA). The cRGDfK peptide (PCI-3696-PI) was purchased from Vivitide (MA, USA). Agarose gels were visualized on Amersham Typhoon laser scanner (Cytiva, Marlborough, MA, USA). Gels were run on a Bio-Rad Powerpac Basic Electrophoresis Supply (Hercules, CA, USA). P2-gels (1504118) were acquired from Bio-Rad (Hercules, CA, USA). TCO-NHS, TCO-PEG<sub>4</sub>-NHS, Methyltetrazine-PEG<sub>4</sub>-azide, Tris-hydroxypropyl triazolyl methylamine (THPTA, 1010-100) and Methyltetrazine-PEG<sub>4</sub>-NHS ester were obtained from Click chemistry tools (Scottsdale, AZ). Azido acetic NHS ester was obtained from BroadPharm (San Diego, CA). ATTO chambers, SMCC (22360), 6× Loading dye (R0611), Bond-Breaker TCEP Solution (77720), 10 kDa amino dextran (D1860) were obtained from ThermoFisher Scientific (Waltham, MA, USA). Amicon Ultra-0.5 mL Centrifugal Filters 30 KDa (UFC503096), Atto 647N NHS ester (18373-1MG-F) were purchased from Millipore Sigma. N,N-dimethylformamide (DMF, 227056), N,N-diisopropylethylamine (DIPEA, 496219), (3-Aminopropyl)triethoxysilane (APTES, 440140, 99% purity), sodium L-ascorbate (A4034-100G), 1-Methyl-2-pyrrolidinone (328634), were purchased from Sigma-Aldrich (St. Louis, MO, USA). Cy3B-NHS ester (PA63101) was purchased from GE Healthcare Life Sciences. Fetal Bovine Serum (35-015-CV), Penicillin–Streptomycin (30-002-CI), Trypsin EDTA (25-053-CI), DMEM (45000-336) from Corning (Tewksbury, MA, USA). Triethylamine Acetate (TEAA, 2.0 M) solution was purchased from Glen Research. Flow cytometry was performed on Beckman Coulter Cytoflex (Pasadena, CA, USA). PerfeCTa SYBR Green FastMix, ROX (95073-05K) was purchased from VWR. RNeasy Mini Kit (74106) was purchased from Qiagen. qPCR was performed with the following: RNeasy Mini Kit from Qiagen (74106; Hilden, NRW, Germany), High-Capacity cDNA Reverse Transcription Kit from Applied Biosystems (4368814; Foster City, CA, USA), and PerfeCTa SYBR Green FastMix Reaction Mix from QuantaBio (101414-278 [VWR]; Beverly, MA, USA).

### 4.5.1 DMC annealing

All the strands of the DMC were prepared at a concentration of 200 nM and mixed with 100  $\mu$ L of 10x TM buffer which was then diluted to 1 ml. The DMCs were annealed at 10-100  $\mu$ L

volumes in a thermal cycler using the following annealing protocol: heat to 95°C in 2 mins; hold at 95°C for 5 mins; cool down to 4°C over 10 mins and then held at 4°C until it was added to the TCO functionalized surfaces. For dextran encapsulation, the DMCs were annealed with an excess of dye-labelled 10 kDa dextran (typically 10  $\mu$ M) using the following protocol: heat to 95°C in 2 mins; hold at 95°C for 5 mins; rapidly cooled down to 4°C and then held at 4°C.

#### 4.5.2 Agarose gel for DMC formation

1.75 g of agarose was dissolved in a conical flask with 1x TAE (50 ml) and was microwaved until its completely dissolved to produce a clear solution. It was allowed to cool for a few minutes and then 5  $\mu$ L of SYBR gold dye was added. It was then cast with a 15 well comb in the dark at r.t. for 2 hrs. The wells were loaded with 6  $\mu$ L of the sample (1  $\mu$ L of 6x loading dye + 5  $\mu$ L DNA sample) and was run at 100 V for 1 hr and visualized using SYBR gold stain.

#### 4.5.3 Trans cyclooctene-functionalization of glass slides

Glass slides were washed with water and then fried using freshly prepared piranha solution (30% v/v H<sub>2</sub>O<sub>2</sub> [9.8 M] in conc. H<sub>2</sub>SO<sub>4</sub>) for 30 min. The slides were washed with 18.2 M $\Omega$  water (x3) and then with ethanol (x3). The washed slides were immersed in 1% v/v (3-Aminopropyl) triethoxysilane in ethanol and stirred for 30 min. Slides were then washed with ethanol (x4) and then baked in a hot air oven for 60 min. TCO-NHS (trans cyclooctene) or TCO-PEG<sub>4</sub>-NHS ester in DMSO (~10 mM) was added to one glass slide (50  $\mu$ L TCO soln. for 25 mm circular slides; 200  $\mu$ L for 25 x 75 mm slides) and sandwiched with another glass slide on top and allowed to react for 12 hrs. Finally, the slides were washed with ethanol (x2) and mounted on ATTO chambers for use.

#### 4.5.4 DMC functionalization on TCO-glass slides

DMCs functionalized with a methyl-tetrazine on the anchoring strand were annealed at 200  $\mu$ M. TCO-functionalized glass circular coverslips were mounted on ATTO chambers after washing with ethanol. The mounted coverslips were then washed with 10 ml continuous flow

of 18.2 M $\Omega$  water, followed by 10 ml of 1x TM buffer. 50  $\mu$ L of annealed DMCs were added to the 1x TM on TCO surfaces (final DMC concentration  $\sim$  16 nM) and allowed to click in the dark at room temperature over 60-90 mins.

#### 4.5.5 Cell culture

NIH3T3 and NIH3T3 cells transfected with GFP-Paxillin were cultured in DMEM (10% CCS, 1% Penicillin-Streptomycin) at 37°C in an incubator with humidified 5% CO<sub>2</sub> atmosphere. MEF, HeLa and MDA-MB-231 cells were cultures under similar conditions but with 10% FBS DMEM and 1% Penicillin-Streptomycin. MCF-10A cells were cultured using Mammary Epithelial Cell Growth Medium supplemented with 100 ng/ml cholera toxin and BulletKit from Lonza. MCF-7 cells were grown in 10% FBS DMEM and 1% Penicillin-Streptomycin added with 0.01 mg/ml human recombinant insulin. Cells were cultured as per ATCC specifications and passaged either using 0.25% trypsin (5 min) or 50 mM EDTA in 1x PBS (10 min) and reseeded in a new flask with suitable media at lower density.

#### 4.5.6 Purification of DMCs using M.W. cut-off filters:

DMCs (20-100  $\mu$ L) were annealed with excess dextrans and diluted to 500  $\mu$ L in 1x TM buffer. Then it was transferred to a 30 kDa M.W. cut-off filter and centrifuged at 14,000 $\times$ g for 5 mins. The filters were then added with 500  $\mu$ L of 10x TM buffer and centrifuged (x3). Then the filters were added with  $\sim$ 200  $\mu$ L of 1x TM buffer, inverted and centrifuged at 200 $\times$ g. The purified DMCs were then used for further experiments.

#### 4.5.7 Fluorescence anisotropy

DMCs (100 nM) were each were annealed with excess Atto488-labelled 10kDa dextran (100  $\mu$ M) and filtered using 30 kDa filter. Atto488-labelled 10kDa dextran were purified using 3kDa filters to remove free Atto488 dye. The purified products were subjected to a second round of M.W. cut-off filtration to ensure high purity. The concentrations of the free dye, labelled dextran, DMC[Dex<sub>488</sub>] were all diluted to be 200  $\mu$ L at 12.5 nM. To correct for background

anisotropy, 1x PBS was used as blank. The fluorescence anisotropy was recorded using a Synergy H1 Biotek Plate Reader (VT, USA) at r.t. over 10 hrs.

#### 4.5.8 Toehold strand displacement

##### 4.5.8.1 Rupturing DMCs in solution

DMCs with toehold and BHQ2 were annealed with 100  $\mu\text{M}$  of Cy3B labelled dextrans. The DMCs were purified twice using M.W. cut-off filters and then challenged with an invader strand (final conc. 1  $\mu\text{M}$ ) in solution and the change in fluorescence was read using a plate reader.

##### 4.5.8.2 Size exclusion chromatography

DMCs (200 nM) were mixed with Cy5 labelled dextrans (40  $\mu\text{M}$ ) and annealed to encapsulate the dextrans. The DMC[Dex<sub>Cy5</sub>] were then purified as mentioned above using 150 mM phosphate buffer. The purified DMCs were then injected into a size exclusion HPLC column (SEC-130) with 150 mM phosphate buffer at 0.3 ml/min as an eluent.

#### 4.5.9 Fluorescence microscopy

##### 4.5.9.1 Imaging non-force mediated degradation

DMCs (50  $\mu\text{L}$ ) each were annealed separately, mixed and clicked directly to 550  $\mu\text{L}$  of 1x TM TCO surfaces. After 1.5 hrs the chambers were washed with 10 ml of DMEM (with 1% P/S, 0% FBS and no phenol red). HeLa cells ( $5.0 \times 10^4$ ) were seeded to DMC grafter coverslips and allowed to spread for 1 hr. It was then imaged at room temperature ( $\sim 5$  min) in RICM and Cy5 channels. The images were quantified using ImageJ2 software as described below. The intensity loss below each cell was normalized to its background.

##### 4.5.9.1 Image analysis

Fluorescence images were processed using the ImageJ2 software. The fluorescence background around a cell was averaged and subtracted from the whole image. Cell spreading

was measured by the total area of cell as observed in RICM. Fluorescence from tension probes or GFP-Paxillin was measured within the cell spread area. Brightness and contrast of microscopy images were adjusted for clearness.

#### 4.5.10 Flow cytometry

##### 4.5.10.1 Force-specific dextran uptake measurements using different DMCs

Binary mixture of DMCs were (50  $\mu$ L) each were annealed and filtered using 30 kDa M.W. cut-off filters. Then they were mixed with an additional 150  $\mu$ L of DMC<sub>39pN</sub> (200 nM) to compensate for losses from purification and to promote cell adhesion. The mixture of DMCs were allowed to click to TCO-PEG<sub>4</sub> surfaces in 1x TM for about 1 hr and then washed with 10% FBS DMEM (with 1% Penicillin-Streptomycin and no phenol red). To the surfaces, HeLa cells ( $2.5 \times 10^4$ ) were seeded to DMC grafted coverslips and allowed to attach for 2 hrs. The cells were then detached from the surfaces using 0.25% trypsin and centrifuged along with the growth media in the chambers at  $400 \times g$  for 3 mins at 4°C. The cells were washed (x3) in DPBS (without Ca<sup>2+</sup> and Mg<sup>2+</sup>) and were resuspended in DPBS. The cells were analyzed using a flow cytometer for to measure the uptake of Atto647N labelled dextrans. The data was analyzed and histograms were prepared using FlowJo software (FlowJo LLC, USA).

##### 4.5.10.2 Differential cargo uptake in a co-culture of high and low force MEF cells

DMC<sub>39pN</sub> [Dex<sub>647N</sub>] were (50  $\mu$ L) each were annealed and filtered using 30 kDa M.W. cut-off filters. Then they were mixed with an additional 150  $\mu$ L of DMC<sub>39pN</sub> (200 nM) to compensate for losses from purification and to promote cell adhesion. The mixture of DMCs were allowed to click to TCO-PEG<sub>4</sub> surfaces in 1x TM for about 1 hr and then washed with 10% FBS DMEM (with 1% Penicillin-Streptomycin and no phenol red). To the surfaces, MEF cells ( $2.5 \times 10^4$ ) were seeded to DMC grafted coverslips and allowed to attach for 2 hrs. The cells were then detached from the surfaces using EDTA (50 mM) and centrifuged along with the growth media in the chambers at  $400 \times g$  for 3 mins at 4°C. The cells were washed (x3) in DPBS (without Ca<sup>2+</sup> and Mg<sup>2+</sup>) and were resuspended in DPBS. The cells were analysed as above in 4.5.10.1

#### 4.5.11 Quantitative polymerase chain reaction (RT-qPCR)

ATTO chambers mounted with TCO surfaces were sterilized by placing them in tissue culture hood UV light for ~2 mins. DMCs were folded and clicked by adding directly to TCO surfaces in 550  $\mu$ L of 1x TM. After 1.5 hrs the chambers were washed with 5 ml of DMEM (with 1% Penicillin-Streptomycin, 0% FBS). HeLa cells detached using to 50 mM EDTA in 1x PBS were seeded to DMC functionalized glass surfaces ( $5.0 \times 10^4$  cells per surface) and allowed to adhere for 6 hr in the incubator at 37°C with 5% CO<sub>2</sub>. After 6 hrs media in chambers (~900  $\mu$ L) was supplemented with 100  $\mu$ L FBS and allowed the cells to grow for 18 hrs. After 24 hrs incubation, the media from the chambers were transferred to 1.5 mL tube cells the chambers were added with 500  $\mu$ L of 0.25% trypsin and incubated for 5 mins. The cells were detached and spun down at 800 $\times$ g for 1 min at 4°C. The cells were washed with 1 ml HBSS and resuspended in 300  $\mu$ L RLT buffer. The cell lysate was immediately used for downstream analysis or stored at -80°C. The cell lysates were added with 300  $\mu$ L 70% ethanol and transferred to Qiagen RNA Miniprep column. RNA was extracted from the lysate as per manufacturer's instructions and was transcribed using a High-capacity cDNA reverse transcription kit. HIF1 $\alpha$  mRNA levels were then quantified by RT-qPCR using PerfeCTa SYBR Green FastMix Reaction Mixes with a 0.25  $\mu$ M concentration of custom-designed primers for HIF1 $\alpha$  and 18S (efficiency ~2). The relative quantification of HIF1 $\alpha$  mRNA levels was performed using the  $\Delta C_t$  method with 18S rRNA as an internal control.

#### 4.5.12 Oligonucleotide modifications

##### 4.5.12.1 NHS-ester amine-DNA coupling

Amine modified DNA was dissolved in 10  $\mu$ L water (1 mM) and added with 2  $\mu$ L of 1 M NaHCO<sub>3</sub>. NHS-modified functional group was dissolved in 10  $\mu$ L DMSO (Cy3B-NHS, Atto647N-NHS, etc.) or 10  $\mu$ L acetonitrile (Methyltetrazine-NHS) or 40  $\mu$ L DMF/NMP (Succinimidyl-4-(N-maleimidomethyl) cyclohexane-1-carboxylate) to obtain a final concentration of 10-100 mM. These solutions were mixed and reacted at r.t. for 30-60 mins. The reaction was quenched with addition of 100  $\mu$ L water and was filtered with P2 gel to remove excess NHS reagent and purified using HPLC. Integrin ligand c(RGD)fk-(PEG<sub>2</sub>)<sub>2</sub>-NH<sub>2</sub>



can be functionalized in a similar manner by reacting it with azido acetic acid NHS in DMSO for 12 hours and directly purifying using HPLC.

#### 4.5.12.2 Thiol-SMCC conjugation protocol

Thiol DNA strand was dissolved (5  $\mu$ L) in 1x PBS at pH 6.8 to obtain a 1 mM concentration and then reduced with 100 equivalences of Tris (2-carboxyethyl) phosphine (0.5M) at room temperature for 15-20 mins. To this, 2 $\times$  equivalences of maleimide-functionalized DNA in 1 $\times$ PBS (10  $\mu$ L) was added at r.t. to react for 3-4 hrs. For the di-maleimide conjugation in the case of cRGD\_TD6-S3a\_(HIF1 $\alpha$ )<sub>2</sub>, 3-4 $\times$  equivalences of maleimide was used. The reaction mixture was filtered using P2 gel and purified by HPLC.

#### 4.5.12.3 Alkyne-azide conjugation

Alkyne functionalized DNA strand was dissolved in 5  $\mu$ L water to yield a 4 mM solution. Azide reagent (10 equivalences, 20 mM) dissolved in 10  $\mu$ L acetonitrile was added to this. In a separate tube, CuSO<sub>4</sub> (1 equivalence, 1  $\mu$ L), Tris (3-hydroxypropyltriazolyl methyl) amine (4 equivalences, 2  $\mu$ L), sodium ascorbate (2 equivalence, 1  $\mu$ L) and 1  $\mu$ L triethylamine were mixed. This was added to the Alkyne-azide mixture and reacted at r.t. for 60-90 mins. The reaction was quenched with addition of 100  $\mu$ L EDTA solution, filtered with 0.2  $\mu$ m filters and purified using HPLC.

#### 4.5.12.4 HPLC purification of peptide and oligonucleotides

Advanced oligonucleotide C18 column was used for the purification of chemically modified DNA. The column was run with 0.1 M TEAA in water as solvent A and acetonitrile as solvent B. DNA was purified using the following method, 10% for 3 minutes followed by 10-35% solvent B gradient over 25 min at 0.5 mL/min flow rate. Tetrazine conjugated DNA was purified using a similar method but using a 10-60% solvent B over 25 min at 0.5 mL/min. Peptides were purified using a Grace C18 column which was eluted with water as solvent A and acetonitrile as B both containing 0.05% TFA. A gradient of 10-40% solvent B over 30 min at 1 mL/min was used for peptide purification. Separated fractions were dried in a vacuum concentrator overnight. The purified oligonucleotide conjugates were reconstituted in 1x TE

buffer and were stored at  $-30^{\circ}\text{C}$ . The concentration of oligonucleotides and peptides were determined using its absorbance at 260 nm and 214 nm, respectively.

#### 4.5.13 Statistics

Quantitative results for experiments unless mentioned otherwise were presented as Mean  $\pm$  SEM. All statistical analysis was performed using GraphPad Prism software package. Statistical analyses were performed by the t-test or analysis of variance (ANOVA) tests. P values were corrected for multiple comparisons unless otherwise noted as individual P values. P values were considered significant if the tested P value was smaller than 0.05(\*), 0.01(\*\*), 0.001(\*\*\*), or 0.0001(\*\*\*\*).

## Appendix




**Table S02: Primer sequences used for RT-qPCR**

Primer sequences used for used for RT-qPCR. DNA strands were custom-synthesized by Integrated DNA Technologies (Coralville, IA, USA).

Name	Sequence
HIF1 $\alpha$ - forward primer	TAT GAG CCA GAA GAA CTT TTA GGC
HIF1 $\alpha$ - reverse primer	CAC CTC TTT TGG CAA GCA TCC TG
18S - forward primer	AGG AAT TGA CGG AAG GGC ACC A
18S - reverse primer	GTG CAG CCC CGG ACA TCT AAG

**Table 03: Oligonucleotides and chemical modifications used for DMCs**

DNA strands were synthesized by Integrated DNA Technologies. The modifications in the oligonucleotides are highlighted depending on the chemistry used for linking the functional group as follows: 1) Alkyne-azide copper click 2) SMCC-thiol 3) Amine NHS-ester 4) commercially available modification. The retention times of the modified strands are also provided wherever applicable.

Name	R <sub>t</sub> (min)	Sequence
TD1-S1a	—	CCAGGCAGTTGAGACGAACAT
TD1-S1b	—	TCCTAAGTCTGAAATTTATCACCCGCCATAGTAGACGTATCA
TD1-S2	—	AGCTTGCTACACGATTCAGACTTAGGAATGTTCTGA CATGCGAGGGTCCAATACCGACGATTAC
Cy3B_TD1-S3b	17.7	/Cy3B/ AGCATGCCCATCCACTACTATGGCGG
Tz_TD1-S4	13.7	/Tetrazine/ CTCGCATGACTCAACTGCCTGGTGATACGAGGATG GGCATGCTCTTCCCGACGGTATTGGACC
Tz_TD3-S4_cRGD	14.4	/Tetrazine/ CTCGCATGACTCAAC /cRGD/ GCCTGGTGATACGAGGATGGGCATGCTCTTCCCGACGGTATTGGACC
S3a Invader	—	CTTCCCGTCGATTACAGCTTGCTACACGTTTTATCA CTCTCTCTC
S3a toe BHQ	—	GAGAGAGA GTGATAAAACGTGTAGCAAGCTGTAATCGACGGGAAG /BHQ2/
S3a toehold	—	GAGAGAGA GTGATAAAACGTGTAGCAAGCTGTAATCGACGGGAAG
TD4-S1	—	CCAGGCAGTTGAGACGAACATTCCTAAGTCTGAAATTT ATCACCCGCCATAGTAGACGTATCA
TD4-S3	—	GTGATAAAACGTGTAGCAAGCTGTAATCGACGGGAAG AGCATGCCCATCCACTACTATGGCGG
cRGD_TD5-S3a_A647	16.3	/cRGD/ GTGATAAAACGTGTAGCAAGCTGTAATCGACGGGAAG /Alexa647/
cRGD_TD6-S3a_HIF1a	15.0	/cRGD/ GTGATAAAACGTGTAGCAAGCTGTAATCGACGGGAAG /Thiol/  +T*+G*+G*C*A*A*G*C*A*T*C*C*+T*+G*+T*A /SMCC/
TD7-S2	—	TAGGAATGTTTCGACATGCGAGGGTCCAATACCGA CGATTACAGCTAGCTACACG A TTCAGACT
cRGD_TD7-S3a	15.0	/cRGD/ GTGATAAAACGTGTAGC /T-NH <sub>2</sub> / A
Cy3B_TD7-S3b	17.0	/Cy3B/ GCTGTAATCGACGGGAAGAGCATGCCCATCCACTACTATGGCGG
cRGD_TD8-S3a	14.9	GTGATAAAACGTG /cRGD/ AGCT /T-NH <sub>2</sub> / A
TD8-S3a no mod	—	GTGATAAA A CGTGTAGCTA
HIF1a_SMCC	19.0	+T*+G*+G*C*A*A*G*C*A*T*C*C*+T*+G*+T*A /SMCC/
HIF1a_SH	—	+T*+G*+G*C*A*A*G*C*A*T*C*C*+T*+G*+T*A /Thiol/
HIF1a_TD1-S3b	15.9	+T*+G*+G*C*A*A*G*C*A*T*C*C*+T*+G*+T*A /Thiol/  /SMCC/ AGCATGCCCA TCCACTACTATGGCGG
TD5-S3a_A647	14.7	GTGATAAAACGTGTAGCAAGCTGTAATCGACGGGAAG /Alexa647/
cRGD_TD1-S3a	15.2	/cRGD/ GTGATAAAACGTGTAGCAAGCTGTAATCGACGGGAAG
cRGD_TD6-S3a_(HIF1a) <sub>2</sub>	18.0	/cRGD/ GTGATAAAACGTGTAGCAAGCTGTAATCGACGGGAAG /dithiol/  2x {+T*+G*+G*C*A*A*G*C*A*T*C*C*+T*+G*+T*A /SMCC/}

### Table 03 continued: Oligonucleotide modifications

DNA strand modifications used for the modification of DMCs. **Cy3B-NHS ester**, **SMCC**, **Alexa 647-NHS ester** and **Tetrazine-NHS ester** were used to modify amine terminus or T-nucleobase amine on DNA strands. **Tetrazine-N<sub>3</sub>** and **cRGD-N<sub>3</sub>** were used to modify alkyne terminus or alkyne on T- nucleobase. Other modifications are obtained commercially from Integrated DNA Technologies.

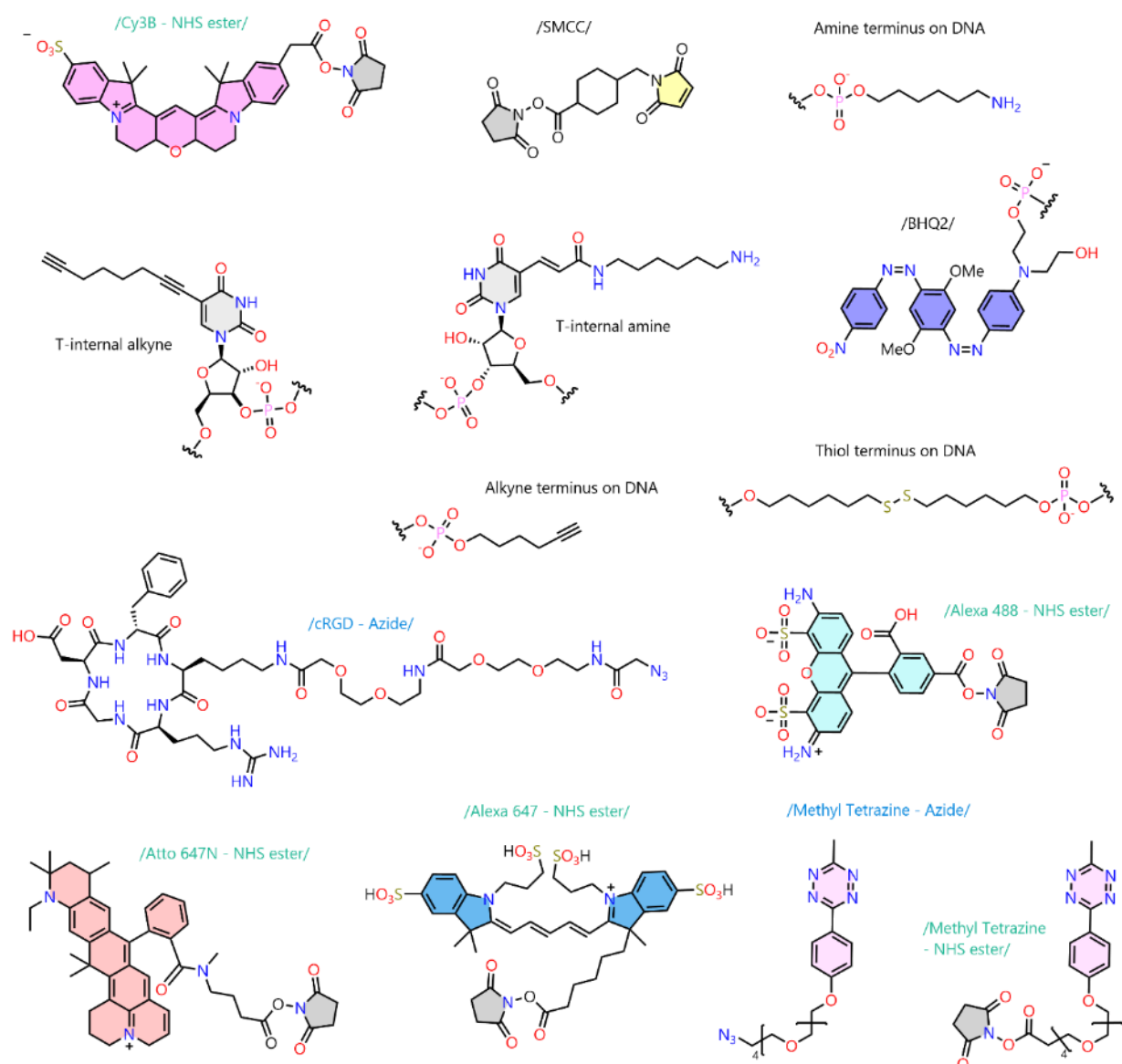


**Figure S1** (a) Schematic of DMC<sub>39pN</sub> [Dox] releasing Doxorubicin upon force-induced rupture. (b) NIH 3T3 cells grown on DMC<sub>39pN</sub> without any loaded doxorubicin and treated with Annexin V. Annexin V fluorescence indicates cells in apoptosis. (c) Cells treated with Dox from DMC<sub>39pN</sub> [Dox] loaded at 10  $\mu$ M. Gray images – RCM, Red images – Annexin V. The calibration bars accompanying the images indicate fluorescence values. Scale bars – 20  $\mu$ M.

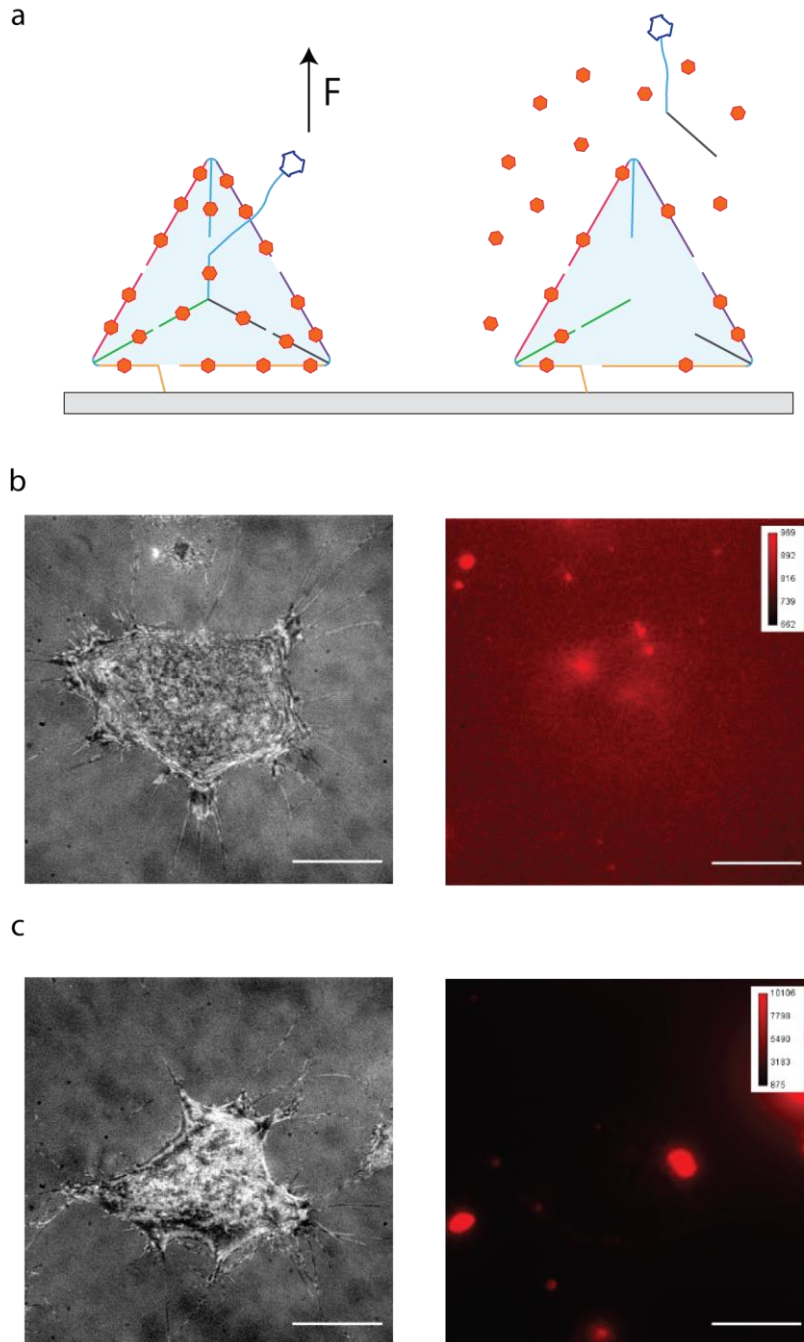


**Figure S2** Dextran encapsulated structures 100 nM DMC with 40  $\mu$ M Dex<sub>Cy5</sub> were analyzed using size exclusion chromatography after 30 kDa amicon filtration a) 10 kDa Dex<sub>Cy5</sub> analyzed using size exclusion chromatography b) reinjected peak without 260 nm absorbance from the purified DMC<sub>39pN</sub> [Dex<sub>Cy5</sub>] having retention time similar to the pure DMC<sub>39pN</sub>.

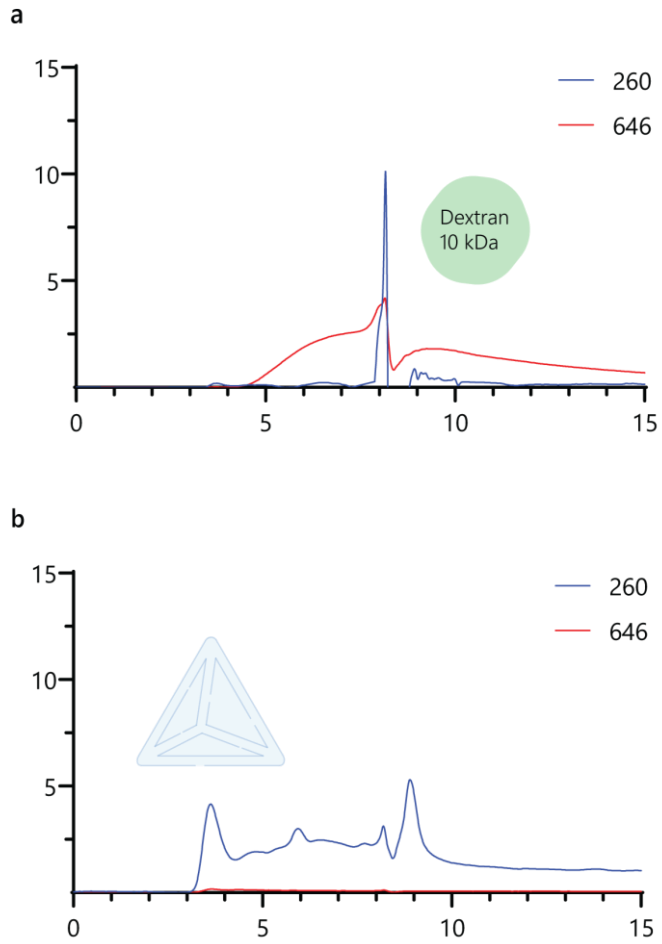


**Figure S3** Agarose gel (3.5%) ran with DMC and varying concentrations of Dex<sub>Cy5</sub> (Standard concentration - 200 nM Dex<sub>Cy5</sub>). Encapsulation (%) =  $100 \times \frac{I_{well}}{I_{standard}}$ , where I is the integrated intensity of the lane after background subtraction.





**Figure S4** a) Dextran 10 kDa conjugates  $\text{Dex}_{647\text{N}}$  (D10-A647N) and  $\text{Dex}_{\text{Cy5}}$  (D10-Cy5) at  $100 \mu\text{M}$  were trapped inside DMC at  $100 \text{ nM}$ . b) Optimal encapsulation concentration for uptake was tested by annealing DMCs with  $1 \mu\text{M}$  and  $0.1 \mu\text{M}$  of  $\text{Dex}_{647\text{N}}$ . Dextran at  $10 \mu\text{M}$  concentration worked well for  $\text{Dex}_{647\text{N}}$

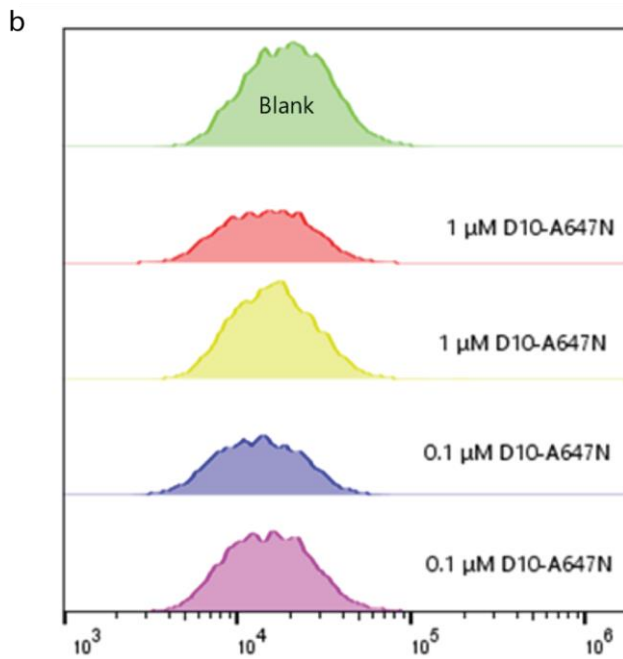
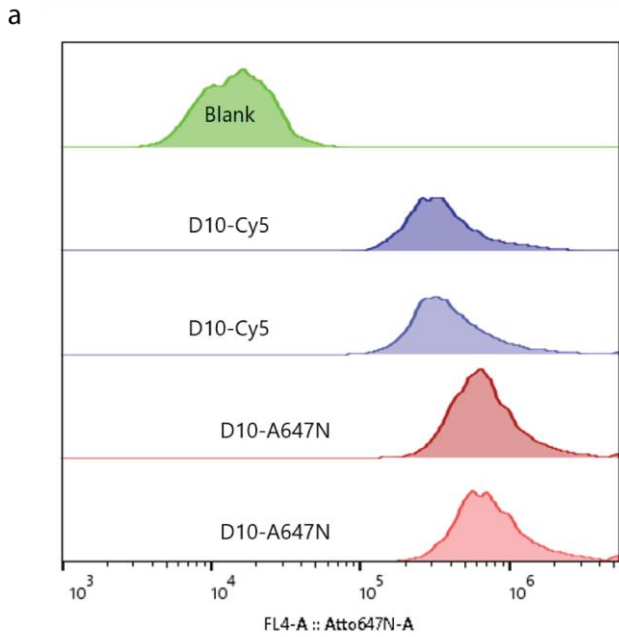


**Figure S5** a)  $DMC_{39pN}$  [ $Dex_{Cy5}$ ] were added to TCO surfaces.  $DMC_{39pN}$  and  $Dex_{Cy5}$  were separately subjected to the annealing protocol and were added together to TCO functionalized surfaces. b) Representative image of  $DMC_{39pN}$  [ $Dex_{Cy5}$ ] d)  $DMC_{39pN}$  and  $Dex_{Cy5}$  were annealed separately. The surface intensity of the  $Dex_{Cy5}$  was much higher than the  $DMC_{39pN}$  [ $Dex_{Cy5}$ ]. The TCO surfaces requires passivation to avoid this nonspecific binding. c) Binding of  $Dex_{Cy5}$  to various surfaces. D10 and BSA refers to TCO and PEG<sub>6</sub>-TCO surfaces passivated by adding unlabelled dextrans at 100 nM and 0.1% BSA respectively.

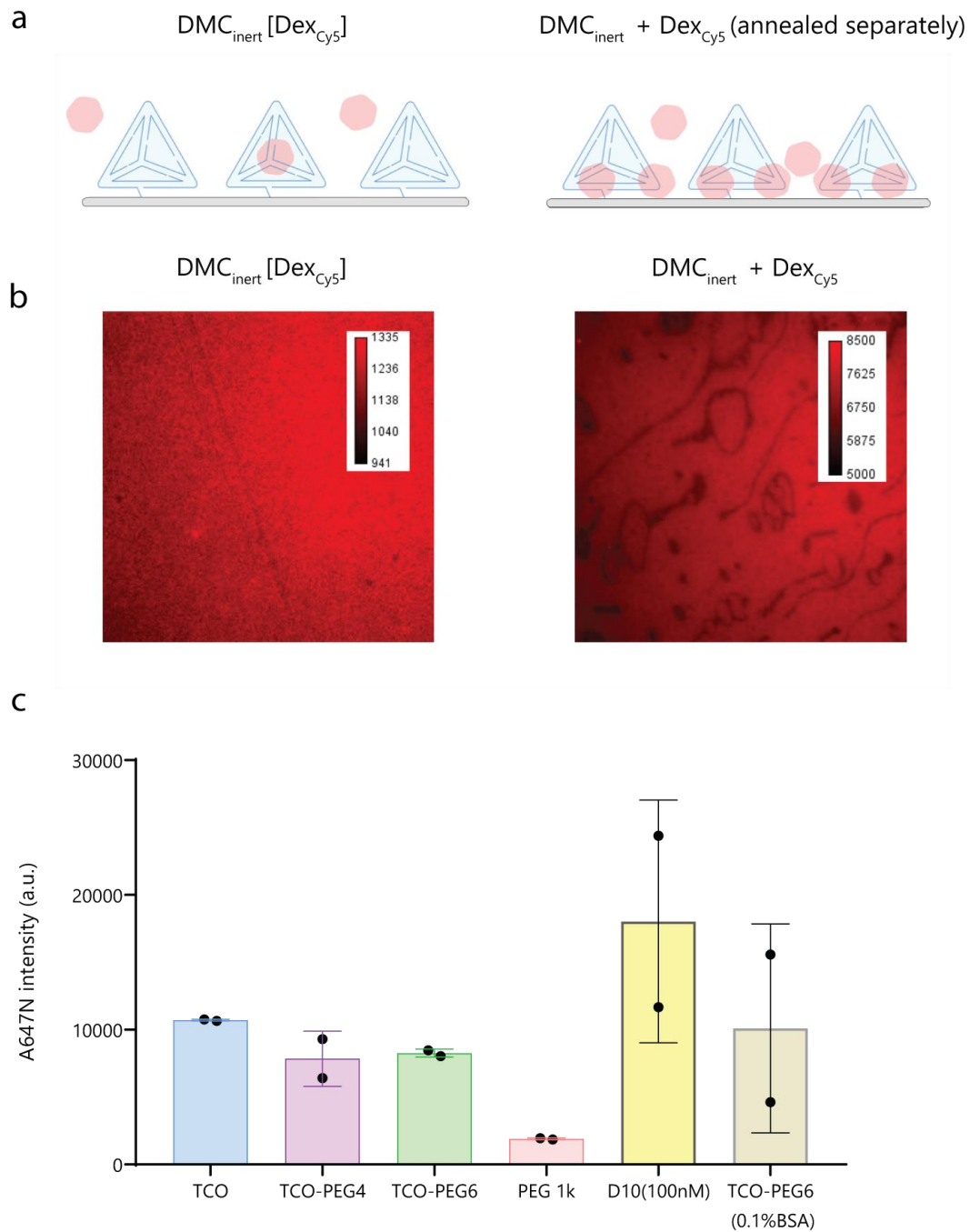


**Figure S6** a) Yield of 30 kDa Amicon filter purified  $\text{DMC}_{39\text{pN}}$  [ $\text{Dex}_{\text{Cy5}}$ ] quantified using SYBR gold and Cy5 fluorescence. The percentage of DMC was calculated by normalizing to the initial concentration. Yield - 42% DMC. b) Concentrations of the empty  $\text{DMC}_{39\text{pN}}$  was increased to an additional a) 10 nM b) 20 nM c) 30 nM to support healthy cell adhesion and  $\text{Dex}_{\text{Cy5}}$  uptake was then quantified after 2 hours using flow cytometry.

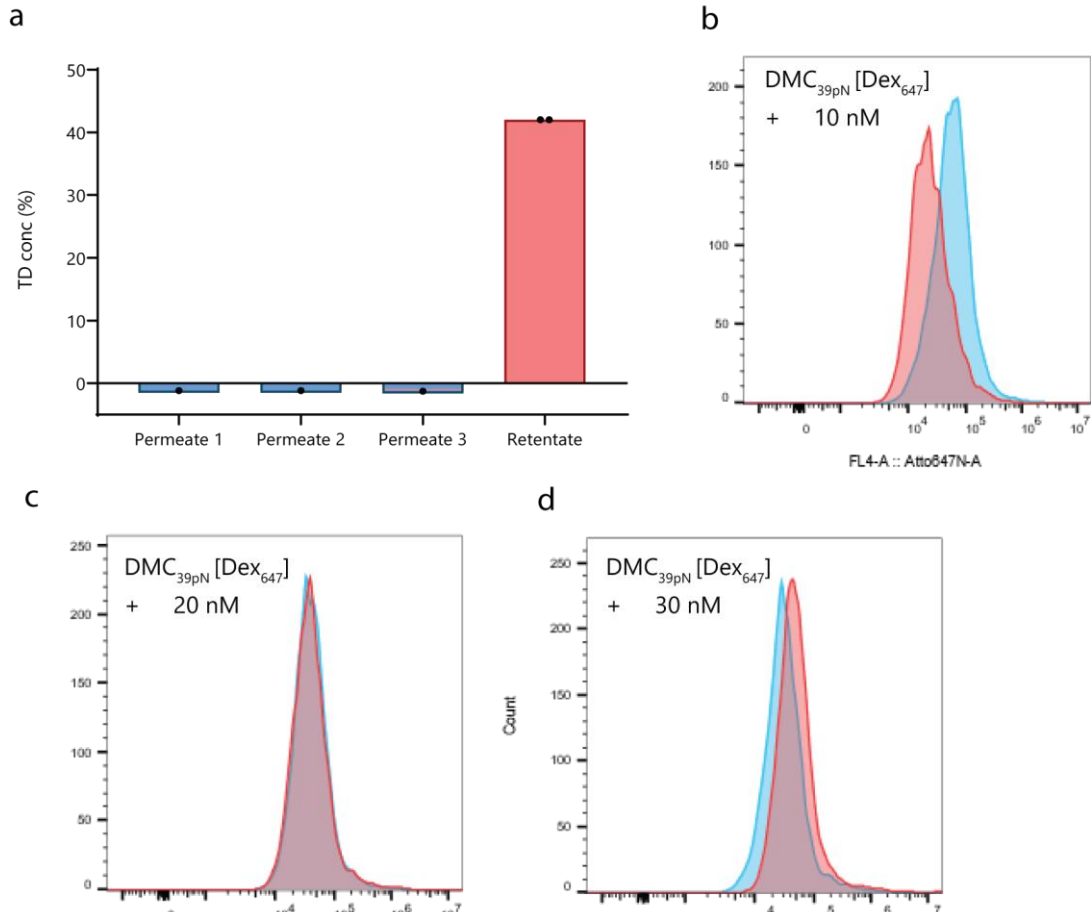
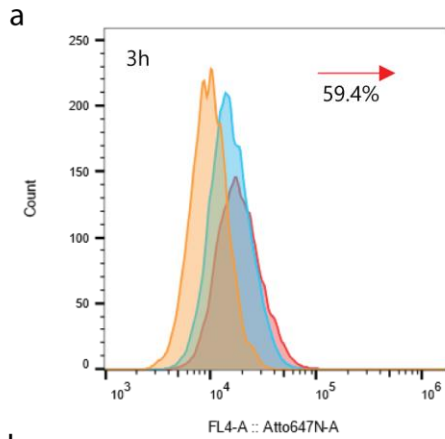
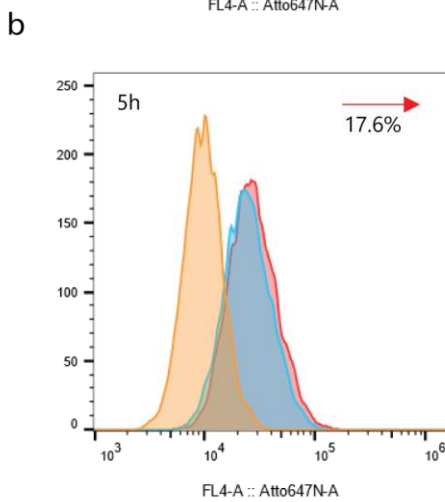


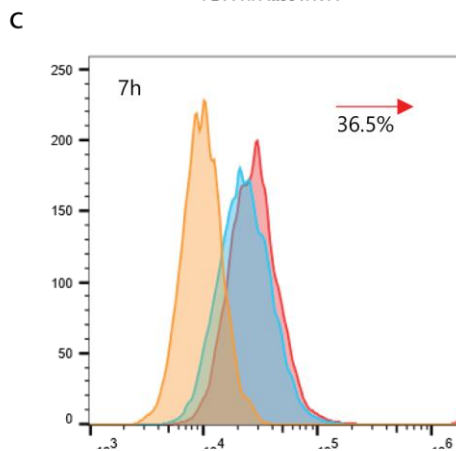
**Figure S7** Force induced uptake of Dex<sub>647N</sub> from DMC<sub>39pN</sub> [Dex<sub>647N</sub>] analyzed using flow cytometry at 3h, 5h and 7h time points. It was observed that the earlier time point produced the maximum signal since the 10% serum in cell media could cause degradation of the DMCs. The reduction in differential uptake could also be due to uptake of nonspecifically bound dextrans from the surfaces.



Sample Name	Geometric Mean : FL4-A	Mean : FL4-A	SD : FL4-A
Blank.fcs	9780	10724	6628
pTD+TD-D10 3h.fcs	15506	17714	28183
pTD-D10+TD 3h.fcs	18910	23513	55899



Sample Name	Geometric Mean : FL4-A	Mean : FL4-A	SD : FL4-A
Blank.fcs	9780	10724	6628
pTD+TD-D10 5h.fcs	24871	30178	55966
pTD-D10+TD 5h.fcs	27522	31718	22269



Sample Name	Geometric Mean : FL4-A	Mean : FL4-A	SD : FL4-A
Blank.fcs	9780	10724	6628
pTD+TD-D10 7h.fcs	23183	27663	37607
pTD-D10+TD 7h.fcs	28081	36222	78062

**Figure S8** MEF cells were seeded on DMC<sub>39pN</sub> [Dex<sub>647N</sub>] functionalized surfaces and the uptake was measured using flow cytometer after 2 hrs. Vinculin (GFP) vs Dextran uptake (Atto647N) plot of (a) MEF cells expressing GFP-tagged Vinculin (GFP-Vin), (b) MEF cells with Vinculin knocked out (VinKO), (c) an overlay of (a,b), (d) a co-culture of MEF GFP-Vin and MEF VinKO on the same DMC<sub>39pN</sub> [Dex<sub>647N</sub>] surfaces, (e) normalized uptake of Vin-GFP compared to the VinKO cells cultured on separate surfaces.

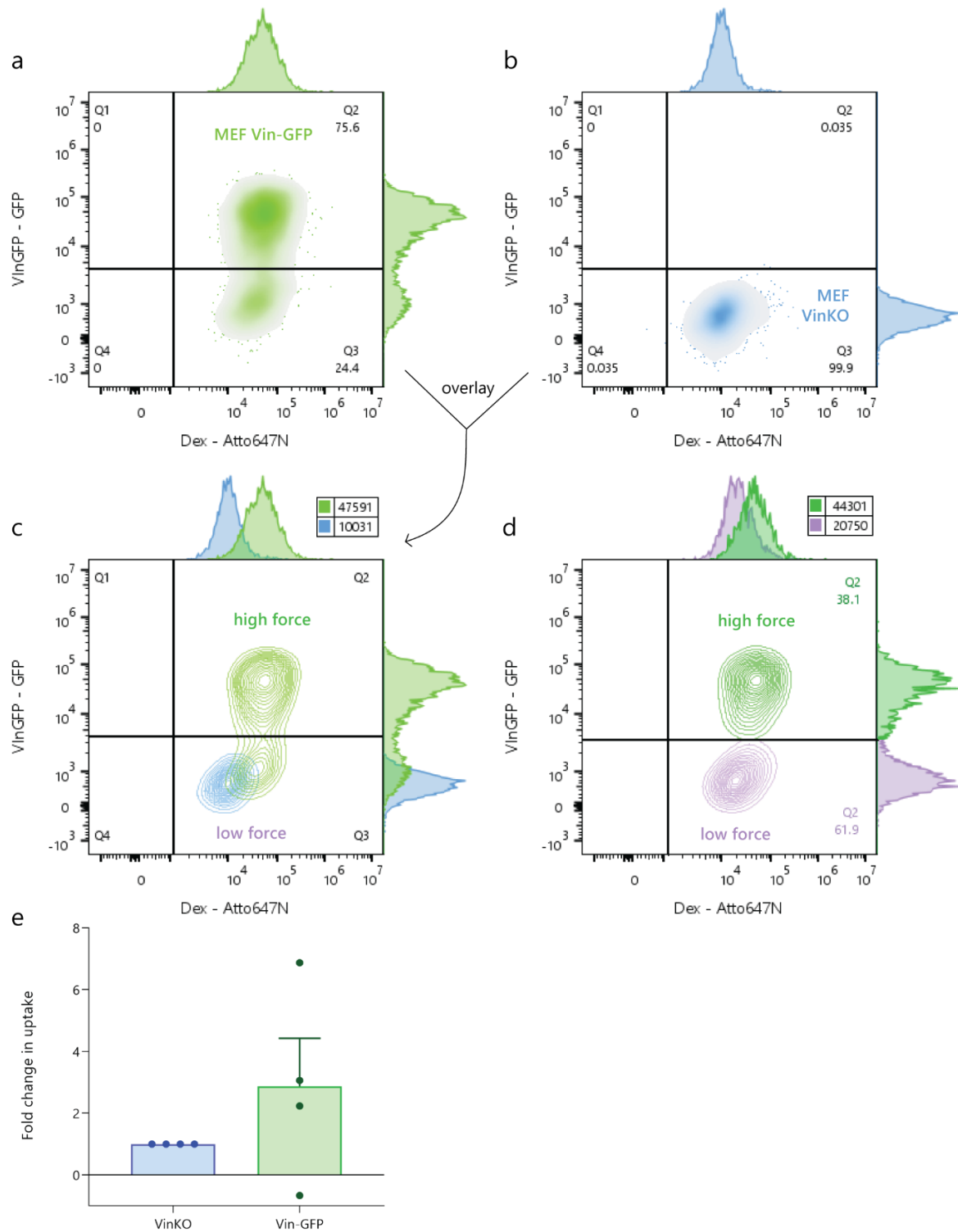
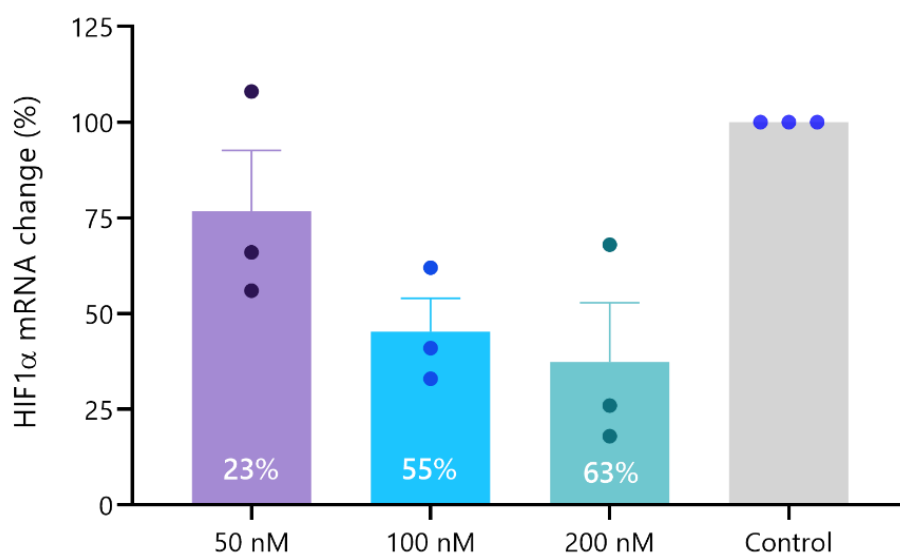


**Figure S9** HeLa cells were treated with HIF1 $\alpha$  antisense oligonucleotide, and the mRNA knockdown was quantified using qRT-PCR. Briefly cells were seeded in 10% FBS in DMEM for 24 hours in 12 well plates and then the media was replaced with 500  $\mu$ l of optiMEM media containing different concentrations of the antisense drug. After 4h the FBS was added to the media and the cells were allowed to grow for another 20 hrs. At the end of 2<sup>nd</sup> day, cells were lysed, and the mRNA levels were analyzed using RT-qPCR. Each dot represents a biological replicate, and the error bars denote SEM. HIF1 $\alpha$  mRNA levels were measured using 18S as a reference gene. The numbers in the bar graph denote the reduction in mRNA expression levels.



To achieve a mRNA knockdown of 23%, a concentration of 50 nM of the drug in 500  $\mu$ l of the media (25 picomoles) was required. The same knockdown can be achieved using a 600  $\mu$ l of 15 nM HIF1 $\alpha$  loaded DMC (10 picomoles). Only a fraction of these DMCs are functionalized to the surfaces. From SLB calibration, we know a concentration of  $\sim$ 13 nM yields a surface density of  $3.01 \pm 0.27$  femtomoles/cm<sup>2</sup>. For an ATTO chamber the surface area is  $\sim$ 3 cm<sup>2</sup> which corresponds to  $\sim$ 10 femtomoles which corresponds to a  $\sim$ 1000-fold increase in potency.

## References

1. Manzari, M. T. *et al.* Targeted drug delivery strategies for precision medicines. *Nat Rev Mater* **6**, 351–370 (2021).
2. Liu, Y. *et al.* Nanoparticle Tension Probes Patterned at the Nanoscale: Impact of Integrin Clustering on Force Transmission. *Nano Lett.* **14**, 5539–5546 (2014).
3. Zhang, Y. *et al.* Platelet integrins exhibit anisotropic mechanosensing and harness piconewton forces to mediate platelet aggregation. *Proceedings of the National Academy of Sciences* **115**, 325–330 (2018).
4. Liu, Y. *et al.* DNA-based nanoparticle tension sensors reveal that T-cell receptors transmit defined pN forces to their antigens for enhanced fidelity. *Proceedings of the National Academy of Sciences* **113**, 5610–5615 (2016).
5. Ma, V. P.-Y. *et al.* The magnitude of LFA-1/ICAM-1 forces fine-tune TCR-triggered T cell activation. *Science Advances* **8**, eabg4485 (2022).
6. Wang, J. *et al.* Profiling the origin, dynamics, and function of traction force in B cell activation. *Science Signaling* **11**, eaai9192 (2018).
7. Ketchum, C. M. *et al.* Subcellular topography modulates actin dynamics and signaling in B-cells. *MBoC* **29**, 1732–1742 (2018).
8. Narui, Y. & Salaita, K. Membrane Tethered Delta Activates Notch and Reveals a Role for Spatio-Mechanical Regulation of the Signaling Pathway. *Biophysical Journal* **105**, 2655–2665 (2013).
9. Wang, X. & Ha, T. Defining Single Molecular Forces Required to Activate Integrin and Notch Signaling. *Science* **340**, 991–994 (2013).
10. Zhang, Y., Ge, C., Zhu, C. & Salaita, K. DNA-based digital tension probes reveal integrin forces during early cell adhesion. *Nat Commun* **5**, 5167 (2014).

11. Brockman, J. M. *et al.* Live-cell super-resolved PAINT imaging of piconewton cellular traction forces. *Nat Methods* **17**, 1018–1024 (2020).
12. Nordenfelt, P., Elliott, H. L. & Springer, T. A. Coordinated integrin activation by actin-dependent force during T-cell migration. *Nat Commun* **7**, 13119 (2016).
13. Mierke, C. T. Mechanical Cues Affect Migration and Invasion of Cells From Three Different Directions. *Frontiers in Cell and Developmental Biology* **8**, (2020).
14. Panagiotakopoulou, M. *et al.* Cell cycle–dependent force transmission in cancer cells. *MBoC* **29**, 2528–2539 (2018).
15. Uroz, M. *et al.* Regulation of cell cycle progression by cell–cell and cell–matrix forces. *Nat Cell Biol* **20**, 646–654 (2018).
16. Wolfenson, H., Yang, B. & Sheetz, M. P. Steps in Mechanotransduction Pathways that Control Cell Morphology. *Annual Review of Physiology* **81**, 585–605 (2019).
17. Korin, N. *et al.* Shear-Activated Nanotherapeutics for Drug Targeting to Obstructed Blood Vessels. *Science* **337**, 738–742 (2012).
18. Stejskalová, A., Oliva, N., England, F. J. & Almquist, B. D. Biologically Inspired, Cell-Selective Release of Aptamer-Trapped Growth Factors by Traction Forces. *Advanced Materials* **31**, 1806380 (2019).
19. Konen, J. *et al.* Image-guided genomics of phenotypically heterogeneous populations reveals vascular signalling during symbiotic collective cancer invasion. *Nat Commun* **8**, 15078 (2017).
20. Ingber, D. Mechanobiology and diseases of mechanotransduction. *Annals of Medicine* **35**, 564–577 (2003).
21. Liu, M., Du, H., Zhang, W. & Zhai, G. Internal stimuli-responsive nanocarriers for drug delivery: Design strategies and applications. *Materials Science and Engineering: C* **71**, 1267–1280 (2017).
22. Layton, T. B. *et al.* Single cell force profiling of human myofibroblasts reveals a biophysical spectrum of cell states. *Biology Open* **9**, bio049809 (2020).



23. Ma, X. *et al.* Changes in biophysical and biochemical properties of single bronchial smooth muscle cells from asthmatic subjects. *American Journal of Physiology-Lung Cellular and Molecular Physiology* **283**, L1181–L1189 (2002).
24. Faffe, D. S. & Zin, W. A. Lung Parenchymal Mechanics in Health and Disease. *Physiological Reviews* **89**, 759–775 (2009).
25. Yanez, L. Z., Han, J., Behr, B. B., Pera, R. A. R. & Camarillo, D. B. Human oocyte developmental potential is predicted by mechanical properties within hours after fertilization. *Nat Commun* **7**, 10809 (2016).
26. Weiden, J. & Bastings, M. M. C. DNA origami nanostructures for controlled therapeutic drug delivery. *Current Opinion in Colloid & Interface Science* **52**, 101411 (2021).
27. Duangrat, R., Udomprasert, A. & Kangsamaksin, T. Tetrahedral DNA nanostructures as drug delivery and bioimaging platforms in cancer therapy. *Cancer Science* **111**, 3164–3173 (2020).
28. Goodman, R. P. *et al.* Rapid Chiral Assembly of Rigid DNA Building Blocks for Molecular Nanofabrication. *Science* **310**, 1661–1665 (2005).
29. Crawford, R. *et al.* Non-covalent Single Transcription Factor Encapsulation Inside a DNA Cage. *Angewandte Chemie International Edition* **52**, 2284–2288 (2013).
30. Lu, H., Xu, S., Guo, Z., Zhao, M. & Liu, Z. Redox-Responsive Molecularly Imprinted Nanoparticles for Targeted Intracellular Delivery of Protein toward Cancer Therapy. *ACS Nano* **15**, 18214–18225 (2021).
31. Qiu, Y., Bai, J., Feng, Y., Shi, X. & Zhao, X. Use of pH-Active Catechol-Bearing Polymeric Nanogels with Glutathione-Responsive Dissociation to Codeliver Bortezomib and Doxorubicin for the Synergistic Therapy of Cancer. *ACS Appl. Mater. Interfaces* **13**, 36926–36937 (2021).
32. Maar, J. S. de *et al.* Phase I feasibility study of Magnetic Resonance guided High Intensity Focused Ultrasound-induced hyperthermia, Lyso-Thermosensitive Liposomal Doxorubicin and

- cyclophosphamide in de novo stage IV breast cancer patients: study protocol of the i-GO study. *BMJ Open* **10**, e040162 (2020).
33. Wang, F. *et al.* Gint4.T-Modified DNA Tetrahedrons Loaded with Doxorubicin Inhibits Glioma Cell Proliferation by Targeting PDGFR $\beta$ . *Nanoscale Research Letters* **15**, 150 (2020).
  34. Ijäs, H. *et al.* Unraveling the interaction between doxorubicin and DNA origami nanostructures for customizable chemotherapeutic drug release. *Nucleic Acids Research* **49**, 3048–3062 (2021).
  35. Blanchard, A. T. & Salaita, K. Emerging uses of DNA mechanical devices. *Science* **365**, 1080–1081 (2019).
  36. Goodman, R. P. *et al.* Rapid Chiral Assembly of Rigid DNA Building Blocks for Molecular Nanofabrication. *Science* **310**, 1661–1665 (2005).
  37. Dai, B., Hu, Y., Duan, J. & Yang, X.-D. Aptamer-guided DNA tetrahedron as a novel targeted drug delivery system for MUC1-expressing breast cancer cells in vitro. *Oncotarget* **7**, 38257–38269 (2016).
  38. Meng, L. *et al.* Tetrahedral DNA Nanostructure-Delivered DNAzyme for Gene Silencing to Suppress Cell Growth. *ACS Appl. Mater. Interfaces* **11**, 6850–6857 (2019).
  39. Guo, W. *et al.* Self-Assembly of a Multifunction DNA Tetrahedron for Effective Delivery of Aptamer PL1 and Pcsk9 siRNA Potentiate Immune Checkpoint Therapy for Colorectal Cancer. *ACS Appl. Mater. Interfaces* **14**, 31634–31644 (2022).
  40. Erben, C. M., Goodman, R. P. & Turberfield, A. J. Single-Molecule Protein Encapsulation in a Rigid DNA Cage. *Angewandte Chemie International Edition* **45**, 7414–7417 (2006).
  41. Kim, K.-R. *et al.* Streptavidin-mirror DNA tetrahedron hybrid as a platform for intracellular and tumor delivery of enzymes. *Journal of Controlled Release* **280**, 1–10 (2018).
  42. Jeong, W. *et al.* Pilot trial of EZN-2968, an antisense oligonucleotide inhibitor of hypoxia-inducible factor-1 alpha (HIF-1 $\alpha$ ), in patients with refractory solid tumors. *Cancer Chemother Pharmacol* **73**, 343–348 (2014).

43. Sass, S. *et al.* Binding affinity data of DNA aptamers for therapeutic anthracyclines from microscale thermophoresis and surface plasmon resonance spectroscopy. *Analyst* **144**, 6064–6073 (2019).
44. Xia, Z. *et al.* Tumor-Penetrating Peptide-Modified DNA Tetrahedron for Targeting Drug Delivery. *Biochemistry* **55**, 1326–1331 (2016).
45. Watson, P. M. D. *et al.* Modelling the endothelial blood-CNS barriers: a method for the production of robust in vitromodels of the rat blood-brain barrier and blood-spinal cord barrier. *BMC Neuroscience* **14**, 59 (2013).
46. Ma, R. *et al.* DNA probes that store mechanical information reveal transient piconewton forces applied by T cells. *Proceedings of the National Academy of Sciences* **116**, 16949–16954 (2019).
47. Kraning-Rush, C. M., Califano, J. P. & Reinhart-King, C. A. Cellular Traction Stresses Increase with Increasing Metastatic Potential. *PLOS ONE* **7**, e32572 (2012).
48. Li, Z. *et al.* Cellular traction forces: a useful parameter in cancer research. *Nanoscale* **9**, 19039–19044 (2017).
49. Young, O. *et al.* Folate Receptor as a Biomarker and Therapeutic Target in Solid Tumors. *Current Problems in Cancer* **47**, 100917 (2023).
50. Rimawi, M. F., Schiff, R. & Osborne, C. K. Targeting HER2 for the Treatment of Breast Cancer. *Annual Review of Medicine* **66**, 111–128 (2015).
51. Semenza, G. L. Targeting HIF-1 for cancer therapy. *Nat Rev Cancer* **3**, 721–732 (2003).
52. Sharma, R., Dong, Y., Hu, Y., Ma, V. P.-Y. & Salaita, K. Gene Regulation Using Nanodiscs Modified with HIF-1- $\alpha$  Antisense Oligonucleotides. *Bioconjugate Chem.* **33**, 279–293 (2022).
53. Hoffmann-La Roche. *A Phase 1b, Proof of Mechanism, Open-label Study of RO7070179, a Hypoxia-inducible Factor 1 $\alpha$  (HIF1A) mRNA Antagonist in Adult Subjects With Hepatocellular Carcinoma (HCC)*. <https://clinicaltrials.gov/ct2/show/NCT02564614> (2018).

54. Bridgewater, R. E., Norman, J. C. & Caswell, P. T. Integrin trafficking at a glance. *Journal of Cell Science* **125**, 3695–3701 (2012).
55. Moreno-Layseca, P., Icha, J., Hamidi, H. & Ivaska, J. Integrin trafficking in cells and tissues. *Nat Cell Biol* **21**, 122–132 (2019).
56. Carnemolla, B. *et al.* Enhancement of the antitumor properties of interleukin-2 by its targeted delivery to the tumor blood vessel extracellular matrix. *Blood* **99**, 1659–1665 (2002).
57. Eigentler, T. K. *et al.* A Dose-Escalation and Signal-Generating Study of the Immunocytokine L19-IL2 in Combination with Dacarbazine for the Therapy of Patients with Metastatic Melanoma. *Clinical Cancer Research* **17**, 7732–7742 (2011).
58. Saw, P. E. *et al.* Aptide-conjugated liposome targeting tumor-associated fibronectin for glioma therapy. *J. Mater. Chem. B* **1**, 4723–4726 (2013).
59. Rudman, S. M. *et al.* A Phase 1 Study of AS1409, a Novel Antibody-Cytokine Fusion Protein, in Patients with Malignant Melanoma or Renal Cell Carcinoma. *Clinical Cancer Research* **17**, 1998–2005 (2011).

# CHAPTER 5

## Summary and Outlook

This chapter is partially adapted from a manuscript in submission: DNA mechanocapsules for programmable piconewton responsive drug delivery. Arventh Velusamy, Radhika Sharma, Sk Aysha Rashid, Hiroaki Ogasawara and Khalid Salaita

### 5.1 Summary

Our understanding of biological systems has progressed drastically in the last decades, which has been possible due to technological advancements. An interesting paradigm that has emerged is that biochemical processes have mechanical interactions that harmoniously work together. This improved understanding of biological systems and subsequently the field of mechanobiology. It is now known that the mechanical dysregulation of cells is associated with several disease states, that span from asthma to tumorigenesis.<sup>1,2</sup> A molecular level insight of the systems has been made possible with the development of single molecule force spectroscopy and molecular tension probes that have elucidated the nanomechanical forces exerted by various biomolecules in the cell.<sup>3,4</sup> DNA based probes have been widely used as force sensors that have illuminated the underlying mechanical processes of many cellular components including various disease states.<sup>5</sup> Mechanical forces generated by cells are associated with unique pathologies and may offer a new frontier in selective drug delivery. Such targeting approach based on dysregulated forces has not been reliably achieved due to the lack of force responsive cargo carriers. Further, cellular force targeting marks a departure from conventional drug delivery based on biochemical detection. Developing a force responsive system that can target the mechanical phenotype of a cell with tunable force thresholds with modular cargo encapsulation techniques would open new avenues in targeted drug delivery. We report DNA mechanocapsules based on the DNA tetrahedron, that represents the first tunable, modular, mechanical triggerable drug delivery system.

The dissertation introduced the role of mechanics experienced by living systems at all scales from tissue to molecular level. The popular methods for measuring cellular forces were described along with the importance of mechanical cues in medicine. Solutions were proposed to develop a mechanically responsive drug delivery platform to facilitate mechanical targeting which represents an unmet need in the field. In **Chapter 2**, DNA mechanocapsules (DMCs) which can be tuned to piconewton force thresholds that meet targeting and drug release requirements were elaborated. Computational modeling demonstrates a force-orientation agnostic, predictable rupture pathway that releases encapsulated contents. These DMCs can also be designed to be mechanically non-responsive structures that do not terminate mechanotransduction. All the designed mechanocapsules had minimal cargo leakage when it is non-covalently encapsulated despite having multiple pores.

In **Chapter 3**, the synthesis of these DNA mechanocapsules with various modifications was elucidated. These DNA mechanocapsules were found to have enhanced resistance to degradation and DMCs functionalized with adhesion ligands were shown to mechanically denature with 3T3 fibroblasts. Further the DMC rupture observed under HeLa cells were shown to overwhelmingly rupture from mechanical activity rather than non-specific degradation. Importantly, the DMCs with a lower threshold were demonstrated to discriminate breast cancer cells from normal breast cells. In **Chapter 4** different techniques to load drugs on the DMCs were explored. Initially, doxorubicin was used as a model drug for force responsive delivery. This was proved to be not possible due to the inherent properties of the small molecule. DMCs were then designed to encapsulate macromolecular dextran cargos. Force-induced uptake of the dextrans as well as high force selectively in a mixed population was validated using flow cytometry. Finally, force-induced knockdown of HIF1 $\alpha$  mRNA was demonstrated. These results show that DMCs can be effectively used to target biophysical phenotypes which may find useful applications in immunology and cancer biology. The consistent mechanical properties of DMCs make them a robust platform for therapeutic release based on cellular forces. DMCs in this regard can not only improve the specificity of existing therapeutics but also make it feasible to cure previously untargetable diseases.

## 5.2 Outlook

DNA mechanocapsule platform offers potential beyond therapeutic dominion into diagnostics and fundamental biological discoveries. DMCs are robust nanostructures with well characterized resistance against nucleases and stability in serum. DMCs can be constructed using commercially off the shelf oligonucleotides that can be customized for specific applications with simple conjugation protocols. These properties can be leveraged to construct *in vitro* tension sensors of varying force thresholds on different substrates with great ease. DMCs can also be used for tagging cells based on mechanical activity or ‘high-force’ phenotype. Finally, DMCs can be used for improving the selectivity of existing drugs ranging from small molecules to macromolecules based on force-triggered drug release. The potential and scope of these applications are elaborated in the following sections

### 5.2.1 DMCs FOR PRECISION BIOPHYSICAL TARGETING *in vivo*

DNA mechanocapsules (DMCs) offer tunable, well-defined force thresholds for targeting and precision drug-delivery to cells with elevated levels of receptor forces. DMCs can improve the specificity of cargoes by utilizing biophysical phenotypes for drug release in addition to the chemical selectivity of ligand-receptor binding.

In principle, DMCs bridging any two macromolecular complexes can be pulled open by piconewton forces to release cargo. Hence, a third layer of selectivity can be stacked upon the current design in an *in vivo* context by simply replacing the methyltetrazine anchor with a tissue specific anchor. For example, DMCs could be tethered to ECM using homing ligands such as fibronectin binding peptides and ECM-specific antibodies<sup>6-8</sup>. The DMCs’ design allows for arbitrarily increasing the anchoring strength that can withstand the molecular forces by decorating the DMC with multiple binders.

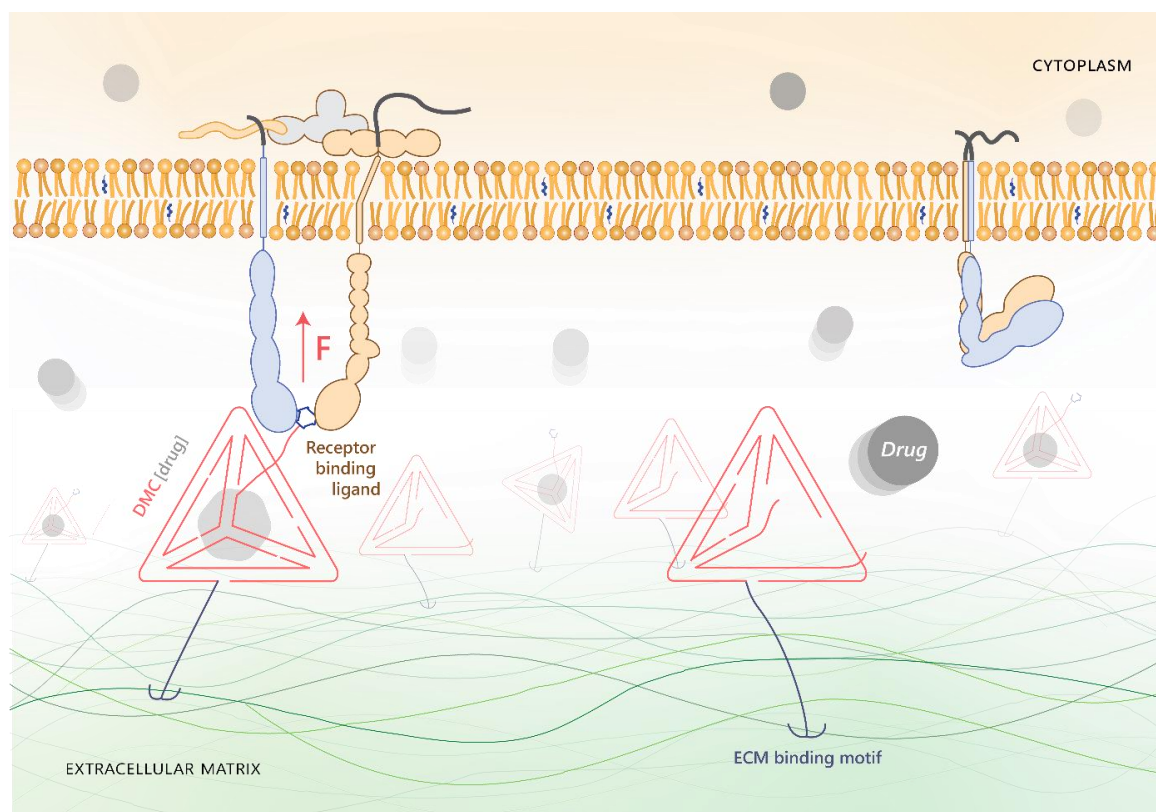


**Figure 5.1** Schematic of drug loaded DMC anchored to extracellular matrix (ECM) for *in vivo* drug delivery. DMCs are anchored to ECM using homing peptides, aptamers, and antibodies. This positions the DMCs adjacent to cells allowing its receptors to bind to the DMC ligands and thereby releasing the encapsulated drugs in a force-specific manner.

Furthermore, a localized force-based release mechanism benefits from the ability to produce a high concentration of drug in intimate proximity to the cell of interest. For example, only 1000 drug molecules are required to achieve a concentration of 1 nM in a HeLa cell. Hence, DMCs can protect a broad-spectrum drug safely until it reaches its destination and release it there for maximum efficacy. This vastly reduces the concentration of therapeutics required thereby minimizing off-target effects of systemic delivery.

### 5.2.2 DMCs AS DURABLE FORCE SENSORS



DNA tetrahedron have a proven record of being robust structures that can be produced in high yield. DNA mechanocapsules can be synthesized using 5-6 oligonucleotides as opposed to conventional DNA force robes which are assembled with 2-3 DNA strands. The conjugation of various chemical moieties such as ligand, anchor and fluorophores are simpler in DMCs as there are minimal requirements for orthogonality of reactions. The modifications can be placed on different strands while being in close proximity. This provides flexibility in the construction of the DMCs as force probes. Further, DMCs can be made to encapsulate a second ligand internally conjugated to the structure that is different from the initial ligand outward. When the first ligand experiences force and opens the structure the second ligand is exposed and can then report the mechanical interactions of its cognate receptor. Such force-based logic sensors can be used for illuminating mechanical events and pathways present among the cell receptors. DMCs can also be constructed for *in vivo* force-sensing using MRI contrast agents as cargo with the anchors being homing ligands for specific tissues to illuminate high-force phenotypic tissues that are associated with malignancies. Contrast agents and DMCs that were not uptaken by cells can be rapidly cleared by the body as DMCs are ideally sized for therapeutic nanoparticles. Hence, DMCs are versatile force sensing nanostructures with numerous applications that are worth further examination.

### 5.2.3 DMCs FOR HIGH THROUGHPUT MECHANOTAGGING

DMCs are well suited to release macromolecular cargo such as dextran based on receptor forces. The demonstration of force-induced release in this dissertation can be expanded further to encapsulate fluorescently coded dextrans in DMCs having different ligands. DMCs can be multiplexed in this fashion to sense forces from different receptors in a high throughput manner. DMCs with different force thresholds and correspondingly barcoded fluorescent dextrans can be used to sense populations of receptors exerting varying levels of forces. Cells can then be sorted using FACS for further downstream applications or analysis. DMCs can also be loaded with reagents and biomolecules which can be released due to specific receptor forces. Notably, such encapsulated cargo will remain inactive until they are released due to forces. Such cargo can then be used for manipulating cell behavior based on biomechanics

using mRNA knockdown, protein degradation or other similar approaches. These applications make DMCs a unique toolkit for force-sensing and offer unprecedented biophysical control for force responsive cell-engineering.

### 5.3 Concluding remarks

This dissertation aimed to elucidate the development novel force responsive drug delivery vehicles. This was achieved by using a DNA tetrahedron based system that was computationally engineered to produce DNA mechanocapsules. DMCs are robust and versatile carriers of various therapeutics with predefined force thresholds for targeting cells with high-force receptors. We envision a strategy similar to antibody-drug conjugates (ADCs) for the DMC platform. Antibodies confer the selectivity to the cytotoxic drugs that is conjugated. Antibodies reduce off-target effects and the high concentrations requirement of the therapeutics. Similarly, DMCs allow the use of a nonspecific drug that is activated only when the DMCs experience forces that rupture the structure. Such mechanically triggered drug activation can be leveraged to target diseases with increased receptor forces. Taken together, DMCs can be used to deliver therapeutic cargo in a force selective manner to target cells with specific biophysical phenotypes.

## 5.4 Other contributions

The following section describes my scientific contributions towards the advancement of other mechanobiology projects in the lab. Each section is adapted from papers that are either published or currently in submission. The papers below utilize oxDNA modeling work of the corresponding DNA force probes and they are summarized in the following sections. The figures are used with permission from the publisher.

- Tension-activated Cell Tagging (TaCT) for Mechanocytometry. Ma, R.; Rashid, A. \*; Velusamy, A. \*; Deal, B. R. \*; Chen, W.; Petrich, B.; Li, R.; Henry, C.; Salaita, K. *Nature Methods*. ([Flowcytometry characterization in addition to oxDNA modeling](#))
- DNA Origami Tension Sensors (DOTS) for measuring T-cell receptor mechanics at fluid interfaces. Hu, Y.; Duan, Y.; Velusamy, A.; Rogers J.; Narum S.; Salaita K. *Nature Immunology*.
- Cell adhesion receptors detect the unfolding pathway of their ligands. Bender R.; Ogasawara H.; Kellner A.V.; Grobe H.; Velusamy A.; Blanchard A. T.; Roca-Cusachs P.; Zaidel-Bar R.; Salaita K. *Nature*
- The magnitude of LFA-1/ICAM-1 forces fine-tune TCR-triggered T cell activation. Ma, V. P.-Y.; Hu, Y.; Kellner, A. V.; Brockman, J. M.; Velusamy, A.; Blanchard, A. T.; Evavold, B. D.; Alon, R.; Salaita, K. *Science Advances*, 2022, 8 (8), eabg4485.
- Measuring the loading rate of force on single integrin-ligand molecular complexes with a fluorescent DNA-based loading rate probe. Combs, J. D.; Ogasawara, H.; Foote, A. K.; Rashid, R.; Arventh, V.; Salaita K.

### 5.4.1 MAGNITUDE OF LFA-1/ICAM-1 FORCES FINE-TUNE TCR-TRIGGERED T CELL ACTIVATION

An unaddressed question in T cell mechanics is whether the forces transmitted through the LFA-1/ICAM-1 complex modulate T cell signaling. Using spectrally encoded DNA tension probes we elucidate the first traction force maps of LFA-1 and TCR generated by the T cell cytoskeleton upon antigen recognition. LFA-1 receptor  $F > 12$  pN potentiates antigen-dependent T cell activation by enhancing T cell–substrate engagement. LFA-1/ICAM-1 mechanical events with  $F > 12$  pN also enhance the discriminatory power of the TCR when presented with near cognate antigens. An important question in the study was if the rupture force of the DNA tension gauge tethers (TGTs) was dependent on the orientation of the receptor force.

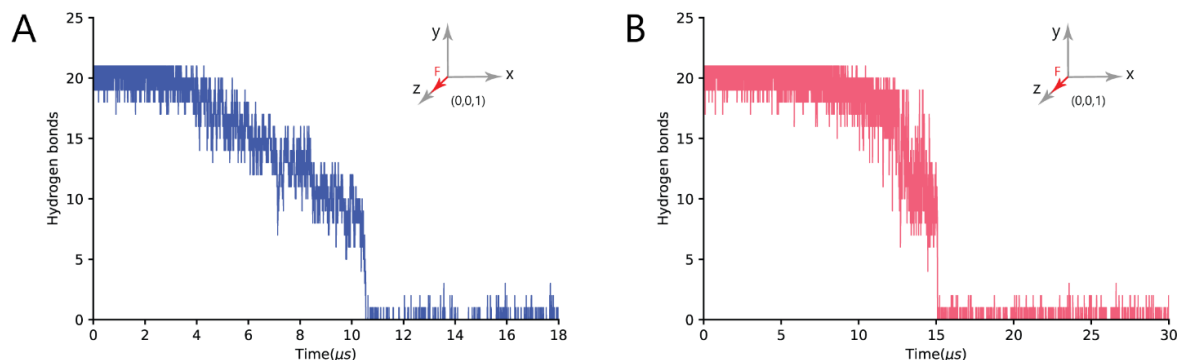


**Figure 5.2** Representative graph of DNA hydrogen bonds as a function of time for **A)** unzipping TGT and **B)** shearing TGT systems with the force application along direction (0,0,1).

To demonstrate that the  $T_{\text{tol}}$  of the TGT does not change based on the orientation of the applied force, we used oxDNA2 to simulate rupture of the dsDNA with different force orientations. TGTs can be designed with geometries that require different rupture forces: the unzipping geometry and the shearing geometry.<sup>9</sup> We ran MD simulations on oxDNA to predict the rupture force of TGTs under force loading from different orientations. TGTs can be designed with geometries that require different rupture forces: the unzipping geometry and the shearing geometry.<sup>10</sup> For each TGT configuration, we applied force along four different orientations  $[(x,y,z) = (1,0,0), (0,0,1), (1,1,1), (0,-1,1)]$  at the center of mass of the nucleotide highlighted

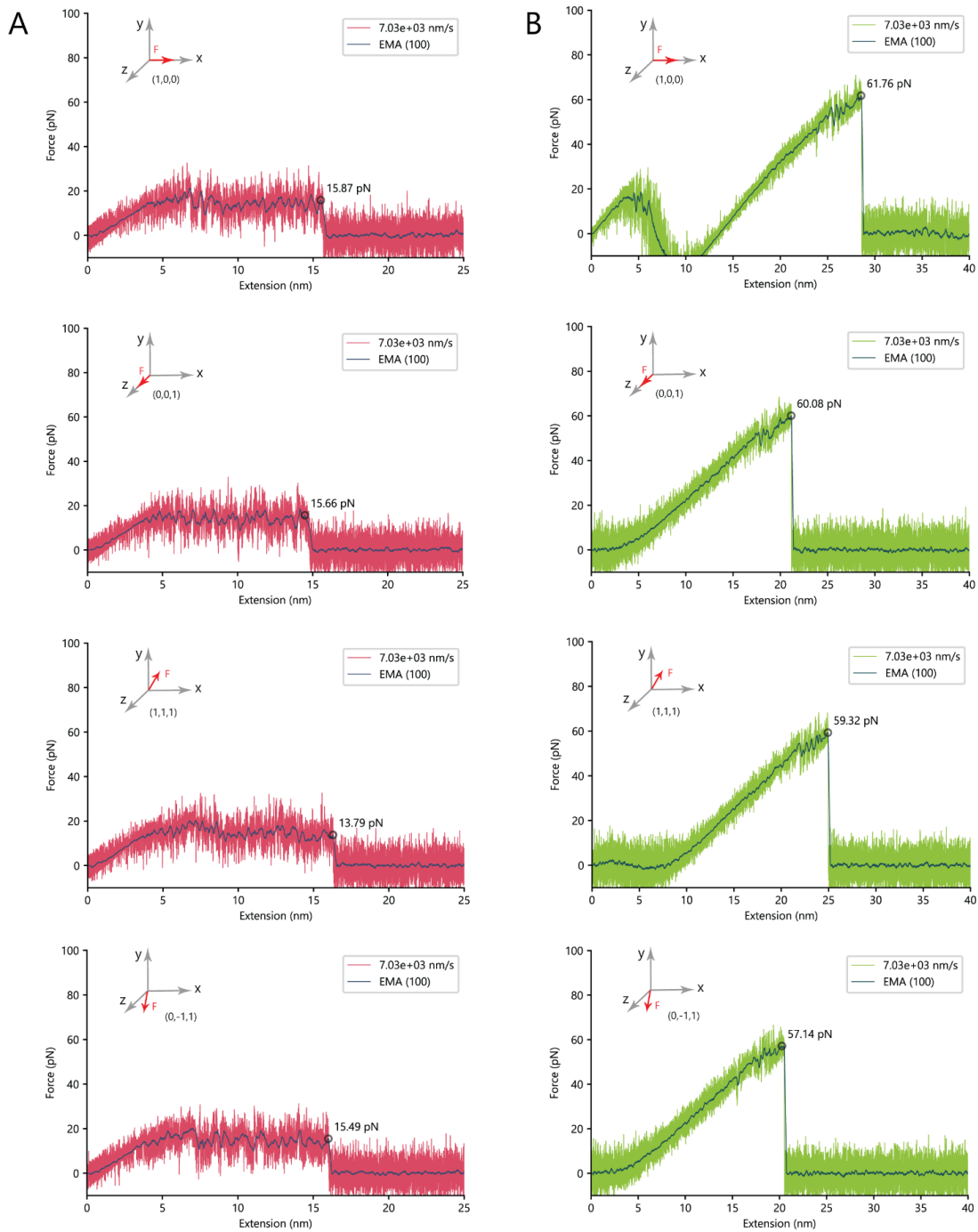


**Figure 5.3** Simulated force application along four directions (as indicated in inset) for A) “unzipping” TGT B) “shearing” TGT. The dark blue curves are 100-point EMA smoothed data.

in pink while keeping the nucleobase on the opposite strand fixed at its initial position. These 4 force orientations represent the application of pure lateral force, pure vertical force and two randomly chosen force vectors.

An extension rate of  $7.03 \times 10^3$  nm/s was used to move the trap along the indicated direction to generate a force-extension curve along the force axis. The force at a given point is calculated by multiplying the total projected extensions with  $k_{\text{eff}}$  (5.71 pN/nm). Force is then plotted against the projected displacement of the two traps from their initial location along with a 100-point exponential moving average (EMA) of the data points using python. We also extracted the number of hydrogen bonds for the system throughout the course of the simulation and plotted them against time. oxDNA considers hydrogen bonds as broken when the hydrogen bonding energy between a base pair is less than 10% that of a fully formed hydrogen bond. The rupture force was estimated by picking the peak at the point of rupture using SciPy find\_peaks module.<sup>11</sup> From the simulations, the  $T_{\text{tot}}$  of TGT subjected to unzipping or shearing remains relatively constant from the four tested pulling orientations [(x,y,z) = (1,0,0), (0,0,1), (1,1,1), (0,-1,1)] indicating the direction of applied force has a minimal impact on the  $T_{\text{tot}}$  (Figure 5.3). It must also be noted oxDNA runs have an inherent level of stochasticity that results in small variations in force estimation. Overall, the results show that the orientation of the receptor does not dictate the rupture force and T cells integrate multiple channels of mechanical information to tune its function.

#### 5.4.2 DNA ORIGAMI TENSION SENSORS (DOTS) TO STUDY T-CELL RECEPTOR MECHANICS AT FLUID INTERFACES

The T-cell receptor (TCR) transmits forces to its pMHC antigen, and its signaling specificity and amplitude is modulated by the magnitude and duration of these forces.<sup>3,12</sup> DNA-based tension probes have previously been used to generate piconewton force maps of TCR and pMHC anchored to a glass slide. A major drawback in this approach is that there is lack of lateral mobility and hence the spatial distribution of the forces remains poorly defined. To address this problem, we developed DNA origami tension sensors (DOTS) which allow measurement of TCR-antigen forces at intermembrane junctions. DOTS show that the TCR-pMHC complex experiences  $>8.4$  pN force at fluid interfaces where the antigen was tethered to a supported lipid bilayer (SLB). TCR forces are found to be dependent on the nanoscopic

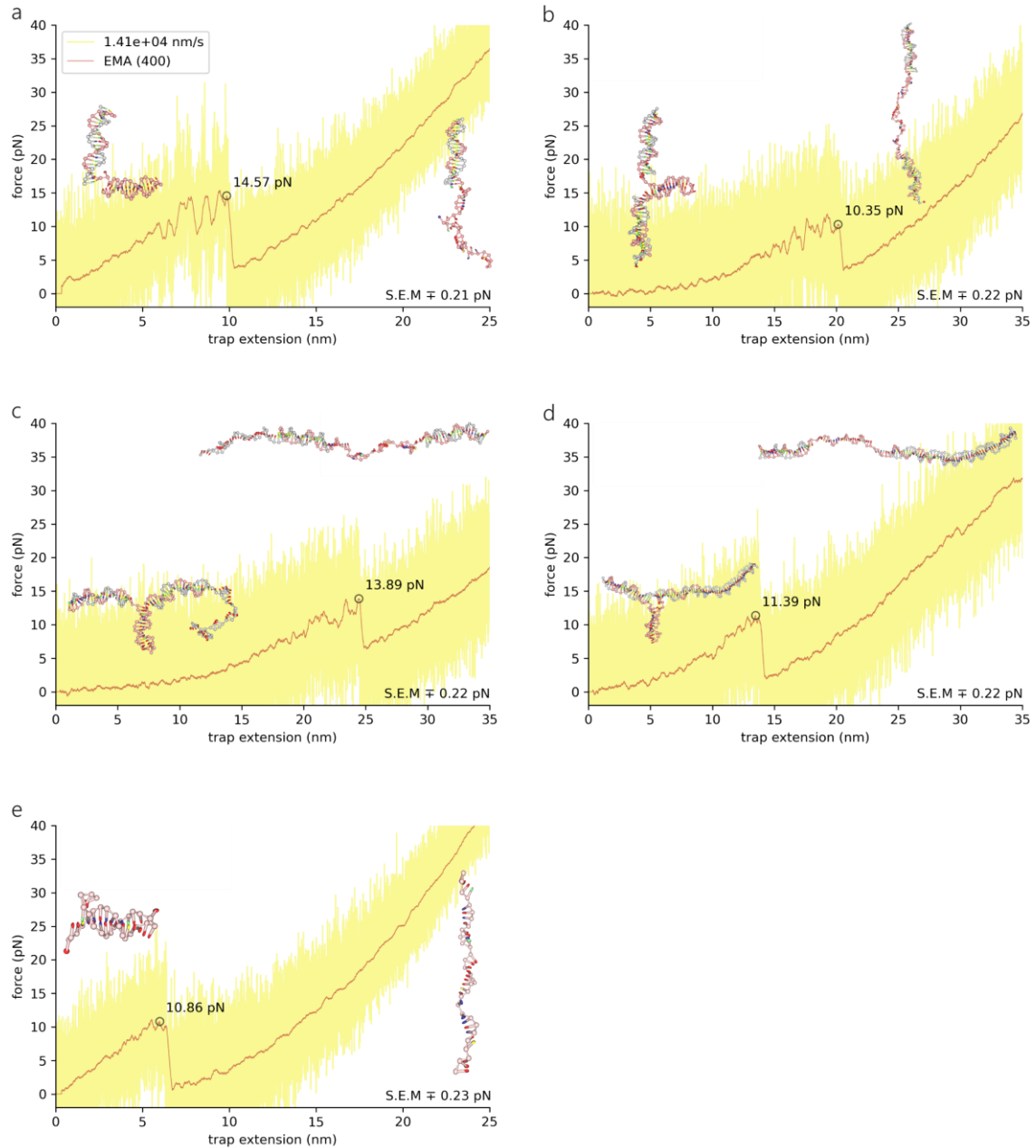


**Figure 5.4** Force-extension curves of hairpins pulled at the rate of  $1.4 \times 10^4$  nm/s in oxDNA simulations (yellow). The red curves indicate the smoothed data point (400-point exponential moving average). The initial configuration of the hairpins was depicted in the left while the final configurations with the opened hairpin are depicted on the right of the graph. The estimated force is marked at its peak in the graph along with its standard error of mean at the bottom right.

height of the antigen which was tuned by altering the height of the DNA hairpin probes on the DOTS. The rupture force of hairpins was then demonstrated to be independent of its height or linker length. Briefly this was done using oxDNA2 to simulate rupture of the hairpins with



different linker lengths. We ran MD simulations on oxDNA to predict the rupture force of hairpins under force along the z-axis. Temperature and [Na<sup>+</sup>] were set to 37°C and 0.156 M respectively to mimic in vitro experimental conditions. An extension rate of  $1.4 \times 10^4$  nm/s was used to move the trap on the ligand nucleotide along the z direction. The force was calculated by multiplying the total projected extension with  $k_{\text{eff}}$  and the graph was then smoothed with a 400-point exponential moving average (EMA) using python. The rupture force was estimated by picking the peak at the point of rupture using SciPy find\_peaks module (Figure 5.4). From the simulations, the rupture of hairpins remained relatively within the range of 10-14 pN and did not correlate with linker length.

### 5.4.3 TENSION-ACTIVATED CELL TAGGING (TaCT) FOR MECHANOCYTOMETRY

The readout of molecular forces generated by cells is traditionally done using fluorescence microscopy which is time consuming and has low throughput. Currently, there are no high throughput techniques that can quantify the magnitude of cellular forces. To address this gap, we introduce Tension-activated Cell Tagging (TaCT) which enables identification and sorting of cells based on the individual receptor forces using flow cytometry-based (Figure 5.5). TaCT uses the overstretching mechanism of dsDNA under force.<sup>13</sup> When a DNA duplex is stretched from both ends of a given strand, the duplex rapidly denatures leading to the complementary DNA separation. TaCT probes are engineered dsDNA with digital response to pN force and it releases a cholesterol-functionalized strand that partitions into the cell membrane.

To confirm the critical peeling force for this 24mer, we used the oxDNA coarse-grained model to apply a load of  $2.81 \times 10^3$  nm/s and recorded the number of base pairs in the duplex. The peeling force ( $F_{\text{peel}}$ ) was defined as the force at which the number of base pairs in the duplex is  $\leq 5$ . We found that  $F_{\text{peel}} = 41.3$  pN by averaging the first 100 data points after the number of base pairs drops below 6 in the simulation (Figure 5.5). Simulation also demonstrated that cholesterol labeled strand separated at force for the force bearing strand which is evident in

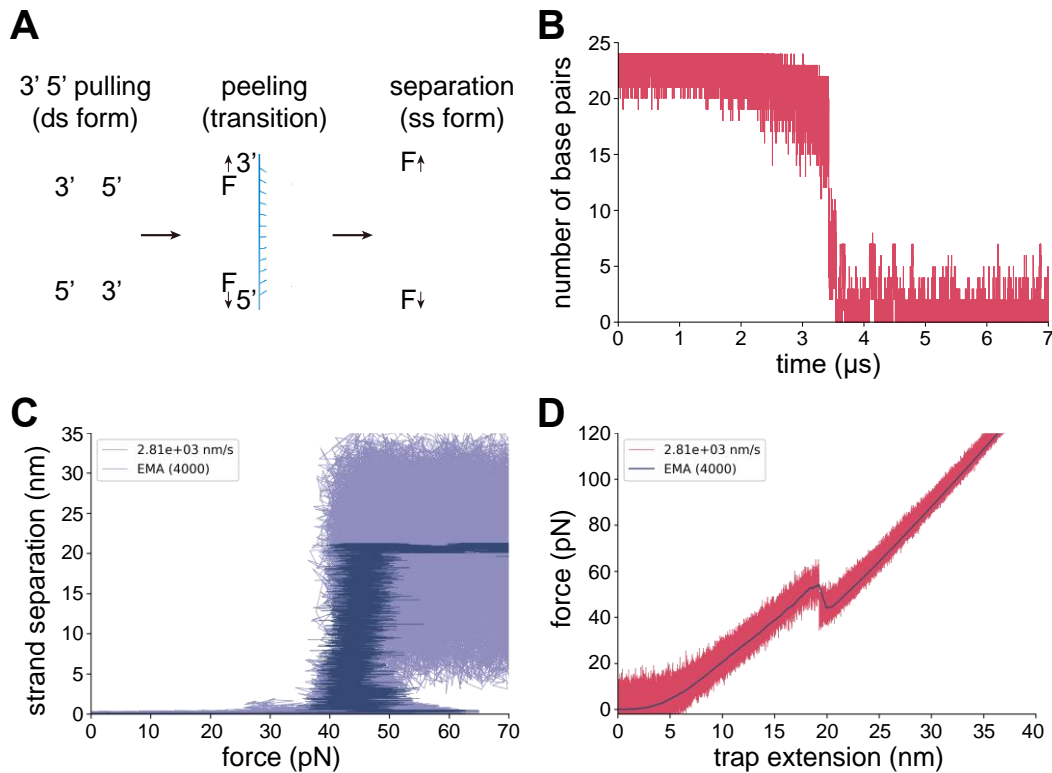


**Figure 5.5** (A) Scheme showing the force-induced peeling mechanism of oligonucleotides. (B) Simulation data of the transition state during force-induced peeling (update graph). The transition occurs on  $\mu\text{s}$  timescale, which further indicates that the transition state of peeling probe can be ignored while using it as a digital tension sensor. (C) Simulation result of the strand separation distance versus force. (D) Simulated force-distance curve. Conditions used for simulation: loading rate =  $2.81 \times 10^3$  nm/s, ionic strength = 0.156 M  $\text{Na}^+$ , and stiffness constant  $k_{\text{eff}} = 5.71$  pN/nm.

the force-strand separation plot. We further characterized the peeling forces of 36 bp oligo using the same protocol and we found  $F_{\text{peel}}$  to be 45.3 pN.

TaCT probes were then used to characterize the mechanical  $\text{IC}_{50}$  of Y27632 which diminishes the mechanical activity of cells by inhibiting Rho-associated coiled kinase. MEF cells were cultured on substrates grafted with 24mer TaCT probes and treated with varying concentrations of Y27632 drug (Figure 5.6). Then the cells were detached and analyzed using flow cytometry. We observed that the number of force events on the TaCT probes and consequently the uptake of the cholesterol strands decreased with increasing drug concentration and we estimated the  $\text{IC}_{50}$  to be 773 nM.

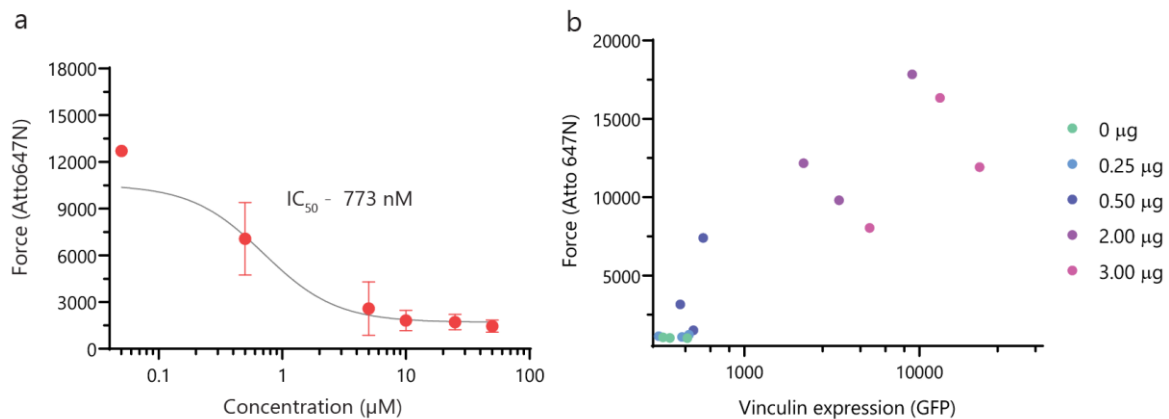


**Figure 5.6** a) MEF cells treated with varying concentration of Y27632 drug and measuring the cells mechanical activity using TaCT probes. Force here represents the median Atto647N intensity observed in flow cytometry ( $n=3$ ). b) MEF Vin-KO cells were transfected with Vin-GFP plasmids at varying concentrations and the corresponding GFP fluorescence were measure using flow cytometry. The force-tagging was then quantified with respect to the vinculin present in the cells. All data points are median intensities measured form a minimum of ten thousand cells in flow cytometry ( $n=3$ ).

To further demonstrate that the probes can report on the varying levels of mechanical activity, Vinculin-knockout MEF cells were transfected with Vinculin-GFP plasmids to restore cellular mechanics (Figure 5.6). We observed that with increasing levels of vinculin transfection, which could be quantified using the GFP fluorescence, the cells had higher number of force events as evident in the Atto647N tagging observed in flow cytometry. TaCT probes leverage the force induced dsDNA peeling mechanism to develop a novel class of tension probes that enable high-throughput quantification of mechanically active cells while being orthogonal to other methods of biochemical analysis. Hence, the TaCT has the potential to expand into new avenues in mechanobiology, potentially linking single-cell mechanicals with genomic and protein expression levels.

#### 5.4.4 CELL ADHESION RECEPTORS DETECT THE UNFOLDING PATHWAY OF THEIR LIGANDS

DNA force probe measurements have shown that integrins are responsible for sensing and activation of downstream signaling in response to piconewton forces from extracellular matrix. While it is known that integrin receptors sense force magnitudes, it is not clear if they also sense the unfolding pathways. To examine this, we synthesized two thermodynamically

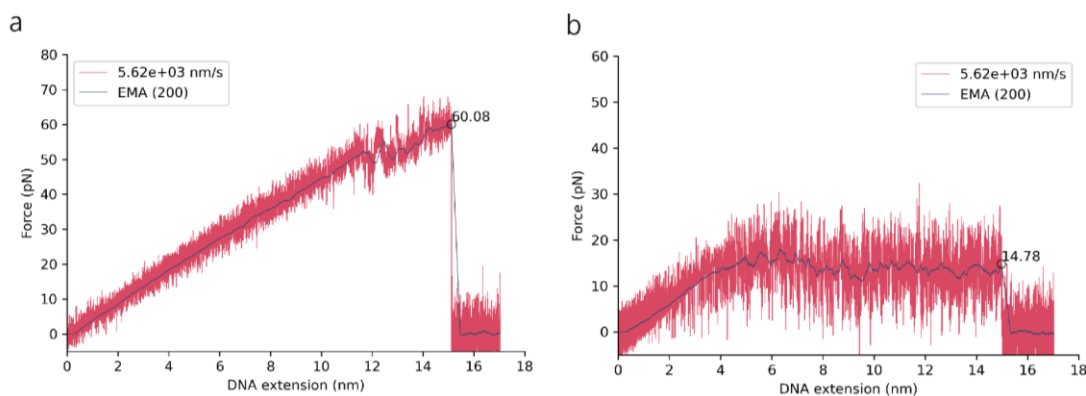


**Figure 5.7** Force-extension curves for the a) reversible shearing (RS) and b) reversible unzipping (RU) probes simulated using oxDNA. The probes were subjected to a loading rate of  $5.62 \times 10^3$  nm/s and the obtained data points were smoothed using 200-point exponential moving average (EMA) smoothing curve.

identical reversible DNA probes with different unfolding pathways. We estimated the rupture forces of these probes using oxDNA and found that one of the probes had a low force barrier of 14 pN (Reversible Shearing - RS) while the unfolded at 60 pN (Reversible Unzipping - RU). We discovered that cells cultured on the RS probes displayed dampened mechanotransduction markers including YAP translocation, integrin activation, focal adhesion turnover, fibronectin production, and stress fiber formation. Molecular clutch modeling supports our experimental data and shows that integrin-ligand complexes dissociate upon mechanical unfolding of the probes. This work demonstrates that cells sense abrupt disruption in mechanical interaction with its ligand.

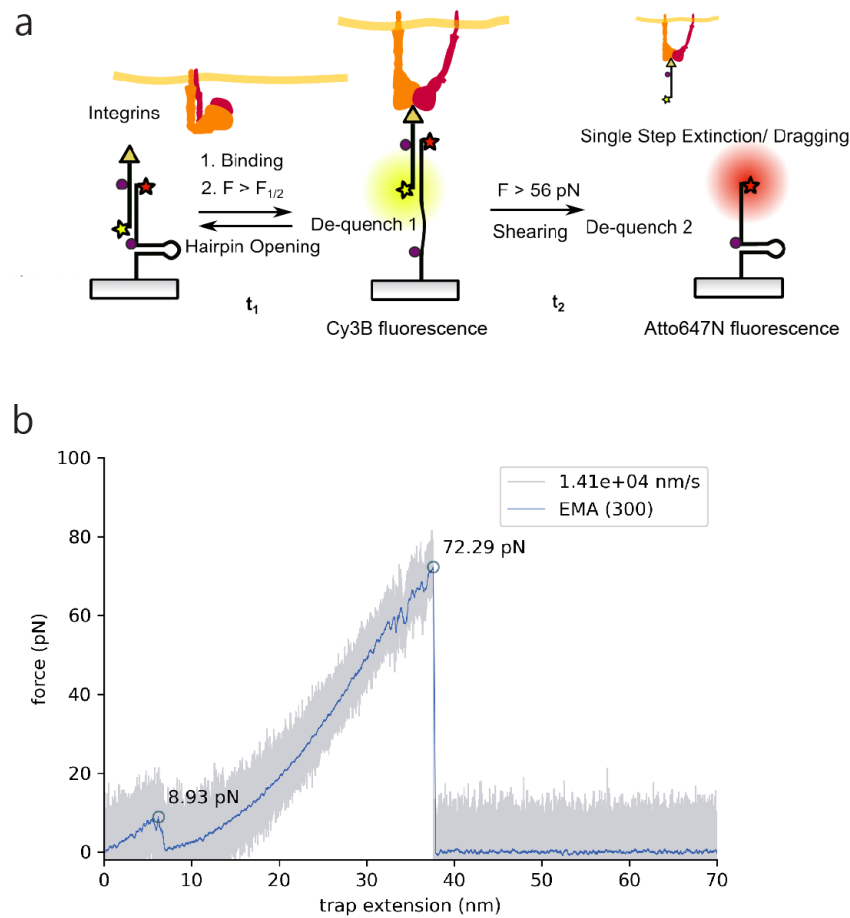


**Figure 5.8** a) Schematic of the loading rate force sensor with a hairpin and dsDNA shear sensor with different fluorophores. b) Force-extension curves for the loading rate probe simulated using oxDNA. The probes were subjected to a loading rate of  $1.4 \times 10^4$  nm/s and the obtained data points were smoothed using 200-point exponential moving average (EMA) smoothing curve.

#### 5.4.5 LOADING RATE ESTIMATION WITH DNA FORCE PROBES

An unresolved issue in the field of mechanobiology is observing the force loading rates of single integrin receptors with their ligand complexes.<sup>14</sup> Despite progress in measuring single cell receptor forces with high spatial and temporal resolution the loading rates of the integrin-ligand complexes are not well characterized. Using DNA force probes that can sense two force rupture thresholds the loading rate of single integrin receptors were measured at single molecule resolution. The probe has a hairpin and dsDNA element that ruptures at two

different force thresholds. Using sequence dependent oxDNA2 model the rupture force thresholds for the hairpin and the shearing motifs were estimated and were found to be 9 pN and 72 pN, respectively. By measuring the time elapsed between the opening of the hairpin and the shearing of the dsDNA the final loading rates of individual integrin receptors can be estimated. We envision that our single molecule loading rate DNA force probe will illuminate unanswered questions in the field of mechanobiology.

## References

1. Suresh, S. Biomechanics and biophysics of cancer cells. *Acta Materialia* **55**, 3989–4014 (2007).
2. Ma, X. *et al.* Changes in biophysical and biochemical properties of single bronchial smooth muscle cells from asthmatic subjects. *American Journal of Physiology-Lung Cellular and Molecular Physiology* **283**, L1181–L1189 (2002).
3. Zhang, Y., Ge, C., Zhu, C. & Salaita, K. DNA-based digital tension probes reveal integrin forces during early cell adhesion. *Nat Commun* **5**, 5167 (2014).
4. Ma, V. P.-Y. & Salaita, K. DNA Nanotechnology as an Emerging Tool to Study Mechanotransduction in Living Systems. *Small* **15**, 1900961 (2019).
5. Galior, K. *et al.* Molecular Tension Probes to Investigate the Mechanopharmacology of Single Cells: A Step toward Personalized Mechanomedicine. *Advanced Healthcare Materials* **7**, 1800069 (2018).
6. Arnoldini, S. *et al.* Novel peptide probes to assess the tensional state of fibronectin fibers in cancer. *Nat Commun* **8**, 1793 (2017).
7. Saw, P. E. *et al.* Aptide-conjugated liposome targeting tumor-associated fibronectin for glioma therapy. *J. Mater. Chem. B* **1**, 4723–4726 (2013).
8. Lo, K.-M. *et al.* huBC1-IL12, an immunocytokine which targets EDB-containing oncofetal fibronectin in tumors and tumor vasculature, shows potent anti-tumor activity in human tumor models. *Cancer Immunol Immunother* **56**, 447–457 (2007).
9. Snodin, B. E. K. *et al.* Introducing improved structural properties and salt dependence into a coarse-grained model of DNA. *J. Chem. Phys.* **142**, 234901 (2015).
10. Mosayebi, M., Louis, A. A., Doye, J. P. K. & Ouldrige, T. E. Force-Induced Rupture of a DNA Duplex: From Fundamentals to Force Sensors. *ACS Nano* **9**, 11993–12003 (2015).

11. Virtanen, P. *et al.* SciPy 1.0: Fundamental Algorithms for Scientific Computing in Python. *Nature Methods* **17**, 261–272 (2020).
12. Ma, R. *et al.* DNA probes that store mechanical information reveal transient piconewton forces applied by T cells. *Proceedings of the National Academy of Sciences* **116**, 16949–16954 (2019).
13. Romano, F., Chakraborty, D., Doye, J. P. K., Ouldridge, T. E. & Louis, A. A. Coarse-grained simulations of DNA overstretching. *J. Chem. Phys.* **138**, 085101 (2013).
14. Kechagia, J. Z., Ivaska, J. & Roca-Cusachs, P. Integrins as biomechanical sensors of the microenvironment. *Nat Rev Mol Cell Biol* **20**, 457–473 (2019).